TECHNISCHE UNIVERSITÄT MÜNCHEN

Fakultät für Medizin

Miniaturized Intravascular Catheters for High-Speed Near-infrared Fluorescence-Ultrasound Imaging of Atherosclerotic Lesions in Coronary Arteries

Philipp Rauschendorfer

Vollständiger Abdruck der von der Fakultät für Medizin der Technischen Universität München zur Erlangung eines

Doctor of Philosophy (Ph.D.)

genehmigten Dissertation.

Vorsitz: Priv.-Doz. Dr. Christian Sorg

Betreuer: Prof. Dr. Vasilis Ntziachristos

Prüfer*innen der Dissertation:

1. Prof. Dr. Michael Joner
2. Prof. Dr. Karl-Hans Englmeier

Die Dissertation wurde am 17.01.2023 bei der Fakultät für Medizin der Technischen Universität München eingereicht und durch die Fakultät für Medizin am 07.03.2023 angenommen.

Abstract

Intravascular near-infrared fluorescence (NIRF) imaging aims to improve the inspection of vascular pathology using fluorescent agents with specificity to biomarkers of atherosclerosis. The method is operating in tandem with an anatomical imaging modality, such as intravascular ultrasound (IVUS), thus combining structural readings and pathophysiological contrast. While previously developed NIRF-IVUS imaging systems have provided fundamental evidence for the potential of the technology, its clinical translation is hindered largely by the dimensions of the employed catheters, the acquisition speed, and the lack of validation in preliminary imaging studies.

This thesis introduces novel technological improvements, which are validated through imaging studies in phantoms and tissues. The main objectives of the thesis are to: 1) design and implement the protocol for developing NIRF-IVUS systems with miniaturized imaging catheters; 2) perform NIRF-IVUS system characterization; implement imaging studies in 3) pre-clinical animal models in vivo and in 4) excised human coronary arteries ex vivo with the developed systems; and 5) introduce a new method for the correction of light attenuation for intravascular NIRF signals measured through blood.

Within the framework of this thesis, two miniaturized NIRF-IVUS imaging catheters (Size 3.7F or 1.24 mm and 3.2F or 1.07 mm) were developed, which afford a size reduction of 15% and 24% compared to current existing catheters. In addition, the 3.2F system enables high-speed imaging with frame rates and pullback speeds up to 20 fps and 5 mm/s, correspondingly, achieving an improvement of at least 4-fold over previously reported systems.

An in vivo pre-clinical study in iliac arteries of various atherosclerotic rabbit models with the 3.2F catheter showed a significant contrast between the tissue areas of endothelial damage and foam cell formation and the healthy controls in indocyanine green (ICG) accumulation (i.e. 2.6-times NIRF signal difference). At the same time, imaging of ICG-perfused human coronary arteries with the 3.7F catheter ex vivo confirmed the correlation of NIRF signals with important pathological markers of atheroma, like inflammation, lipid accumulations, and signs of endothelial leakage and neovascularization. It also demonstrated, for the first time, that ICG concentration can be quantified and associated with different atherosclerotic disease states. The results of this study further suggest that NIRF-IVUS can be used to detect early-stage lesions featuring initial foam cell formation, while maintaining imaging contrast to healthy tissue and enabling quantitative inspection of atherosclerotic progression.

Finally, a method for correction of blood attenuation and quantification of NIRF signals based on a fluorophore-coated guidewire is introduced. The results from phantom ex vivo tissue measurements showed an improvement of up to 4.5-fold over uncorrected signals and errors of less than 11%.

The technology advancements and validation results presented in this thesis highlight the capabilities of intravascular NIRF-IVUS, setting the path for the next steps towards the clinical translation of this novel imaging technology.

Zusamenfassung

Die intravaskuläre Nahinfrarot-Fluoreszenz (NIRF) Bildgebung bestrebt die Untersuchung von vaskulärer Pathologie mittels Atherosklerose-spezifischen Fluoreszenzfarbstoffen zu verbessern. Die Methode wird zusammen mit einer anatomischen Bildgebungsmodalität wie intravaskulärer Ultraschall (IVUS) betrieben und kombiniert daher Strukturmessungen mit pathophysiologischen Kontrast. Vorherig entwickeltete NIRF-IVUS Bildgebungssysteme konnten fundamentale Beweise für das Potential der Technologie liefern. Jedoch ist die klinische Umsetzung momentan hauptsächlich von den Dimensionen der Bildgbeungskatheter, der Messaufnahmegeschwindigkeit und dem Fehlen von vorläufigen Bildgebungstudien limitiert.

Diese Dissertation stellt neuartige Verbesserungen der Technologie vor welche durch Bildgebungsstudien in Phantomen und Gewebe validiert werden. Die Hauptziele dieser Dissertation sind: 1) ein Protokoll für die Entwicklung von NIRF-IVUS Bildgebungssystemen mit miniaturisierten Kathetern zu erstellen und umzusetzen; 2) die NIRF-IVUS Systeme zu charackterisieren; Bildgebungsstudien mit den entwickelten Systemen in 3) lebenden präklinischen Tiermodellen und in 4) explantierten humanen Koronararterien durchzuführen; und 5) eine Methode für die Korrektur von Lichtabschächung während intravaskulären Messung durch Blut zu entwickeln.

Im Rahmen dieser Dissertation wurden zwei miniaturisierte NIRF-IVUS Bildgebungskatheter (Größe 3.7F oder 1.24 mm und 3.2F oder 1.07 mm) entwickelt was einer Verkleinerung von 15% und 24% im Vergleich zu bestehenden Kathetern entspricht. Zusätzlich wurde mit dem 3.2F System Hochgeschwindigkeitsbildgebung mit Bildraten und Rückziehgeschwindigkeiten von bis zu 20 fps und 5 mm/s erreicht was einer vierfachen Verbesserung im Vergleich zu vorherig beschriebenen Systemen entspricht.

In einer präklinischen Studie in den Beckenarterien (Arteria Iliaca) von verschiedenen lebenden atherosklerotischen Kaninchenmodellen wurde ein signifikanter Kontrast in Ansammlung von Indocyaningrün (ICG) in Gewebebereichen mit Endothelschädigunen und Schaumzellen im Vergleich zu gesunden Kontrollarterien detektiert (z.B 2.6-facher Unterschied in NIRF-Signalstärke). Zudem haben Messungen in ICG-perfundierten menschlichen Koronararterien die Korrelation von NIRF-Signalen mit relevanten pathologischen Markern von atherosklerotischen Plaques wie Entzündung, Lipidansammlungen und Anzeichen von Endothelschädigungen und Neovaskularisation bestätigt. Zusätzlich wurde zum ersten mal demonstriert, dass die quantifizierte ICG-Konzentration in Verbindung mit den verschiedenen atherosklerotischen Krankheitsstadien steht. Die Ergebnisse dieser Studie weisen auch darauf hin, dass die NIRF-IVUS Bildgebung für die Erkennung von Läsionen im Frühstadium mit initialer Schaumzellbildung benutzt werden kann während der Bildgebungskontrast zu gesundem Gewebe erhalten bleibt. Dies könnte letztendlich eine quantifizierbare Inspektion vom Fortschreiten der atherosklerotischen Entwicklung ermöglichen.

Zum Abschluss wird eine Methode für die Korrektur von Lichtabschwächung durch Blut und die Quantifizierung von NIRF-Signalen basierend auf einen mit Fluoreszenzfarbstoff beschichteten Führungsdraht vorgestellt. Die Ergebnisse von Messungen in Phantomen und explantiertem Gewebe zeigen eine bis zu 4.5-fache Verbessung im Vergleich zu unkorregierten Signalen und Fehler geringer als 11% auf.

Die technologischen Verbesserungen und Validierungsergebnisse, die in dieser Dissertation vorgestellt wurden, unterstreichen das Pontential von intravaskulärerm NIRF-IVUS und bereiten den Weg für die nächsten Schritte für eine klinische Anwendung dieser neuartigen Bildgebungstechnologie.

Acknowledgments

I want to dedicate this section to mention numerous people who have directly or indirectly helped me during the last 3+ years with the work presented in this PhD thesis.
First, I would like to thank Prof. Dr. Vasilis Ntziachristos for giving me the opportunity to work on this exciting research project at the Chair of Biological Imaging (CBI)/Institute for Biological and Medical Imaging (IBMI) and the invaluable knowledge and guidance he has provided me with over the last years.

Similarly, I want to thank Prof. Dr. Michael Joner for sharing his expertise in coronary pathology and pre-clinical animal models and his constant support and supervision throughout the years. The collaboration with Michael and the whole research team at the German Heart Center Munich has been a great pleasure and produced results presented in chapter 4 and 5 of this thesis. I want to specifically acknowledge Léa Utsch, Emina Sabic, Alicia Beele and Dr. Tobias Lenz for their contributions in the in vivo animal and ex vivo human cadaver study.

Over the last years I had the pleasure to be part of the fluorescence imaging group at CBI/IBMI which is lead by Dr. Dimitris Gorpas. Thank you Dimitris for the guidance, all the valuable lessons and countless discussions which allowed me to progress in all projects and become a better researcher. I also want to thank all current and former members of the fluorescence imaging group for not only their scientific help and advises but also the good times during lunch or coffee breaks. Many thanks to Prof. Dr. Karl-Hans Englmeier who has been a great mentor and assisted me with many administrative aspects of my PhD. I would like to also acknowledge former IBMI member Dr. Dmitry Bhozko for his contributions towards the development the 3.7F imaging catheter. I am very grateful to Dr. Georg Wissmeyer for his help with the assembly of the 3.2F imaging catheters, transferring his knowledge and sharing his expertise especially in the field of optics which helped me substantially for accomplishing several project goals. I want to thank Claudia Hofmann for working on the development of the software for the 3.2F NIRF-IVUS system as part of her Master thesis and for her great support for the high-speed imaging experiments. I want to also extend a big thank you to Dr. Antonios Stylogiannis who introduced me to 3D printing and other valuable lab techniques and has been a good friend to also discuss matters beyond work. I feel privileged to had the chance working with collaborators from Boston over the entire time span of my PhD. Thank you Dr. Farouc Jaffer and Scott Jones for the inspiring collaboration and the countless discussions with the shared goal to advance the intravascular NIRF-IVUS project. There are many great people working in administration at IBMI/CBI who I want to thank all for supporting me throughout my time at the institute. Thank you also to Dr. Robert Wilson for helping me with the writing process of publications and improving my scientific writing skills.

Finally, I want to thank all my friends and family for their invaluable support throughout my PhD journey. I am very grateful for my siblings, Clara and Max, who give me nothing but joy and have always been a beacon of light especially during challenging times. Words could not describe how grateful I am for my parents Christa and Andreas. I will be forever thankful for their indefatigable commitment in helping me with all matters in life. Last but not least I want to thank my fiance Savannah who has not only helped me significantly with numerous work-related questions but also with her tireless emotional support throughout the entire time working on my PhD. Thank you for your patience and giving me the energy to overcome all challenges on my path to finish my research projects and in life in general.

List of Abbreviations

αSMA alpha-Smooth Muscle Actin.

ACS Acute Coronary Syndrom.

BF Bright-Field Microscopy.

CABG Coronary Artery Bypass Graft.

CAC Coronary Artery Calcium Scoring.

CAD Coronary Artery Disease.

CHD Coronary Heart Disease.

CMR Cardiovascular Magnetic Resonance.

CMRA Cardiovascular Magnetic Resonance Angiography.

CS Compressed Sensing.

CT Computer Tomography.

CTCA Computer Tomography Coronary Angiography.

CVDs Cardiovascular Diseases.

CW Continuous Wave.

DAQ Data Acquisition.

DMSO Dimethyl Sulfoxide.

FD Frequency Domain.

FDA Food and Drug Agency.

FLIm Fluorescence Lifetime Imaging.

FM Fluorescence Microscopy.

FMT Fluorescence Molecular Tomography.

FORJ Fiber-Optic Rotary Joint.

fps Frame Per Second.

FRI Fluorescence Reflectance Imaging.

FWHM Full Width at Half Maximum.

GLP Good Laboratory Practices.

GUI Graphical User Interface.

HD-IVUS High-definition Intravascular Ultrasound.

ICA Invasive Coronary Angiography.

ICG Indocyanine Green.

IVOCT Intravascular Optical Coherence Tomography.

IVPA Intravascular Photoacoustic.

IVUS Intravascular Ultrasound.

LAD Left Anterior Descending Coronary Artery.

LCA Left Coronary Artery.

LCX Left Circumflex Coronary Artery.

LDL Low-density Lipoprotein.

LDPE Low-Density Polyethylene.

LIA Left Illiac Artery.

LIMA Left Internal Mammary Artery.

LOR Line of Response.

MDR Medical Device Regulations.

MI Myocardial Infarction.

MMA Methyl Methacrylate.

MP Movat Pentachrome.

MPE Maximum Permissible Exposure.

MRI Magnetic Resonance Imaging.

NA Numerical Aperture.

NIRF Near-Infrared Fluorescence.

NIRS Near-Infrared Spectroscopy.

ORO Oil Red O.

PBS Phosphate-buffered saline.

PCI Percutaneous Coronary Intervention.

PET Positron Emission Tomography.

PMT Photomultiplier Tube.

PSF Point Spread Function.

PW Pulsed Wave.

PZT Lead Zirconate Titanate.

RCA Right Coronary Artery.

RF Radio Frequency.

RIA Right Illiac Artery.

ROI Region of Interest.

rpm rounds per minute.

SNR Signal-to-Noise Ratio.

STEMI ST-Elevation Myocardial Infarction.

TD Time Domain.

VH-IVUS Virtual Histology Intravascular Ultrasound.

Contents

Chapter 1

Introduction

1.1 Coronary Artery Disease

According to the World Health Organization, cardiovascular diseases (CVDs) are the leading cause of death worldwide [1]. CVDs are a group of diseases that involves the circulatory system and can be further classified based on the location they are affecting. Specifically, CVDs can be differentiated between coronary heart disease (CHD) or coronary artery disease (CAD), cerebrovascular disease, peripheral artery disease, rheumatic and congenital heart disease and venous thromboembolism (Table 1.1, [2]).

Name	Location
Coronary heart disease	Disease of the vessels supplying the heart
Cerebrovascular disease	Disease of the vessels supplying the brain
Peripheral arterial disease	Disease of the vessels supplying the arms and legs
Rheumatic heart disease	Damage to the heart muscle and valves from rheumatic fever
Congenital heart disease	Birth defects affecting the development and functioning of the heart
Venous thromboembolism	Blood clots in the leg veins

Table 1.1: Overview of cardiovascular diseases [2].

Out of the group of CVDs, CAD represents one of the most relevant ones from a clinical perspective. The reason why this disease is so significant becomes more clear when considering the physiological function of coronary arteries. The human heart is an essential organ functioning as a pump to supply the entire body with oxygen-rich blood. In order to maintain its function, the heart requires blood supply just like all other organs. For this purpose, the heart has its own vascular system, named cardiovascular circulation, which provides blood to the cardiac muscle, called myocardium. The two main vessels of the cardiovascular circulation are the right (RCA) and left coronary artery (LCA) which branch off the aorta right above the aortic valve. The LCA further separates into the left anterior descending (LAD) and circumflex (LCX) artery (Fig. 1.1).
Over the last decades it has been recognized that these arteries can develop lesions underlying pathological processes which are nowadays summarized under the umbrella term atherosclerosis. A major observation was published in 1976 by Davies et al. describing that coronary occlusion in the form of a thrombus led to acute myocardial infarction (MI), commonly known as heart attack, and sudden death [3]. Furthermore, it was reported that rupture or erosion of atherosclerotic plaques are the cause for thrombus formation [3, 4]. Despite most recent advances in the fields

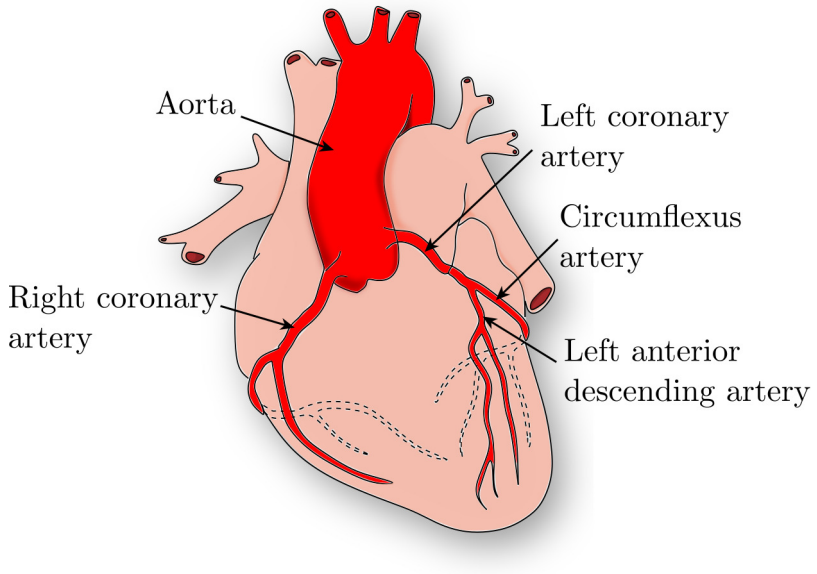

Figure 1.1: The Cardiovascular Circulation.

of diagnostics and therapy as well as a significantly improved understanding of the underlying pathobiology, CAD and MI remain a major clinical challenge. Specifically, CAD is a a global healthcare burden being associated with 17.8 million deaths annually and responsible for healthcare costs of around 200 billion dollars in the United States per year [5]. Furthermore, it is predicted that CVDs become even more relevant in the future as as the prevalence of risk factors like smoking, hypertension, abdominal obesity, diabetes and lack of exercise increase, especially in developing nations formerly regraded as low-risk countries [2].

1.2 The Pathobiology of Human Coronary Atherosclerosis

To understand how a healthy artery wall can transform into lesions, also called plaques, which can rupture and cause MI (Further described below), it is necessary to take a closer look at the pathobiological process of atherosclerosis. In general, atherosclerosis is understood as a chronic inflammatory disease which causes focal thickening of the tunica intima layer of the artery (Fig. 1.2, reviewed in [6–8]).
The development of atherosclerosis is triggered by damage or dysfunction of the endothelium which is part of the intima layer lining the interior surface of all vessels. While a functioning endothelial layer acts as a semipermeable barrier to blood flow inside the lumen, an increase in endothelial permeability represents the onset of an inflammatory response which ultimately drives the progression of atherosclerotic lesions (reviewed in [9, 10]).
Endothelial dysfunction can be stimulated by deviations in heamdoynamics like disturbance of laminar blood flow and corresponding decrease in shear-stress at e.g arterial bifurcation points (reviewed in [9, 11]).The active transport of low-density lipoprotein (LDL) and its accumulation in the subendothelial region can be regarded as a kick-off event for atherogensis [12].
Specifically, the secretion of chemokines by endothelial cells attracts monocytes and T lymphocytes which undergo three steps: 1) rolling adhesion, 2) activiation including cytokine production and 3) firm adhesion to the endothelial cells. Consequent activiation of the endothelium leads

to disruption of intercellular junctions and allows the migration of leucoyctes through the endothelium into the arterial tissue (reviewed in [6]).
Upon uptake of oxidized LDL (LDL can be oxidized by reactive oxygen species or lipoxygenases/myloperoxdiases) macrophages, previously migrated into the subintimal space, transform to foam cells which represents a key step in the progression of atherosclerosis (reviewed in [6–8]). This transformation further promotes inflammation by secretion of cytokines and growth factors. Consequently, foam cells undergo apoptosis and form a necrotic core (reviewed in [6, 7]). Furthermore, smooth muscle cells, originally located in the media, migrate to the intima, proliferate, take up oxidized LDL and finally form a fibrous cap. Angiogenisis (vasa vasorum) and neovascularization inside the vascular wall represents another characteristic of advanced plaque progression triggered by the hypoxic environment within the plaque (reviewed in [6–8]).

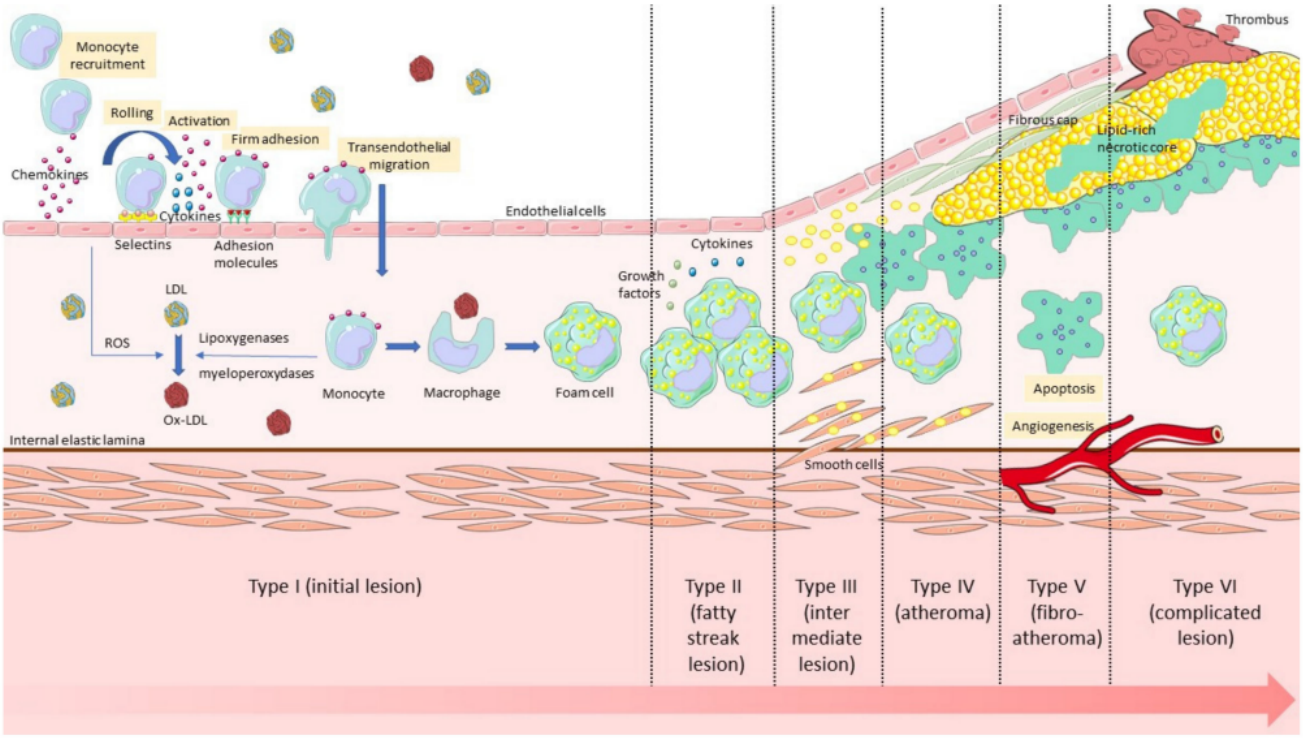

Figure 1.2: The stages of the development of atherosclerosis [6].

Calcification of the vasculature is an important process during the progression of atherosclerosis. There has been an ongoing debate whether the presence of calcification has a positive or negative effect on atherosclerotic lesions [13, 14]. In general, the process of calcification has been often regarded as the tissue's reaction to stabilize the unresolved source of inflammation which initially indicates a positive influence. However, it has been suggested that the overall influence of calcification on plaque stability depends on factors like size, shape and location of the calcification [13, 14]. For instance, while the presence of large calcified structures (macrocalcifications) has been inversely correlated to plaque rupture, smaller spotty calcifications (microcalcifications, 0.5–50 µm in size), which are often present in the early stages of the mineralization process, can contribute to plaque destabilization [8, 13, 14]. In addition to mircocalcifications, inflammatory processes and endothelial erosion can also increase the risk for plaque rupture by thinning of the fibrous cap (reviewed in [7]).

In general, lesions in coronary arteries can be categorized depending on their stage of disease progression [15]. Early non-atherosclerotic coronary lesions are categorized as intimal thickening and xanthoma (Intimal thickening with the presence of macrophage foam cells). Figure 1.3 provides an overview of the progression of atherosclerotic lesions. The next stages are defined as pathological intimal thickening without (Fig. 1.3-a) and with (Fig. 1.3-b) macrophage infiltration. The development of a necrotic core due to macrophages infiltrating lipid pools defines the next categories of early (Fig. 1.3-c) and late (Fig. 1.3-d) fibroatheromas. The necrotic core of the late fibroatheroma is characterized by the presence of less extra-cellular matrix and more cholesterol clefts, intraplaque hemorrhage as well as higher degrees of calcification compared to the earlier stage [15]. Finally, lesions of the last category are referred to as thin-cap fibroatheromas which typically feature a large necrotic core with an overlying thin fibrous cap featuring collagen and infiltrated macrophages/lymphocytes. Because of the fact that these type of lesions have been linked to plaque rupture, they are also commonly known as rupture-prone or vulnerable plaques [8, 15].

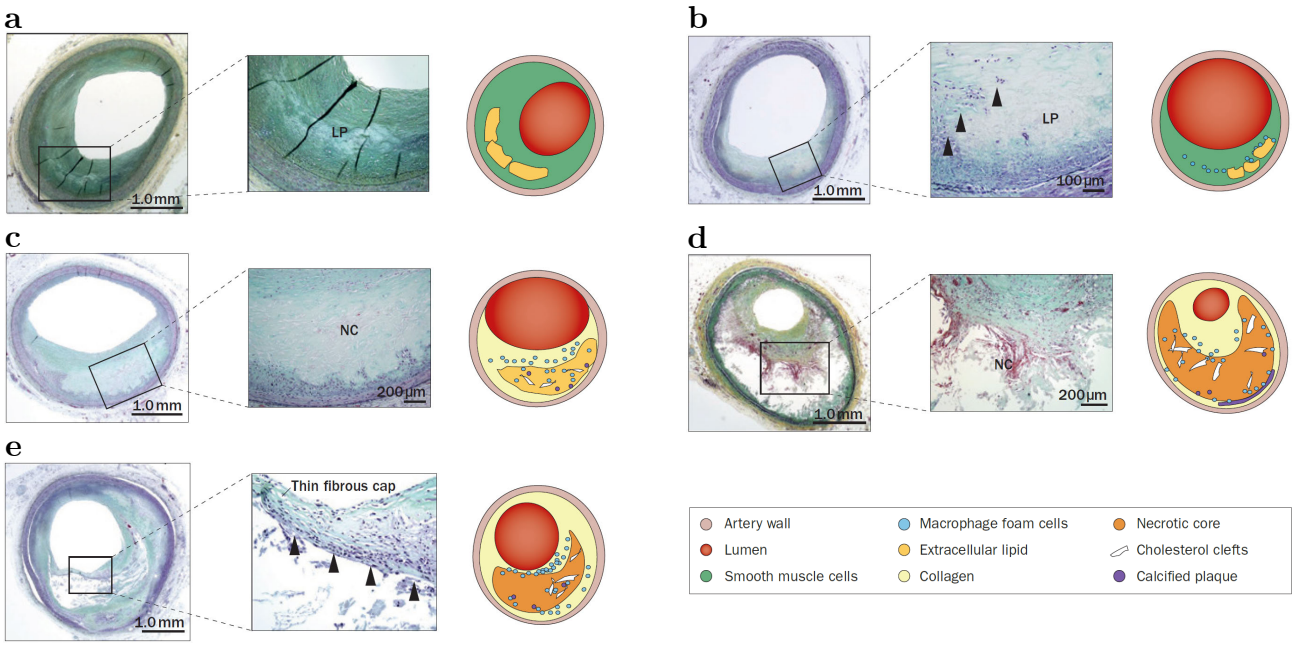

Figure 1.3: Progressive atherosclerotic coronary lesions. **a** - Pathological intimal thickening without macrophage infiltration, **b** - Pathological intimal thickening with macrophage infiltration, **c** - Early fibroatheroma, **d** - Late fibroatheroma, **e** - Thin-cap fibroatheroma. Arrowheads indicate macrophages; LP: lipid pool; NC: necrotic core; (Adapted from [15]).

The exposure of the necrotic core into the coronary blood flow due to fissuring of the thin cap causes an inflammatory reaction and thrombus formation which is the most common cause for fatal MI. However, it must be mentioned that the event of plaque destabilisation and rupture not only depends on the structural features of the lesion itself but also on the surrounding stress it is exposed to. Thus, the phenomenon of plaque rupture has been understood as a complex biomechanical process characterized as a tug-of-war between applied stress and biomechanical toughness of advanced coronary lesions [8].

1.3 Physical Background of Relevant Imaging Modalities

Before currently available clinical and pre-clinical imaging techniques for the assessment of CAD are reviewed, some basic physical background of the two most relevant imaging modalities for this thesis, ultrasound and fluorescence imaging, is provided in this section.

1.3.1 Ultrasound Imaging

1.3.1.1 Introduction to Ultrasound Imaging

Ultrasound (US) are sound or acoustic or mechanical waves with a frequency higher than 20 kHz which makes them not audible for the human ear anymore (Fig. 1.4, reviewed in [16]). In contrast to light which is an electromagnetic wave, US waves require a medium to propagate through. Many animal species such as bats and dolphins use US for e.g. navigation and food location. One of the first human applications of US waves were for nautical purposes termed as echolocation over century ago (Reviewed in [17]). Karl Dussik was the first who used US as a medical diagnostic tool when he tried to locate brain tumours by transmitting US beams through the head in 1942 [18].

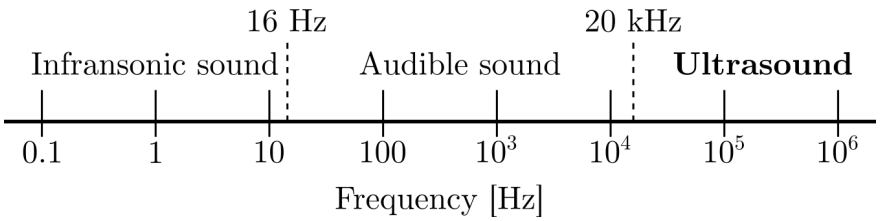

Figure 1.4: Frequency range of sound waves.

US imaging offers some advantageous characteristics which is why it has become very popular for diagnostic purposes since its discovery. Table 1.2 briefly summarizes the advantages this technology can offer compared to other available imaging techniques like X-ray, Computer Tomography (CT), Magnetic Resonance Imaging (MRI), Angiography and imaging in nuclear medicine which will be discussed in more detail in section 1.4.1. For instance, US imaging can provide a sectional image of an area of interest in real time while other imaging modalities like CT, MRI and X-ray require more time to generate imaging frames due to prolonged scan duration and the need for extensive image reconstruction methods. Furthermore, an US scan can be performed at relatively low costs and without the use of ionizing radiation and any other known negative health impacts on patients. On the contrary, the spatial resolution of US imaging is usually lower than in CT and MRI.

1.3.1.2 Ultrasound Generation and Detection

US waves can be generated by piezoelectric crystals which are industrially manufactured out of compounds like lead zirconate titanate (PZT) or other ceramics. These crystals feature a unique characteristics known as the (reverse and direct) piezoelectric effect which is described in the following. A voltage that is applied to electrodes sandwiching a piezoelectric crystals induces a displacement due to molecular rearrangements within the crystal caused by the external electric potential (Reverse piezoelectric effect, Fig. 1.5-a). The polarity of the voltage determines whether the piezoelectric crystal dilates or contracts.

Imaging characteristics	US	CT	MRI	X-ray	Angio	Nuclear Medicine
Ionizing radiation	No	Yes	No	Yes	Yes	Yes
Real-time	Yes	No	No	No	Yes	(Yes)
Type of Image	Slice	Slice	Slice	Section	Section	Section
Overall costs	Low	Very high	Very high	High	High	Very high

Table 1.2: Overview of the advantages and disadvantages of non-invasive imaging modalities (Reviewed in [16]). US: Ultrasound; CT: Computer Tomography; MRI: Magnetic Resonance Imaging; Angio: Angiography

Thus, if an alternating current is applied at high frequencies the corresponding oscillations of the crystal produce high frequency sound waves.

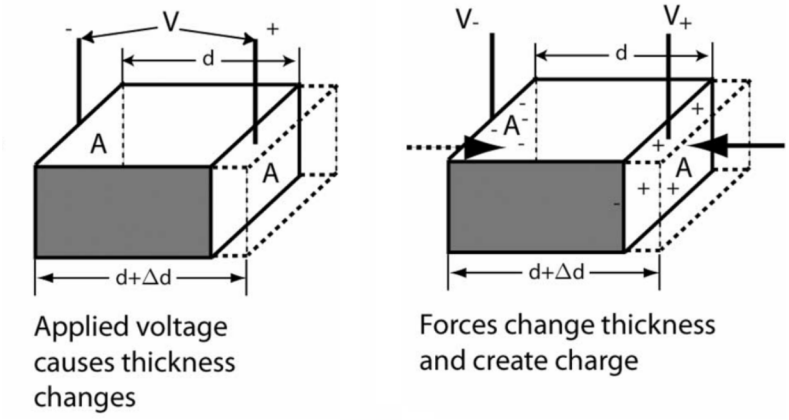

Figure 1.5: Piezoelectric effect. a - Reverse piezoelectric effect, **b** - Direct piezoelectric effect; [19].

US transducers for medical imaging are often made out of piezoelectric elements which are used in a single transducer configuration combining the transmitter and receiver to function as the source and detector for US waves [20]. This transducer setup is known as a pulse-echo configuration and is feasible due to the direct piezoelectric effect for US detection. Specifically, compression of the piezoelectric crystal produces an electric potential (Fig. 1.5-b) and, thus, an incoming US waves can be detected as voltage changes measured at the electrodes.
An US transducer is usually designed as a three-port network which includes two mechanical ports, a front and back acoustic port, and one electrical port in the middle (Fig. 1.6-a, [21]). While the electrical port ensures the electrical connection of the piezeoelectric element to the electrical source, the front and back ports significantly improve the performance of the transducer. Specifically, the front layer or matching layer (Fig. 1.6-b) reduces the acoustic impedance miss-match between the piezoelectric material and the surrounding medium and,

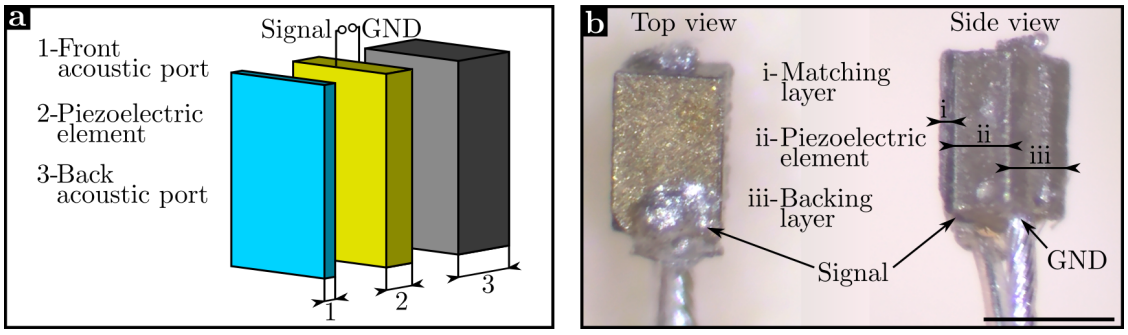

Figure 1.6: Single-element US transducer. a - Three-port network of a single-element US transducer; **b** - Different layers of a connectorized PZT element (Size: 0.6 x 0.4 x 0.3 mm; center frequency: 40 MHz; bandwidth: 68%; Blatek, Boalsburg, Pennsylvania, USA); Scale bar: 500 μm; GND: Ground;

thus, improves US wave transmission from the transducer. The working principle of this strategy is further described in section 1.3.1.4. Generated US waves naturally reflect on the surface of the piezoelectric element which causes reverberation of the reflected wave inside the transducer element. This so called ringing effect, prolongs the pulse duration which deteriorates US axial resolution as further described in figure 1.11 and equation 1.6. The purpose of the backport or backing layer (Fig. 1.6-b), is to damp out the ringing and act as a supporting layer for the piezoelectric element. From an electrical perspective, the piezoelectric material can be regarded as a capacitor and care should be taken to match the input electrical resistance of the US transducer with the electrical impedance of the source (Usually 50 Ω) to maximize power transmission [21]. Important characteristics for imaging like US resolution and penetration depth (Further described in section 1.3.1.5) are influenced by the resonant frequency (ω_0) of the piezoelectric element which depends on speed of sound (c_p) inside the material and its thickness (t) according to eq. 1.1:

$$\omega_0 = \frac{2 * \pi * c_p}{t}. \tag{1.1}$$

This relationship allows to design transducers for specific imaging applications by choosing element thickness to adapt the US frequency.
Many US probes employed in the clinics use multiple piezoelectric elements in an array configuration. However, for intravascular ultrasound (IVUS) imaging a miniaturized US transducer is essential which is why usually single, plane piezeoelectric elements are employed similar like shown in figure 1.6-b. Since IVUS is one of the modalities developed in the scope of this thesis (Further described in section 1.4.2.1), the following introduction about US characteristics will focus on plane single element transducers.

1.3.1.3 Ultrasound Propagation

In general, the propagation of an US wave can be described as an alternating pressure due to density changes of the particles in the medium the US wave is travelling in [20]. Introducing US energy into a medium results in a push causing a local pressure increase (compression) while other areas are exposed to a release and corresponding low pressure (rarefaction). The US wavelength (λ) is the distance between the peak or valley of two consecutive areas of compression or rarefraction, respectively (Fig. 1.7).

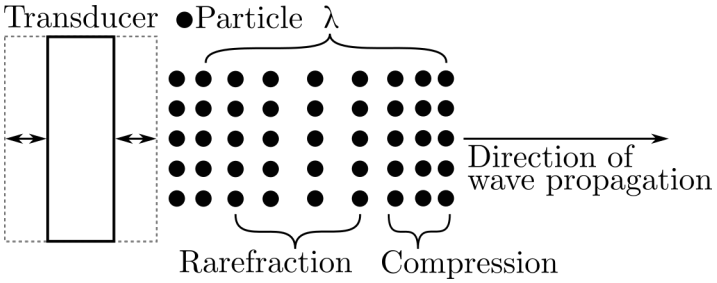

Figure 1.7: Illustration of ultrasound wave propagation (Adapted from [22]).

Most of the US waves used for imaging are longitudinal which means the oscillation of the particles in the medium occurs in the same direction as the wave propagation. In contrast, transversal waves (shear waves), feature an oscillation of the particles in the medium orthogonal to the direction of wave propagation. Due to increased energy loss of transversal waves in the medium at the frequencies required for imaging (MHz range), they are not used for traditional US imaging but only for special applications like elastography.
Depending on the voltage that is applied to the piezoelectric element(s), continuous or pulsed US waves can be generated. For a continuous wave (CW) alternating voltage is applied continuously and for a pulsed wave (PW) the voltage is applied in short bursts. IVUS imaging and most of the standard machines for US imaging work with pulsed US waves as the reflected signal can be detected in the pause after the pulse was emitted ("Listening-phase"). For applications of US imaging in CW mode, an additional receiver is required.

1.3.1.4 Ultrasound Reflection

For invasive IVUS imaging, the transducer is implemented into a catheter and inserted into arteries for intravascular measurements. As the sound waves travel through the tissue, parts of it are reflected at interfaces with different physical properties. The reflection of the US wave primarily depends on differences in the so called wave impedance (Z) of the individual tissue parts which form an interface. Z is defined as the product of the density (ϱ) and the sound velocity (c) of the individual medium according to eq. 1.2:

$$Z = \varrho * c. \tag{1.2}$$

The different wave (acoustic) impedances of two media (Z_1 and Z_2) which make up a tissue interface can be used to calculate the corresponding reflection coefficient R (Eq. 1.3):

$$R = (\frac{Z_2 - Z_1}{Z_2 + Z_1})^2. \tag{1.3}$$

R can take on values between 0 and 1, whereas R = 0 is associated with no US reflection and R = 1 correlates to total US reflection.

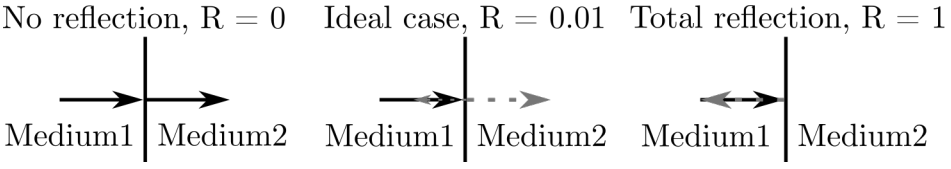

Figure 1.8: Ultrasound reflection coefficient.

A reflection coefficient of around 0.01 is commonly considered to be ideal for imaging which means that 1% of the initial US wave is reflected at the interface and recorded as a signal while majority of the energy can propagate further into the tissue to generate contrast also at larger depths (Fig. 1.8). The reflection of US waves is crucial for receiving a signal at the probe and, ultimately, creating an image. Therefore, the difference in acoustic impedances between e.g tissue types is the source for contrast in US images. Figure 1.9 gives an overview of various acoustic impedances and reflection coefficients at interfaces of different media.

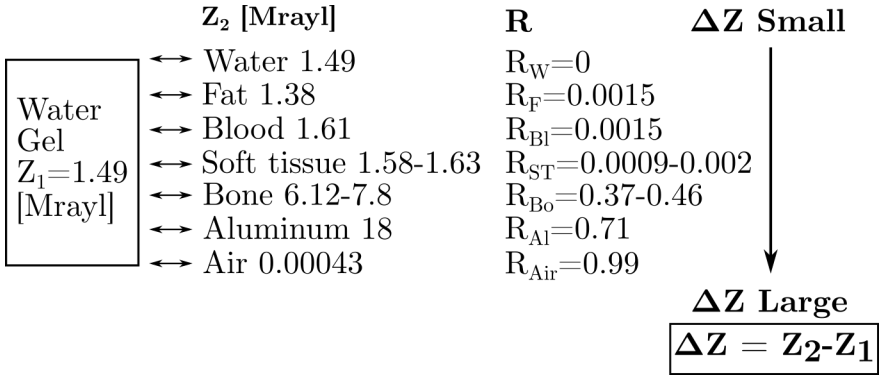

Figure 1.9: Acoustic impedances and corresponding ultrasound reflection coefficients at interfaces of different media; (Reviewed in [16] and [20]).

Evidently, the difference in acoustic impedance between air and soft tissues is significantly high (Z_{Air}: 0.00043 vs. $Z_{SoftTissue}$: 1.58-1.63). In order to transmit as much energy as possible from the transducer into the tissue, the catheter sheath (Further described in section 1.4.2) surrounding the transducer is flushed with water or saline. The water functions as a coupling medium with similar wave impedances as tissue resulting in a reflection coefficient of around R = 0 and, thus, reduces reflections at the surface of the transducer similar like the matching layer described in section 1.3.1.2. For standard, non-invasive US imaging, a gel is regularly applied on top of the skin to improve coupling efficiency [16].
The amplitude of the detected voltage signal corresponds to magnitude of the echo of the US wave as it propagates through the tissue along a scanning axis. The signal amplitude recorded over time is called an A-line. By taking into account the time, Δt, which has passed between transmission of a pulse and the detection of a reflection from an object (time-of-flight), the distance, d, to the transducer can be calculated with eq. 1.4:

$$d = \frac{c * \Delta t}{2} \tag{1.4}$$

where c is the sound velocity in the corresponding medium. Finally, A-lines are transferred into pixel values during post-processing to create an image. Traditionally, US images are displayed in gray scale (Pixel value range: 0-255) for which high voltage values or strong US reflections are translated to high pixel values or white color and low voltage values or weak US reflections into low pixel values or black color.
´

1.3.1.5 Ultrasound Resolution

An important physical property of the US wave in relation to image quality is the US frequency, f, as already mentioned in section 1.3.1.2. The US propagation velocity, c, can be calculated by the product of wavelength, (λ), and f according to eq. 1.5:

$$c = \lambda * f. \tag{1.5}$$

Considering this relationship, a high frequency relates to a short US wavelength at same propagation velocity of the wave and vice versa. High transmission frequencies suffer from high energy loss (attenuation) over the same traveling distance causing a shorter penetration depth than lower frequencies. On the contrary, high frequencies advantageously influence the spatial resolution which can be further distinguished between axial and lateral resolution. The axial resolution describes the minimum distance that can be differentiated between two interfaces located parallel to the propagation direction of the US wave.

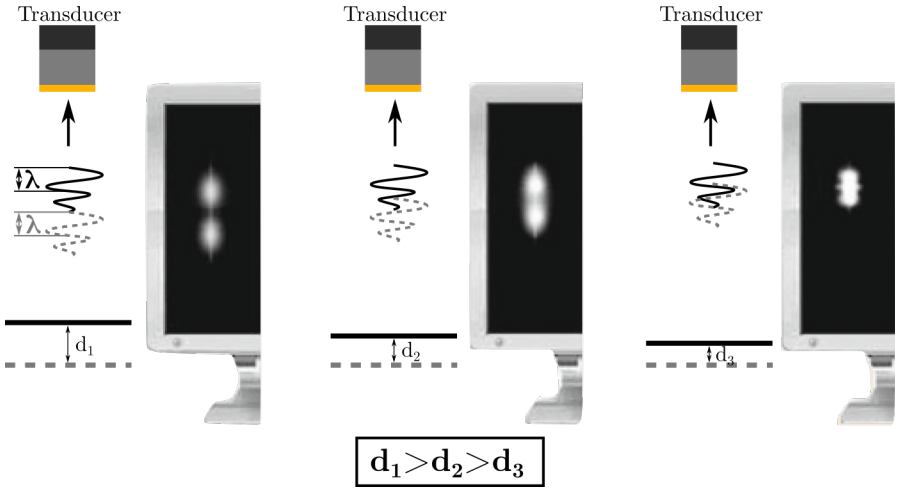

Figure 1.10: Demonstration of axial resolution in ultrasound imaging based on two reflective surfaces located at different distances from each other (d_1-d_3); (Adapted from [16]).

Figure 1.10 shows two US signals originating from two different reflective surfaces which are located at different distances from each other (d_1-d_3). While both signals can be clearly distinguished from each other at distance d_1, this becomes more difficult for smaller distances between the two reflectors due to overlapping of the reflected US pulse waves. The theoretical limit for the axial resolution can be estimated by the length of one wavelength. However, are more realistic approach to estimate the axial resolution of US imaging must consider the total length of the effective pulse duration, τ_p, which usually consist out of several US wave cycles [20]. As already mentioned in section 1.3.1.2, damping material is used to reduce the vibration length ("ring-down" effect) after excitation of US waves in transducers. Successful damping will generate a shorter US pulse (Smaller τ_p) which, in turn, will result in a bigger frequency bandwidth and finally in higher axial resolution (Fig. 1.11).
Thus, US axial resolution can be calculated more realistically by eq. 1.6:

$$Resolution_{axial} = \tau_p * c. \tag{1.6}$$

In conclusion, small US wavelengths in combination with effective use of damping result in smaller pulse length and, thus, increase in axial resolution allowing to differentiate objects located more closely together in the axial direction of propagation.
Lateral resolution can be defined as the minimum distance, d_{min}, distinguishable between two reflectors located perpendicular to the propagation direction of the US beam and is limited by the lateral US beam width, d, (Fig. 1.12-a, [20]). If d is smaller than the distance between the

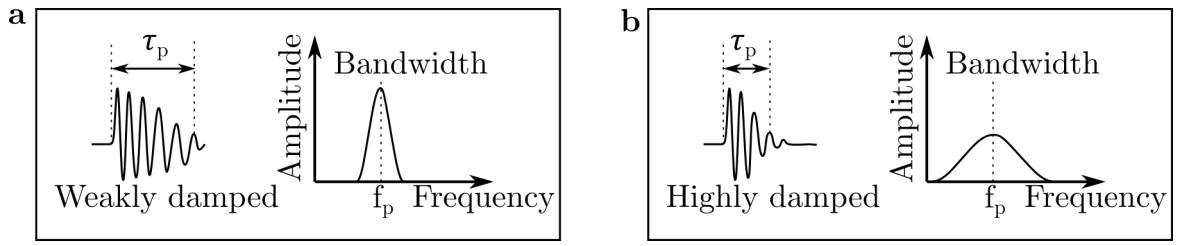

Figure 1.11: Impact of damping on ultrasound pulse duration (τ_p); a - Weak damping resulting in longer (τ_p) and narrow bandwidth, **b** - Effective damping resulting in shorter (τ_p) and large bandwidth; (Adapted from [20]).

two objects. two independent signals can be detected allowing to distinguish between them. Therefore, high lateral resolution corresponds to a narrow beam width which varies with distance from the transducer. Close to an unfocused transducer (Near-field zone) the US beam has a lateral width, D, of approximately the footprint of the transducer element (Fig. 1.12-b). In order to improve lateral resolution for standard non-invasvie US imaging, beam focusing is commonly applied by e.g designing the active element of the transducer in a concave shape or using a lens (Fig. 1.12-c, [20]). This reduces the beam width d in the focal zone and, thus, improves the lateral resolution. For an unfocused transducer the length of the near-field zone (N) can be calculated according to eq. 1.7:

$$N = \frac{D^2 f}{4c}. \tag{1.7}$$

Assuming a 40 MHz IVUS transducer with a single-element size of 0.4 mm and approximating the US propagation velocity c as 1500 m/s, N can be assumed as around 1 mm. The average distance from the catheter to the vascular wall can be estimated as around 1 mm when considering an average outer diameter of 1 mm of the imaging catheter and inner diameter of 3 mm of human coronary arteries. Thus, IVUS imaging of coronary tissue occurs predominantly in the far-field zone which is why focusing of single-element IVUS transducers is usually not required.
The beam width of an unfocused transducer in the far-field zone is influenced by the divergence angle (Fig. 1.12-b, ϑ) which can be estimated by eq. 1.8:

$$sin(\vartheta) = \frac{1.2\lambda}{D}. \tag{1.8}$$

Therefore, higher US frequencies and corresponding smaller wavelengths result in more narrow beam widths and higher lateral resolution of plane, unfocused transducers.

In conclusion, the presented relationships between frequency, resolution and penetration depth, dictate that the actual choice of US frequency depends usually on the location of the ROI in the tissue. According to that, high frequencies are chosen for imaging superficial structures at high resolution and low frequencies to visualize tissue at larger depths. While, US frequencies in the range of 2-10 MHz have been traditionally used in the clinics for the assessment of e.g abdominal organs and muscles, IVUS imaging uses high frequency ultrasound (<35 MHz) to visualize high details of vessels at small imaging depths.

1.3.1.6 Physical Phenomenons Relevant for Ultrasound Imaging

As already mentioned in section 1.3.1.4, US waves will be reflected back when encountering an interface between the two media which feature a difference in acoustic impedance [20].

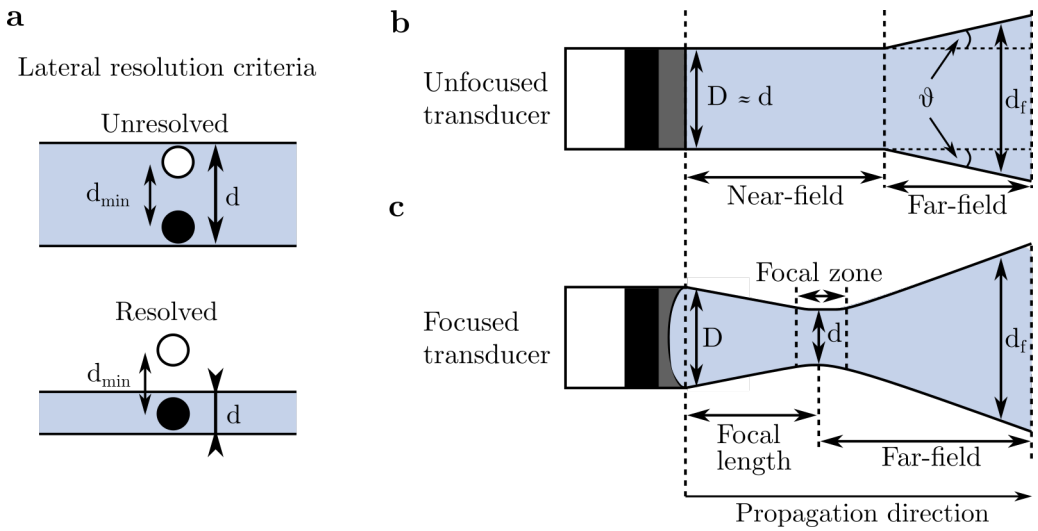

Figure 1.12: Lateral resolution in ultrasound imaging; a - Lateral resolution is defined as the minimum distance (d_{min}) distinguishable between two reflectors and is limited by the lateral beam width (d). When d is larger than the d_{min} the two objects can not be resolved. When d is smaller than the d_{min} the two objects can be resolved. **b** - Unfocused US beam features a beam width d in the near-field and a diverging beam width (d_f) depending on the divergence angle (ϑ) in the far-field; **c** - A focused US beam features a smaller beam width d at the focal length and highly diverging beam width (d_f) in the far-field; (Adapted from [20]).

If the US wave hits the interface at an orthogonal angle the trajectories of any transmitted and reflected fractions of the US wave will be also orthogonal (Fig. 1.13-a). However, if the angle of incidence, θ_i, is different from the orthogonal axis, the beam will be reflected away from the orthogonal axis at angle θ_i and the path of the transmitted beam will be refracted resulting in an transmission angle, θ_t, (Fig. 1.13-b).

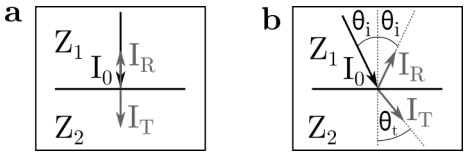

Figure 1.13: Reflection of an ultrasound wave at an interface of two different media with impedance Z_1 and Z_2 depends on angle of incidence; a - Reflection and transmission paths for perpendicular incidence angle; **b** - Incidence angle θ_i results in a reflection path at angle θ_i and transmission path at angle θ_t; (Adapted from [20]).

The angles θ_i and θ_t depend on the speeds of sound in the two corresponding media according to eq. 1.9:

$$\frac{\theta_i}{\theta_t} = \frac{c_1}{c_2}. \tag{1.9}$$

If an US wave encounters and object with dimensions similar or smaller than its wavelength, a fraction of the US wave will scatter instead of reflect (Fig. 1.14).
While red blood cells (diameter $\simeq 7\mu$m) are still below the scattering limit for high frequency US (20-40 MHz with λ=75-38 μm in soft tissues), collagen, elastin or even cell nuclei might introduce scattering. In general, an increase in US frequency decreases the scattering limit meaning smaller structures start contributing to scattering events [20].
Attenuation of US waves describes the energy loss (Intensity and pressure) while propagating

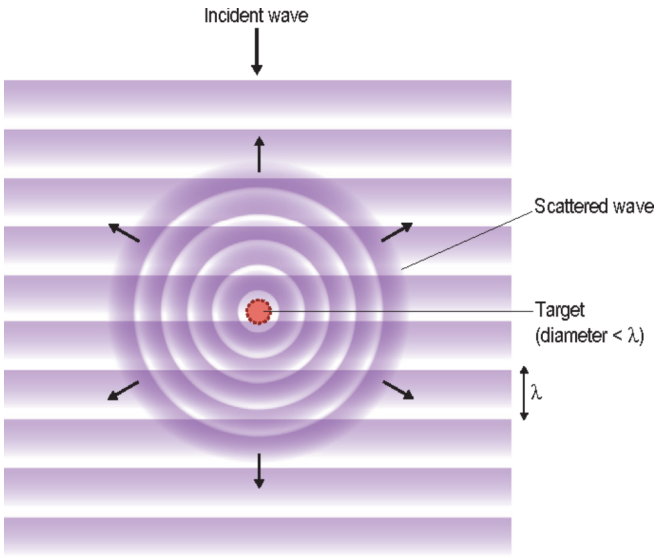

Figure 1.14: Scattering of an ultrasound wave when encountering an object with a diameter smaller than the wavelength λ [23].

through a medium [20]. The decrease in intensity over the propagation distance z can be described by an exponential function according to eq. 1.10:

$$I(z) = I_0 * e^{(-2\alpha * z)} \tag{1.10}$$

where I_0 represents in the initial intensity at z = 0 and α the attenuation coefficient of the propagation medium. Both, absorption for which mechanical energy is transformed into heat, and scattering for which fractions of the beam are scattered away from the propagation direction, contribute to the overall attenuation. For medical imaging, US attenuation depends on the tissue type and increases with US frequency (Fig. 1.15) which results in smaller penetration depths (several millimeters for high frequencies) as already mentioned in section 1.3.1.5.

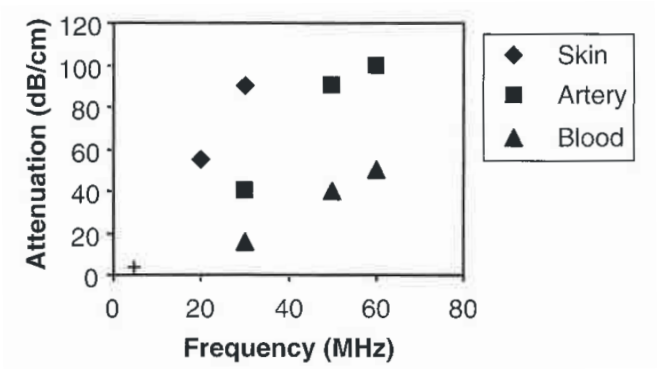

Figure 1.15: Ultrasound attenuation related to frequency as measured ex vivo in different biological tissues; The small cross close to 5 MHz (typical clinical imaging of soft tissue) corresponds to attenuation of around 1-5 $dBcm^{-1}$ [20].

1.3.2 Fluorescence Imaging

Optical imaging methods like fluorescence imaging have become a fundamental tool enabling numerous groundbreaking discoveries in biomedical research and have been also widely implemented in clinical settings for the assessment of different types of diseases.

Fluorescence imaging can visualize tissue with molecular contrast which has significantly improved our understanding of important biological processes and has proven invaluable for medical diagnosis. Furthermore, it has been applied to investigate tissue at different scales, microscopically in the form of fluorescence microscopy to macroscopic techniques like fluorescence imaging of whole small-animal bodies or human organs and tissue structures [24].

1.3.2.1 Basic Physics of Light and Fluorescence

In comparison to US (acoustic wave), light is an electromagnetic wave which features a wavelength spectrum ranging from ultra-violet to the near-infrared. Over this entire spectrum only a small range between 400-700 nm is visible to the human eye (Fig. 1.16).

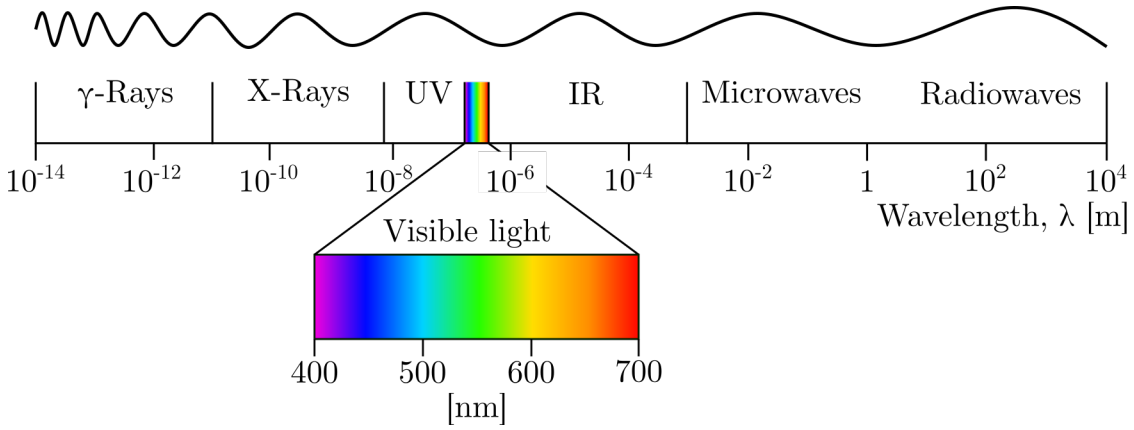

Figure 1.16: Light in the electromagnetic spectrum.

Light features characteristics of both, particles and waves, which has been described as the wave-particle duality. The elementary particles of light are photons which have either mass or electrical charge and move in a vacuum on a straight trajectory at the speed of light. When light is propagating through tissue it interacts with the micro-environment which can be described microscopically by its photon characteristics and by electromagnetic wave theory on a macroscopic level.

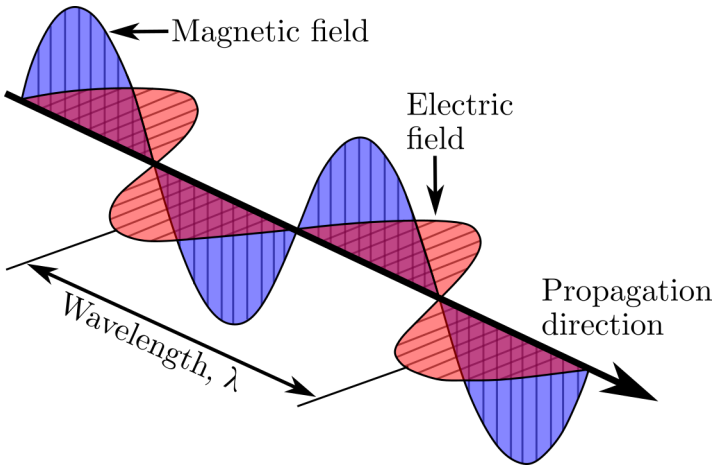

Figure 1.17: Electromagnetic wave with wavelength (λ) featuring oscillating electric and magnetic fields (Adapted from [24]).

An electromagnetic wave can be characterized as a combination of a magnetic and electric field which oscillate orthogonal to each other and in planes parallel to the propagation direction (Fig. 1.17). The individual photons that are transported by the electromagnetic wave have an energy E which can be described by eq. 1.11:

$$E = h\nu. \tag{1.11}$$

where h is the Planck constant and ν the frequency of the wave (ν=c_0/λ_o, where c_0 is the speed of light in vacuum, e.g c_0=3*10^{10} cm/s). A light wave hitting an interface made out of two media with refractive indexes n_0 and n_1 will be partly reflected at the same angle , θ_0, like the incident wave and refracted at the angle, θ_1 (Fig. 1.18-a, [24]). The reflection angle θ_0 and

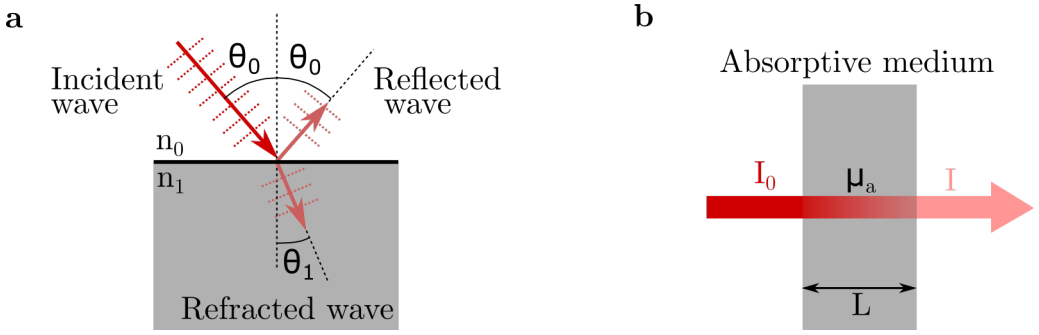

Figure 1.18: Illustration of light reflection, refraction and absorption. a - One part of an incident light wave encountering an interface made out of two media featuring refractive indexes n_0 and n_1 is reflected with a reflection angle θ_0, the other part is refracted at a refraction angle θ_1. **b** - Absorption of light in a medium of thickness L and with an absorption coefficient μ_a reduces the incidence irradiance I_0 to I. (Adapted from [24]).

refraction angle θ_1 are related to each other through the refractive indexes of the two media forming the interface as described by the Snell's law, eq. 1.12:

$$n_0 sin(\theta_0) = n_1 sin(\theta_1). \tag{1.12}$$

Internal reflection is an event that refers to total reflection of a light wave without any refraction and is observed for incidence angles exceeding a critical threshold $\theta_c = sin^{-1}(n_1/n_0)$ when $n_0 > n_1$. This phenomenon has found wide application to minimize energy losses when designing silica fibers for light transmission.
Scattering and absorption are one of the fundamental light-matter interactions relevant for optical imaging [24]. Absorption can be described on a macroscopic level when light propagates through an absorptive medium with thickness L and an absorption coefficient μ_a. The incidence irradiance (Optical power per unit area), I_0, will be absorbed in the medium resulting in a reduced irradiance, I, exiting the medium [24]. In an non-scattering media this absorption process can be described by the Beer-Lambert law, eq. 1.13:

$$I = I_0 * e^{(-\mu_a * L)}. \tag{1.13}$$

Scattering of light can be defined on a macroscopic level as a change in propagation direction of an incident light wave interacting with matter. The direction of scattered photons depends on the relation between λ and the geometrical cross-section, σ_{geom}, of the scattering object (Fig. 1.19-a). Isotropic scattering, also called Rayleigh scattering, occurs for conditions $\sigma_{geom} << \lambda^2$, forward scattering regimes, also called Mie and Geometrical scattering, can be observed for conditions, $\sigma_{geom} \approx \lambda^2$ and $\sigma_{geom} >> \lambda^2$, respectively (Fig. 1.19-b).

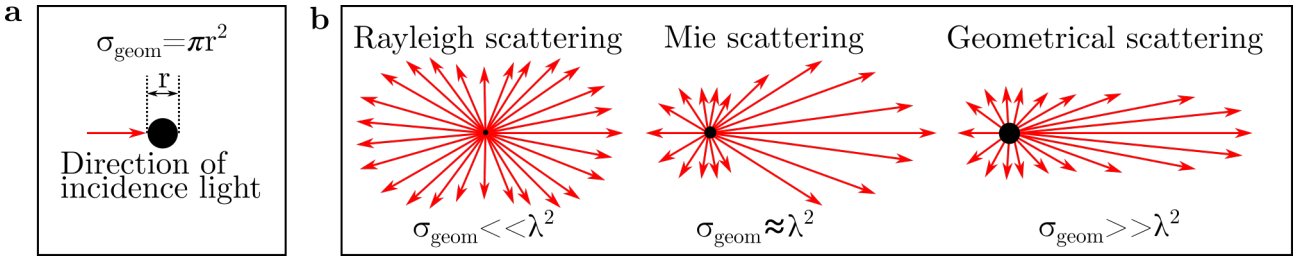

Figure 1.19: Light scattering regimes. a - The scattering direction of an incident light wave depends on the geometrical cross-section σ_{geom} of a spherical scattering object describd by it its radius r. **b** - Isotropic scattering regime, Rayleigh scattering, observable for $\sigma_{geom} << \lambda^2$ and forward scattering regime, Mie and geometrical scattering, for $\sigma_{geom} \approx \lambda^2$ and $\sigma_{geom} >> \lambda^2$, respectively.

The scattering coefficient μ_s can be further adapted by considering the direction of scattering in form of an anistropy factor g (g≈0 for isotropic and g≈1 for anisotropic scattering) which has been measured for different tissue types. Thus, to estimate scattering in biological media the reduced scattering coefficient $\mu_s^{'}$ can be calculated by eq. 1.14:

$$\mu_s^{'} = \mu_s(1 - g). \tag{1.14}$$

In the field of optical imaging, the number of photons that can be detected as light propagates through tissue is reduced due to both, absorption and scattering. Therefore, this process is often summarized under the term attenuation and an overall attenuation coefficient can be calculated combining μ_a and $\mu_s^{'}$ according to eq. 1.15:

$$\mu_{att} = \mu_a + \mu_s^{'}. \tag{1.15}$$

On a microscopic level, photon-matter interactions can be outlined by the Jablonski diagram (Fig. 1.20, [24]).
If the direction of the radiation of a photon changes after interacting with matter it is called scattering as mentioned above [24]. Two types of scattering processes can be differentiated:

1. Rayleigh scattering (elastic): There is no energy transfer between the photon and the matter. The incident photon and the scattered photon have the same wavelength.

2. Raman scattering (inelastic): There is an energy transfer between the photon and the matter. The scattered photon has a smaller wavelength (less energy) than the incident photon.

If a photon interacts with the electrons of a molecule it can transfer its energy to them and move the electrons to a higher energy state (S_1, S_2, ...) resulting in the loss of the incident photon. This process is called absorption and requires that the energy of the incident photon must match the energy difference between two electronic states (e.g energy difference between S_0 and S_1). This excitation process can also occur via a virtual level if two (or multiple) low-energy photons are absorbed simultaneously and their combined energy matches the transition difference. Excited molecules can either convert their energy to another energy form or re-emit it again through different types of photo-luminescence:

1. Non-radiative decay: Energy transfer through collisions to the surrounding environment is referred to as vibrational relaxations and represents the most common non-radiative decay.

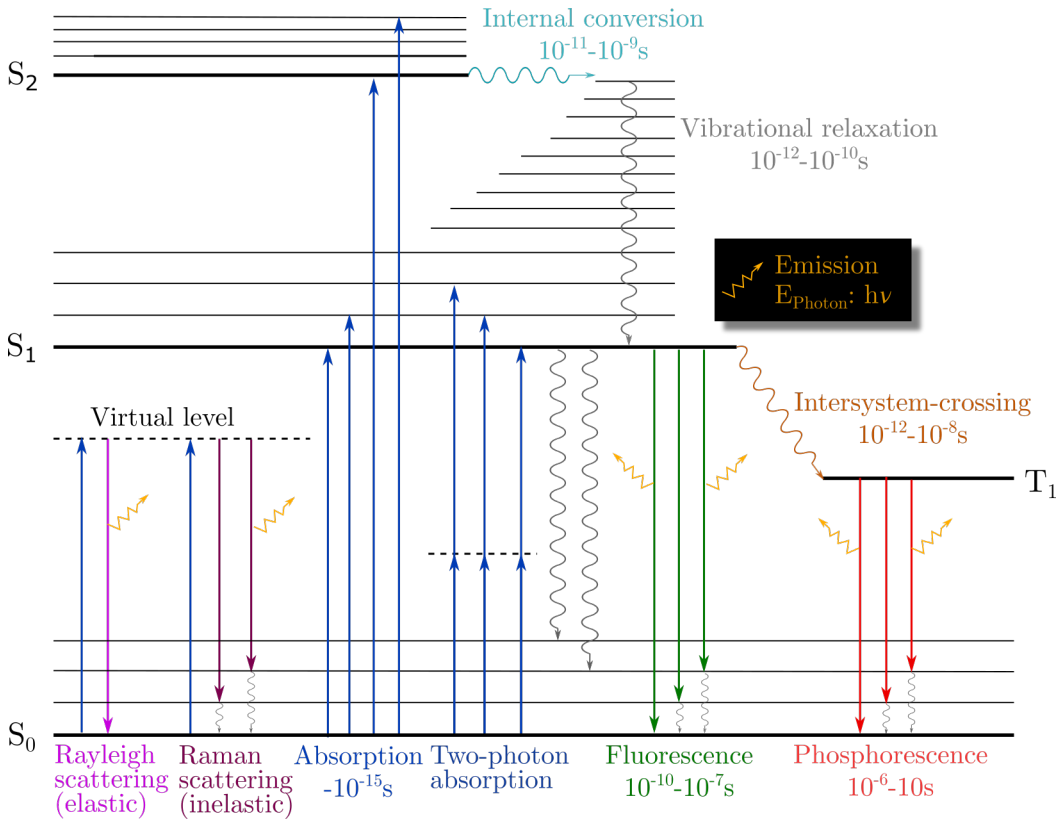

Figure 1.20: Jablonksi diagram illustrating light-matter interactions at different energy levels. The ground (S_0), first (S_1), and second singlet electronic states (S_2) as well as the first electronic triplet state (T_1) are shown as bold horizontal lines. The different vibrational and rotational energy levels of molecules are indicated as thin horizontal lines. The energy of a photon depends on the Planck constant (h) and its frequency (ν); (Adapted from [24]).

Intersystem crossing is process for which a singlet spin state transitions to e.g a triplet spin state. A process that involves transition between two energy states featuring the same spin angular momentum (e.g. singlet - singlet state) is called internal conversions. All of these processes happen without any emission of photons.

2. Fluorescence and phosphorescence: Photoluminscence effects describe emission of radiation due to decay of an excited molecule to lower energy levels. Light emission from singlet-excited states is called fluorescence which is fast process resulting in fluoresecence lifetimes of around 1-10ns for typical organic fluorophores. Light emission from triplet-excited states is called phosphorescence and corresponds to slow transition rates resulting in phosphorescence lifetimes in the range of milliseconds to seconds.

The emission spectra and characteristics of photoluminescence processes depend on the chemical structure of the fluorophores and the medium they are dissolved in. Another important characteristics of fluorescence emission of a fluorphore is its quantum yield. The quantum yield, η_{fluo}, (or quantum efficiency) can be described as the ratio between the number of emitted fluorescence photons and the number of photons absorbed during excitation. Fluorophores with high η_{fluo} are often desired for imaging because they can usually be detected more easily promising better signal-to-noise ratio (SNR). Furthermore, the time duration for which fluorescence emission can be detected after excitation is defined as fluorescence lifetime τ_{fluo} and depends on the local micro-environment of the fluorophore.

1.3.2.2 Reporter Technologies

Fluorescence imaging utilizes reporters that can target molecular processes in vivo. These mechanisms can be then detected and quantified through the reporter's fluorescence emission. There are two major strategies for designing fluorescence reporters which can be categorized as direct and indirect approaches [25]:

1. Direct fluorescence imaging: Images an exogenous fluorescence probe that has been administered to e.g an animal model or patient. These probes can be either active, meaning they fluorescence at all times even if they are not bound to their target yet, and activatable, which means the probe is designed to only fluorescence when attached to its target acting like an optical switch. The advantage of activatable probes are minimized background signals resulting in improved contrast and detection sensitivity.

2. Indirect fluorescence imaging: Involves cell engineering methods for which a transgene can be introduced into a cell. This transgene encodes information for the production of a fluorescent protein. Thus, after successful transcription of the transgene, the fluorescence probe is produced intrinsically and can be detected by e.g a fluorescence microscope. This strategy is especially suitable to investigate gene expression and regulation.

In comparison to engineered direct and indirect fluorescence probes, there is also intrinsic fluorescence of cells and tissue called, autofluorescence [26]. Different proteins and coenzymes that are widely distributed in cells and tissue act as endogenous fluorophores when excited with light at certain wavelengths. Autofluorescence often represents a challenge for fluorescence imaging of target probes because it acts as a background signal which is hard to separate from the target signal due to its typical broad emission spectrum. Thus, the presence of high intensity autofluorescence during fluorescence imaging of e.g tissue usually decreases contrast. On the other hand there have been recent efforts to make use of the autofluorescent properties of e.g tissue components and detect it as an endogenous contrast source without the use of engineered probes.

1.3.2.3 Imaging Technologies

While the focus of the review lies on in vivo fluorescence imaging technologies on a macroscopic level, it must be noted that there are also fluorescence microscopy techniques. Specifically, intravital microscopes like confocal or two-photon have been developed to visualize fluorescent reporters with high resolution (0.5 - 3 μm) located several hundred microns deep in the tissue [25]. Macroscopic detection of fluorescence emitted from deeper tissue layers is commonly achieved by illuminating the tissue with an expanded light beam (plane wave) and detecting the corresponding fluorescence signals with e.g a camera. Two modes can be differentiated for planar imaging of fluorescence [24]:

1. Epi-illumination imaging: Light is shined onto the surface of tissue to excite superficial and subsurface fluorophores (A few millimeters below the surface if appropriate wavelengths are chosen) and fluorescence emission is detected on the same side of the tissue (Fig. 1.21-a). Fluorescence imaging in this epi-illumination mode is also commonly known as fluorescence reflectance imaging (FRI). The advantage of these kind of imaging setup is that it can be easily developed and operated. On the other hand, the depth of the fluorescence source can not be quantified which becomes a challenge when attempting to correct for fluorescence signal attenuation in tissue.

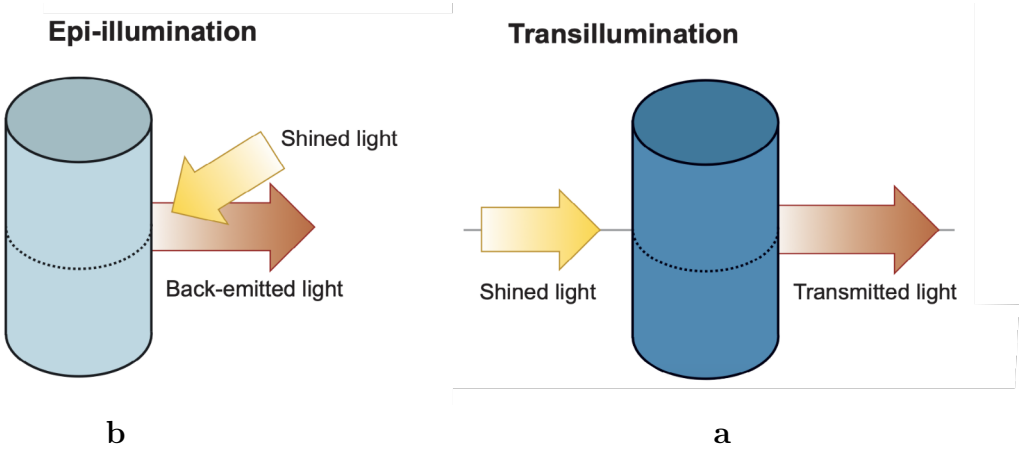

Figure 1.21: Planar fluorescence imaging modes can be differentiated in, **a** - Epi-illumination and, **b** - Transillumination; (Adapted from [25]).

The overall fluorescence attenuation depends on the attenuating characteristics of the tissue for light and the distance the photons are propagating (e.g the location of the fluorescence source inside the tissue). This subject will be further discussed below for the application of intravascular fluorescence imaging in chapter 7.

2. Transillumination imaging: In contrast to epi-illumination, transillumination shines light through the tissue detecting fluorescence signals on the other side, meaning the excitation source and the detector are placed on opposite sides (Fig.1.21-b). While transillumination methods suffer from similar drawbacks as epi-illumination in terms of uncertainty of the location of the fluorescent source and signal attenuation, an object of interest with appropriate thickness can be entirely sampled.

More advanced fluorescence imaging methods, like fluorescence molecular tomography (FMT) have been investigated over the years. FMT attempts to reconstruct fluorophore distribution in tissues in three dimensions by recording fluorescence signals from multiple viewing points and applying tomographic reconstruction methods in combination with mathematical models simulating light propagation through tissue.

1.3.2.4 Near-Infrared Fluorescence

As introduced in 1.3.2.1, the optical properties of tissues dictate how light propagates through it which is essential for fluorescence imaging and the field of optical imaging because it determines fundamental imaging characteristics like image generation, resolution, contrast, sensitivity and penetration depth. Bashkatov et al. have reviewed and characterized the optical properties of human tissue in the spectral range between 400 to 2000 nm presenting absorption and reduced scattering coefficients for human skin (Fig. 1.22-a-b) and human subcutaneous adipose tissue (Fig. 1.22-c-d, [27]).
In order to provide more information of the optical properties of tissue, figure 1.23 presents the scattering coefficient and absorption coefficients for oxygenated and deoxygenated whole blood in the spectral range from 400 to 1000 nm. Both figures (Fig. 1.22 and Fig. 1.23) indicate that:

1. Light propagation through tissue is diffusive because scattering is the dominant photon-matter interaction in tissue resulting in scattering coefficients which are on average at least an order of magnitude larger than absorption coefficients [29].

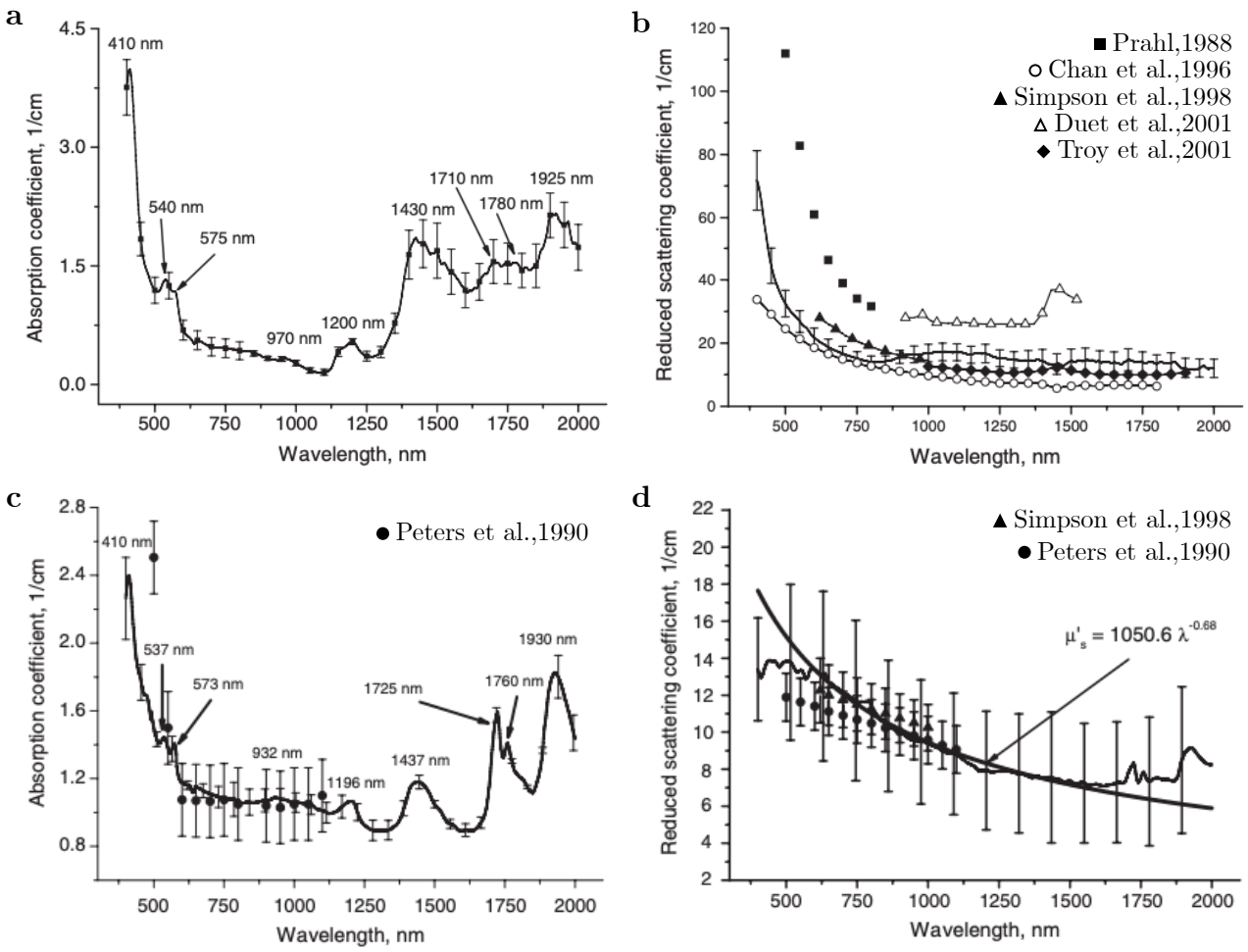

Figure 1.22: Optical properties of human skin and subcutaneous tissue in the spectral range from 400-2000 nm, **a** - Absorption and, **b** - reduced scattering coefficients for human skin. **c** - Absorption and, **d** - reduced scattering coefficients for human subcutaneous adipose tissue. Averaged experimental data is shown as solid lines and standard deviation values as vertical lines. Data from reviewed studies is presented as corresponding symbols; (Adapted from [27]).

2. Scattering and, especially absorbance of light is reduced in the NIR spectral range ($\lambda > 750nm$) compared to smaller wavelengths.

This second observation has given rise to Near-Infrared Fluorescence (NIRF) for macroscopic imaging which enables increased penetration depths (up to several centimeters) in contrast to imaging in the e.g the visible spectral range for which penetrations depth are limited to 1-2 mm [30]. Additionally, autofluorescence is less prominent in the NIR region which offers improved imaging contrast. Therefore, NIRF has been identified as a powerful tool for the assessment of human diseases due to its molecular contrast and increased penetration depths which will be also capitalized in the framework of this thesis.

1.3.2.5 Indocyanine Green

Indocyanine Green (ICG) is a fluorophore from the family of cyanine dyes and is commonly used as an active reporter for direct fluorescence imaging (see section 1.3.2.2). ICG shows an absorption peak at around 780 nm and a fluorescence emission peak at around 830 nm

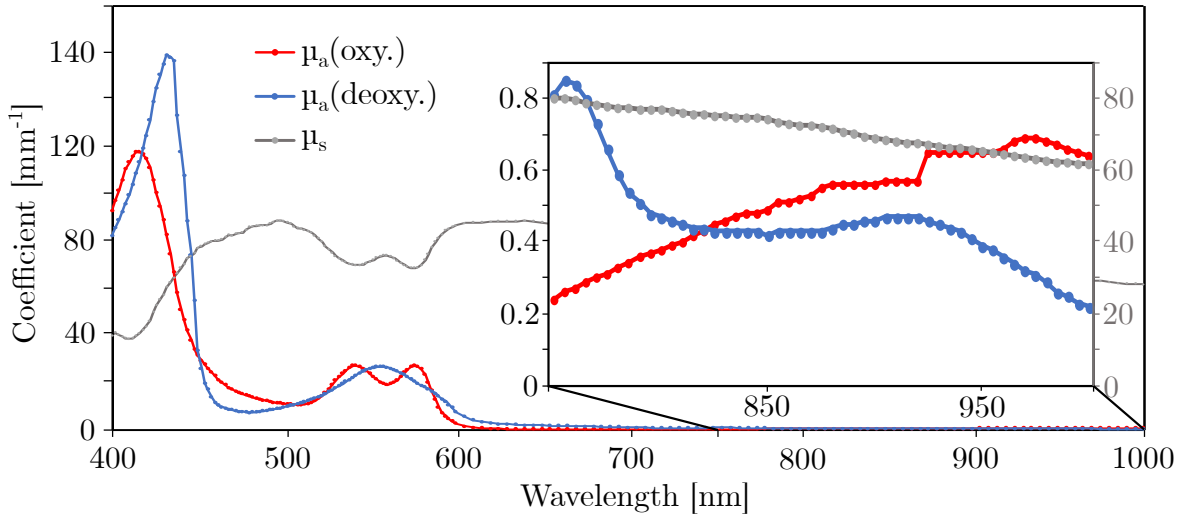

Figure 1.23: Optical properties of whole blood in the spectral range from 400-1000 nm; (Data from [28]).

resulting in a stokes shift (Difference in λ between absorption and emission peak) of around 50 nm making it a suitable probe for NIRF imaging (Fig. 1.24). Stokes shifts of adequate size are important for fluorescence imaging because excitation and detection wavelengths must be separated with optics like dichroic mirrors and filters. ICG has been originally applied for hepatic and cardiac function diagnostics in the clinics over 60 years ago. To this day, ICG is still the only fluorescent dye approved for human applications which has resulted in a large number of published studies using ICG for fluorescence imaging. For instance, ICG has been used for intraoperative assessment of graft patency during vascular surgery, image-guided oncologic surgery and sentinel lymphnode detection [31, 32]. As mentioned in 1.3.2.1, the photo-physical properties of fluorophores depend on the local micro-environment. This becomes also evident when comparing η_{fluo} of ICG for different solvents as shown in table 1.3.

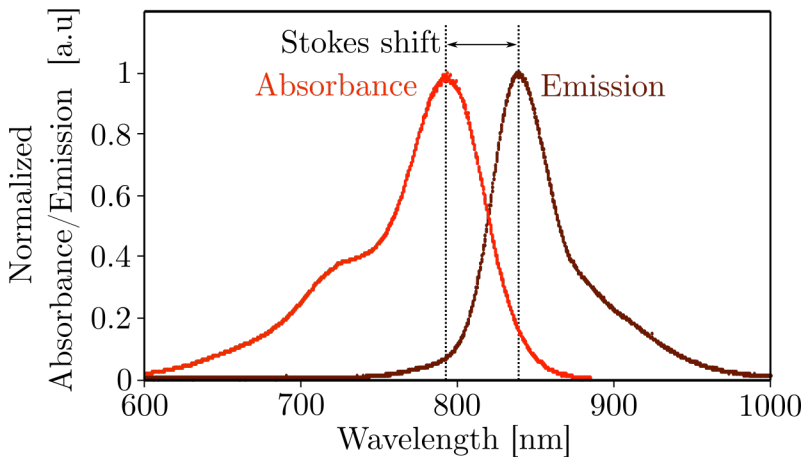

Figure 1.24: Normalized absorbance and emission spectrum of indocyanine green (ICG) dissolved in dimethyl sulfoxide (DMSO); Data was measured with a spectrometer (Ocean Optics - USB4000).

The η_{fluo} of ICG is comparably low, ranging from 2.9% in water to 14% in ethanol (EtOH). Building up on the success story of ICG several other NIR probes for in vivo NIRF imaging of preclinical animal models have been developed which can be differentiated between inorganic

(Quantum dots and nanoparticles) and organic dyes [33]. Examples of additional organic dyes are the newly developed cyanine dyes like AlexaFluor750, Cy7, IRDye800cw 1.3. Overcoming the limitations associated with ICG for NIRF imaging like poor photostability, low quantum yield, mild fluorescence in aqueous solutions and non-specific binding in vivo havs been the major motivation for the development of most recent NIR dyes. Thus, the new generation of fluorescent dyes are conjugatabe with targeting ligands which signficiantly improves their specificity for e.g targeting tumors or other diseases.

Dye	**Max.** $\lambda_{abs}/\lambda_{em}$	**Quantum yield** η_{fluo} **(Solvent)**
ICG	780/830 nm	14% (EtOH) 2.9% (Water) 12% (FBS) 5.1% (Micelles) 13% (Blood) [34]
AlexaFluo750	752/779 nm	12% (PBS) [35]
Cy7	750/773 nm	30% (PBS) [36]
IRDye800cw	774/789 nm	12% (Aqueous solution) [37]

Table 1.3: Overview of fluorescent cyanine NIRF dyes.

Despite its shortcomings, ICG remains an invaluable tool for in vivo NIRF imaging in humans today mainly because of the extensive experience that has been collected over the last decades for its clinical application and because approval of several newly developed NIR dyes by the food and drug agency (FDA) is a lengthy process.

1.4 Clinical Coronary Imaging

It has been an ongoing search to find methods and techniques that can detect coronary plaques which are at high risk to cause acute cardiac events like MI. The identification of precursors of culprit lesions has remained a major challenge but led to the development of a number of different imaging techniques which have been also widely implemented into the clinics over the years. In general, these clinical imaging modalities can be differentiated between non-invasive and invasive. The field of non-invasive imaging comprises a variety of different technologies which are applied in the clinics. This review aims to only briefly introduce the modalities of this field since the focus of this thesis is on invasive intravascular imaging techniques.

1.4.1 Non-invasive Coronary Imaging Techniques

Typically, the aims of non-invasive coronary imaging techniques depend on their application for either symptomatic or asymptomatic patients. For patients with acute symptoms, like stable angina pectoris, the goal is to diagnose whether limitation of myocardial blow, caused by an obstructive plaque, results in ischemic myocardial conditions. Whereas for asymptomatic patients coronary imaging is applied as a screening tool to estimate the likelihood for acute clinical events in the future by identifying overall atherosclerotic risk status through the assessment of early-stage lesions and vulnerable, high-risk plaques [38].

1.4.1.1 Coronary Angiography

Angiography was among the first imaging techniques that allowed to visualize vessels in the human body. Major contributions towards the development of the technique were achieved in the 1930s by Brooks and Moniz who were the first to use angiography to image human peripheral and cerebral vessels [39, 40]. In general, angiography detects x-rays which are generated by a x-ray source and propagate through tissue [24]. Imaging contrast is generated by the tissue's characteristics to absorb these x-rays differently. In the case of angiography, a radiopaque contrast media is injected into vessels under investigation which absorbs emitted x-rays and, thus, enhances contrast to generate a projection (two-dimensional image) or luminogram of the particular vasculature. In modern angiography systems, x-ray source and detector are mounted on a C-arm which allows to rotate the imaging trajectory around the tissue to take section views from different angles (Fig. 1.25-a).

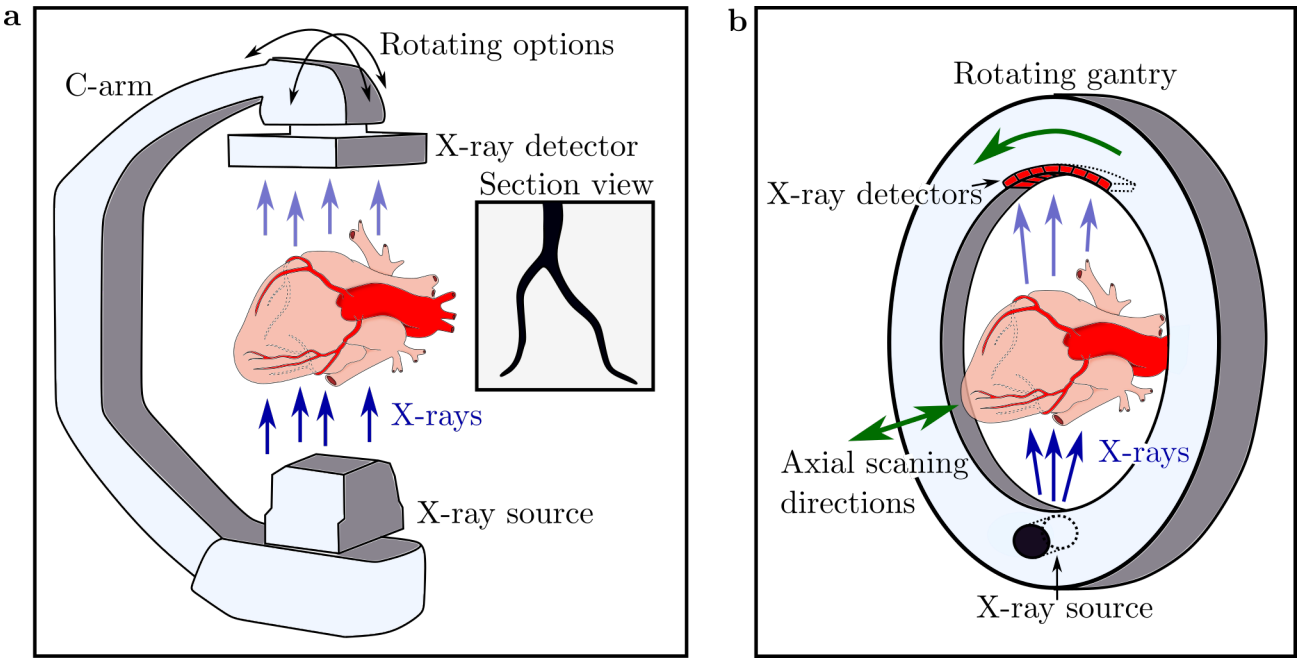

Figure 1.25: Principle of a - Coronary Angiography and **b** - Computer Tomography (CT) Coronary Angiography.

This imaging technique has been widely applied to visualize the lumen of coronary arteries and identify stenotic areas for guidance prior to percutaneous coronary interventions in the clinics. Figure 1.26 shows exemplary angiography images of a lesion located in a human LCA [41]. The obstruction of the coronary blood flow due to the stenotic segment can be clearly identified (Fig. 1.26-a). Blood flow could be restored after stent implantation into the stenotic segment as part of a coronary intervention as visualized by coronary angiography (Fig. 1.26-b).
Due to the fact that the contrast agent must be administered as specifically as possible to ensure best image quality, an intravascular catheter is used to deliver the radiopaque solution into the coronary arteries in the clinics. It must be noted that this catheterization process technically makes this imaging technique an invasive intervention, giving it the name invasive coronary angiography (ICA). Nevertheless, ICA is reviewed in this section because the imaging process itself is non-invasive and other non-invasive modalities, described below, are directly compared to ICA.

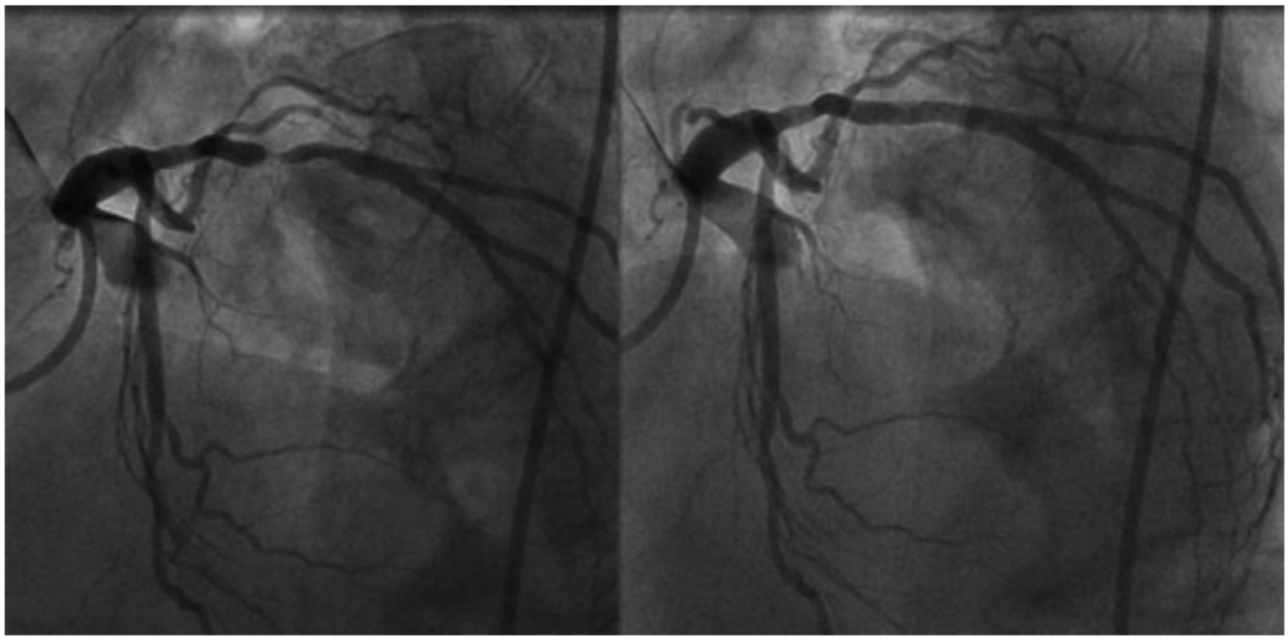

a **b**

Figure 1.26: Angiography of a lesion in the left coronary artery, **a** - prior to coronary intevention and **b** - after coronary intervention with stent implantation; [41]

1.4.1.2 Computed Tomography Coronary Angiography

To further improve visualization of the vasculature, Napel et al. applied computer tomography (CT) to angiography to enable 3D reconstruction of vessels in 1992 [42]. This is achieved by rotating a gantry holding the x-ray source and detector around the patient to collect data that allows to reconstruct different cross-sectional imaging frames which can be combined to 3D images of the tissue (Fig. 1.25-b). Initially, the application of this technique for imaging coronary arteries (CTCA) was limited by slow acquisition times which requires the patient to hold their breath for up to 40 seconds to avoid motion artefacts. Additionally, these early CT systems were limited to 4-slice data acquisition. This resulted in datasets of insufficient quality for the assessment of coronary lesions in the clinics due to limited temporal and spatial resolution [43]. However, this was improved by speeding up gantry rotation, x-ray slice collimation, image noise reduction by strengthening X-ray tubes and increasing slice number per rotational acquisition to up to 64 [43]. These new generation of CTCA systems allows to visualize stenosis of coronary arteries in the clinics as it can been seen in sectional views (Fig. 1.27-A-C) and 3D-reconstructed images (Fig. 1.27-D) as confirmed by standard ICA (Fig. 1.27-E).

In comparison to ICA, CTCA is non-invasive because imaging systems are sensitive enough to detect the contrast agents when administered intravenously. However, CTCA is a purely diagnostic tool which targets patients without any clinical symptoms (typical chest pain due to stenosis) in contrast to ICA which is usually performed as part of a cardiac intervention. In conclusion, although CTCA has shown good sensitivty and specificty to detect stenotic segments in coronary arteries, it is currently not widely replacing ICA for visualizing stenosis but rather represent an alternative for certain clinical situations and selected patients [38, 43]. The role of CTCA to image and characterize high-risk plaques in vivo has been systematically reviewed including 18 different studies [44]. The authors conclude that CTCA has the potential to identify low attenuation (non-calcified) plaques, plaques showing spotty calcification and can be used to measure an index describing positive remodelling of plaques.

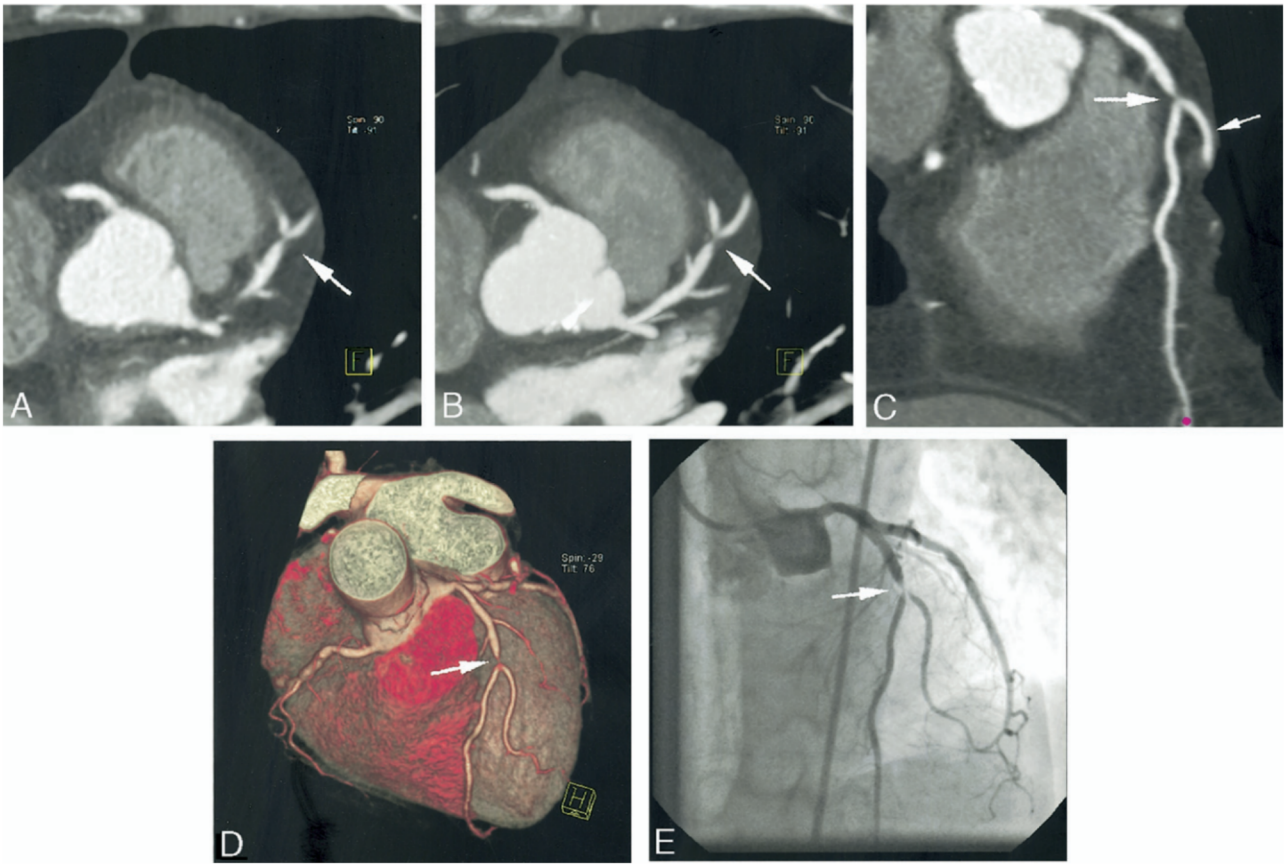

Figure 1.27: Stenotic lesion in a human LAD coronary artery visualized by computer tomography coronary angiography. A - Transaxial CT image (0.75 mm slice thickness) showing the stenosis (Arrow) in the LAD coronary artery; **B** - Improved visualization of the stenotic segment (Arrow) in a maximum intensity projection (5mm slice thickness); **C** - Curved multiplanar reconstruction visualizes that the stenosis affects the main LAD (Larger arrow) and a side branch (Smaller arrow); **D** - 3D reconstruction shows the stenosis of the LAD located proximal to the side branch bifurcation (Arrow); **E** - Corresponding invasive angiography image of the stenosis (Arrow); [43].

These plaque characteristics were more frequently correlated to the presence and probability of subsequent acute coronary syndrom (ACS) events (12-fold increased risk) in comparison to low-risk plaques [38, 44].

1.4.1.3 Coronary Artery Calcium Scoring

Similar like CTCA, Coronary Artery Calcium scoring (CAC) applies CT for imaging coronary arteries. However in the case of CAC, no radiopaque contrast medium is administered because this modality aims to assess coronary artery calcification which offers inherent tissue contrast without the need for exogenous contrast enhancement. As described above, calcification of arterial tissue is an important process of atheroscleorosis and the presence of microcalcifications and their transformation into larger calcified nodules have been both linked to increased plaque vulnerability. CAC aims to visualize these calcified nodules in more advanced lesions and to quantify coronary calcification in the form of a measure called Agatston units which describes calcium density and distribution [38].

1.4.1.4 Magnetic Resonance Coronary Angiography

Magnetic Resonance Imaging (MRI) makes use of an inherent property of elementary particles like protons and neutrons, called spin (Reviewed in [24]).
The application of MRI in the field of cardiovascular imaging has been referred to as Cardiovascular Magnetic Resonance (CMR). While CMR has become the clinical gold standard for macroscopic cardiac assessments, like overall cardiac structure and myocardial perfusion, Coronary Magnetic Resonance Angiography (CMRA) has not been widely used [45]. This is because in comparison to CTCA, CMRA suffers from limitations in regards to resolution (CMRA: 1 mm vs. CTCA: 0.4 to 0.6 mm) and long acquisition times [45, 46]. Nevertheless, using an imaging sequence called steady-state-free-precession has made CMRA imaging at 1.5 T more attractive because it can utilize the intrinsic high blood signal intensity in the coronary arteries resulting in good blood-myocardial contrast even without the administration of exogenous contrast agents [47]. Moreover, recent advances, like compensation for respiratory motion and acceleration of the imaging process have further improved CMRA. For instance, it has been demonstrated that acquisition time of CMRA can be reduced by using a technique called compressed sensing (CS) which speeds up image reconstruction while maintaining image quality (CS CMRA: 2 min, Conventional CMRA: 10 min; [46]). Figure 1.28 shows CMRA images of a stenosis in the RCA of a patient suffering from chest pain. The stenosis is clearly visible in both, the CS CMRA (Fig. 1.28-a) and the conventional CMRA image (Fig. 1.28-b) as confirmed by coronary angiography (Fig. 1.28-c). Thus, CS CMRA holds great potential to reduce motion artefacts and overall patient burden.

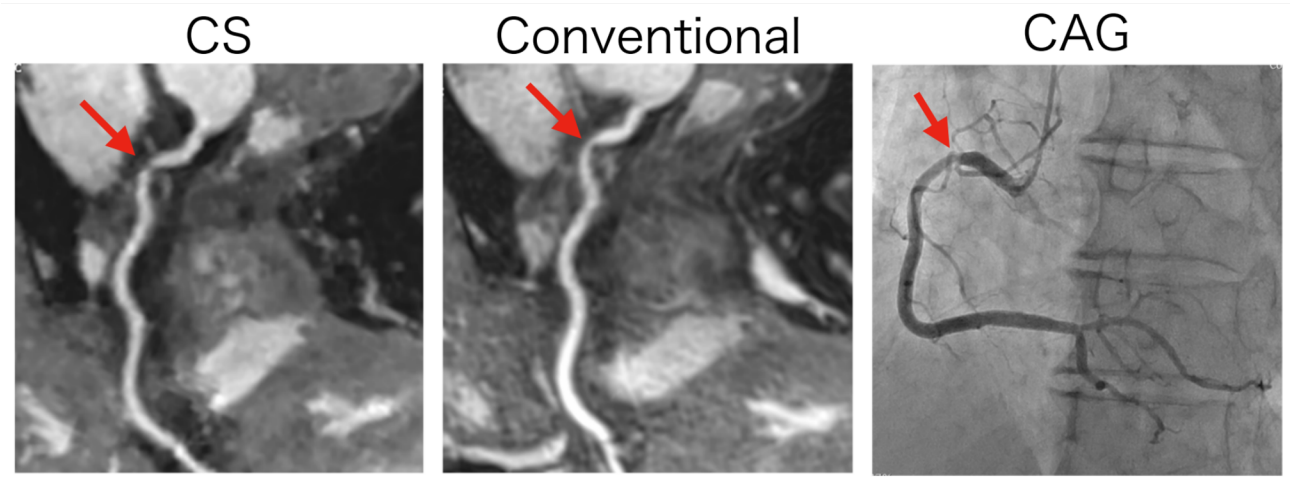

Figure 1.28: Coronary Magnetic Resonance Angiography (CMRA) of a patient with chest pain revealing significant stenosis in the RCA visible in, a - compressed sensing CMRA, **b** - conventional CMRA and **c** - angiography images; RCA: Right coronary artery; CS: Compressed sensing; CAG: Conventional angiography; [46].

1.4.1.5 Positron Emission Tomography

Positron Emission Tomography (PET) Imaging uses positron-emitting radionuclides like ^{11}C,^{13}N,^{15}O and ^{18}F which can be produced in e.g medical cyclotrons (Reviewed in [48]).
The working principle for PET imaging is described in short below. A proton transforms into a neutron by emitting a positron inside the nucleus which looses its kinetic energy due to random interactions with surrounding matter. After the emitted positron hits an electron, a positronium pair is formed which annihilates and emits two anti-parallel gamma rays with a kinetic energy of 511 keV (Fig. 1.29-a).

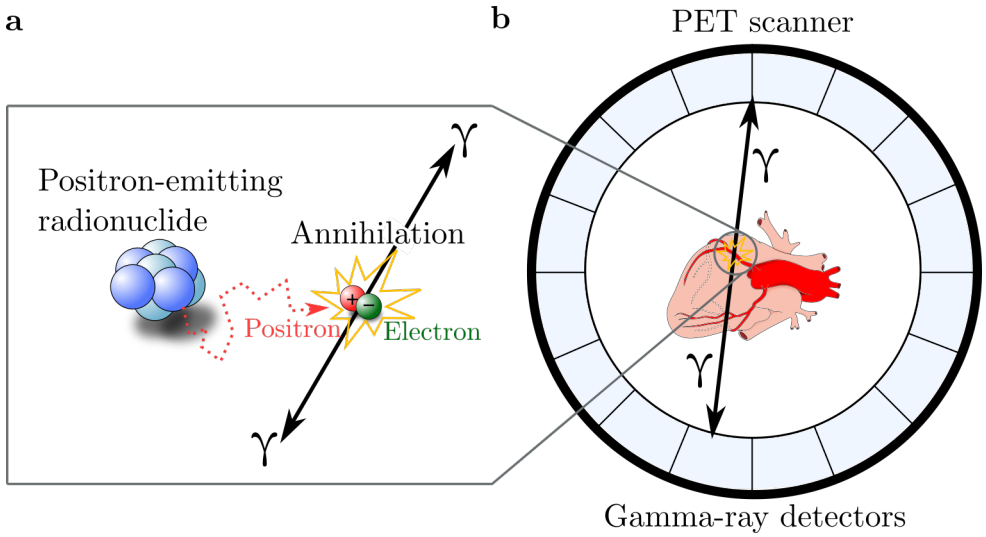

Figure 1.29: Principle of Positron Emission Tomography (PET); a - Annihilation of a positron-electron pair results in anti-parallel gamma-ray emission. **b** - Overview of a PET scanner.

The emitted pair of gamma rays can be simultaneously recorded by a detector ring surrounding the sample. The detection of a gamma-ray pair which is associated to a single annihilation event is called coincidence event and the trajectory between the opposite detectors is named line of response (LOR). The number of events recorded in a LOR is then summed up to estimate the concentration of radionuclides. Small amounts of radionuclides are packed into molecules (radiotracers) which can bind to specific proteins and accumulate in areas of interest like tumors or inflammation. Imaging the distribution of radiotracers after intravenous injection allows PET to visualize metabolic or biochemical functions. In general, the tomographic reconstruction for PET imaging is similar to CT besides the fact that the energy source for PET is inside rather than outside the sample (Fig. 1.29-b). A lot of times PET imaging is combined with CT to co-register functional and precise anatomical information. Although PET imaging of coronary arteries has been challenged by long scan times and limited spatial resolution, the assessment of CAD with PET has been realized by using tracers like ^{18}F-Fluorodeoxyglucose (^{18}F-FDG) which is a marker for inflammation and ^{18}F-Fluoride which can be used to image vascular calcification (Reviewed in [38]). Over the recent years PET has been combined with CT to overlay anatomical information about the coronary arteries (Provided by CT) with their functional status (Provided by PET) for a more comprehensive assessment. For instance, a study showed how tracers like ^{18}F-FDG and ^{18}F-FDG can be used to image patients suffering from MI when using hybrid PET-CT. Joshi et al. identified an occlusion located in the LAD of a patient with MI and stable angina by ICA (Fig. 1.30-A, [49]).

^{18}F-Fluoride was detected in the culprit plaque area by PET-CT (Fig. 1.30-B) while uptake of ^{18}F-FDG was only found in the myocardium and oesophagus (Fig. 1.30-C). Additionally, a stented LCA of patient with was investigated revealing a culprit lesion in the LAD and a non-culprit lesion in the LCX by ICA (Fig. 1.30-D). Figure 1.30-E demonstrates that hybrid PET-CT was able to detect increased ^{18}F-NaF uptake in the culprit but not in the non-culprit lesion. No uptake of ^{18}F-FDG was found in either of the lesions but in the ascending aorta.

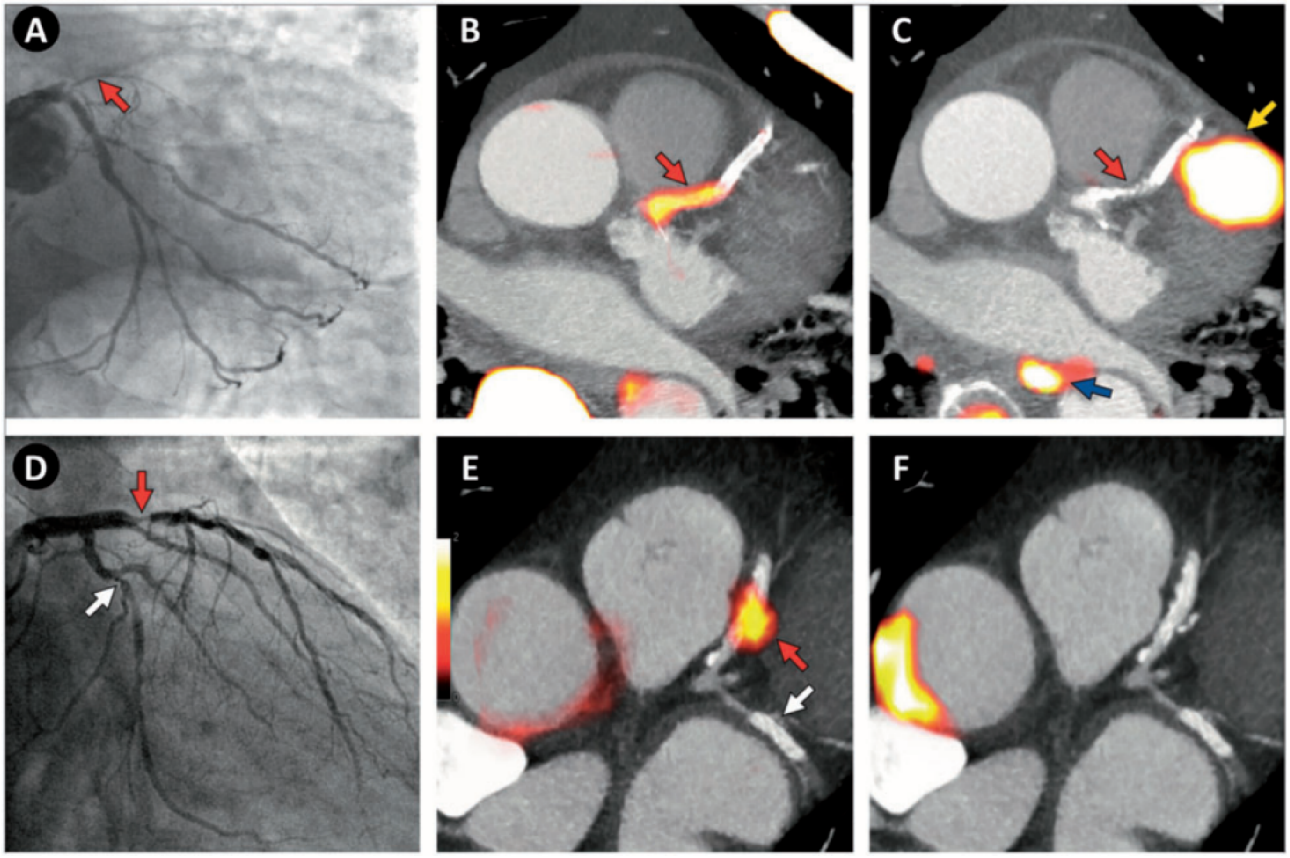

Figure 1.30: Hybrid positron emission tomography and computer tomography (PET-CT) imaging of patients suffering from myocardial infarction and stable angina. (Top row, A-C) Occlusion of the left anterior descending artery shown by invasive coronary angiography (**A**; Red arrow) and significant uptake (yellow-red) of ^{18}F-Fluoride in the culprit plaque area (red arrow) visible in PET-CT imaging (**B**). No uptake of ^{18}F-Fluorodeoxyglucose in the culprit plaque area (red arrow) and significant uptake in the myocardium (yellow arrow) and oesophagus (blue arrow) shown in the PET-CT image (**C**). **(Bottom row, D-F)** Invasive coronary angiography shows culprit (red arrow; left anterior descending artery) and non-culprit (white arrow; circumflexus artery) stented lesions (**D**). While PET-Ct revealed increased ^{18}F-NaF uptake in the culprit lesion, no uptake was detected in the non-culprit lesions (**E**). No uptake of ^{18}F-Fluorodeoxyglucose in either of the lesions but increased uptake in the ascending aorta detected in PET-CT (**F**); (Reviewed in [38] and adapted from [49]).

1.4.1.6 Comparison and Conclusion of Non-invasive Coronary Imaging modalities

Table 1.4 compares the presented non-invasive imaging modalities between each other based on relevant imaging characteristics like scan duration, spatial and temporal resolution and radiation exposure and concludes corresponding advantages, limitations and fields of application

(Reviewed in [38]). While CAC scoring offers a widely available and low-cost option to quantify calcification in coronary arteries with relatively low radiation exposure, it is limited by its spatial resolution and can not detect non-calcified plaques which are regularly associated with high risk for rupture. CAC scoring is usually applied to estimate risk as part of prevention in patients associated with low to intermediate risk for cardiovascular events. Due to recent technological advancements, CTCA has become more popular for the non-invasive assessment of suspected stable angina because of its short scan times and superior spatial resolution. However, CTCA requires precise heart rate control, shows imaging limitations in the presence of stents or coronary clarifications and suffers from patient risks like reaction to administered contrast agent and increased radiation exposure. MCRCA offers a radiation-free characterization of soft tissue usually used to identify anomalies in coronary arteries and assess coronary bypass grafts. In contrast to CTCA, MRCA is limited by its spatial resolution and prolonged scan duration. Furthermore, MRCA is not widely available mainly due to its high costs. Finally, PET enables the detection of pathological processes of interest by modifying corresponding tracers. The full potential of PET is made use by combining it with CT which significantly increases the radiation exposure (Can be reduced with PET-MRI). Further limitations are its very limited availability, high costs, long acquisition time and poor spatial resolution which, so far, has limited it to research purposes only.

Imaging characteristics	**CAC Scoring**	**CTCA**	**MRCA**	**PET**
Scan duration	0.5 - 10 s	0.5 - 10 s	10 - 20 min	60 - 90 min (Tracer uptake) + 15 - 30 min scan
Spatial resolution	1.5 - 3.0 mm	0.5 - 1.0 mm	1.0 - 2.0 mm	4.0 - 10.0 mm (Tracer dependent)
Temporal resolution	240 - 420 ms	240 - 420 ms	<60 ms	Minutes
Radiation exposure	<1 mSv	1 - 10 mSv (Protocol dependent)	-	6 - 15 mSv
Advantages	Wide availability, Low cost, Low radiation exposure, Large evidence base to support prognostic implications	Short scan time, Wide availability, Best spatial resolution, Robust evidence to support use	Radiation free imaging, Allows concurrent assessment of cardiac function, Not limited by coronary calcification, Soft tissue characterization	Tracers can be modified to target almost any structural or pathophysiological process of interest
Limitations	Limited spatial resolution, Non-calcified (potentially high-risk) plaques not detectable	Requires adequate heart rate control, Risk of contrast reaction/nephropathy, Imaging limited by dense coronary calcification and stents, Radiation exposure	Limited spatial resolution, Prolonged scan duration, High cost, Limited availability, Claustrophobia, Metallic implants	Poor spatial resolution, Prolonged tracer uptake time and long scan duration, Relatively high radiation exposure (PET-CT) although this can be substantially reduced with PET-MR, High cost, Very limited availability
Indications	Risk stratification in primary prevention for individuals at low intermediate risk of cardiovascular events	Non-invasive assessment of suspected stable angina in patients with intermediate pretest probability of coronary artery disease	Anomalous coronary arteries, Follow-up of Kawasaki disease (coronary aneurysms), Assessment of coronary bypass grafts	Research purposes only at present

Table 1.4: Comparison of non-invasive coronary imaging modalities; (Adapted from [38]).

1.4.2 Invasive Coronary Imaging techniques

Intravascular imaging comprises a field of invasive imaging techniques. For this purpose, imaging sensors are implemented into catheters inserted into a sheath which can be described as tubing often made out of low-density polyethylene (LDPE). The catheter sheaths serves three purposes, namely, i) to protect the sensors from the intravascular blood flow which can compromise their functionality, ii) to ensure that if parts of the catheter ever detach they are trapped inside the sheath and not exposed to the coronary blood flow and tissue and iii) in the case of IVUS to be able to flush the surrounding space of the US transducer and the whole catheter with water or saline to ensure US coupling into the tissue and reduce friction during catheter motion. Imaging catheters can be inserted into the vessels of interest and collect imaging data from inside the lumen. Intravascular imaging has become a standard clinical method alongside standard angiography during coronary interventions because it overcomes certain imaging limitations of angiography and non-invasive imaging techniques. For instance, angiography provides a lumenogram by visualizing planar projections of a vessel lumen filled with contrast agent (See section 1.4.1.1) instead of imaging the vessel directly [50]. In contrast, intravascular imaging techniques can visualize e.g artery lumen and stents with high contrast and provide high-resolution cross-sectional images of the vessel wall. This type of imaging information has proven to be valuable for the identification of inadequate stent expansions, dissections, thrombus formation which are indicative for adverse events like stent thrombosis and restensosis [51]. Furthermore, intravascular imaging is regularly applied prior to coronary inteventions to collect precise information on vessel dimensions. There are currently two intravascular imaging technologies for the anatomical assessment of coronary arteries commercially available, IVUS and intravascular optical coherence tomography (IVOCT).

1.4.2.1 Intravascular Ultrasound

IVUS utilizes the standard principle for US image generation which includes the emission of US waves, their reflection at tissue interfaces and detection to reconstruct gray-scale images. For IVUS, a miniaturized single-element US transducer is mounted at the tip of a catheter (See section 1.3.1.2). The emitted US beam is directed perpendicular to the catheter axis (side-looking) and scans the whole circumference of the arterial tissue when the imaging catheter is rotated to create cross-sectional images. This catheter based US imaging technique was first developed for intrarectal scanning of the prostate in 1957 [52] and then further developed for intravascular applications. Early technical designs of IVUS featured multiple US transducers which were arranged circumstantially around the catheter tip (Fig. 1.31-a, [53]). Sequential operation of the individual transducers allowed to sweep the generated US beam in a radial imaging plane covering 360°. Further technical developments introduced a mechanical system which employs a single transducer configuration for which the transducer crystal is mounted at a rotating shaft creating a cone-shape imaging plane (Fig. 1.31-b) or a fixed transducer orientated towards a rotating reflector which re-directs the US beam perpendicularly to the catheter axis creating a radial imaging plane (Fig. 1.31-c). Currently available IVUS imaging systems in the clinics usually employ catheters with a single transducer which is fixed and slightly tilted backwards (approx. 4-6°) while emitting an US beam with a center frequency of usually 40 MHz (Fig. 1.31-d) . For imaging, the whole catheter is rotated and advanced or pulled back generating a helical pullback movement within the lumen to scan the artery segment of interest.

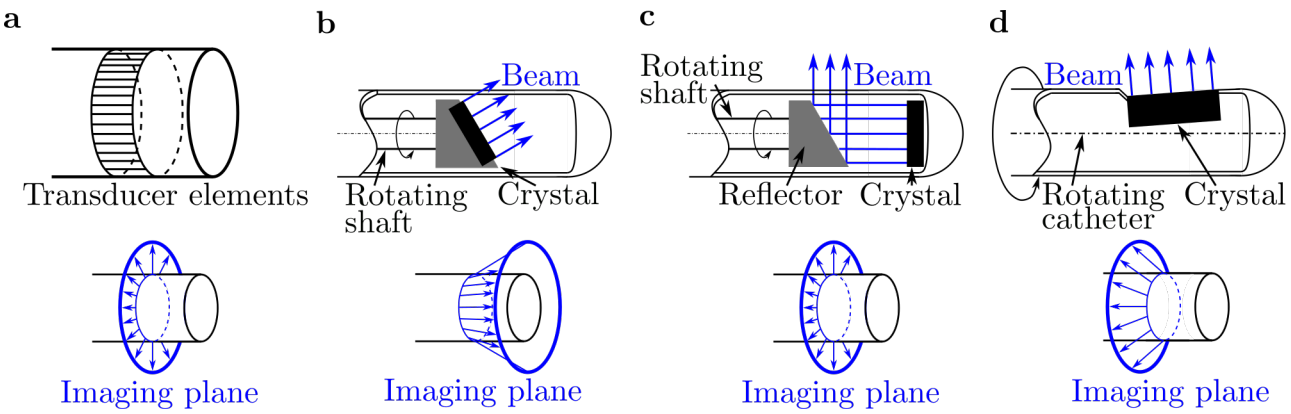

Figure 1.31: Different sensor designs for intravascular ultrasound imaging catheters; **a** - IVUS catheter design featuring multiple US transducers arranged circumstantially which generate a radial imaging plane; **b** - IVUS catheter design featuring a single, rotating US transducer crystal which generates a cone-shape imaging plane; **c** - IVUS catheter design featuring a single US transducer crystal and a rotating reflector which generates a radial imaging plane; **d** - Typical IVUS catheter design of currently available imaging systems in the clinics featuring a single US transducer crystal which is fixed and tilted slightly backwards to create a cone-shaped imaging plane when the whole catheter is rotated; (Adapted from [54]).

1.4.2.2 Intravascular Optical Coherence Tomography

IVOCT was introduced about a decade later than IVUS in the 1990s [55, 56]. Similar like IVUS, IVOCT employs a side-looking imaging catheter with a sensor located at its tip to provide cross-sectional images of e.g coronary arteries. However, instead of sound waves, IVOCT utilizes NIR light (wavelength range is typically between 1250 and 1350 nm provided by a swept laser source) which is guided in an optical fiber inside the catheter, reflected outwards perpendicular to the catheter axis and focused at a mirror-coated ball lens located at the tip of the catheter (Fig. 1.32). The detection principle of IVOCT is based on low-coherence interferometry.

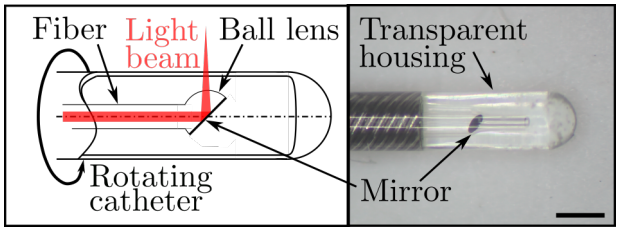

Figure 1.32: Sensor design of an intravascular optical coherence tomography imaging catheter (Dragonfly, Abbot Medical, Westford, MA 01886 USA); Scale bar: 500 μm.

Specifically, it analyzes the interference signal of the the light which is back-scattered from a reference mirror with the back-scattered light from the tissue. There are two methods for analyzing the interference signal

1. Time domain (TD) analysis: Measures the interference signal as a function of time for each wavelength separately by moving the reference mirror.

2. Frequency domain (FD) analysis: In contrast to TD, the reference mirror remains stationary and the whole NIR spectrum is recorded. The interference signal of all wavelengths can be derived in the frequency domain at once by applying a Fourier transformation.

Nowadays, IVOCT systems apply FD analysis because it significantly speeds up the acquisition time which was a major requirement for clinical applicability of the technology [57].

1.4.2.3 Comparison Between Intravascular Ultrasound and Optical Coherence tomography

IVUS and IVOCT have different strength and weaknesses in regards to imaging of coronary arteries which are based on their technical imaging characteristics (Tab. 1.5).

Imaging characteristic	IVOCT	IVUS	HD-IVUS
Wave length [μm]	1.3	37-74 (40-20 MHz)	24 (60 MHz)
Penetration depth [mm]	1-2	5-10	6
Axial Resolution [μm]	10-20	70-200	22-40
Flushing required	yes	no	no

Table 1.5: Comparison of technical characteristics of IVOCT and IVUS. IVOCT: Intravascular Optical Coherence Tomography; IVUS: Intravascular Ultrasound; HD-IVUS: High-definition Intravascular Ultrasound; (Adapted from [58]).

IVOCT delivers cross-sectional images with almost 10-times higher resolution and improved contrast compared to standard IVUS and, thus, allows to determine the vessel lumen with higher accuracy and resolve more details for the assessment of superficial plaque structures like a thin-cap, presence of macrophages and features at the endoluminal level like stent struts [50,51,59,60]. For instance, it was shown that the identification of suboptimal Percutaneous coronary intervention PCI results, like stent struts malapposition, is improved when IVOCT was used compared to IVUS [61]. In contrast, IVUS offers superior penetration depth and, thus, is more reliable for imaging larger vessels because it enables the assessment of deeper tissue layers and allows to determine whole plaque burden including outward vessel remodelling which is regarded as a relevant characteristic of plaque vulnerability [50, 51, 59]. Furthermore, IVUS can image coronary tissue through blood, while IVOCT requires flushing for blood clearance to prevent significant light attenuation and, thus, can not be used in patients with kidney dysfunction who are intolerant towards the required contrast agent [51].
To provide a visual comparison between both modalities, figure 1.33 shows exemplary intravascular images of a human coronary artery section (Fig. 1.33-a) indicating superior penetration depth in IVUS (Fig. 1.33-b) and improved resolution of the vessel wall in IVOCT (Fig. 1.33-c).
In general, intravascular imaging has proved valuable as a clinical support tool in different randomized trails over the years. For instance, IVUS imaging guidance during implantation of drug-eluting stents significantly reduced the emergence of adverse clinical events like MI, target vessel revascularization and stent thrombosis compared to standard angiography-guided implantations [62, 63]. Moreover, IVOCT-guided PCI is associated with a higher fractional flow reserve (Low values associated with higher degree of stenosis) than standalone angiography-guided PCI after completion of the intervention in patients suffering from ACS [64].
While these studies have shown that intravascular imaging is an invaluable tool for guiding coronary interventions like PCI and stent implantation in the clinics and improving corresponding patient outcomes, a higher goal for imaging could be defined as the detection of progressive and high-risk plaques for predicting future events and apply preventive interventions.

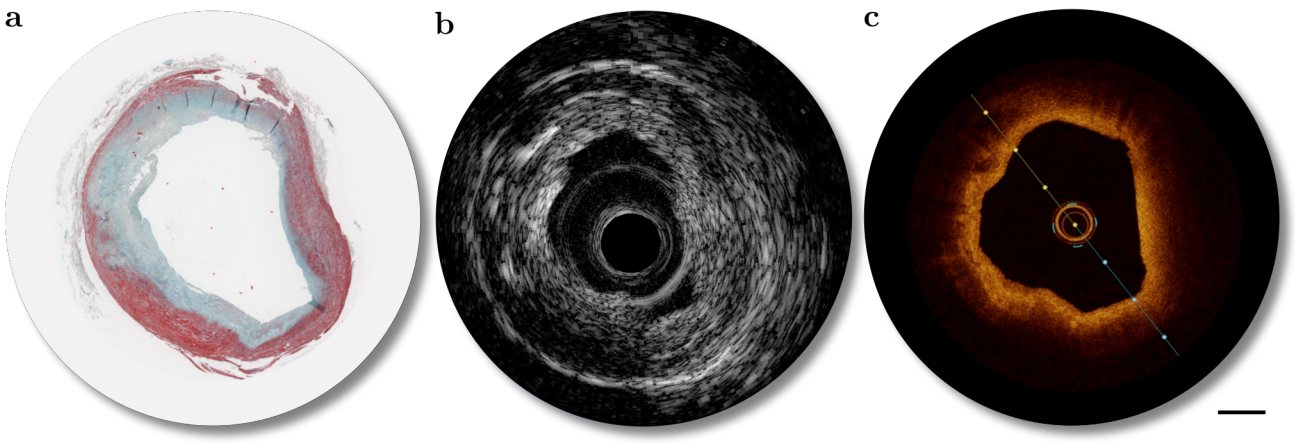

Figure 1.33: Exemplary intravascular anatomical images of a human coronary artery; a - Histology section of a human coronary artery stained with movat pentachrome and co-registered, **b** - IVUS (custom-made 40 MHz imaging catheter) and **c** - IVOCT images (Dragonfly, Abbot Medical, Westford, MA 01886 USA); Scale bar: 1 mm.

Clinically, this screening method could have an immediate beneficial impact when applied in patients presenting for check ups or in the case of symptoms for coronary revascularization. A lot of times additional non-culprit plaques can be found in these patients besides the one generating the symptoms while a method for checking these currently silent (asymptomatic) lesions for instability has remained elusive [51]. As already mentioned in 1.2 target features for the detection of progressive and vulnerable plaques are a lipid-rich necrotic core with an overlaying thin-fibrous cap (50-100 λm) compromised by inflammation (TCFA) and the presence of additional characteristics like microcalcifications, increased microvessel density and positive or outward remodelling of the entire artery [51].

Due to its high-resolution imaging capabilities, IVOCT can detect fibrous caps as thin as 65 μm and an underlying lipid pool. Features of inflammation, like macrophages, can be also visualized, however, the detection reliability remains unknown and more evidence based on imaging studies is required [50, 51]. IVUS can quantify whole plaque burden and most recent advances in IVUS imaging has opened up new possibilities for plaque characterization. For instance, improvements in IVUS transducer technology has enabled higher imaging frequencies which has introduced high-definition intravascular ultrasound (HD-IVUS, Tab.1.5). For instance, the commercially available 60 MHz Opticross HD imaging catheter from Boston Scientific allows clinical imaging with improved resolution. Furthermore, virtual histology IVUS (VH-IVUS) has been developed [65] which, instead of reconstructing US signals to gray-scale images, utilizes the raw back-scattered IVUS radiofrequency (RF) data and applies more advanced frequency analysis to provide information for the assessment of plaque morphology, tissue characterization and potentially improve vulnerable plaque detection [66]. This was also investigated in large clinical trails like the PROSPECT study. Here it was demonstrated that the analysis of IVUS-RF data has the potential to identify TCFAs through the detection of a necrotic core which proved to be predictors for major adverse cardiac events in patients with ACS [67]. However, VH-IVUS has not been widely used in the clinics yet which might be explained by the current lack for systemic validation and corresponding scientific analysis in comparison to what has been available for standard IVUS for many years [68].

1.5 Hybrid Intravascular Anatomical and Molecular Imaging

A limitation of IVUS and IVOCT is that they are anatomical or structural imaging modalities meaning they can provide anatomical information of the vessel wall and on plaque features like cap thickness (IVOCT) or plaque burden (IVUS) but lack sensitivity for visualizing key pathological markers. To overcome these limitations of currently available anatomical modalities, molecular imaging has been introduced to the field of intravascular imaging [51, 69]. This strategy has given rise to a variety of hybrid intravascular imaging technologies combining standard IVOCT or IVUS with a novel molecular imaging modality (Fig. 1.34) which will be described in more detail in the following sections.

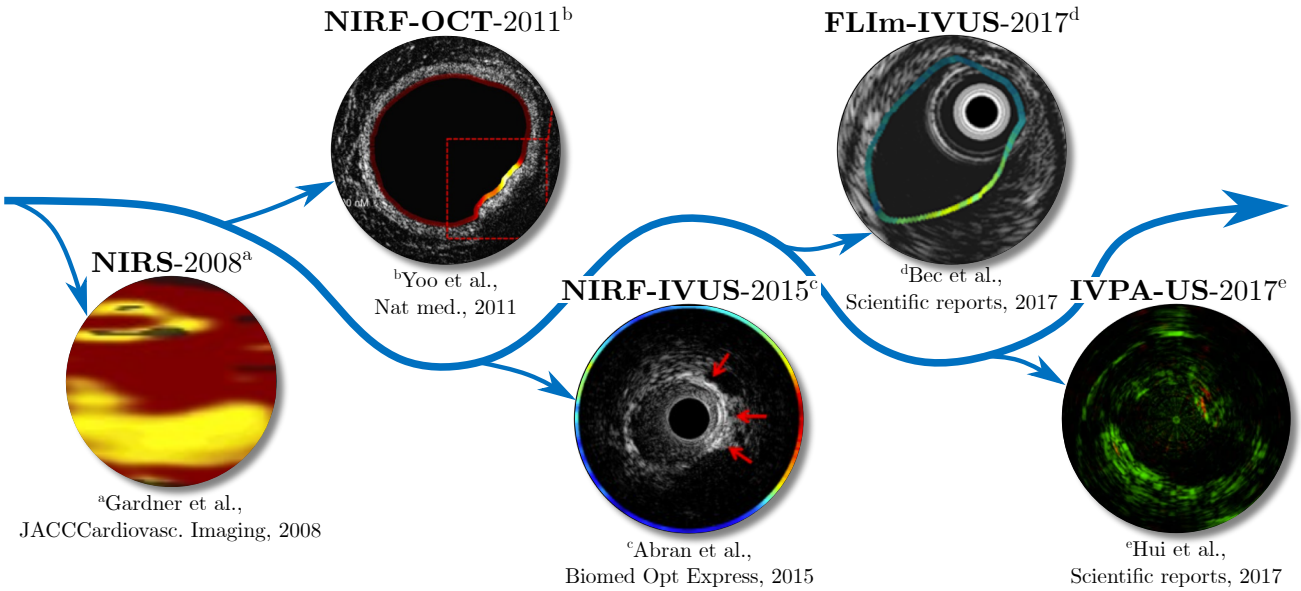

Figure 1.34: The evolution of intravascular hybrid molecular and anatomical imaging; NIRS: Near-Infrared spectroscopy; NIRF: Near-Infrared fluorescence; FLIm: Fluorescence lifetime imaging; IVPA: Intravascular photoacoustic.

The potential to detect important pathological characteristics of progressive and vulnerable plaques like lipid accumulation and inflammation in the form of macrophage foam cells (Fig. 1.35-a) has been demonstrated with these novel molecular intravascular imaging techniques (Fig. 1.35-b).
Most of these newly developed hybrid imaging technologies are currently at the stage of preclinical testing and validation except the near-Infrared spectroscopy (NIRS)-IVUS catheter which has been commercialized by Infraredx.

1.5.1 Intravascular Near-Infrared Spectroscopy

NIRS uses light at wavelengths of around 800-2500 nm to illuminate tissue and detect the diffusely reflected light for further spectral analysis. The reflection spectrum is based on the photon-tissue interaction in form of scattering and absorption which depends on the molecular composition of the sample (See section 1.3.2.1). A processing algorithm analyses the detected spectra to generate a chemogram which indicates the probability of lipid presence in tissue with a false color scale from red (Low probability) to yellow (High probability) [70, 71].

a

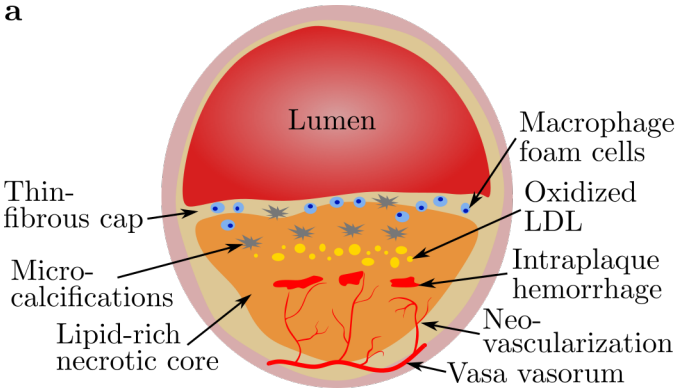

b

Plaque feature	NIRS	IVPA	FLIm	NIRF
Inflammation		✓*	✓	✓*
Lipid-rich necrotic core	✓	✓	✓	✓*
Intraplaque hemorrhage				✓*

Figure 1.35: Characteristics of vulnerable plaques as molecular imaging targets; **a** - High risk features include a thin fibrous cap ($< 65\mu$m), a large lipid-rich necrotic core, macrophage foam cells, mircocalcifications, oxidized low-density lipoproteins (LDL), intraplaque hemorrhage and neovascularization; **b** - The ability of novel intravascular molecular imaging technologies for visualizing characteristics of vulnerable plaques; *: Can be detected when an exogenous contrast agent is applied; NIRS: Near-Infrared spectroscopy; NIRF: Near-Infrared Fluorescence; FLIm: Fluorescence lifetime imaging; IVPA: Intravascular photoacoustic.

The commercially available NIRS-IVUS imaging catheter (Infraredx, a Nipro company, Bedford, MA 01730, US) has been FDA approved in 2010. The catheter is 3.2F ($\approx$ 1.07 mm) in size when inserted into the sheath, contains two optical fibers for light delivery and detection of approximately 1300 NIRS spectra per scanned millimeter of the vessel and a PZT element for IVUS imaging. It has been demonstrated that NIRS-IVUS can detect lipid core plaques (Receiver-operator characteristic area: 0.80) in coronary autopsy specimens as validated by histology [72]. Furthermore, the NIRS-derived lipid core burden index has shown prognostic value in patients suffering from CAD for major adverse cardiac events [73].

1.5.2 Intravascular Photoacoustic/Optoacoustic

The photoacoustic or optoacoustic effect describes the generation of US through light absorption of nanosecond laser pulses in the sample. Corresponding photoacoustic images are based on the detection of these US waves. Tissue-specific contrast can be generated by tuning the excitation wavelength for the absorption of different molecules. The benefit of photoacoustic imaging is the possibility to achieve molecular contrast through optical excitation while taking advantage of superior penetration depth of US signals. Intravascular photoacoustic (IVPA) imaging has been mainly focused on lipid detection in atherosclerotic plaques by using excitation wavelengths at 1.2 and 1.7 μm. Therefore, IVPA targets the same plaque characteristics than NIRS, however adds depth information of the lipid signals as opposed to NIRS signals which can only provide angular information mapped around the circumference of the vessel lumen. Real-time IVPA-US imaging of lipids has been demonstrated in vivo in atherosclerotic porcine coronary arteries [74] and ex vivo in excised human coronary arteries [75, 76]. Furthermore, the possibility to visualize inflammatory processes with targeted gold nanorods has been demonstrated [77]. A typical IVPA-US imaging catheter contains a single fiber for delivering laser pulses for IVPA excitation and a PZT element for both, detection of IVPA and IVUS signals. It is critical that the orientation of the PZT and optical elements are optimized to achieve sufficient overlap of optical excitation beam and acoustic signals. Major challenges for IVPA imaging are associated with detection of weak signals with limited options for further improvements due to limitations

in optical power that can be applied for excitation and the required catheter sheath which significantly attenuates weak IVPA signals and generates artefacts overlapping with lipid signals. Furthermore, while imaging through luminal blood has been demonstrated [78], most studies preferred saline flushing of arteries during imaging which is not always possible in a clinical environment [51]. In conclusion, hybrid IVPA-US catheters implemented into a sheath need to undergo further reduction in total outer diameter to fulfill clinical size requirements as a next step towards the translation of the technology.

1.5.3 Intravascular Fluorescence Lifetime Imaging

Fluorescence lifetime is a spectral imaging technique that uses UV light to illuminate the sample and excite autofluorescence which is an intrinsic property of different tissue components present in e.g healthy and diseased artery walls (See section 1.3.2.2). The lifetime of the excited autofluorescence state is a specific characteristic of different biochemical constituents of atherosclerotic plaques like structural proteins, lipids present in macrophages and lipid pools [51]. Thus, recent intravascular FLIm-IVUS imaging catheter can provide label-free molecular contrast and anatomical information of atherosclerotic arteries. However, this contrast is limited to very superficial areas of the vessel wall like the intima or fibrotic cap since penetration depth of light in the UV spectral region is limited. Nevertheless, it has been shown that intravascular FLIm-IVUS can detect the superficial presence of macrophage foam cells, calcium and extracellular lipid accumulation in advanced atherosclerotic lesions in human coronary arteries ex vivo [79]. Further validation of intravascular FLIm is required in in vivo animal models of atherosclerosis which will require flushing of the blood to be able to detect weak autofluorescence signals and to compensate for the limited penetration depth.

1.5.4 Intravascular Near-Infrared Fluorescence

As introduced in section 1.3.2.4, NIRF allows to image injected molecular imaging probes which bind or accumulate in tissue regions to visualize a range of pathobiological processes of atherosclerosis in vivo [80]. Intravascular NIRF imaging is operated in epi-illumination mode (see section 1.3.2.3) and usually utilizes a single fiber to deliver NIR light for fluorescence excitation while simultaneously collecting corresponding NIRF signals. In 2011, Jaffer et al. tested the first two-dimensional intravascular NIRF catheter based on an optical fiber for NIRF excitation and detection. The possibility to visualize plaque inflammation and stent-induced arterial injury through blood was demonstrated in a rabbit model of atherosclerosis in vivo via the detection of the NIRF agent ProSense750/VM110 [81]. Subsequently, intravascular NIRF has been combined with both IVOCT and IVUS into a hybrid imaging catheter. The tandem operation of NIRF and IVOCT/IVUS allows to co-register molecular with anatomical information of plaques. Furthermore, IVOCT and IVUS can measure the distance between the hybrid imaging catheter and the vascular wall. This information is critical to correct signals for the distance-dependent decrease in NIRF intensity and, thus improve quantification of NIRF probes located in the tissue. Combining NIRF with either IVOCT or IVUS has benefits and drawbacks based on their imaging characterisitcs as already summarized in Table 1.5. Importantly, it must be mentioned that one of the advantages of NIRF for intravascular applications is the reduced light attenuation by blood in the NIR region (Fig. 1.23) allowing to image arteries without the need for flushing. However, this potential can only be capitalized when combining NIRF with IVUS since IVOCT requires flushing for imaging.

NIRF-OCT:
In 2011, a hybrid NIRF-IVOCT catheter 2.4F in size was introduced containing a single dual-clad fiber for which the core was used for OCT and the cladding for NIRF imaging [82]. The system was validated by imaging a NIRF-fibrin labeled stent implanted into an excised human coronary artery ex vivo and rabbit arteries with acute endothelial injury in vivo. Following this first-generation system, Lee et al. developed a 2.6F NIRF-IVOCT system with increased acquisition rate (100 fps) and demonstrated detection of ICG in lipid- and macrophage-rich plaques in atherosclerotic rabbit models in vivo [83]. The same system was subsequently validated for imaging ICG accumulation behind drug-eluting stent and within atheroma in porcine coronary arteries [84]. Moreover, it was demonstrated that ex vivo NIRF-OCT can detect ICG accumulated in excised human carotid plaques exhibiting areas of impaired endothelial barrier function, macrophage infiltration, lipid accumulation and intraplaque hemorrhage [85].

NIRF-IVUS:
The first hybird NIRF-IVUS catheter was introduced by Dixon and Hossack and was validated in phantoms and ex vivo porcine carotid artery [86]. This first prototype was not a fully integrated hybrid imaging catheter but a NIRF fiber which was attached on the outside of the sheath of a commercially available IVUS catheter. Thus, one of the limitations was the missing sheath protection of the NIRF sensor and a large probe size of 4.2F (1.4 mm). The next generation prototype was designed by Abran et. al which featured a serial arrangement of the NIRF and IVUS sensor allowing to insert the hybrid imaging catheter into a single sheath with a total outer diameter of 4.2F (1.4 mm) [87]. This catheter was tested in phantoms and in vivo for imaging ICG accumulation in areas of atherosclerotic plaque formation in rabbit arteries [88]. Bozhko et al. further improved NIRF-IVUS imaging through blood by introducing a novel approach for correcting NIRF signals for distance-depend attenuation by blood which was demonstrated by in vivo NIRF-IVUS imaging of swine and rabbit arteries using the NIRF probes AlexaFluor750, ICG and ProSense750/VM110 [89].
Over the last years, several groups have demonstrated great evidence to underline the potential of intravascular NIRF-IVUS for the detection of atherosclerotic plaques. However, further technical improvements and validating imaging studies are currently needed to advance this novel imaging technology and provide more evidence about its value for visualization of atherosclerosis.

1.6 Motivation and Objectives of Thesis

Intravascular NIRF imaging can visualize a variety of fluorophores which have been recently developed to specifically target key molecular processes in atheroma like protease activity (ProSense/VM110), oxidized low-density Lipoprotein (LO1-750), endothelial permeability (CLIO-CyAm7), fibrin deposition (FTP11-Cy7) and microcalcifications (OsteoSense750) [69]. While this NIRF target specificity holds unprecedented potential to detect and classify coronary plaques in vivo, FDA approval of these fluorophores is a complex and lengthy process and, thus, none of these agents are expected to be applied in the clinics in the near future. In contrast, as mentioned in section 1.3.2.5, ICG has been used in the clinics for many years and has shown potential for targeting atherosclerosis in initial studies. **Therefore, the motivation of this thesis is to further improve and validate intravascular NIRF-IVUS imaging with ICG to provide the next steps towards the clinical translation of this hybrid imaging technology**. For this purpose, several objectives are defined:

1. The size of the smallest currently reported NIRF-IVUS imaging catheter is 4.2F or 1.4 mm including the sheath [87]. The size requirement for clinical application of intravascular imaging applications calls for significantly smaller outer catheter diameters of e.g. 3.2F or 1.07 mm including the sheath. Therefore, the first objective is to **develop a miniaturized, fully integrated NIRF-IVUS imaging system**.

2. Second, the newly developed imaging system must be **characterized in ex vivo phantoms using ICG and during high-speed operation** for the assessment of important technical specifications.

3. Third, the miniaturized NIRF-IVUS system must be validated **in vivo animal models of atherosclerosis using ICG as contrast agent**.

4. Fourth, there is a current lack of evidence how NIRF-IVUS can visualize plaques in human coronary arteries using ICG. Therefore, an ex vivo imaging study was conducted to **provide novel data for the validation of intravascular NIRF-IVUS imaging in excised human coronary arteries**.

5. Fifth, currently available methods for the correction of NIRF signals for intravascular blood attenuation suffer from limitations which challenge the accurate quantification of NIRF signals and the application of the technology in a clinical environment. To address this, a new method was developed to **improve the correction of intravascular NIRF signals for attenuation by blood**. This method could reduce inaccuracies for the quantification of ICG or other fluorophores accumulated in artery walls and, thus, improve the inspection of atherosclerotic lesions.

1.7 Structure of Thesis

According to the objectives defined above, the remaining of this thesis is structured as follows:

Chapter2 describes the development of a miniaturized 3.7F and 3.2F NIRF-IVUS imaging system.

Chapter3 presents the technical characterization of the developed NIRF-IVUS systems for imaging of ICG and, additionally, during high-speed imaging when operating the 3.2F system.

Chapter4 presents the application of the new 3.2F NIRF-IVUS imaging system for in vivo imaging of pre-clinical rabbit models of atherosclerosis.

Chapter5 demonstrates for the first time NIRF-IVUS imaging of whole human coronary arteries ex vivo using ICG and the 3.7F imaging system.

Chapter6 presents a novel method for the correction of NIRF signals for light attenuation by blood.

Chapter 2

Development of NIRF-IVUS Imaging Systems

2.1 Introduction

This chapter describes the development of two NIRF-IVUS systems including the corresponding imaging catheters. Both systems enable NIRF-IVUS imaging with miniaturized catheters which are 3.7F (⌀1.24 mm) and 3.2F (⌀1.07 mm) in size. These dimensions include the catheter sheath which is required to shield the imaging catheter from the tissue (Artery wall and blood) and allow saline flushing inside the catheter sheath to insure i) US coupling into the tissue (see section 1.4.2) and ii) prevent blood deposition on the imaging sensors.

2.2 3.7F NIRF-IVUS System

As a first step towards miniaturization for future clinical applications, a system was developed which allowed the operation of a 3.7F NIRF-IVUS imaging catheter. The goal was to develop a robust and highly sensitive imaging system to provide high quality IVUS and NIRF images while achieving first improvements in size reduction. Figure 2.1 gives an overview of the 3.7F intravascular NIRF-IVUS imaging system. The system can be differentiated between the NIRF-IVUS imaging catheter (Fig. 2.1-a) and the back-end system (Fig. 2.1-b).
The development of the 3.7F imaging catheter is described first. Subsequently, the components of the back-end system are presented including all hardware components and corresponding software.

2.2.1 Catheter Development - 3.7F

The 3.7F NIRF-IVUS catheter featured a right-angle micro prism with a 250 μm leg length and width (8531-608-1, Precision Optics Corporation, Gardner, Massachusetts, US) attached to a multimode optical fiber (200/220 μm, Numerical Aperture (NA) 0.22, FG200LEA, Thorlabs, Newton, NJ, USA) and a PZT element (size: 0.6 x 0.5 mm; center frequency: 40 MHz; bandwidth: 72%; Blatek, Boalsburg, Pennsylvania, USA) for NIRF-IVUS signal excitation and detection (Fig. 2.2-a). Both sensors were implemented into a ferrule located at the tip of the catheter to afford an outer diameter of 1 mm. This micro assembly process was outsourced to a specialized company (Precision Optics Corporation, Gardner, Massachusetts, USA). The prism was coated with aluminum at the hypotenuse to create a reflective surface angled at 45° to guide the NIRF

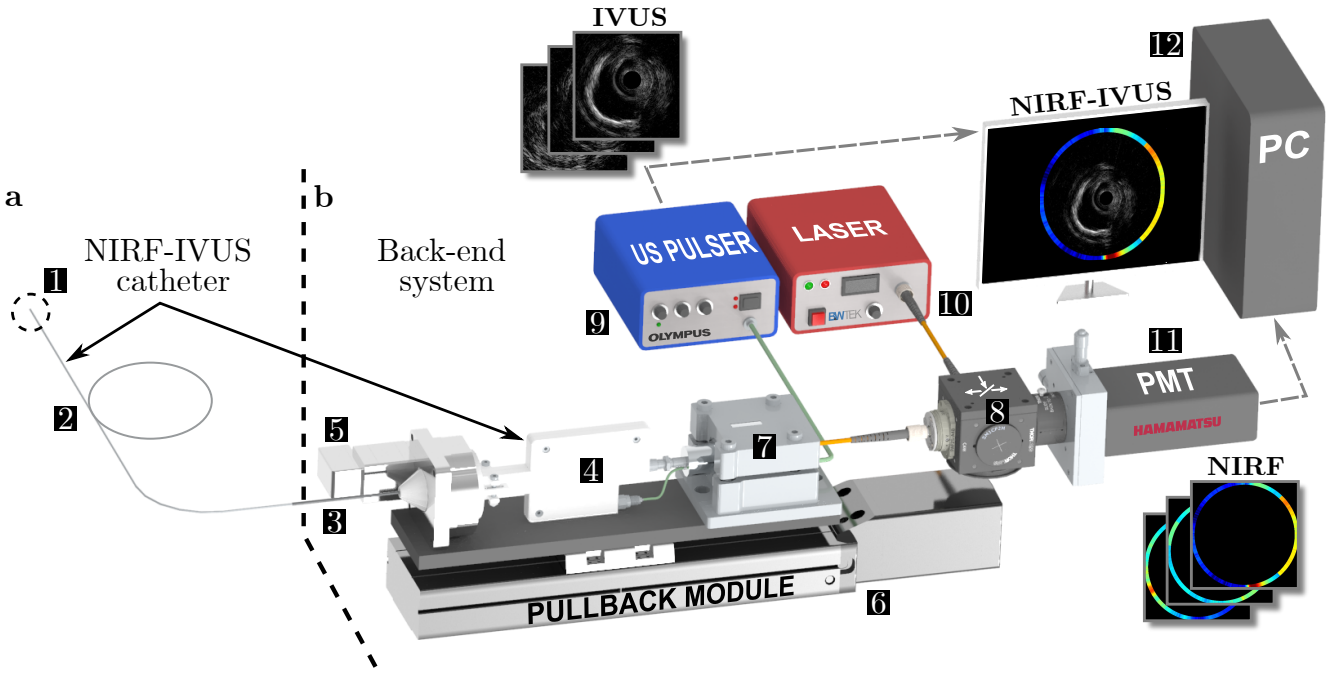

Figure 2.1: Illustrative overview of the 3.7F NIRF-IVUS imaging system. a - NIRF-IVUS imaging catheter including the sensor tip (1), torque coil (2), hypotube (3) and 3D-printed connector-interface (4); **b** - Back-end NIRF-IVUS system including a helical pullback module run by rotational motor (5) and linear stage (6), a fiber optical rotary joint with an electrical slip ring (7), an optical separation module (8), a ultrasound pulser-reciever (9), a laser source (10), a photomultiplier tube (PMT, 11) and a PC (12); Some CAD components are courtesy of Thorlabs (www.thorlabs.com).

excitation light through an opening in the ferrule (∅: 0.5 mm) to a plane perpendicular to the rotational axis of the fiber/catheter. This optical design allows to illuminate the vessel wall during intravascular imaging (Fig. 2.2-b) and collect corresponding fluorescence emission as NIRF signals. Using epoxy resin, the ferrule was connected to a torque coil in which the NIRF fiber and IVUS signal wire were inserted (Fig. 2.2-a-b). The torque coil translates the rotation introduced at the helical pullback module (Part of the back-end system) to the ferrule or sensor tip. The torque coil was connected to a hypotube (∅: 2mm) with epoxy resin at the distal part of the catheter (Fig. 2.2-c).
The catheter was inserted into a sheath which was custom-made out of a 6F introducer sheath (RT-R60G10PQ, Terumo Europe) connected to tubing (Material: Low-density polyethylene (LDPE), ZEUS, Orangeburg, USA) and resulted in the final catheter diameter of 1.24 mm or 3.7F (Fig. 2.2-c). The introducer featured a flush port and a hemostatic valve which acted as a sealing to flush the entire catheter sheath with saline while ensuring catheter rotation with minimal friction between the hypotube and the valve. The distal part of the NIRF-IVUS catheter comprised a 3D-printed housing which allowed integration of the catheter into the pullback module (Fig. 2.2-d). Specifically, an adjustable interface attached the imaging catheter to the rotational motor and an optical FC/PC and electrical SMA adapter connected the NIRF fiber and IVUS signal/ground wire to a fiber-optic rotary joint (FORJ) combined with an electrical slip ring (Part of the back-end system). Aluminum foil was used to create an electrical connection from the hypotube/torque coil to the ground of the electrical SMA connector to establish an additional ground connection of the imaging catheter minimizing noise in the IVUS

data.

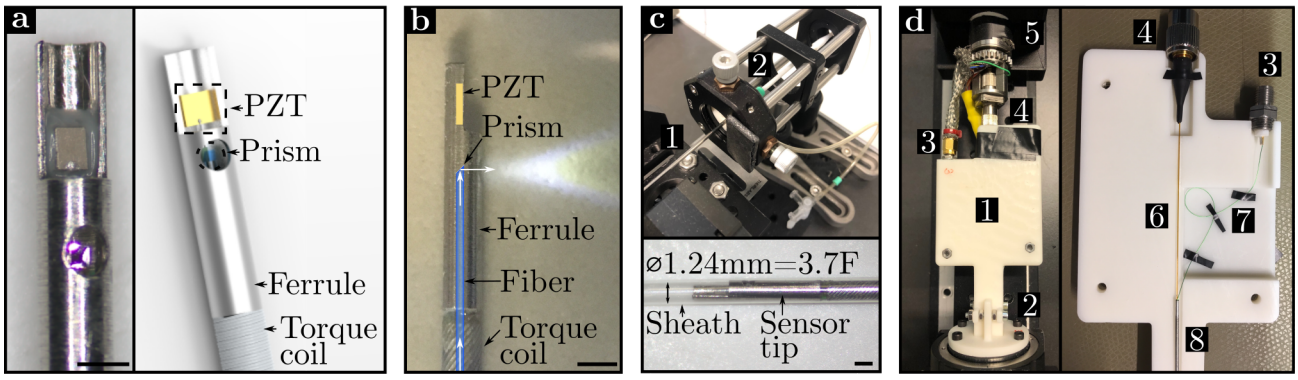

Figure 2.2: 3.7F NIRF-IVUS imaging catheter. **a** - A micro prism and PZT are integrated into a ferrule functioning as the NIRF-IVUS sensor tip which is connected to the distal part of the catheter via a torque coil; **b** - The micro prism reflects the NIRF excitation light from the fiber perpendicularly to the catheter axis; **c** - The catheter hypotube (1) is inserted in the hemostatic valve (2) of the catheter sheath featuring a flush port; Outer diameter of the catheter is 1.24 mm or 3.7F when inserted into the sheath; **d** - The 3D-printed housing (1) includes an adjustable interface to the rotary motor (2), an electrical SMA (3) and optical FC/PC adapter (4) connecting to the FORJ-Slip Ring (5) and houses the exposed NIRF fiber (6) and IVUS wire which are inserted into the torque coil (8); Scale bars: 500 μm.

2.2.2 Development of the Back-end System - 3.7F

The description of the development of the the back-end system is differentiated between hardware and software components.

2.2.2.1 Hardware - 3.7F

Figure 2.1-b provides an overview of the hardware components used for assembly of the 3.7F imaging system.

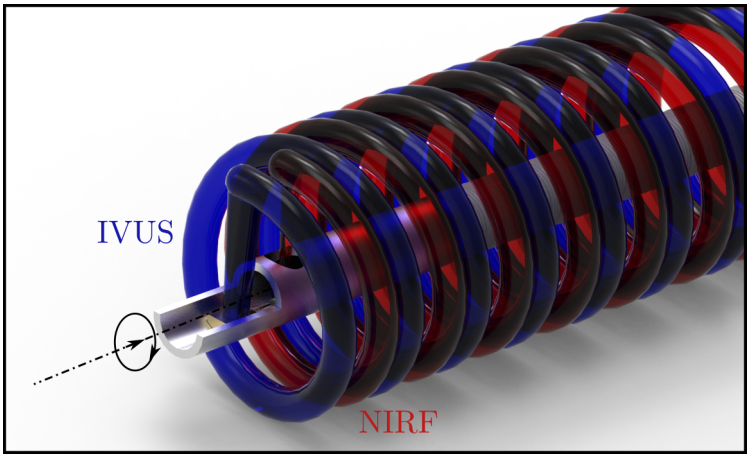

Figure 2.3: Illustration of a NIRF-IVUS helical pullback scan.

The pullback module includes a FORJ combined with an electrical slip ring (Princetel Inc., Hamilton Township, New Jersey, USA) which connects the NIRF-IVUS signal channels (Fiber

and electrical wire) of the rotating front part of the system (Imaging catheter) to the stationary back-end. A rotary motor (Motor model DGM60-ASAK, controller model ASD10A-K, Oriental Motor, Tokyo, Japan) and a linear stage (Stage model EZSM3D020K, controller model CK1, Oriental Motor, Tokyo, Japan) were used to generate the helical pullback movements of the catheter for imaging (Fig. 2.3). An US pulser-receiver (Model 5073PR, Panametrics, Waltham, USA) was used to excite and detect IVUS signals. A 750 nm fiber-coupled laser (B&W Tek, Newark, DE, USA) was implemented to excite NIRF while a photomultiplier tube (PMT, Model H6780-20, Hamamatsu, Japan) detects corresponding NIRF signals.

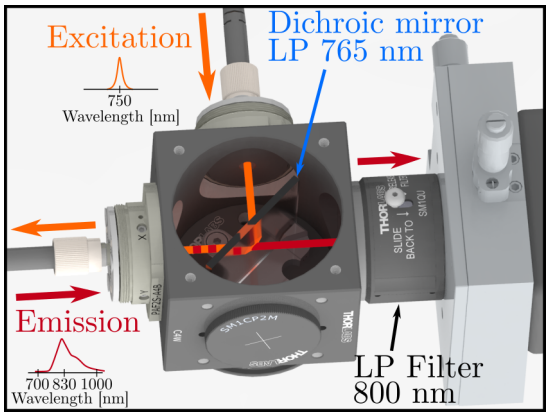

Figure 2.4: Optical filters for separation of NIRF excitation and emission light. CAD components are courtesy of Thorlabs (www.thorlabs.com).

An optical free-space arrangement allowed to separate NIRF excitation from emission light (Fig. 2.4). The excitation light from the laser (λ=750nm) was coupled into a fiber (200/220 μm, 0.22 NA, Thorlabs), collimated with the first aspheric fiber-port (PAF2P-11B, Thorlabs) and reflected at a dichroic beamsplitter (λ cut-on=765nm, FF765-Di01, Semrock) mounted inside an optics free-space (Cage cube, C4W, Thorlabs). The reflected excitation light was then focused with a second fiber-port (PAF2P-11B, Thorlabs) into a second fiber (200/220 μm, 0.22 NA, Thorlabs) which guides the light towards the FORJ-Slip ring and imaging catheter. On the return path, NIRF emission light collected with the imaging catheter was collimated at the second fiber-port and transmitted through the dichroic beamsplitter and a long-pass filter (λ cut-on=800nm, FELH0800, Thorlabs) towards the PMT where it is converted into an electrical signal. The long-pass filter was installed to remove any light leakage, e.g. reflected excitation light, to minimize noise detected with the NIRF modality.
All system components were mounted onto a cart (Fig. 2.5-a) including the helical pullback module (Fig. 2.5-b) to mobilize the system. A data acquisition (DAQ) card (PCI-5124, National Instruments Corp., Austin, Texas, USA) was installed in the PC to sample the analog signals with a sample rate of 200 MS/s and convert them to a digital output with a resolution of 12-Bit for further post-processing and NIRF-IVUS image display. Additionally, the PC functions as an interface via a developed software which is required for user input and hardware control to enable imaging scans.

2.2.2.2 Software - 3.7F

A custom-made LabVIEW (National Instruments Corp., Austin, Texas, USA) software was designed to i) control both motors for operating helical imaging pullbacks and ii) enable data acquistion and visualization. The flowchart in figure 2.7 provides an overview of the program structure of the developed software. The first process is the initialization of the DAQ and

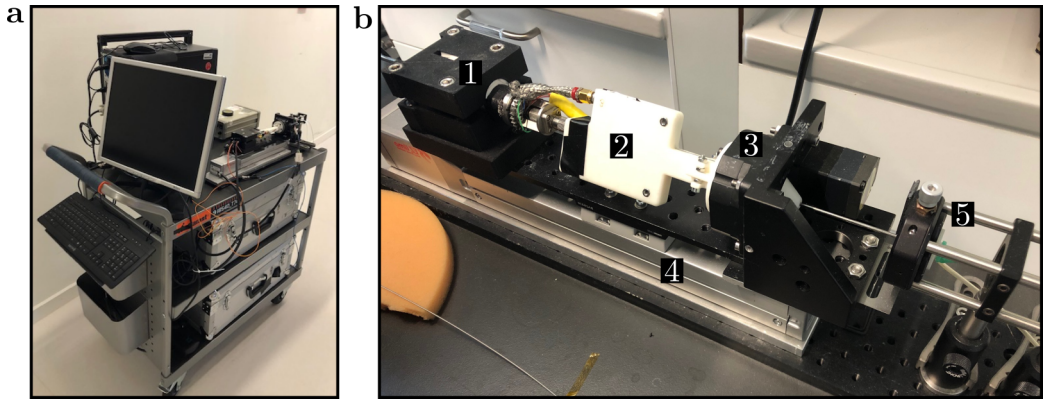

Figure 2.5: Mobilized 3.7F NIRF-IVUS imaging system. a - 3.7F NIRF-IVUS imaging system mounted on a cart; **b** - Helical pullback module including the fiber-optic rotary joint-slip ring (1), catheter housing (2), rotary motor (3), linear stage (4) and flush-port (5) functioning as the interface to the sheath.

the motors. Specifically, two channels are designated in the DAQ card for NIRF and IVUS measurements and the trigger source is defined as external. The internal 10 kHz trigger of the US pulser-reciever unit is used to trigger and synchronize the DAQ with the pullback motion. Next, the user must provide input parameters via a graphical user interface (GUI) to configure the DAQ and the motors for the helical pullback motion of the catheter. These input parameters are described in figure 2.6.

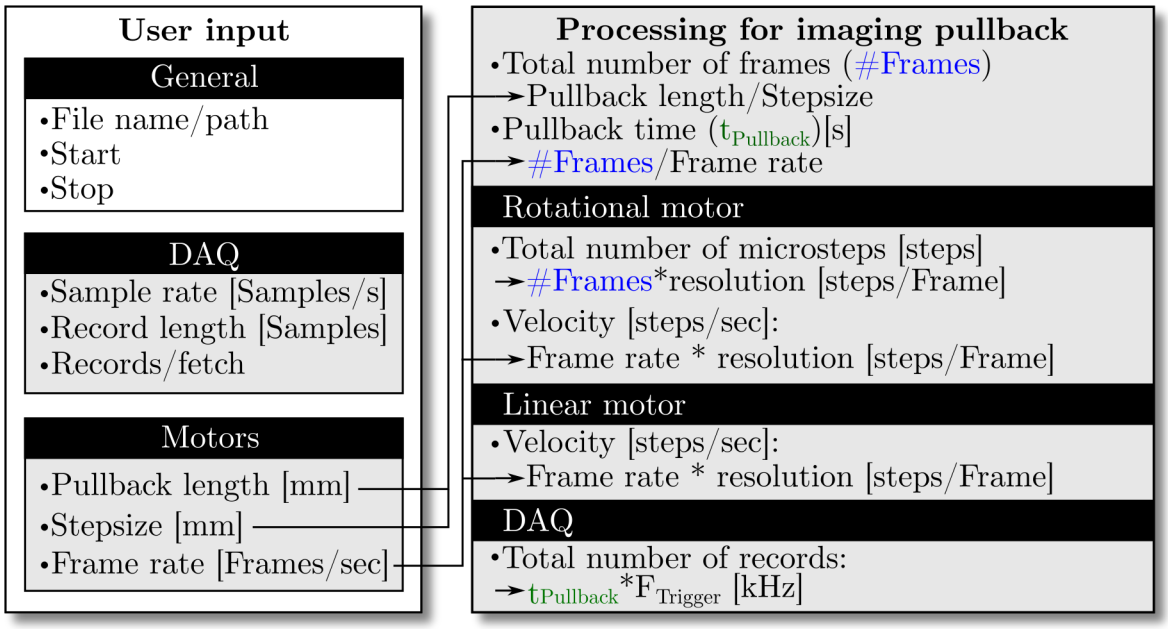

Figure 2.6: Overview of the input parameters for the Labview software running the 3.7F NIRF-IVUS imaging system.

Specifically, a record is defined as an A-line that is recorded per trigger event and features a certain sampling depth (record length). The pullback length is the total length the imaging catheter is pulled back by the linear motor while the rotary motor rotates the catheter at a certain velocity dependent on the desired frame rate. The step size is defined as the pullback

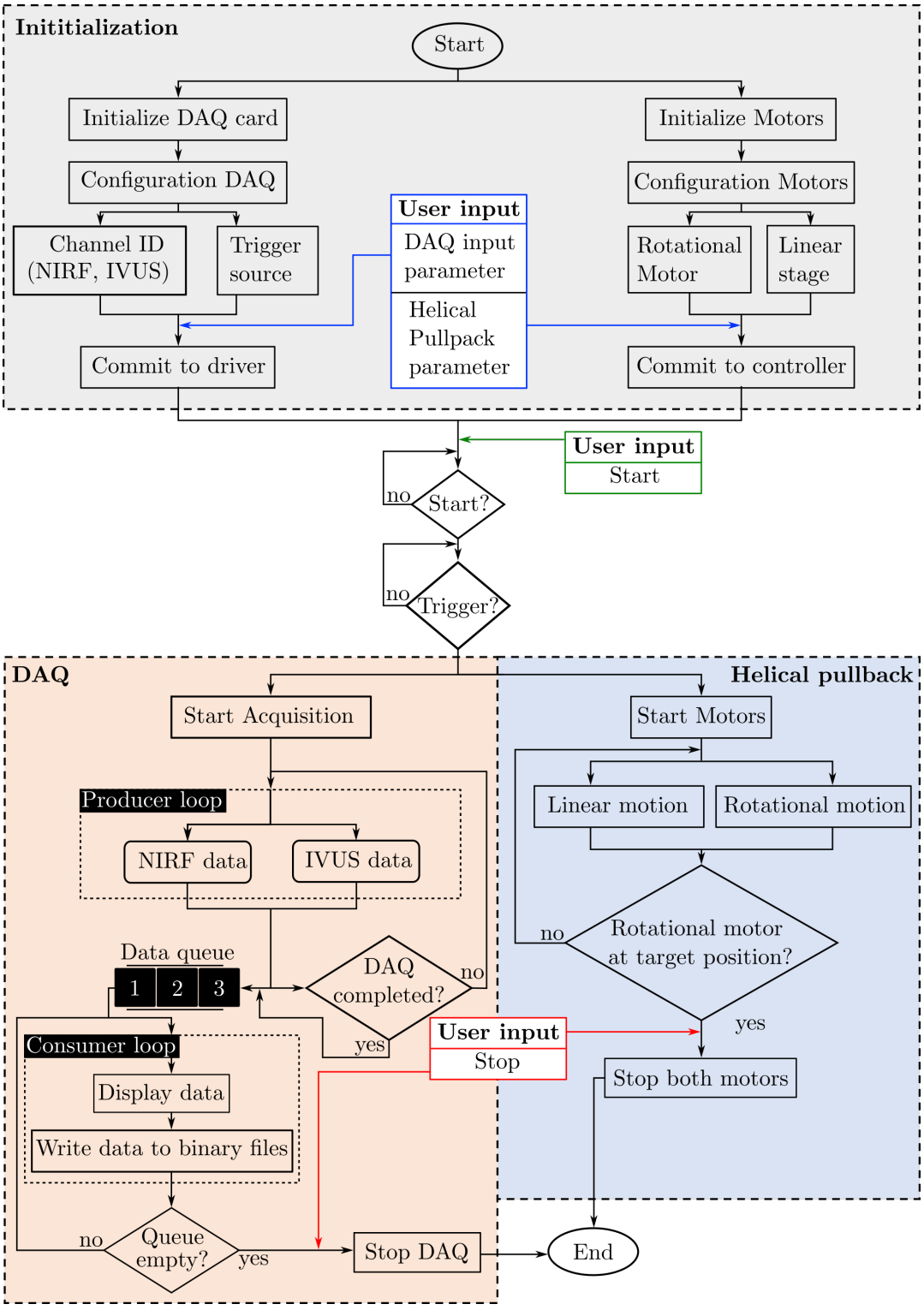

Figure 2.7: Overview of the Labview software running the 3.7F NIRF-IVUS imaging system.

length during one full catheter revolution or frame. Once the user provides the start signal via clicking a button in the GUI, the program waits for a first trigger signal to start DAQ and helical pullback motion simultaneously.
The helical pullback motion is completed and stops once the rotational motor reaches its pre-defined target position. For DAQ, a producer loop acquires NIRF and IVUS data from the

two channels and stores a pre-defined volume of data per loop (records per fetch) in a queue on the on-board memory of the DAQ card. In parallel, a consumer loop fetches the data from the queue, displays it in designated plots in the GUI and, finally, writes it into binary files on the hard drive of the PC. This acquisition structure allows to access the data for visualization during the ongoing DAQ process without interruption. However, it must be mentioned that a prerequisite for a successfully working producer-consumer loop structure without any data loss is the prevention of data overflow in the queue stored on the on-board memory of the card. For this purpose, the onboard memory must be sufficient in size and the consumer loop must be able to fetch the data from the queue fast enough before the producer loop fills it up completely and data overwriting occurs. Figure 2.8 displays the GUI for the definition of input parameters for the imaging pullback and visualization of NIRF-IVUS A-lines.

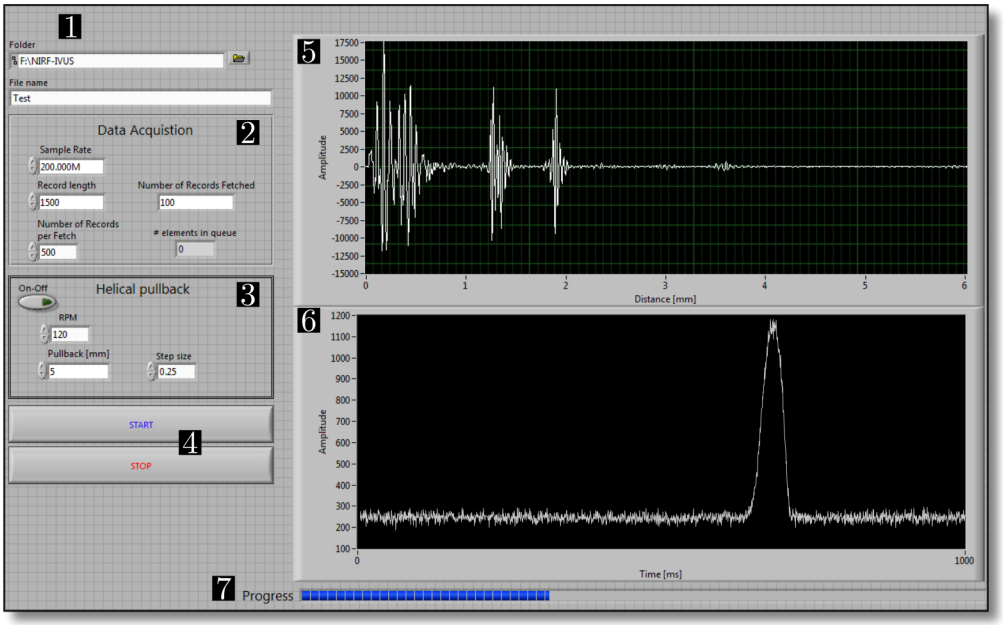

Figure 2.8: Graphical user interface for the Labview software running the 3.7F NIRF-IVUS imaging system including input parameters for file path and name (1), data acquisition (2), helical pullback movement (3), start and stop buttons (4), A-line display for IVUS (5) and NIRF (6) and an acquisition progress bar (7).

2.3 3.2F NIRF-IVUS System

The second system was developed to operate a 3.2F NIRF-IVUS imaging catheter which, for the first time, achieves size requirements for clinical intravascular applications. Important contributions of the development of the 3.2F NIRF-IVUS imaging system were separately published [90].

Figure 2.9 gives an overview of the 3.2F intravascular NIRF-IVUS imaging system. Similar like the 3.7F system, it can be differentiated between the NIRF-IVUS imaging catheter (Fig. 2.9-a) and the back-end system (Fig. 2.9-b). As for the 3.7F system, the development of the 3.2F imaging catheter is presented first, followed by a description of the components of the back-end system including hardware and corresponding software.

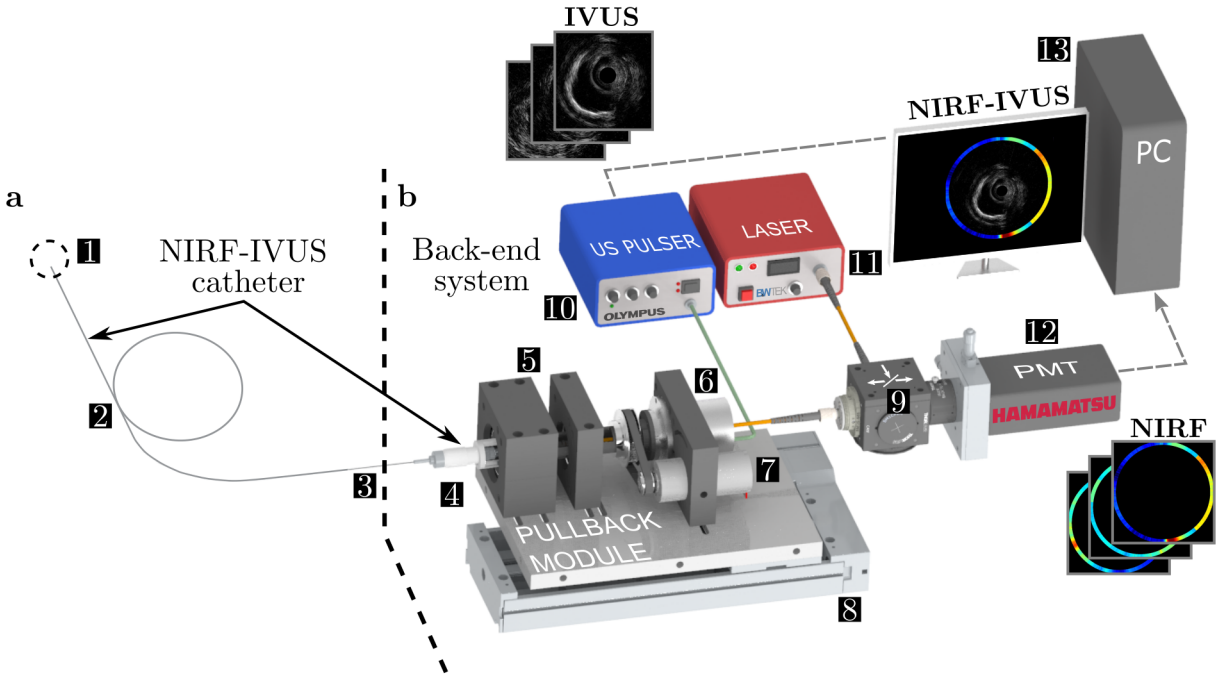

Figure 2.9: Illustrative overview of the 3.2F NIRF-IVUS imaging system. a - NIRF-IVUS imaging catheter including the sensor tip (1), torque coil (2), hypotube (3) and 3D-printed connector-interface (4); **b** - Back-end NIRF-IVUS system including a helical pullback module comprising an interface with rotational joints(5), a fiber optical rotary joint with an electrical slip ring (6) and a rotational motor (7) and linear stage (8), an optical separation module (9), a ultrasound pulser-reciever (10), a laser source (11), a photomultiplier tube (12) and a PC (13); Some CAD components are courtesy of Thorlabs (www.thorlabs.com).

2.3.1 Catheter Development - 3.2F

For the 3.2F catheter two different NIRF sensors were developed featuring either a right-angle micro prism with a 180 μm leg length and width (8531-607-1, Precision Optics Corporation, Gardner, Massachusetts, US) coated with a reflective aluminum layer at the hypotenuse or a ball lens (WT&T, Quebec, Canada) coated with a reflective gold layer (Nano4Energy, Madrid, Spain). Both optics, the prism (Fig. 2.10-a) and the ball lens (Fig. 2.10-b), were attached to a multimode fiber (50/125μm, FG050LGA, Thorlabs) by a sepcialized company (WT&T, Quebec, Canada). The prism-fiber assembly featured metal tubing in the uncoated fiber section to protect it from damage. A PZT element (Size: 0.6 x 0.4 x 0.3 mm; center frequency: 40 MHz; bandwidth: 68%; Blatek, Boalsburg, Pennsylvania, USA) was used for IVUS signal excitation and detection (Fig. 2.10-c).

The subsequent assembly steps of the 3.2F NIRF-IVUS catheters were completed in the laboratory and are described in the following. Both sensors were implemented into designated windows (1: NIRF; 2: IVUS) in a ferrule (Fig. 2.10-d, Pulse Systems, Concord, Carlifornia, USA) located at the tip of the catheter with an outer diameter of 550 μm. A torque coil with the same outer diameter (Fig. 2.10-e, Asahi-Intecc, Japan) was micro-welded to the ferrule to transmit the rotation for the helical pullback movement similar like for the 3.7F imaging catheter. While the surface of the PZT element for the prism catheter was kept parallel to the catheter axis (Fig. 2.10-f), the PZTs for two ball lens catheters were tilted by about 11° and 13° (Fig. 2.10-g-h) to achieve overlap of NIRF and IVUS excitation beams and minimize IVUS reflection losses at

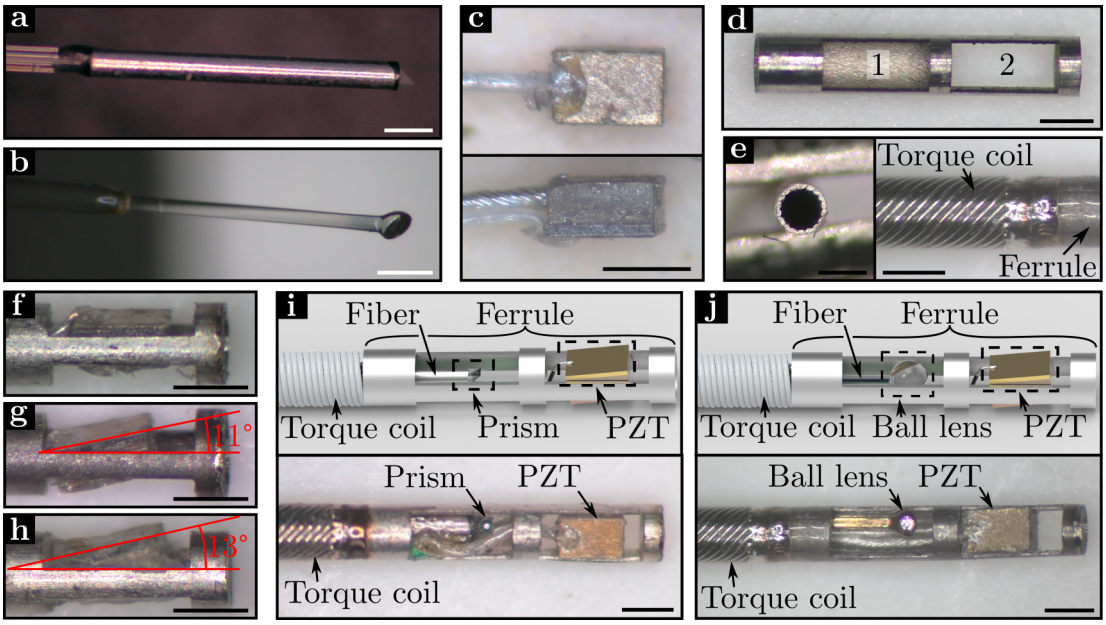

Figure 2.10: 3.2F NIRF-IVUS imaging catheter - Sensor tip. a - Micro prism attached to a fiber with metal tubing as reinforcement; **b** - Ball lens with gold coating as a reflective surface attached to a fiber; **c** - PZT element for IVUS signal excitation and detection; **d** - Ferrule featuring two windows for housing the NIRF (1) and IVUS (2) sensors; **e** - Torque coil attached to the ferrule for transmission of rotational forces; **f** - PZT angulation in the ferrule of the prism catheter; **g-h** - PZT angulation in the ferrule of the ball lens catheter; **i** - Final assembly of the sensor tip of the prism NIRF-IVUS catheter; **j** - Final assembly of the sensor tip of one of the ball lens NIRF-IVUS catheter; Scale bars: 500 μm.

the sheath encapsulating the catheter. The final assembly of the NIRF-IVUS catheter tip with either the prism or ball lens can be seen in figure 2.10-i-j. As a next step, the fiber and coaxial cable were threaded through the torque coil and finally through two stainless steel hypotubes (Hypotube#1-$\varnothing$: 600 μm; Hypotube#2-$\varnothing$: 800 μm) at the side of the catheter which connects to the back-end system.

The hypotubes were inserted into a metal cap (Opticross 3.0 Fr catheter, Boston Scientific Corporation, Marlborough,Massachusetts) which was connected with epoxy resin to a 3D printed housing (Fig. 2.11-a). The coaxial cable and the fiber were threaded all the way through the housing and prepared for connection (Orange box: Uncoating of the fiber) to the designated electrical and optical adapters. The hypotube#1 and torque coil were connected with epoxy resin (Fig. 2.11-b). The surrounding isolation of the coaxial cable was removed, ground wires were separated from the signal wire, the isolation of the signal wire was removed and both, signal and ground wires were soldered to the designates pins of a mirco-electrical adapter (Fig. 2.11-c; OMNETICS, A79109-001, MSA components, Attendorn, Germany). Finally, the uncoated fiber was inserted into an angled optical adapter (FC/APC, 30127A3, Thorlabs), fixed with fiber optic epoxy (F120, Thorlabs) and polished. A 3D printed fork featuring two prongs was attached to the housing (Fig. 2.11-d). The connected electrical adapter was placed on one of the prongs and was orientated with help of a mock-up interface resembling the one at the back-end system (Fig. 2.11-e) to align the notch of the electrical adapter with the optical adapter (Fig. 2.11-f). The catheter sheath was made out of LDPE tubing (Fig. 2.12-a; Outer $\varnothing$ =1.07mm; Inner $\varnothing$ = 0.9mm) connected via a 3D printed flexible adapter to a 5F introducer sheath (RT-R50G10PQ, Terumo Europe) which was cut to a length of 75mm (Fig. 2.12-b).

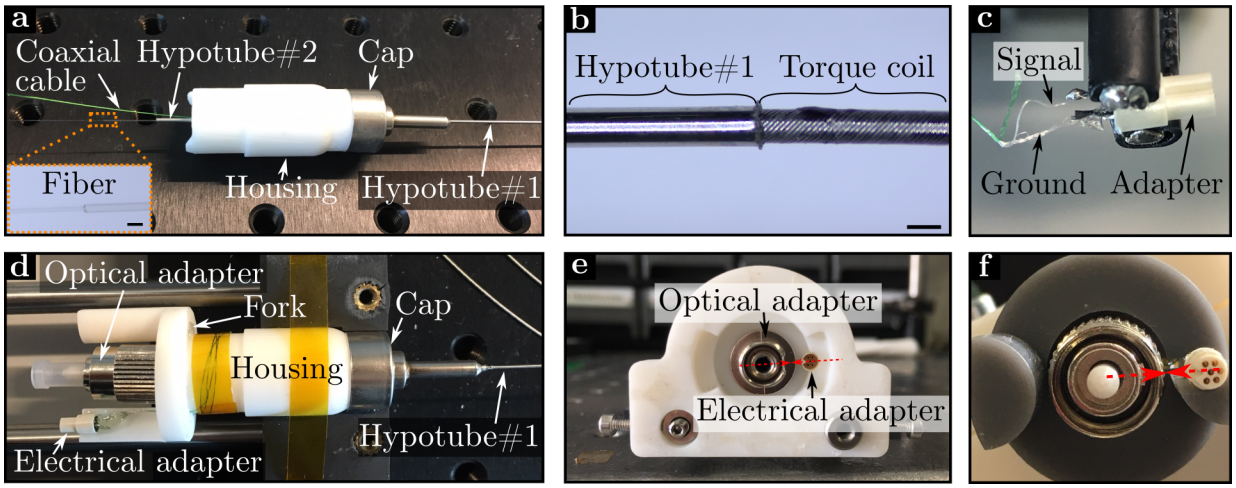

Figure 2.11: 3.2F NIRF-IVUS imaging catheter - Back-end interface. **a** - Integration of coaxial cable, fiber and hypotubes into the back-end catheter housing; **b** - Connection of the torque coil into hypotube#1; **c** - Connection of the electrical signal and ground wire to the adapter; **d** - Finalized assembly of the back-end catheter interface; **e** - Mock-up interface resembling the back-end system; **f** - Alignment of the electrical adapter to the optical adapter at the catheter; Scale bars: 500 μm.

Once the catheter was inserted into the sheath the final outer diameter was 1.07 mm or 3.2F (Fig. 2.12-c). Water or saline flushing of the catheter was possible via a port at the introducer sheath and the implementation of a x-y translator (CXY1A, Thorlabs) enabled co-axial alignment of the catheter inside the sheath when connected to the back-end system (Fig. 2.12-d).

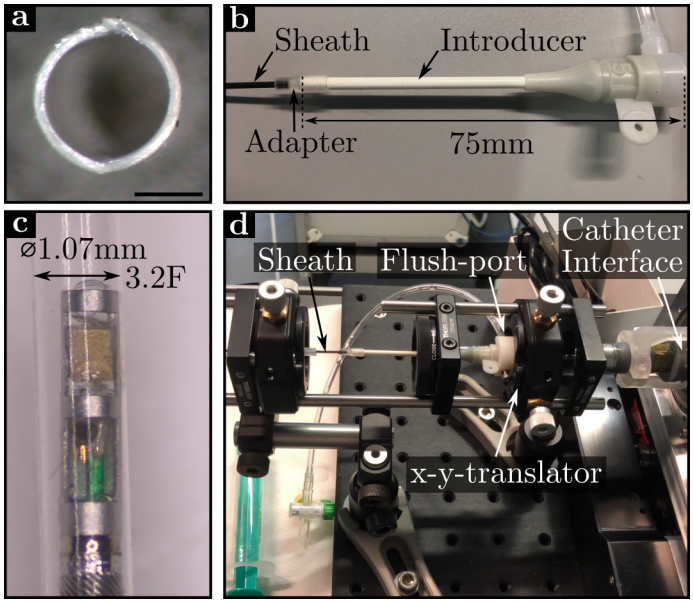

Figure 2.12: 3.2F NIRF-IVUS imaging catheter - Sheath. **a** - Cross-section of LDPE tubing; **b** - Connection of the sheath to a 5F introducer sheath via a 3D printed adapter; **c** - Insertion of the imaging catheter into the sheath afforded a final outer diameter of 3.2F; **d** - Co-axial catheter alignment inside the sheath when connected to the back-end system; Scale bars: 500 μm.

2.3.2 Development of the Back-end System - 3.2F

Similar like for the 3.7F back-end system, the description of the 3.2F back-end system development is differentiated between hardware and software.

2.3.2.1 Hardware - 3.2F

An overview of the assembly of the hardware components can be seen in figure 2.9-b.

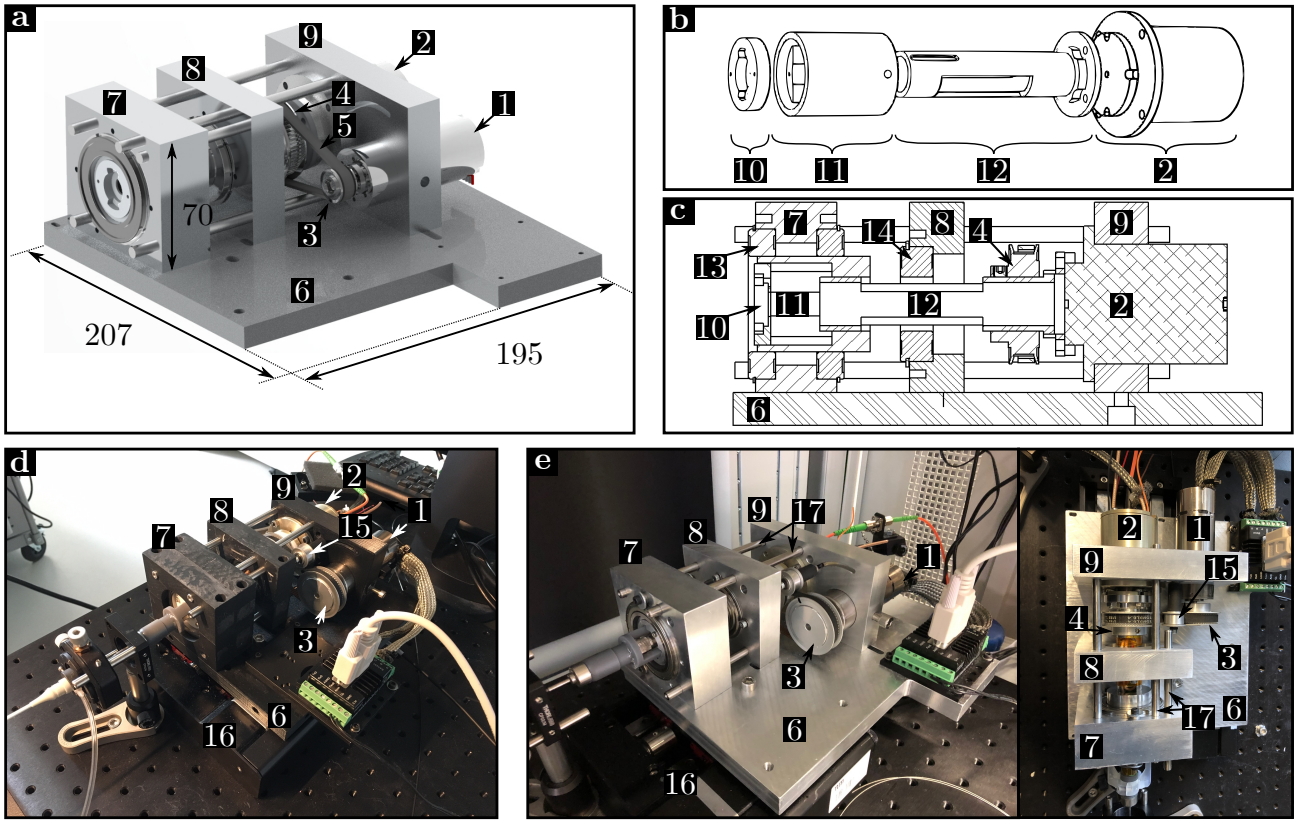

Figure 2.13: 3.2F NIRF-IVUS imaging system - Pullback module. **a** - Illustrative overview of the pullback module; 1: Rotary motor, 2: FORJ-Slip ring, 3 and 4: pulleys, 5: Driving belt, 6: Ground plate, 7: Front-clamp, 8: Mid-clamp, 9: Back-clamp; Units in mm; **b** - Rotational axis of the pullback module; 10: Interface plate, 11: Rotary adapter, 12: Rotational shaft; **c** - Cross-sectional view of the pullback-module; 13 and 14: Ball bearings; **d** - Pullback module assembled out of 3D printed components; 15: Idler, 16: Linear motor; **e** - Pullback module assembled out of manufactured aluminum components; 17: aluminum rods.

The pullback module (Fig. 2.13) includes a FORJ-slip ring (Alpha Slip Rings, Austin, Texas, USA), a rotary motor (3268G042BX4AES-4096, Faulhaber, Germany) and a linear stage (X-LRQ stage, Zaber, Vancouver, BC, Canada) which enable helical pullback scans with the imaging catheter as already illustrated for the 3.7F system (Fig. 2.3). The rotation is transferred from the rotary motor to the rotational axis of the pullback module via two pulleys (Fig. 2.13-a; 3: ATP60MXL025-B-P5; 4: ATP60MXL025-B-P20; Misumi, Tokio, Japan) and a driving belt (Fig. 2.13-a; 5: TBN114MXL025, Misumi, Tokio, Japan). Three clamps (7-9) serve as a framework to house all components of the pullback module and are mounted onto a ground plate (6) as illustrated in figure 2.13-a. The front of the pullback module features an interface plate (10) for connecting the imaging catheter with designated slots to house the matching

electrical and optical adapters and the catheter prongs (Fig. 2.11-e, Fig. 2.13-b). The interface plate was mounted to a rotary adapter (11) which connects the rotational axis of the pullback module to the FORJ-Slip ring via a rotary shaft (12). The front-clamp (7) houses two ball bearings (13: B6907ZZNR, Misumi, Tokio, Japan) to mount the rotary adapter (11) with the interface plate (10), the mid-clamp (8) houses one ball bearing (14: B6004ZZNR, Misumi, Tokio, Japan) to mount the rotary shaft (12), and the back-clamp (9) features two bore holes to mount the FORJ-Slip ring and the rotary motor (Fig. 2.13-c). For the first prototype of the pullback module, components were 3D printed (Fig. 2.13-d) which allowed to evaluate general functionality of the system with an initial characterization. As a next step, the design of the pullback module was slightly adapted and components were precisely manufactured out of aluminum (Fig. 2.13-e) to significantly increase the stability and enhance the alignment of the system for improved NIRF-IVUS imaging results, especially at higher imaging speeds.
The rest of the hardware components are similar to the 3.7F system. The same US pulser-receiver (Model 5073PR, Panametrics, Waltham, USA) and 750 nm fiber-coupled laser (B&W Tek, Newark, DE, USA) was used in combination with a new PMT (Model H7422-50, Hamamatsu, Japan) which also incorporates a cooling fan. As for the 3.7F system, the US pulser-receiver and laser/PMT was used to excite and detect IVUS and NIRF signals, respectively. For the 3.2F system, the same optics were used as for the 3.7F besides the fibers and the corresponding ports. The fiber size was reduced from 200/220 μm to 50/125 μm (FG050LGA, 0.22 NA, Thorlabs). The first fiber-port comprised a lens with an increased numerical aperture (NA: 0.5), a clear aperture and a focus length of 2 mm (PAF2P-2B, Thorlabs) while the second fiber-port contains a lens with a smaller NA (0.22), a clear aperture of 1.8 mm and a focus length of 4 mm (PAF2P-A4B, Thorlabs). All system components were mounted onto a cart (Arthrex, Naples,

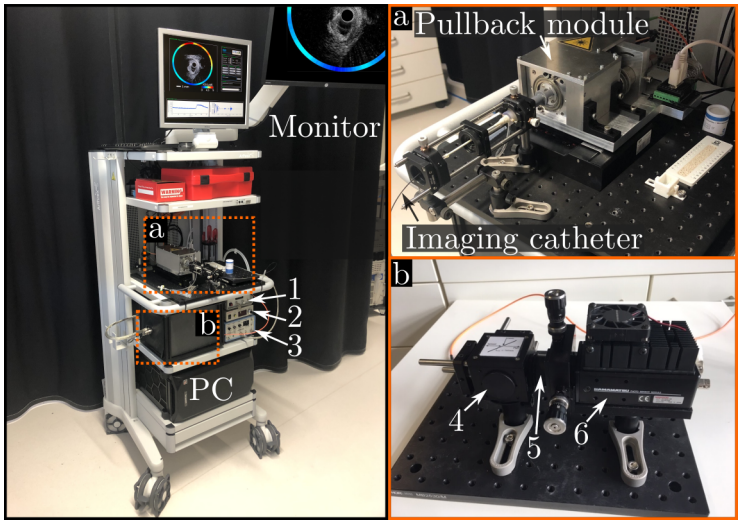

Figure 2.14: Mobilized 3.2F NIRF-IVUS imaging system; 1: Laser, 2: PMT voltage supply, 3: US pulser-reciever. **a** - Pullback module with imaging catheter; **b** - NIRF module; 4: Optics free-space containing fiber-ports and the dichroic mirror, 5: Long-pass filters, 6: PMT.

Florida, USA; Fig. 2.14) including the helical pullback module with imaging the catheter (Fig. 2.14-a) and the NIRF module (Fig. 2.14-b) to mobilize the system and guarantee electrical and laser safety for operation in a clinical environment. A DAQ card (CSE50216, GaGe, Lockport, Illinois, USA) was implemented into the PC which comprises two input channels allowing to sample the analog signals with a sample rate of 200 MS/s and convert them to a digital output with a resolution of 16-Bit for further post-processing and NIRF-IVUS image display.

2.3.2.2 Software - 3.2F

Initially, a Labview software was developed which was similar to the 3.7F system (see section 2.2.2.2). To speed up NIRF-IVUS data visualization towards real-time image display, a software was developed in C++ using the QT framework to decrease processing time by taking advantage of the data streaming capability of the DAQ card.

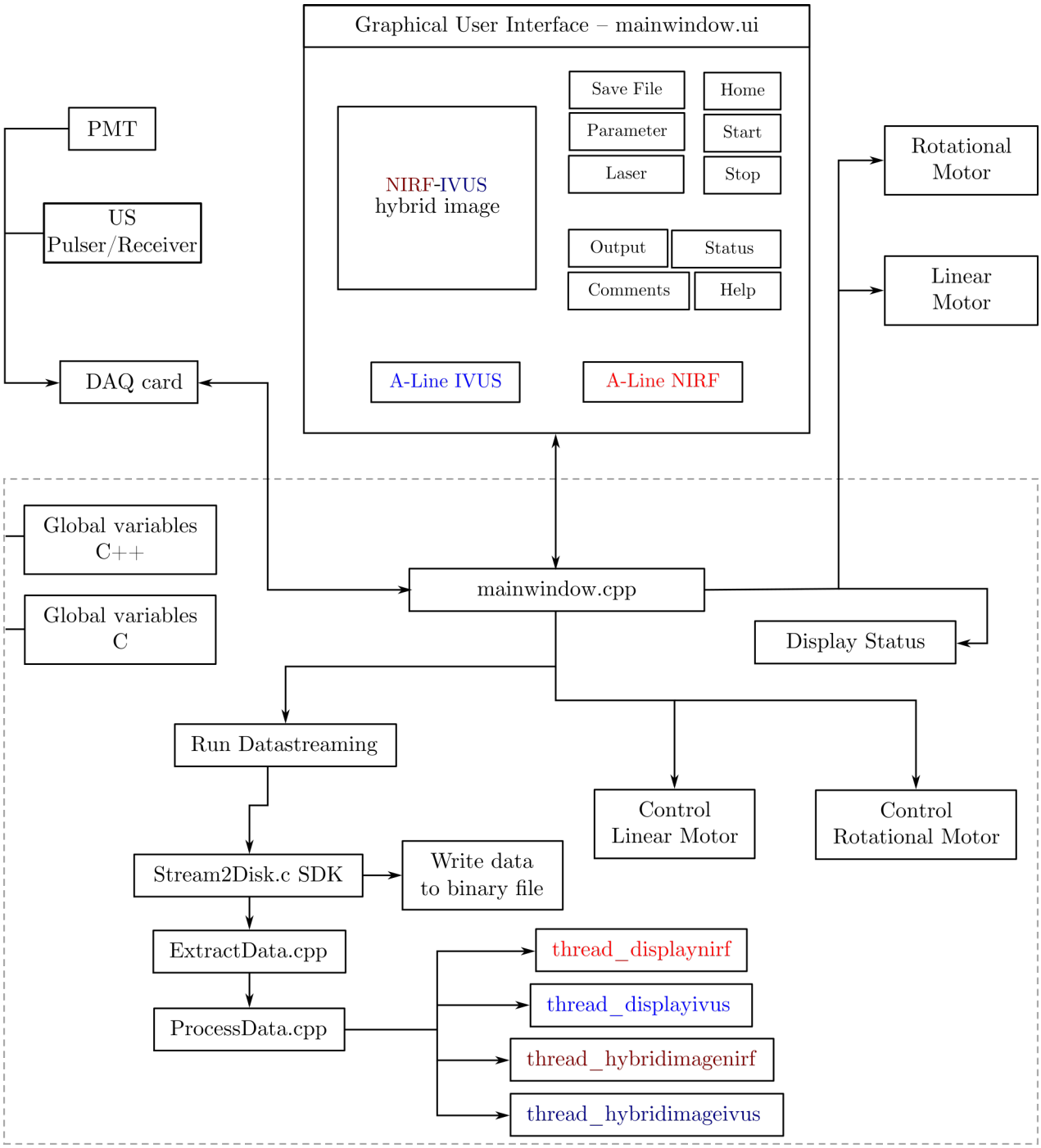

Figure 2.15: Block diagram of the C++ software running the 3.2F NIRF-IVUS imaging system.

Figure 2.15 provides an overview of the structure of the developed C++ software indicating how user inputs in the GUI allow to define the imaging pullback via the control of the hardware

and DAQ. Moreover, it is outlined how the data streaming process writes the NIRF-IVUS data directly into binary files while simultaneously displays raw A-line and reconstructed hybrid images. Similar like the previous Labview GUI for the 3.7F system (Fig. 2.8), the C++ GUI allows definition of parameters for the imaging pullback, works as an interface for controlling the pullback including a home function for moving the catheter to a pre-defined starting position and enables real-time data visualization not only as raw A-lines but also, for the first time, as fully reconstructed hybrid NIRF-IVUS imaging frames (Fig. 2.16). Throughout the DAQ presented in this thesis, sampling rate and record length was kept constant at 200 MS/s and 1120 samples for both channels.

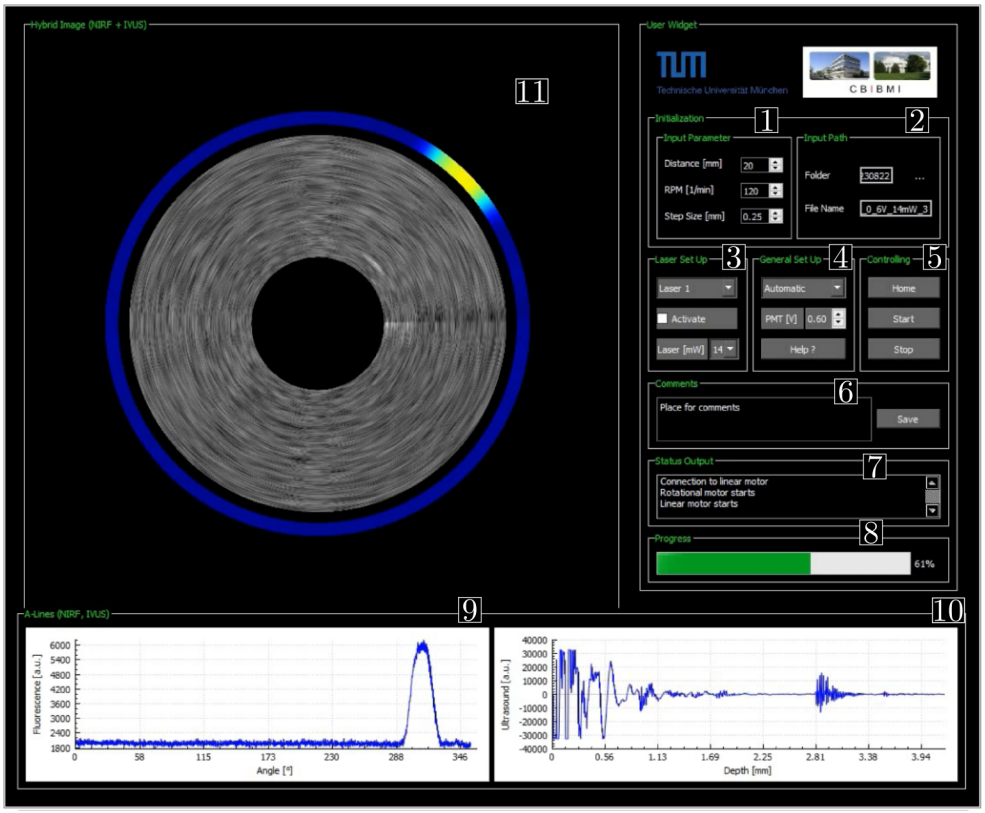

Figure 2.16: Software GUI for the 3.2F NIRF-IVUS imaging system; 1: Pullback input parameters; 2: Folder path and file name; 3: Configuration of Laser control; 4: Configuration of PMT; 5: Pullback control; 6: Input section for comments; 7: Software status output; 8: Pullback progress bar; 9: Display raw A-line NIRF; 10: Display raw A-line IVUS; 11: Display reconstructed hybrid NIRF-IVUS image.

2.4 Post-Processing for Hybrid NIRF-IVUS Images

This sections describes the general steps for NIRF-IVUS data post-processing in Matlab to reconstruct hybrid images. The processing for data visualisation in the C++ software is almost identical, however some steps need to be replaced to increase processing speed for real-time display and because certain Matlab functions are not available in the QT environment. The post-processing can be divided into the following steps:

1) Read in NIRF and IVUS data from binary file into separate arrays containing the total number of acquired samples for each channel (Fig. 2.17-a).

2) Re-organize the data from a consecutive array into a matrix by concatenating the records or A-lines in the columns. Thus, the lines of the resulting matrix correspond to the record depth (Fig. 2.17-b).

3) Since standard intravascular NIRF signals lack depth information and only provide angular resolution, the NIRF A-lines are averaged in depth to one value creating an array for which each entry encodes a NIRF signal at a certain angular location (Fig. 2.17-c). Next, the data in the NIRF array and IVUS matrix are averaged in angular direction (columns) and are re-organized again. The averaged samples of the NIRF array, corresponding to a full catheter revolution or one frame, are concatenated in the directions of the rows resulting in a matrix which features the samples per frame in the columns and the individual frames in the rows. The averaged samples of the IVUS matrix corresponding to a full catheter revolution are also concatenated in row direction, however, in contrast to the NIRF data, the rows hold the samples describing the depth of each IVUS record or A-line. Therefore, one of this matrix can be computed per frame which are stacked up to hold the samples of the entire data set. While the NIRF data is ready for display with a colormap (e.g "jet") after normalization is completed (Exemplary NIRF map of an ICG filled capillary shown), the IVUS data requires further post-processing.

4) Each IVUS A-line is cut at a depth of around 250 samples to remove the initial IVUS excitation pulse and reflections from the catheter sheath (Fig. 2.17-d).

5) Next, a band-pass in the form of a 4th order Butterworth filter is applied to remove low and high frequency noise from the IVUS data (Band-pass: 24-99 MHz). This filter significantly improves IVUS image quality which can be seen in the two exemplary cross-sectional images (Cartesian coordinates) showing the circular signal of a tube made out of polyethylene (Fig. 2.17-e). Both images are reconstructed from the same data, however the band-pass filter was applied only for one of them during post-processing.

6) The envelopes of the filtered IVUS A-lines are extracted using the Hilbert transformation and each A-line is normalized to its maximum value (Fig. 2.17-f).

7) At this stage, there is the option to change to a logarithmic scaling to compress the dynamic range of the IVUS signals. This process enhances the contrast of smaller IVUS signals corresponding to e.g. structures located behind a previous reflector and, thus improves IVUS visualization especially in depth.

8) Finally, NIRF-IVUS data visualization is possible. Originally, NIRF-IVUS data is defined in polar coordinates, meaning that the axes of a re-constructed image or frame are described as angle over depth. As previously mentioned, the NIRF data is one dimensional containing only angular information and can be added on top and/or below of the two dimensional IVUS data to create a hybrid NIRF-IVUS image (Fig. 2.17-g). The polar image can be transferred into Cartesian coordinates to create a cross-sectional image which is typically shown for intravascular imaging data. IVUS images are traditionally displayed with a gray scale colormap.

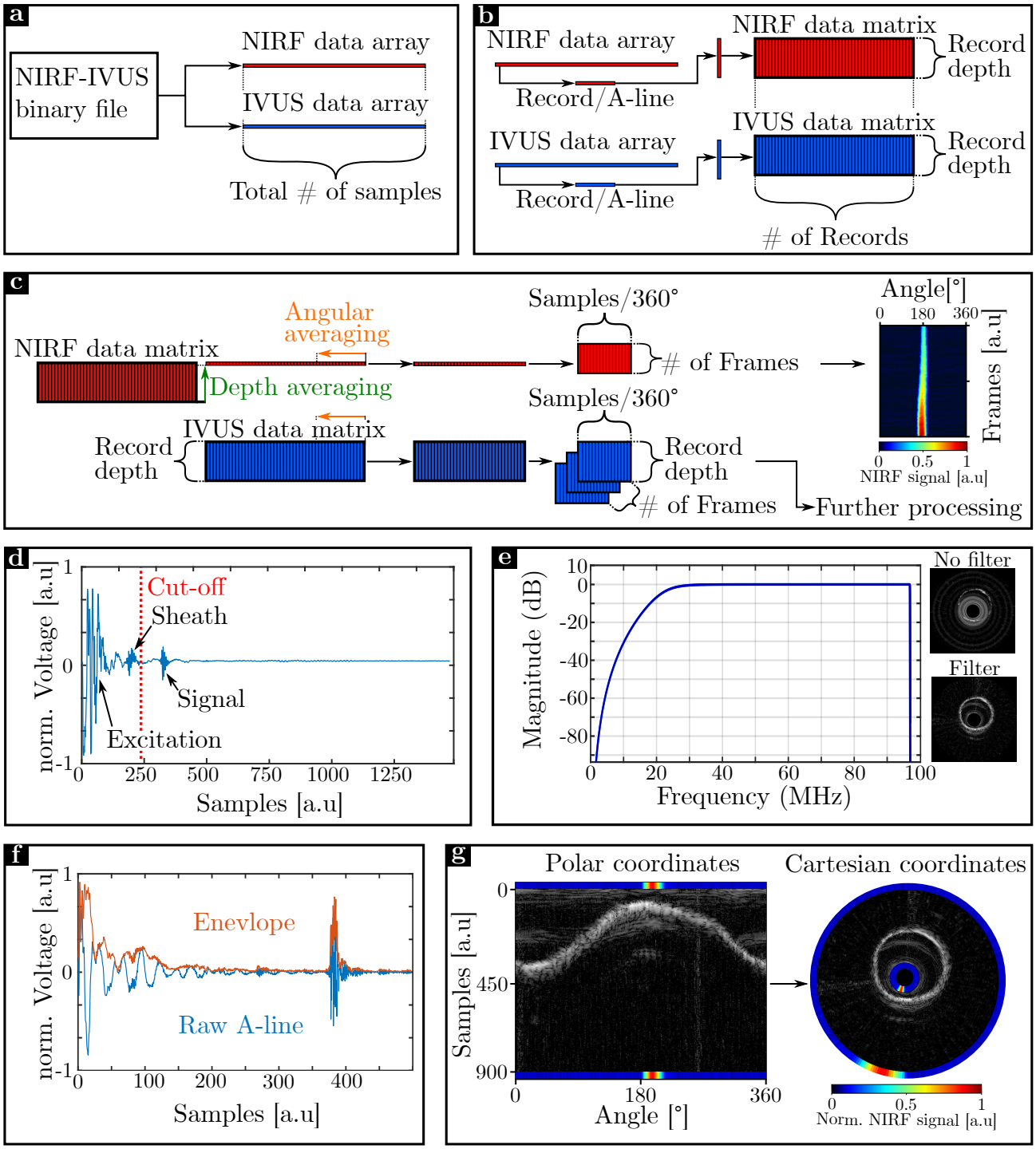

Figure 2.17: Overview of post-processing steps for NIRF-IVUS data; **a** - Read in NIRF-IVUS data from binary files; **b** - Re-organization of data from consecutive arrays into matrices; **c** - Data averaging and second re-organization; **d** - IVUS-A-line cropping; **e** - Application of band pass frequency filter; **f** - Extraction of IVUS envelope from raw A-line; **g** - Hybrid NIRF-IVUS image visualization in polar and cartesian coordinates.

2.5 Conclusion

Both systems contain fully integrated hardware components with corresponding software control that allow to acquire NIRF-IVUS imaging pullbacks while offering user input and control

via a GUI. The corresponding imaging catheters include a sheath with a flush port to fulfill requirements for intravascular applications in vivo. Furthermore, the total dimensions of the catheters (including the sheath) represent a significant size reduction of 15% (3.7F catheter) and 24% (3.2F catheter) compared to the smallest previously reported system (4.2F or 1.4mm, [87]). This miniaturization represent a critical step forward for the clinical translation of the technology and marks the successful completion of the first objective of this thesis.

Chapter 3

Technical Characterization of NIRF-IVUS Imaging Systems

3.1 Introduction

This chapter describes the technical characterization of the two NIRF-IVUS imaging systems which is based on bench-top measurements assessing important specifications for NIRF-IVUS imaging. These measurements included the optical characterization of the NIRF excitation beam, the quantification of catheter's throughput efficiency of NIR light, the assessment of the co-registration between the NIRF and IVUS modality, IVUS and NIRF sensitivity and NIRF-IVUS lateral resolution. Furthermore, the 3.2F system was also characterized for high-speed imaging which is described in a separate sub-section.

3.2 Optical Characterization

The NIRF excitation beam was characterized in an experimental setup including a beam profiler (BC106N-VIS/M, Thorlabs) and a 3D printed alignment holder for the catheters to enable reproducible measurements (Fig. 3.1-a). Laser light at 750 nm was coupled into the catheter to measure the reflected output beam in a perpendicular plane to the rotation axis of the catheter. First, the beam profile was characterized trough air at 15 mm distance from the different NIRF sensors without inserting the catheters into a sheath. Full width at half maximum (FWHM) was quantified and compared between the different NIRF optics. The ball lens optic of the 3.2F catheter featured a NA of 0.13 resulting in a slightly focused beam with a FWHM of 1.8 mm (Fig. 3.1-b). In comparison, the prism optics created a more divergent output beam with a NA of 0.23 and a FWHM of 2.7 mm (Fig. 3.1-c). The prism implemented into the 3.7F imaging catheter featured a NA of 0.24, similar like the smaller version of the 3.2F catheter, however FWHM was larger with 3.7 mm (Fig. 3.1-d) due to the increased fiber core size (200 μm compared to 50 μm). To investigate the influence of the catheter sheath on the NIRF excitation beam, two different sheaths for the 3.2F catheters were tested (Fig. 3.1-e). The first one was a commercial IVUS sheath (Opticross 3.0 Fr catheter, Boston Scientific Corporation, Marlborough, Massachusetts) designed for acoustic transparency. The second was previously described (see section 2.3.1) and custom-made out of LDPE. Both sheaths were flushed with saline during the measurements. First a reference measurement of the ball lens catheter was taken without a sheath at 25 mm distance (Fig. 3.1-f). NIR light transmission through the commercial IVUS sheath (Fig. 3.1-g) resulted in an increase in average FWHM of 40% and through the LDPE sheath (Fig. 3.1-h)

in an increase in avearge FWHM of only 3% in comparison to the reference measurements. While a larger excitation beam reduces spatial resolution of NIRF, optical throughput efficiency was also influenced. Specifically, increased NIR light attenuation of 18% was quantified when using the water-flushed IVUS sheath in comparison to 12% when measuring through the LDPE sheath. These results underline the importance of using a NIRF-IVUS catheter sheath featuring high transparency for both, acoustic and optical energy. It must be mentioned that for a more accurate beam characterization, measurements should be taken through water instead of air to minimize beam alterations at the sheath-medium interface. However, this requires a water-sealed detector which should be custom-made in the future. Furthermore, the FWHM of the NIRF beam will be significantly larger in the presence of blood due to increased optical scattering. Thus, the presented measurements can be regarded as an optimal assessment of the NIRF excitation profile.

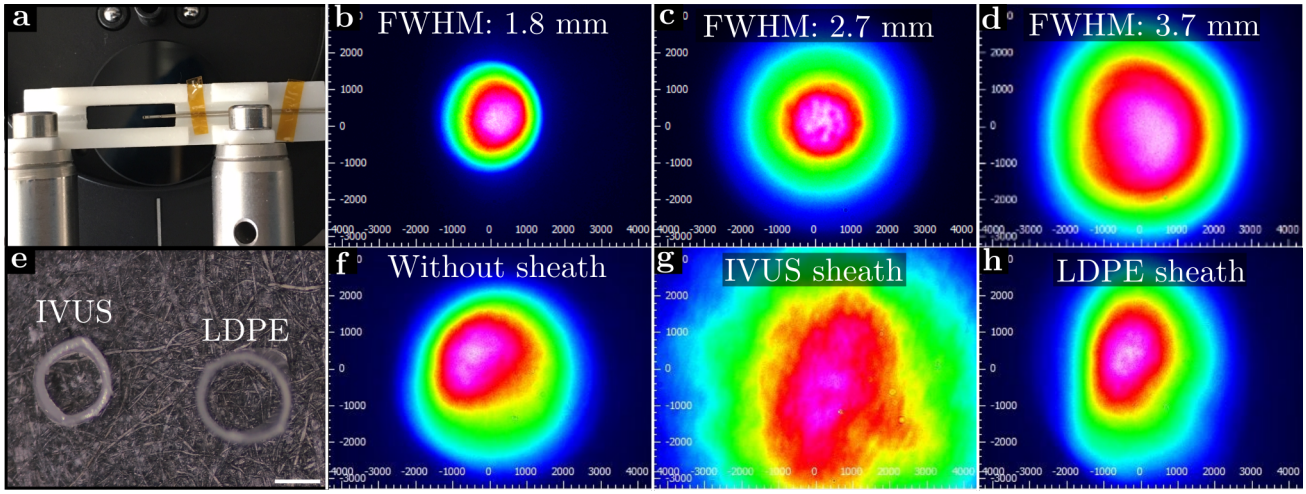

Figure 3.1: Optical characterization of the NIRF excitation beam. a - Overview of the measurement setup characterizing the NIRF excitation beam using a beam profiler; **b** - Beam profile of the 3.2F ball lens catheter without a sheath; **c** - Beam profile of the 3.2F prism catheter without a sheath; **d** - Beam profile of the 3.7F prism catheter without a sheath; Profiles from b-d measured at a 15 mm distance from the NIRF sensor; **e** - Cross-sectional images of a commercial IVUS catheter sheath (Opticross 3.0 Fr catheter, Boston Scientific Corporation, Marlborough, Massachusetts) and the custom-made sheath made out LDPE; **f** - Beam profile of the 3.2F ball lens catheter without a sheath as reference; **g** - Beam profile of the 3.2F ball lens catheter with the commercial IVUS sheath; **h** - Beam profile of the 3.2F ball lens catheter with the costume-made LDPE sheath. Profiles from f-h measured at a 20 mm distance from the NIRF sensor.

The optical throughput efficiency was also quantified throughout different locations in both of the systems. Losses in optical throughput were quantified after the optical free space arrangement (1), the FORJ-Slip ring (2) and the final catheter output (3, Fig. 3.2-a). The 3.2F and 3.7F system featured optical losses of 28% and 23% between the laser input and the output of the optical free-space arrangement (Fig. 3.2-b). Optical losses at the free-space arrangement of the 3.7F system were smaller probably due to simplified light coupling into fibers with a larger core size. In contrast, the 3.2F system included a next generation FORJ-Slip Ring resulting in reduced throughput losses (Between 1-2) compared to the 3.7F system (35% vs. 47%). Finally, throughput efficiency of the catheters was quantified (Fig. 3.2-c). Here, losses mainly depend

on the quality of the fiber polishing at the connector, the glue connection between fiber and the prism or the ball lens and the reflective coating on both the prism and ball lens. The 3.7F catheter featured the smallest losses with 25% compared to 28% for the 3.2F ball lens and 40% for the 3.2F prism catheter. Overall this resulted in a NIR excitation throughput efficiency for the 3.2F system of 34% when using the ball lens catheter and 28% when using the prism catheter and 29% for the 3.7F system with corresponding prism catheter. Collection efficiency of the intravascular NIRF system will be assessed as part of the sensitivity characterization in 3.5.

a

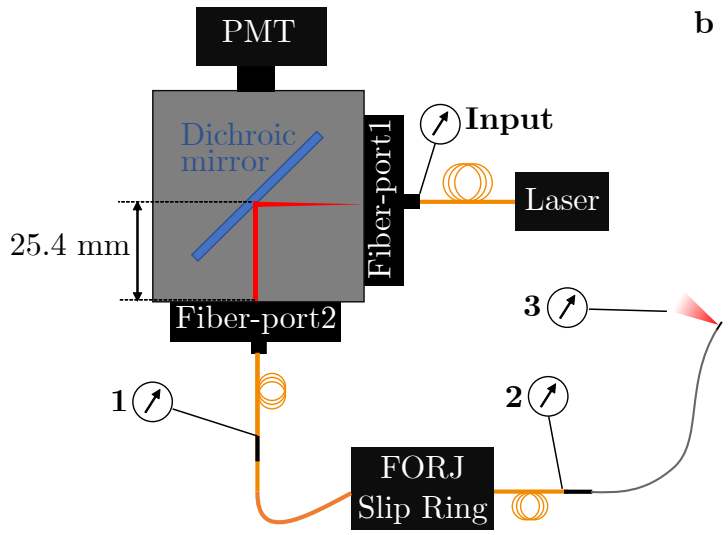

b

	3.2F system	3.7F system
Input-1	28%	23%
1-2	35%	47%

c

2-3	Loss
3.2F Prism-Catheter	40%
3.2F Ball lens-Catheter	28%
3.7F Prism-Catheter	25%

Figure 3.2: Optical throughput efficiency throughout the NIRF-IVUS imaging systems. a - Optical losses were quantified after the optical free-space arrangement (1), the FORJ-Slip ring (2) and the final catheter output (3); **b** - Optical losses of both imaging systems measured between the laser input and location 1 and between location 1 and 2; **c** - Optical losses of the different NIRF-IVUS catheters (2-3).

3.3 Co-registration

Co-registration between the NIRF and IVUS modality is an important requirement to ensure signals from both modalities can be combined for a hybrid inspection. Initially, an angular and axial shift between the IVUS and NIRF pullback data can be expected due to the physical off-set of both sensors. However, this data shift should be constant and, thus, can be quantified and corrected for. The remaining inaccuracies in co-registration will depend on overall imaging quality which is mainly influenced by rotational friction of the catheter and signal-to-noise ratio (SNR). To assess co-registration of the NIRF and IVUS modalities a phantom was imaged at 1 frame per second (fps) containing 4 glass capillaries filled with ICG (Fig. 3.3-a) which could be detected as signals by both modalities.
The measurements of the phantom with the 3.7F and 3.2F prism catheters are presented in figure 3.3-b showing NIRF and IVUS pullback maps. The angular offset between the NIRF and IVUS modality was measured by comparing the angular location of the peak signals per frame for all 4 capillaries and resulted in 1° for the 3.2F ball lens, 9° for the 3.2F prism and 13° for the 3.7F prism catheter. The axial offset between both modalities was measured as 0.75mm for the 3.2F ball lens, 1.25mm for the 3.2F prism and 1.75mm for the 3.7F prism catheter.

After the data was corrected for angular and axial offsets, IVUS signals were plotted on top of the NIRF maps for validation. The remaining angular deviation between both modalities was quantified throughout the pullback (Fig. 3.3-c). The average error was 0.7% for the 3.7F and 0.5% for the 3.2F system confirming that NIRF and IVUS signals can be co-registered with high accuracy in both systems.

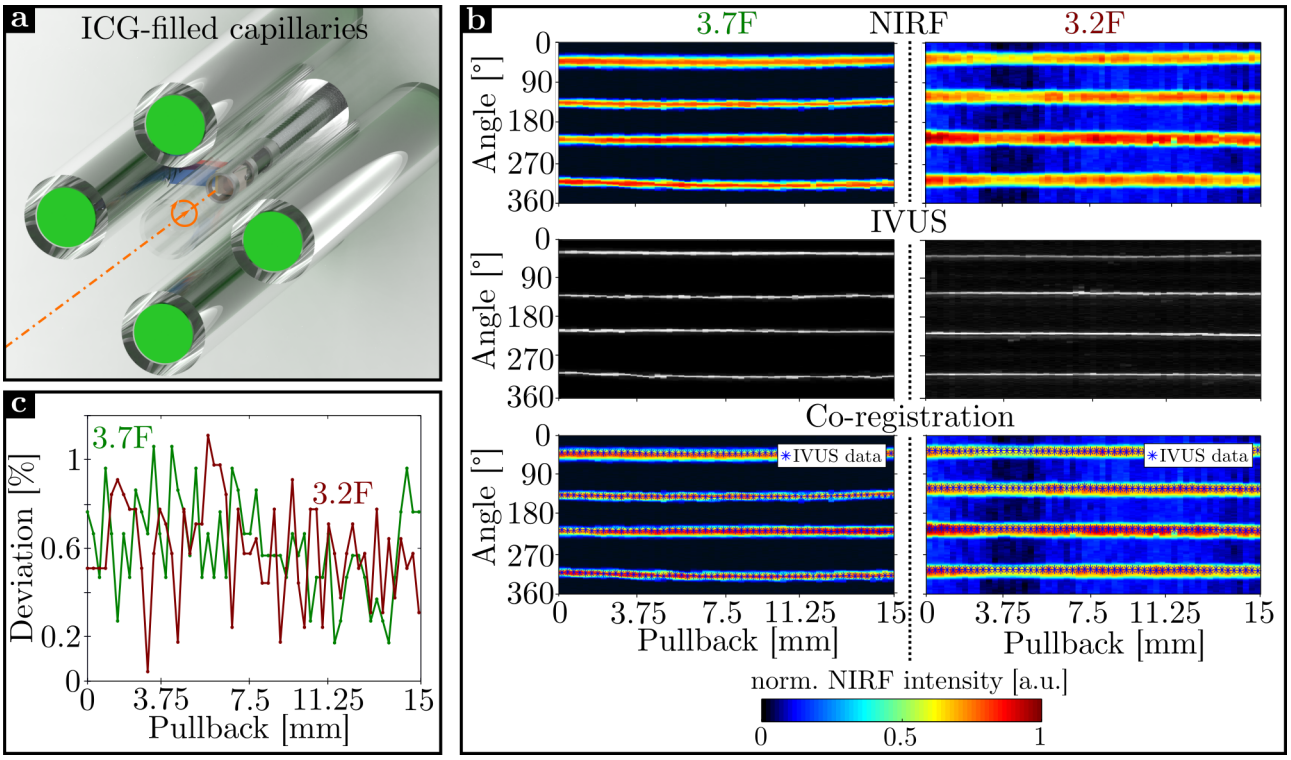

Figure 3.3: Assessment of NIRF-IVUS co-registration of the 3.7F and 3.2F imaging system using prism catheters. **a** - Illustration describing measurements of the co-registration phantom containing four ICG-filled capillaries; **b** - Measurements of the co-registration phantom with the 3.7F and 3.2F system displaying NIRF, IVUS and co-registered pullback maps; **c** - Quantification of remaining angular deviation between NIRF and IVUS signals after offset correction.

Additionally, co-registration was also validated for smaller features in a phantom containing a coronary stent (Orsiro, ∅: 3.5mm, length: 15mm, Biotronik, Bülach, Switzerland). The stent was deployed inside a transparent plastic tube, flushed with water and immersed in a bath of ICG dissolved in saline during the pullback measurements using a 3.2F ball lens catheter (Fig. 3.4-a). IVUS measurements were reconstructed as maximum intensity projections which resulted in a pullback image of the stent revealing structural details as small as 250 μm in size in the form of individual stent struts (Fig. 3.4-b). In the NIRF data the stent was visible as a shadow due to a homogeneous NIRF signal originating from the ICG bath surrounding the tube (Fig. 3.4-c). After the pullback data from both modalities was corrected for the angular and axial offset (Quantified in the capillary experiment as described above) and overlaid, the ability of the catheter for co-registered NIRF-IVUS measurements with high accuracy could be confirmed even when imaging small structures like stent struts.

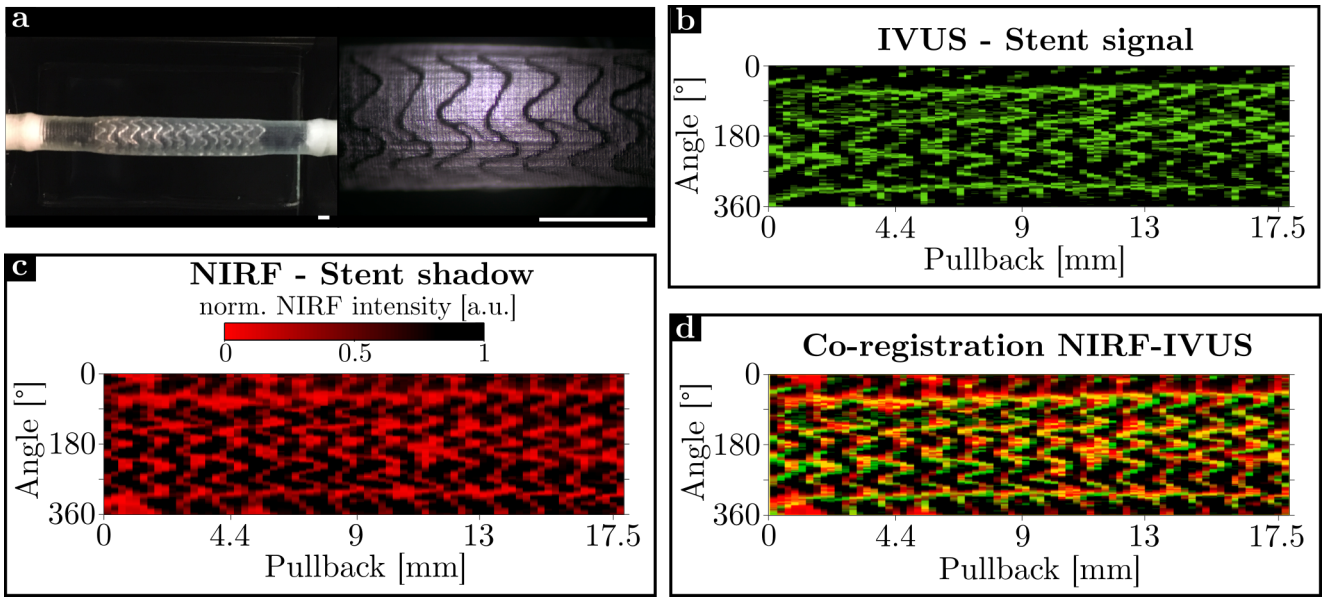

Figure 3.4: Imaging of a stent phantom with a 3.2F ball lens catheter for validation of NIRF-IVUS co-registration. a - Picture of the phantom containing a stent implanted into a transparent plastic tube; **b** - Maximum intensity projection of the IVUS measurements of the stent phantom; **c** - NIRF measurements of the stent phantom; **d** - NIRF and IVUS data overlay for validation of co-registration; Scale bars: 1 mm.

3.4 IVUS Sensitivity

The IVUS sensitivity of the 3.7F and 3.2F prism and of one of the 3.2F ball lens catheters was assessed by performing helical pullback scans at 1 fps (0.25 mm/s pullback speed) inside a 3D printed tube which featured an inner and outer diameter of 3 mm and 4 mm, respectively (Fig. 3.5-a). The tube was submerged in a water bath and the different catheters were inserted via introducers and luer locks. Additionally, the tube and catheter sheath was flushed with water during the experiments to ensure IVUS transmission and remove trapped air bubbles. The IVUS sensitivity of the 3.7F catheter was compared to two 3.2F catheters featuring different PZT angulations (0° and 13°, Fig. 2.2-a, Fig. 2.10-f,h). The energy level for IVUS excitation can be adjusted at the US pulser-receiver and was kept at the lowest level (1) for the series of these measurements.
Figure 3.5-b displays exemplary IVUS frames acquired with the different catheters showing the IVUS signal of the inner tube wall. The RF noise was quantified by calculating the root mean square of the image areas without a tube signal and was averaged per frame. SNR images were then calculated according to eq. 3.1:

$$Image_{SNR} = 20 * log(\frac{Image_{IVUS}}{Noise}). \tag{3.1}$$

Exemplary SNR images are displayed below the corresponding IVUS images. Measurements with the 3.7F catheter detected IVUS signals which were on average 16% higher than with the 3.2F catheter featuring a similar PZT angulation of 0°(Fig. 3.5-c). This can be mainly explained by the larger PZT surface area (20%) implemented in the 3.7F catheter compared to the 3.2F catheter. Although the same PZT was used for all 3.2F catheters, the catheter without PZT angulation detected on average 32% higher IVUS signals than the one with a 13° PZT angulation. During these phantom experiments the rotational axis of the catheter was rather co-axial with

the longitudinal axis of the tube which makes IVUS signal detection more efficient for sensors which are orientated perpendicular to the catheter/tube axis. Thus, a smaller percentage of reflected US waves can be detected by the PZT with the 13° angulation which explains the difference in signal detection between both 3.2F catheters. However, perpendicular orientation of the PZT resulted in more US back-reflections at the sheath wall which is visible in IVUS measurements with the 3.7F and 3.2F catheter with 0° PZT angulation. These back-reflections at the sheath resulted in overall higher imaging noise, especially close to the catheter. Thus, there is a trade-off between the detection efficiency and noise reduction which resulted in an average SNR of 44.2 dB for the 3.7F catheter and 38.9 and 43.9 for the 3.2F catheters featuring 0° and 13° PZT angulation, respectively (Fig. 3.5-d).

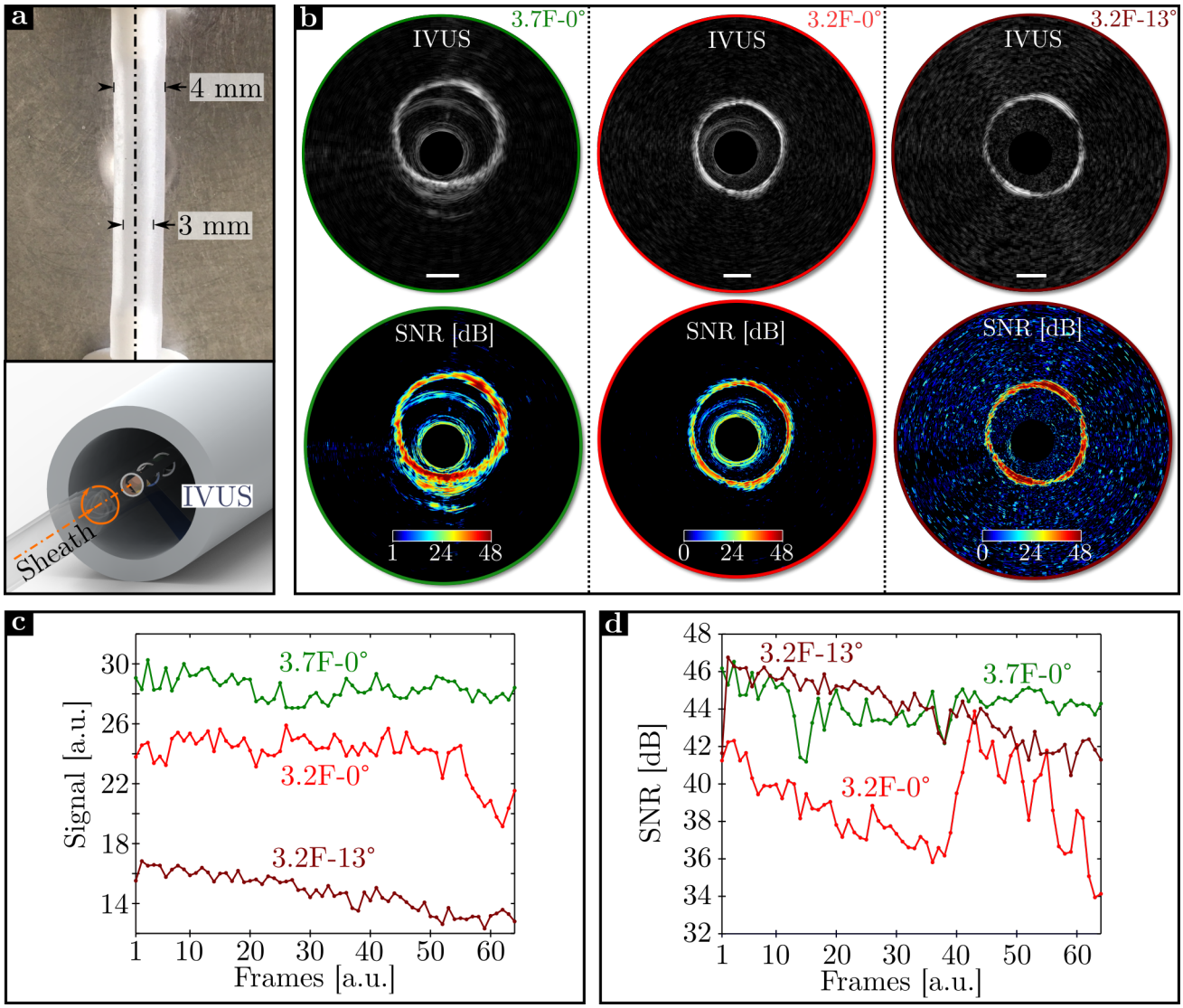

Figure 3.5: Imaging of a tube phantom with a 3.7F and 3.2F catheter with different PZT angulation for validation of IVUS sensitivity. **a** - Picture and illustration of the tube phantom measurements; **b** - Exemplary IVUS and corresponding SNR images recorded with different NIRF-IVUS catheters; **c** - Detected signal of the tube wall in the IVUS images for the acquired frames; **d** - Calculated SNR of the IVUS images for the acquired frames; Scale bars: 1 mm.

3.5 NIRF Sensitivity

The NIRF sensitivity of the 3.7F and 3.2F prism and one of the 3.2F ball lens catheters was assessed in water by performing helical pullback scans at 1 fps inside a phantom which contained an ICG-filled glass capillary (Fig. 3.6-a).

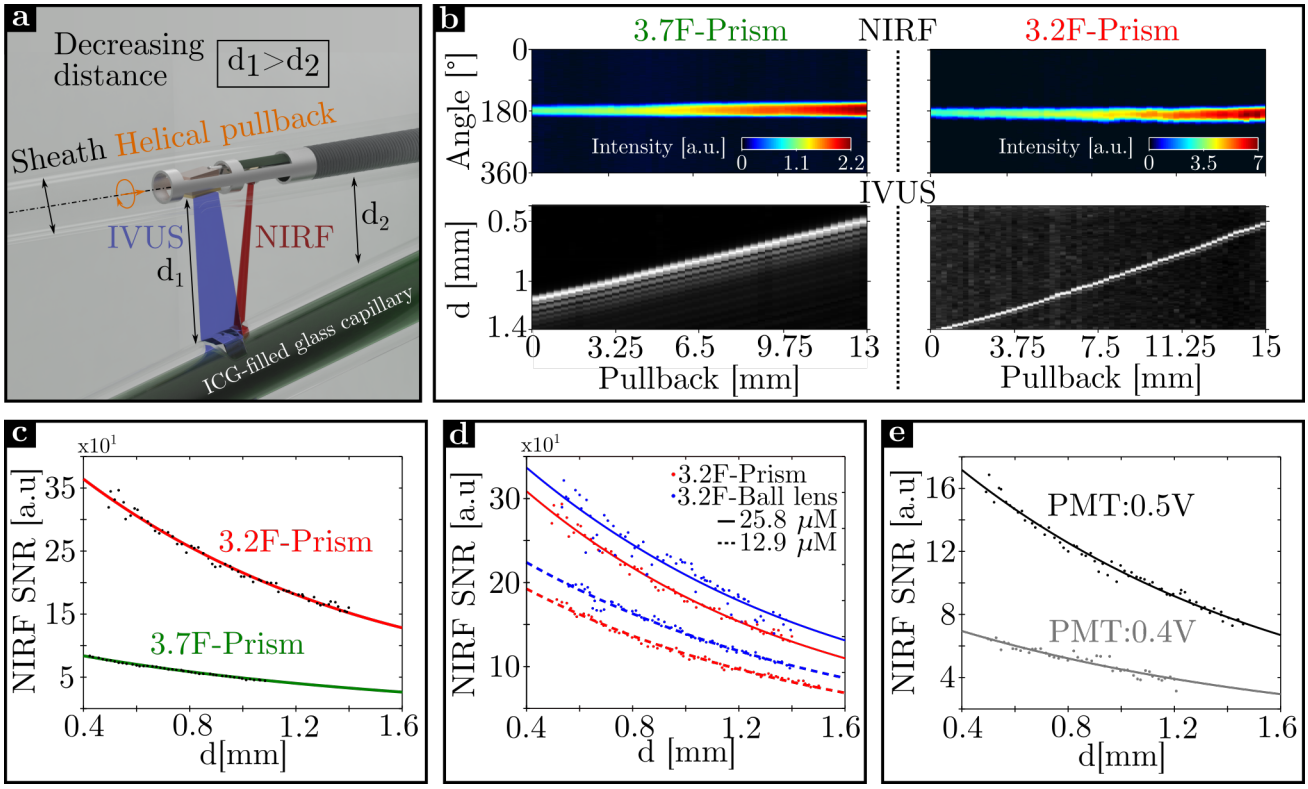

Figure 3.6: Assessment of NIRF sensitivity in water at variable distances with a phantom containing an ICG-filled capillary. **a** - Illustration of the phantom measurements of an ICG-filled capillary at variable distances (d); **b** - NIRF and IVUS maps of the phantom measurements acquired with the 3.7F and 3.2F prism catheter; **c** - Comparison of NIRF SNR between the 3.7F and 3.2F prism catheter; **d** - Comparison of NIRF SNR between the 3.2F prism and ball lens catheter for two different ICG concentrations; **e** - Comparison of NIRF SNR for different PMT voltages when imaging 500nM of ICG with the 3.2F prism catheter.

The capillary was angled within the phantom to create different distances (d) between the catheter sheath and the ICG which was dissolved in DMSO at variable concentrations. The phantom can be described as a 3D printed reservoir which was filled with water during the measurements and featured holes for inserting the catheter and capillary. The ICG-filled capillary was exchanged after every measurement to avoid bleaching of the ICG. The optical output for NIRF excitation was kept at 40 mW for all measurements. Figure 3.6-b displays exemplary NIRF and IVUS maps acquired with the 3.7F and 3.2F prism catheter when imaging 25.8 μM of ICG in the capillary. The detected NIRF intensity of the ICG increased over the pullback position because the distance between the catheter sheath and the capillary decreased which is visible in the IVUS pullback maps. NIRF SNR was calculated by dividing the peak NIRF signal intensities per frame through the averaged background intensity and was plotted over distance quantified by the co-registered IVUS measurements (Fig. 3.6-c). Although the fiber core size integrated in the 3.7F catheter is 4 times larger than in the 3.2F catheter resulting in increased detection efficiency of the 3.7F catheter, the NIRF SNR of the 3.2F system was on average 4.3

times higher than the 3.7F system. This difference in NIRF sensitivity between both imaging systems can be explained by the system's PMT which was significantly more sensitive in the 3.2F system compared to the one built into the 3.7F system.
NIRF sensitivity was also compared between the 3.2F prism and ball lens catheter when imaging two different ICG concentrations, 12.9 μM and 25.8 μM. The NIRF SNR of the ball lens catheter was on average 18% higher than the prism catheter (Fig. 3.6-d). In general, there seems to be no significant difference in NIRF sensitivity between the two otics per se. Differences in NIRF sensitivity can be rather correlated to the optical throughput efficiency of the catheters which was 12% higher in the ball lens catheter compared to the prism catheter. Finally, the influence of PMT voltage on NIRF SNR in the 3.2F system was investigated. For this purpose, 500 nM of ICG was imaged with the 3.2F prism catheter while providing either 0.4V or 0.5V to the PMT (Fig. 3.6-e). As expected, higher voltage supply increases the sensitivity of the PMT and, thus of the entire NIRF measurements resulting in 4.1-times higher NIRF SNR for the 0.5V measurements compared to the 0.4V. In conclusion, increasing the power supply to the PMT will increase the NIRF sensitivity of the system, however this can only be maximized until a certain limit before the built-in protection circuit switches the PMT off to avoid signal current overload. Thus, maximum signal intensity needs to be estimated prior the measurements for adjusting the PMT voltage to enable NIRF detection with maximum sensitivity. The experiments described in this section enabled an initial assessment of intravascular NIRF sensitivity and allowed to compare the different systems and catheters. However, there are limitations of this initial sensitivity characterization:

1. Intravascular NIRF-IVUS imaging considers measurements through blood inside of arteries. Thus, NIRF sensitivity must be quantified for more realistic conditions through blood which will be significantly decreased compared to water due to the increase of light attenuation.

2. The optical output power was set to 40 mW which is too high for in vivo tissue measurements according to the ANSI standard limits describing the maximum permissible exposure (MPE). Considering the catheter-specific optical specifications and referring to the equations and tables provided by the ANSI standard limits, maximum output power is limited to 14 mW.

Theses limitations in regards to the estimation of NIRF sensitivity are addressed by an assessment under more realistic conditions which is presented in section 3.7.3.

3.6 Lateral Resolution

The lateral resolution of the NIRF and IVUS modality was characterized through the assessment of the point spread function (PSF) of the system. For this purpose, two copper wires (∅: 100 μm) were assumed to function as a point source. The wires were crossed and fixed in a phantom at a distance of 1-1.2 mm from the catheter sheath (Fig. 3.7-a) and were imaged with the the 3.2F prism catheter. Additionally, the copper wires were coated with a mixture of epoxy resin and ICG to enable NIRF measurements (Fig. 3.7-b).
The lateral resolution was estimated in two steps. First, the PSF was quantified by measuring the FWHM of the two wire signals and taking the average value. Second, the lateral resolution was defined as the minimum distance between two signals peaks which still exceeds the FWHM measured in the first step. Figure 3.7-c displays the IVUS pullback map showing the signals of both wires and two vertical lines which indicate the frames which were used for quantifying

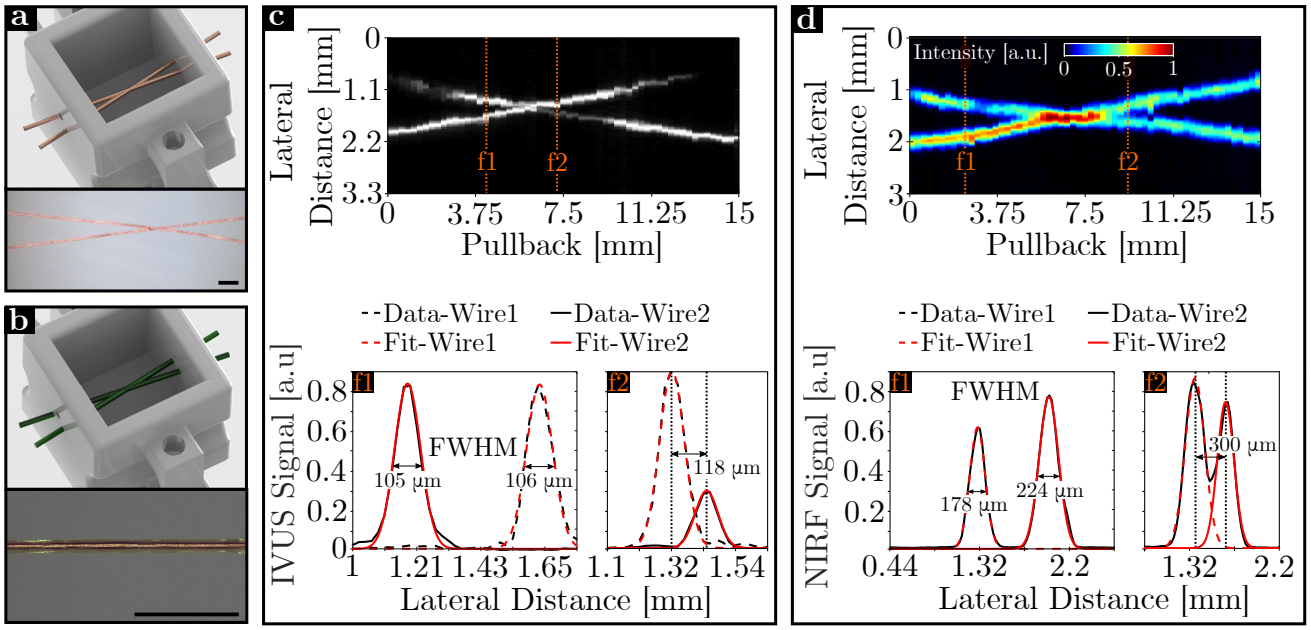

Figure 3.7: Assessment of the lateral resolution of the 3.2F NIRF-IVUS prism catheter in water. a - Illustration of the phantom measurements for the assessment of IVUS lateral resolution featuring crossed copper wires; **b** - Illustration of the phantom measurements for the assessment of NIRF lateral resolution featuring crossed copper wires coated with ICG; **c** - Measurements for assessing IVUS lateral resolution; **d** - Measurements for assessing NIRF lateral resolution; Scale bars: 1 mm.

the FWHM and lateral resolution. The FWHM was measured in the first frame (f1) by fitting the IVUS signals with a Gaussian function which resulted in an average of 105.5 μm. In the second frame (f2) the lateral resolution of the IVUS modality was estimated as 118 μm. The same process was repeated for the NIRF measurement of the wires when coated with ICG (Fig. 3.7-d), which resulted in an average FWHM of 201 μm and a lateral resolution of 300 μm for the NIRF modality. It must be noted that the assessment of the lateral resolution presented in this section depends on the assumption that the wires provided a point signal otherwise values will be underestimated. Furthermore, lateral resolution for NIRF imaging was assessed under ideal conditions in water since measurement through blood will decrease resolution due to diffusive light propagation.

3.7 Efforts Towards High-Speed NIRF-IVUS Imaging

The above sections present the NIRF-IVUS system characterization at slow imaging speeds (1 fps and 0.25 mm/s) and, thus for favourable conditions. However, the goal is to apply the NIRF-IVUS technology in the beating heart of large animal models and, ultimately translate it into the clinics for imaging human coronary arteries. For this application, NIRF-IVUS measurements at low frame rates will result in imaging artefacts due to motions of the heart and breathing which will significantly deteriorate image quality and overall validity of the imaging assessment. Thus, high-speed imaging is desirable but faces certain challenges which can be summarized as:

1. Increased demands for mechanical stability for both the catheter and pullback module.
2. Increased impact of friction between the imaging catheter and sheath on image quality.

3. Decreased number of acquired A-lines deteriorating image SNR.

Therefore, as a first step the 3.2F system was further improved by increasing the mechanical stability of the NIRF-IVUS pullback module and optimizing the co-axial alignment of the imaging catheter within the sheath to reduce friction. In addition, an acceleration and deceleration phase of the rotational motor was implemented in the software. A step-wise acceleration and deceleration of the rotational speed reduced forces on all components of the system and the catheter in comparison to direct torque transfer for reaching the target velocity of e.g 1200 rounds per minute (rpm). Furthermore, DAQ and pullback motion was started with a delay of around 3 seconds to allow the rotational speed of the imaging catheter to reach a constant target velocity.
The following sections present the characterization of important technical specifications of NIRF-IVUS like co-registration and sensitivity at a frame rate of 20 fps and pullback speed of 5 mm/s and compares them to imaging at 2 fps and 0.5 mm/s respectively. Optical output power of the catheter was set to 14 mW for all measurements considering MPE limits which makes results more relevant for potential clinical applications in the future.

3.7.1 Co-registration - High-Speed

The measurements of the capillary phantom for the assessment of NIRF-IVUS co-registration (see section 3.3) were repeated at 2 and 20 fps.

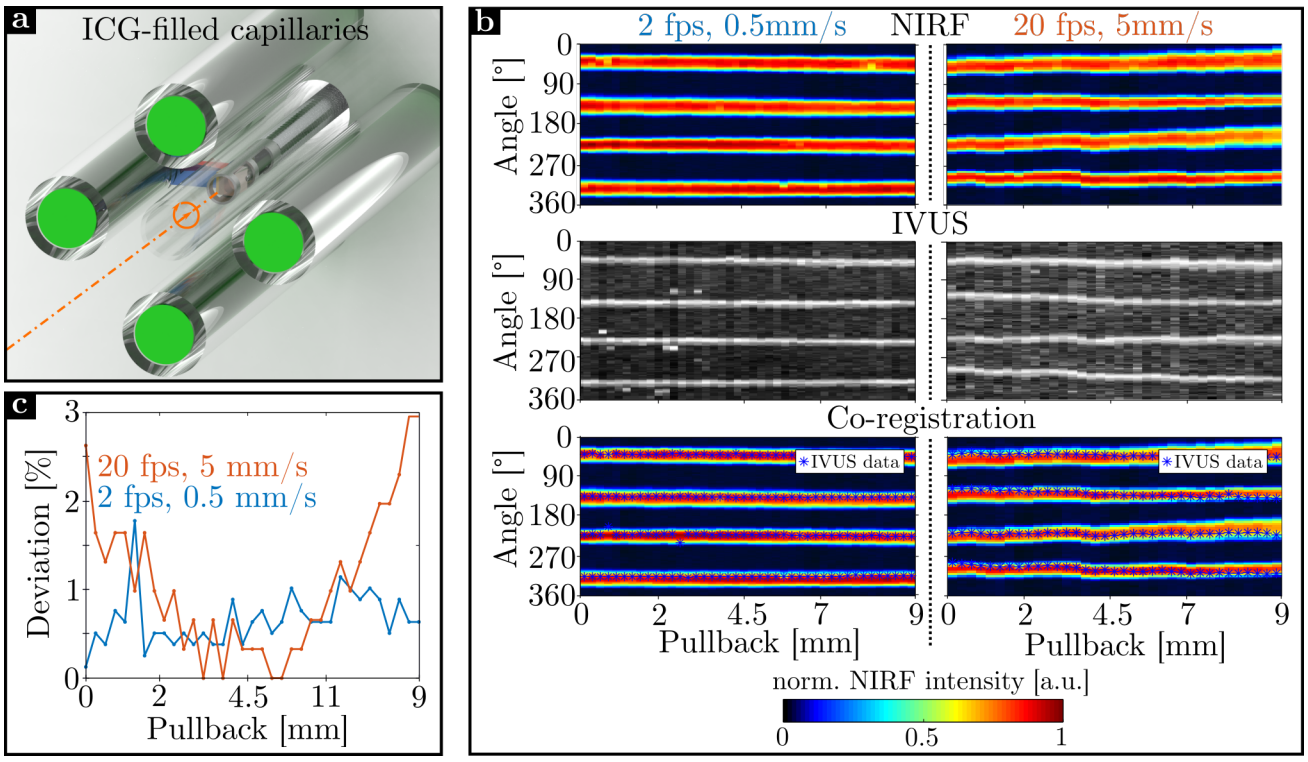

Figure 3.8: Comparison of NIRF-IVUS co-registration of the 3.2F imaging system between low and high imaging speed. **a** - Illustration describing measurements of the co-registration phantom containing four ICG-filled capillaries; **b** - Measurements of the co-registration phantom with the 3.2F system at two and twenty fps displaying NIRF, IVUS and co-registered pullback maps; **c** - Quantification of remaining angular deviation between NIRF and IVUS signals after offset correction.

A 3.2F ball lens catheter was used to image the phantom which contained 4 ICG-filled capillaries (Fig. 3.8-a). Figure 3.8-b displays the NIRF, IVUS and co-registered NIRF-IVUS pullback maps which were reconstructed from the phantom measurements acquired at both imaging speeds. The increased influence of catheter friction and reduction in the total number of recorded A-lines is visible in the form of a larger variability in angular location of the NIRF and IVUS signals in the data acquired at increased imaging speed. This effect was confirmed when calculating the remaining angular deviation which was on average 1.1 % for the measurements at 20 fps and 5 mm/s compared to 0.6 % when imaging at 2 fps and 0.5 mm/s (Fig. 3.8-c). Although co-registration errors were slightly increased for the high-speed measurements, errors are still small enough to ensure accurate NIRF-IVUS imaging.

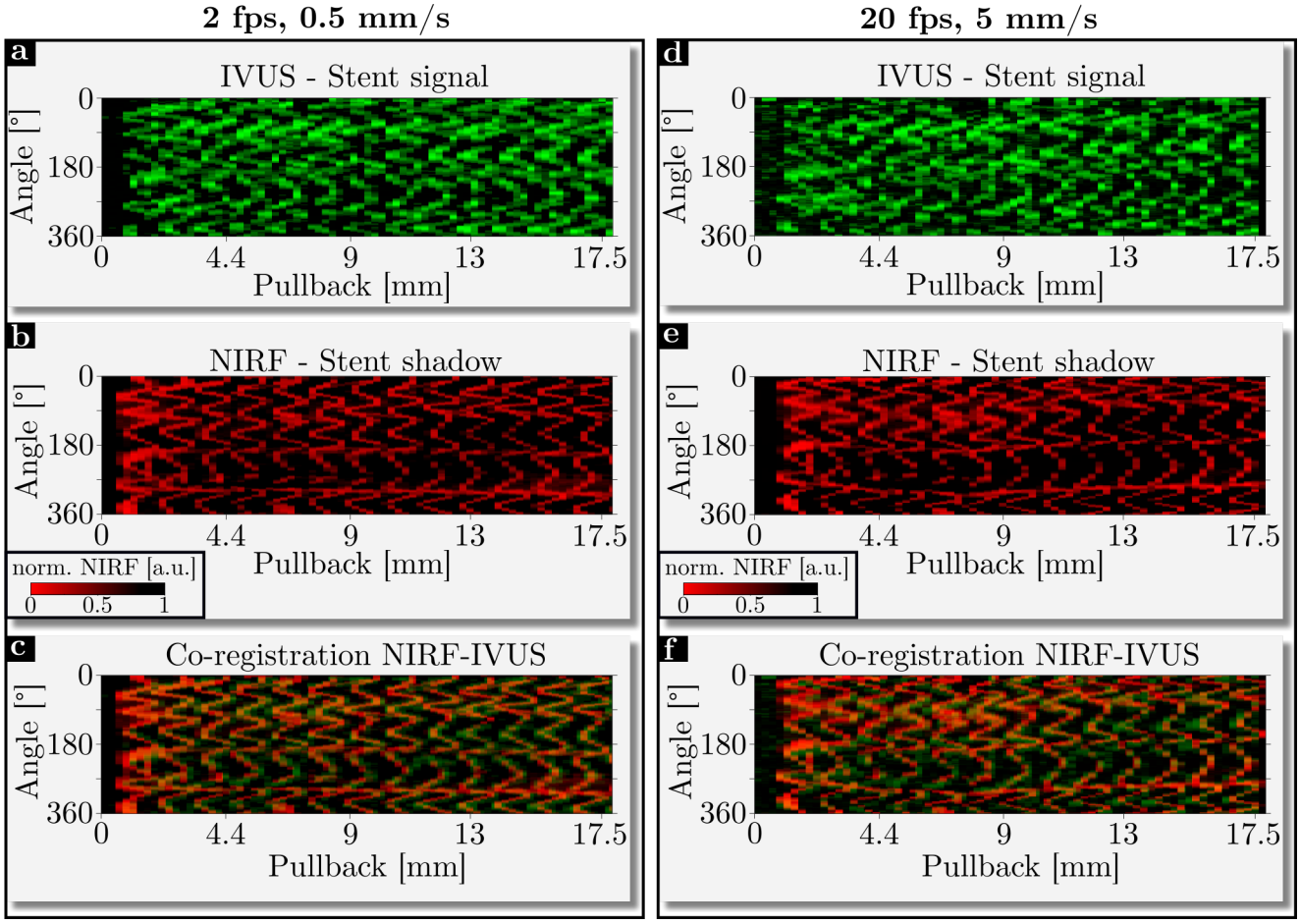

Figure 3.9: Imaging of a stent phantom for to compare NIRF-IVUS co-registration of the 3.2F imaging system between low and high imaging speeds. Imaging data acquired at 2 fps and 0.5 mm/s pullback speed shown as **a** - IVUS measurements of the stent phantom; **b** - NIRF measurements of the stent phantom; **c** - NIRF and IVUS data overlay for validation of co-registration; Imaging data acquired at 20 fps and 5 mm/s pullback speed shown as **d** - IVUS measurements of the stent phantom; **e** - NIRF measurements of the stent phantom; **f** - NIRF and IVUS data overlay for validation of co-registration

In order to further validate NIRF-IVUS co-registration for high-speed imaging, the measurements of the stent phantom (see section 3.3) were also repeated using the 3.2F ball lens catheter featuring the 11° PZT angulation. Figure 3.9-a-c presents IVUS, NIRF and and overlaid NIRF-IVUS maps acquired at 2 fps and 0.5 mm/s pullback speed. In comparison, figure 3.9-d-f displays IVUS, NIRF and and overlaid NIRF-IVUS maps acquired at 20 fps and 5 mm/s pullback speed.

Although IVUS image quality is decreased in the high-speed data mainly due to the smaller number of recorded A-lines deteriorating IVUS SNR, a high-degree of NIRF-IVUS co-registration was still achieved even when imaging small stent structures at 20 fps and 5 mm/s (Fig. 3.9-f).

Finally, NIRF-IVUS co-registration at high imaging speeds was also assessed for more realistic imaging conditions. For this purpose, the same stent type used in all previous experiments (see section 3.3) was implanted into the RCA of an excised pig heart using a standard inflation balloon (Fig. 3.10-a). In order to make the implanted stent visible as a shadow in the NIRF data, ICG-Lipid-Agar patches were laid on top of the stented region of the RCA to create a homogeneous NIRF background signal (Fig. 3.10-b). The patches were created by heating 20% Intralipid (I141-100ML, Sigma-Aldrich) to 90°C to dissolve 3% of Agar (A0950 Agar, Noble, United States Biological). The mixture was then cooled down at room-temperature during continuous mixing and 20 μL of ICG (Dissolved in DMSO) was added when the mixture reached a temperature of around 40°C to create a final concentration of 21.4 μM. The liquid mixture was then poured between two microscope cover slips to solidify and create the final patches. Next, the NIRF-IVUS catheter was inserted into the RCA via an introducer sheath and advanced to the artery region containing the stent with the ICG-Lipid-Agar patches positioned on top of it on the outside of the artery. NIRF-IVUS pullback maps were recorded at 20 fps and 5 mm/s pullback speed while flushing saline through the artery to ensure US coupling. The stent was visible in IVUS pullback maps as directly measured signals (Fig. 3.10-c) and as a shadow in the NIRF data (Fig. 3.10-d) in areas where NIRF background signals were detected (approx. between 90° and 270° angular position) originating from the ICG-Lipid-Agar patches. Overlay of NIRF and IVUS pullback maps revealed high degree of co-registration between both modalities (Fig. 3.10-e). This was further validated when analyzing exemplary hybrid cross-sectional NIRF-IVUS frames (F8, F19 and F30) which showed accurate co-registration between both modalities when comparing angular sectors containing IVUS stent signals and NIRF stent shadows (Fig. 3.10-f).

3.7.2 IVUS Sensitivity - High-Speed

The measurements for the assessment of IVUS sensitivity (Section 3.4) were repeated to characterize the influence of high-speed imaging.
For this purpose the tube phantom was imaged at 2 and 20 fps using the 3.2F ball lens catheter with the 11° PZT angulation (Fig. 3.11-a). For these experiments the energy level for IVUS excitation was increased to 2 to afford optimal imaging quality. Currently, the number of acquired A-lines is limited to the maximum trigger frequency of 10 kHz as provided by the US pulser-receiver. As already mentioned, a decrease in IVUS SNR is therefore expected for higher imaging speeds since the amount of acquired A-lines is reduced which ultimately limits the possibility of data averaging for noise reduction during post-processing. For this reason, a third data set was recorded at 20 fps but with a reduced step size of 0.05 mm instead of 0.25 mm. Five imaging frames were then averaged to simulate the effect of a higher trigger frequency on IVUS SNR which could be implemented in the future. This strategy resulted in 3 different pullback speeds comparing IVUS SNR at 2 fps and 0.5 mm/s pullback speed, 20 fps and 5 mm/s pullback speed and 20 fps and 1 mm/s pullback speed. Figure 3.11-b displays exemplary IVUS and corresponding SNR frames acquired at the different imaging speeds. Figure 3.11-c shows IVUS SNR of the tube averaged per imaging frame.

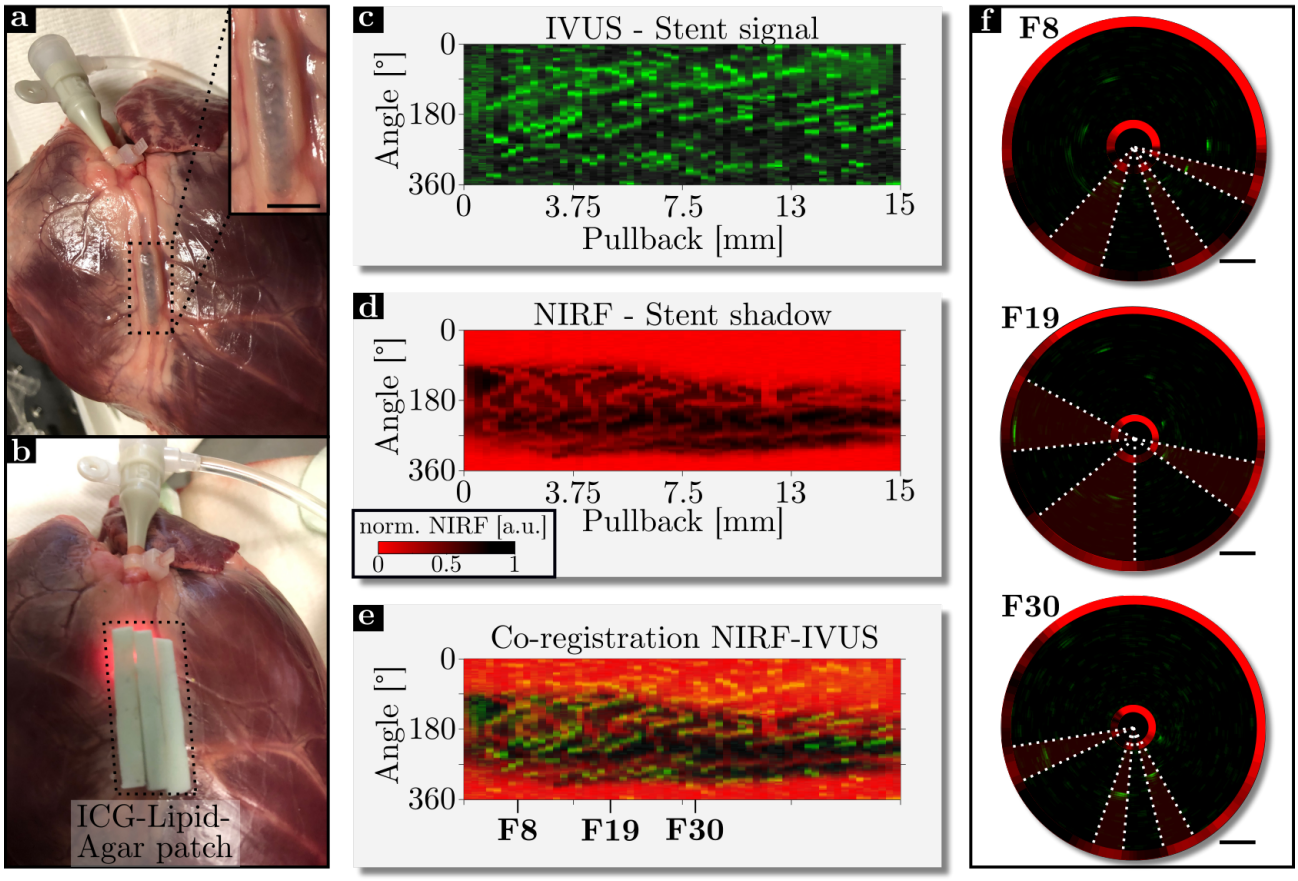

Figure 3.10: Imaging of a stent implanted into a pig heart to assess NIRF-IVUS co-registration of the 3.2F imaging system for realistic conditions a high imaging speed; a - Coronary stent implanted into the RCA of an excised pig heart; Scale bar: 5 mm; **b** - ICG-Lipid-Agar patches laid on top of the RCA to create a shadow of the stent in the NIRF data; **c** - IVUS pullback map indicating stent signals; **d** - NIRF pullback map making the stent visible as a shadow; **e** - Overlay of NIRF and IVUS pullback maps and indication of positions of imaging frames for further validation of co-registration; **f** - Exemplary cross-sectional NIRF-IVUS imaging frames indicating co-registration between IVUS stent signals and shadows in the NIRF data; Scale bars: 0.5 mm.

Overall IVUS SNR was reduced from 51.1 dB to 37.4 dB on average when increasing imaging speed from 2 (0.5 mm/s) to 20 (5 mm/s) fps. However, axial averaging and corresponding reduction in pullback speed to 1 mm/s at 20 fps afforded an average SNR of 45 dB.

3.7.3 NIRF Sensitivity - High-Speed

Finally, the same phantom as described in section 3.5 was used to compare NIRF sensitivity for different ICG concentrations and imaging speeds and also for measurements through water and blood (Fig. 3.12-a).
For this purpose, the volume of the 3D printed reservoir was filled with either water or blood diluted with NaCl (75% blood), the glass capillary was filled with either 1μM or 500nM of ICG and NIRF-IVUS measurements were acquired at 2, 5, 10 and 20 fps. Figure 3.12-b displays exemplary NIRF and IVUS pullback maps when imaging the capillary containing 1μM of ICG through water at 2 fps and 0.5 mm/s pullback speed and 20 fps and 5 mm/s pullback speed.

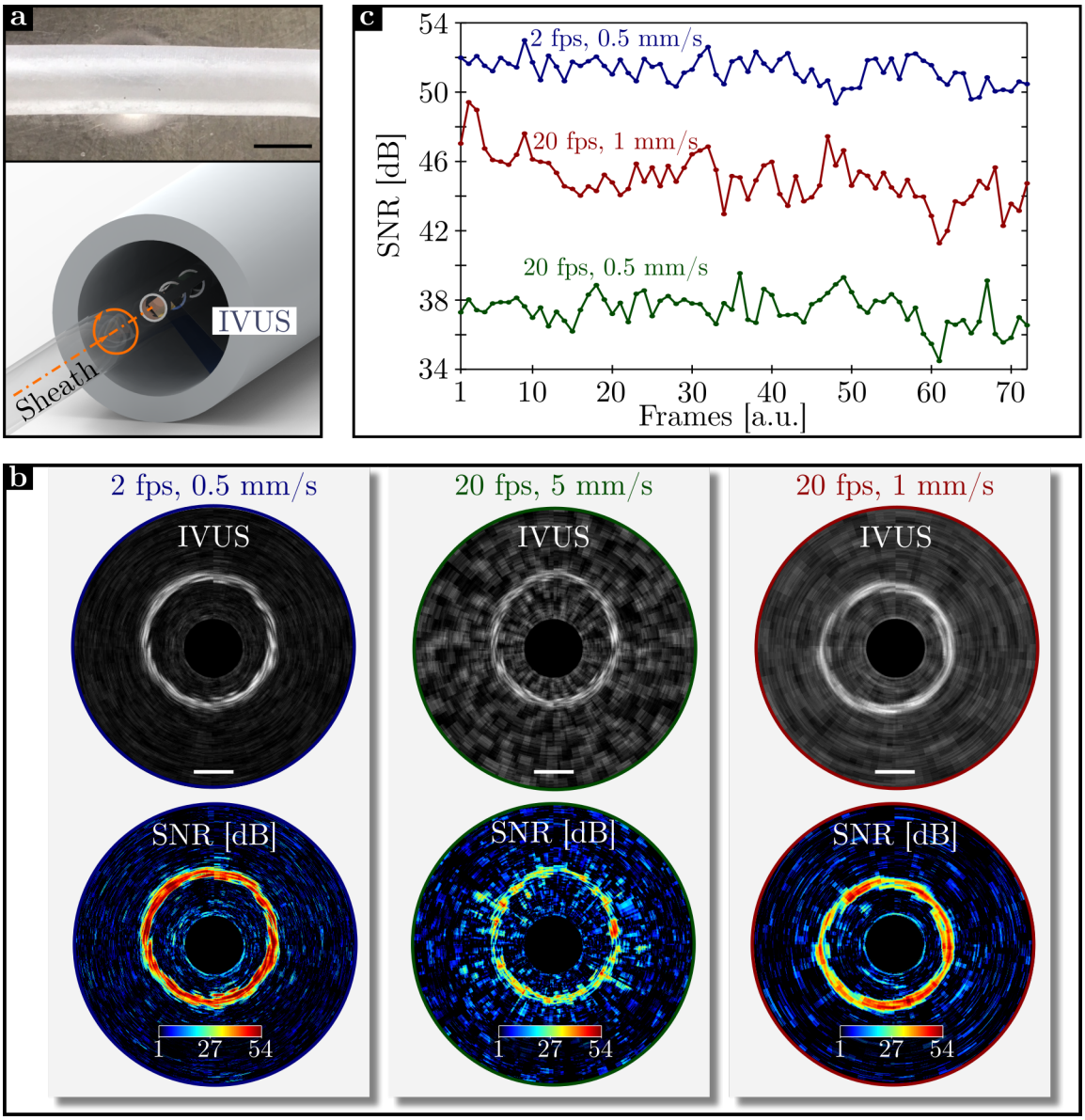

Figure 3.11: Imaging of a tube phantom with a 3.2F catheter at low and high imaging speed for the comparison of IVUS sensitivity. a - Picture and illustration of the tube phantom measurements; **b** - Exemplary IVUS and corresponding SNR images at 2 and 20 fps with various pullback speeds of 0.5, 5 and 1 mm/s ; **c** - Comparison of the SNR of the IVUS acquired at 2 and 20 fps with various pullback speeds of 0.5, 5 and 1 mm/s; Scale bars: 1 mm.

NIRF SNR was significantly higher when imaging 1μM (Fig. 3.12-b) compared to 500 nM (Fig. 3.12-c) of ICG and for measurements through water compared to blood mixture due to increased NIRF attenuation through blood (Fig. 3.12-b-c).
Specifically, NIRF SNR at a distance of 0.5 mm was 53 in water and 3 in the blood mixture for 1μM of ICG and 29 in water and 2.4 in the blood mixture for 500 nM of ICG. In contrast, there was no significant influence of imaging speed on NIRF SNR when comparing the measurements through water and blood and for imaging of different ICG concentrations. Since NIRF data is averaged in depth, the amount of acquired A-lines and corresponding averaging in angular direction has a smaller impact on noise levels compared to the IVUS data which gives reason why there was no correlation between imaging speed and NIRF SNR found.

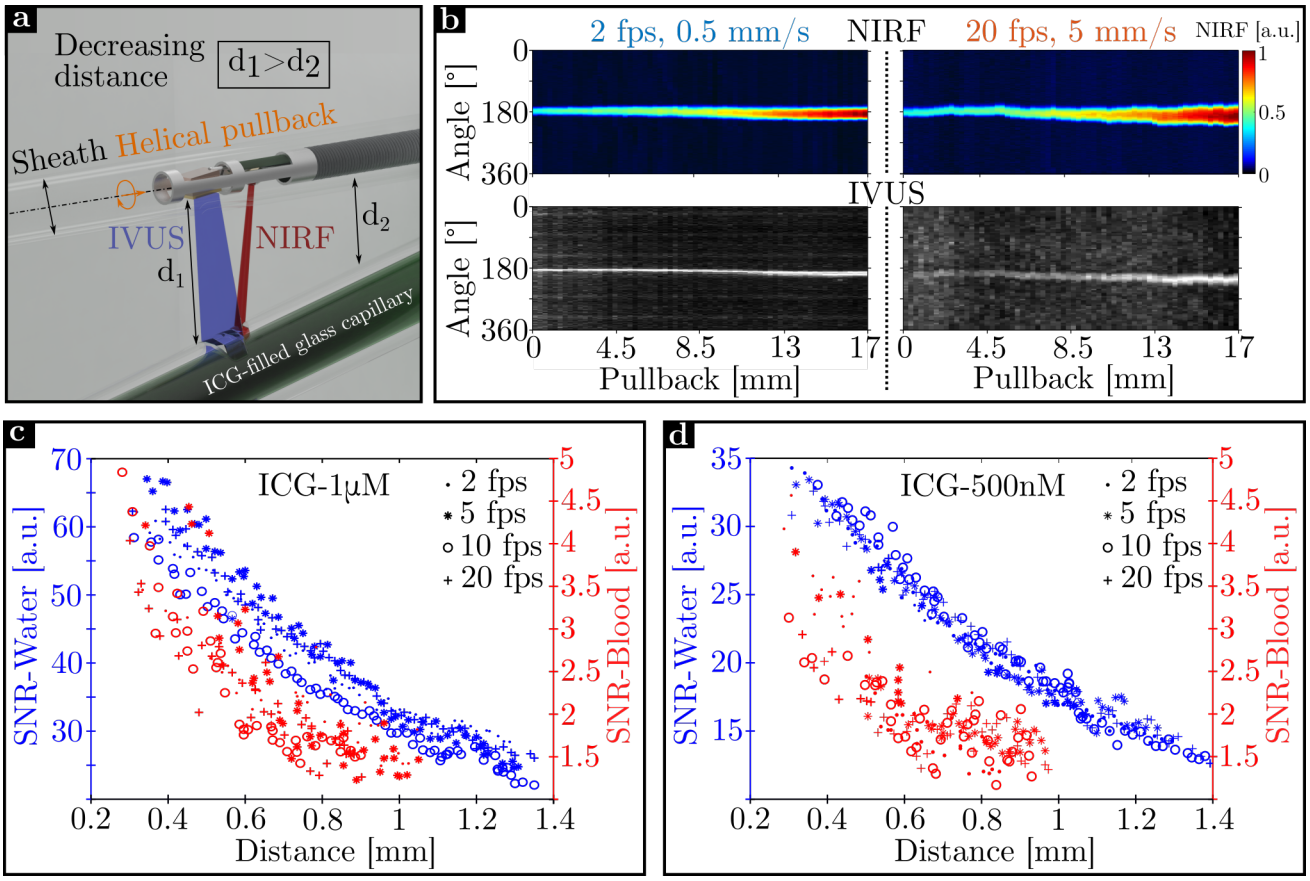

Figure 3.12: Comparison of NIRF sensitivity for different imaging speeds. **a** - Illustration of the phantom measurements of an ICG-filled capillary at variable distances (d); **b** - NIRF and IVUS map of the phantom measurements acquired through water at 2 and 20 fps; **c** - Comparison of NIRF SNR for different imaging speeds when imaging 1μM of ICG trough water and blood-mixture; **d** - Comparison of NIRF SNR for different imaging speeds when imaging 500nM of ICG trough water and blood-mixture.

3.8 Conclusion and Outlook

In conclusion, both imaging systems enable precisely co-registered NIRF and IVUS measurements. Using the 3.7F imaging system, stable measurements with a high IVUS sensitivity are possible due to i) the system's accurate alignment of the imaging catheter within the pullback module resulting in co-axial catheter rotation, ii) increased PZT area and iii) efficient electrical grounding. The miniaturized 3.2F system enables NIRF measurement of small concentrations of ICG with high SNR due to the implementation of a PMT which afforded high sensitivity in the NIR region. As a next step, it was demonstrated that imaging at higher speeds is possible with the 3.2F system without compromising co-registration and NIRF sensitivity. Specifically, imaging a stent in a phantom and implanted in a coronary artery of a pig heart at 20 fps and 5 mm/s pullback speed allowed to maintain co-registration between NIRF and IVUS signals of micrometer structures without sacrificing accuracy (Fig. 3.9 and 3.10). Furthermore, 500 nM of ICG (Realistic concentration range to accumulate in tissue in vivo) can be still detected at a distance of up to 1 mm through blood when imaging at high speed (SNR $\approx$ 1.5) and exciting NIRF with a permissible optical output power of 14 mW. The achievements of these specifications describe a significant improvement over previously reported NIRF-IVUS systems [86, 87, 89, 90]

and provide the required technical foundation for in vivo NIRF-IVUS imaging in a beating heart in the future. In conclusion, the technical characterization presented in this chapter confirm the successful completion of the second objective of this thesis.

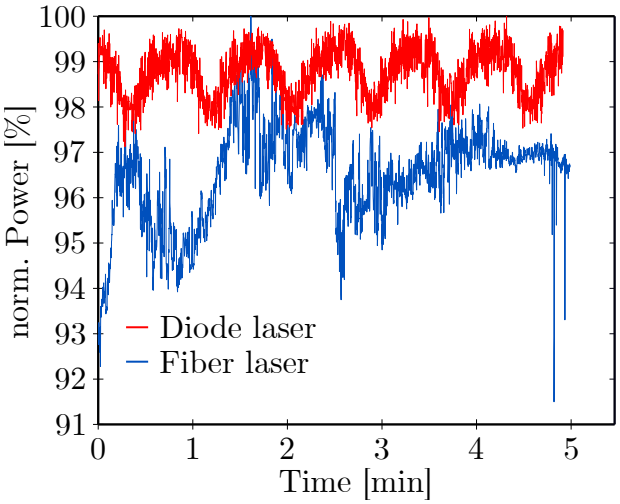

Figure 3.13: Comparison of laser output stability between a standard fiber-coupled laser source and temperature controlled laser diode system; Measured at 50 mW and 750 nm;

Further technical improvements should target the IVUS modality of the 3.2F system. Specifically, the PZT should be angled at around 5° to achieve an compromise between signal detection and noise reduction as demonstrated in figure 3.5. Furthermore, for high-speed imaging a faster trigger should be implemented to increase the number of acquired A-lines which will improve IVUS SNR as shown in figure 3.11. In contrast to the axial averaging described in section 3.7.2, a faster trigger will enable angular averaging which will improve SNR at high frame rates without compromising pullback speed. Moreover, moving the rotational axis of the rotary motor closer to the catheter axis will further improve co-axial catheter rotation within the sheath and, thus, decrease friction and corresponding imaging artefacts especially when operating the system at high frame rates. Finally, a more sophisticated laser source for NIRF excitation should be integrated into the system to enable more stable NIRF measurements. For instance, the integration of a e.g. laser diode system would enable more accurate NIRF measurements as fluctuation in NIRF excitation could be minimized and accounted for. To demonstrate this, a diode laser was set up which consists of a laser diode mount (LDM90, Thorlabs) with a corresponding controller (PRO8000-4, LDC8040, TED8040, Thorlabs) and a laser diode (FLX-750-1500M-100, Frankfurt Laser Company, Friedrichsdorf, Germany) delivering 750 nm light up to 1.5 W which was focused into a fiber. Figure 3.13 compares the laser output stability between the previously used standard fiber-coupled laser source (Described in sections 2.2.2.1 and 2.3.2.1) and the new laser diode system. The fiber-coupled laser system suffered from fluctuations in laser output power which were twice as large compared to the diode laser system (Standard deviation: 1.07% vs 0.53%). The laser diode system was able to deliver more stable laser output due to its implemented temperature and optical output control circuit. Furthermore, the control system provides an interface which can be accessed by the software of the NIRF-IVUS imaging system to record and save the detected laser output as an addition to the binary file containing the imaging data. This data could be used to correct NIRF measurements for recorded fluctuations in excitation power during post-processing.

Chapter 4

Application of Intravascular NIRF-IVUS for Imaging Pre-clinical Animal Models of Atherosclerosis

4.1 Introduction

This chapter presents the application of the 3.2F NIRF-IVUS system for imaging atherosclerosis in human-relevant animal models. The purpose of this pre-clinical study was to comprehensively assess the feasibility of NIRF-IVUS to detect ICG accumulation in tissue areas featuring important pathobiological characteristics of atherosclerosis like endothelial permeability, lipid deposition and inflammation. The experiments aimed to answer questions in regards to ICG location, distribution and accumulation in diseased vs. non-diseased arterial tissue. It was hypothesized that in vivo NIRF-IVUS imaging detects an increased ICG accumulation in atherosclerotic tissue compared to healthy tissue due to the presence of a leaky endoluminal endothelial layer, vasa vasorum in the adventitial layer and increased chronic inflammatory response of the arterial wall. Furthermore, the experiments provided evidence if NIRF-IVUS imaging can be performed in in vivo atherosclerotic animals without relevant safety concerns. All animal experiments presented herein were approved by the District Government of Upper Bavaria (Animal trial reference: ROB$-55.2-2532.Vet_02-19-139$) and conducted in accordance with the Directive 2010/63/EU on the protection of animals used for scientific purposes and TierSchG.

In the framework of this pre-clinical study, atherosclerotic lesions were created in one of the external iliac arteries of New Zealand White Rabbits via vascular injury introduced by balloon denudation (Fig. 4.1-a). The contralateral external iliac artery served as a non-injured, healthy control. Figure 4.1-b shows a picture of the involved arteries in situ after dissection of the abdomen of a chronic rabbit model. The injured artery shows visual signs of increased lipid accumulation in contrast to the healthy control and aorta. The study included four different groups which model different aspects of atherosclerosis. The differences between the animal models will aid in understanding pharmacological interactions of ICG with atherosclerotic and healthy tissue as described above. For all animal experiments, ICG was mixed with distilled water to a concentration of either 5 or 1 mg/kg body weight and was administered by an intravenous injection at a volume of 5 ml. Table A.1 provides an overview of the different stainings which were used to evaluate histopathology of artery tissue in this and the following chapter (see chapter 5). A description and workflow of the individual study groups is provided below:

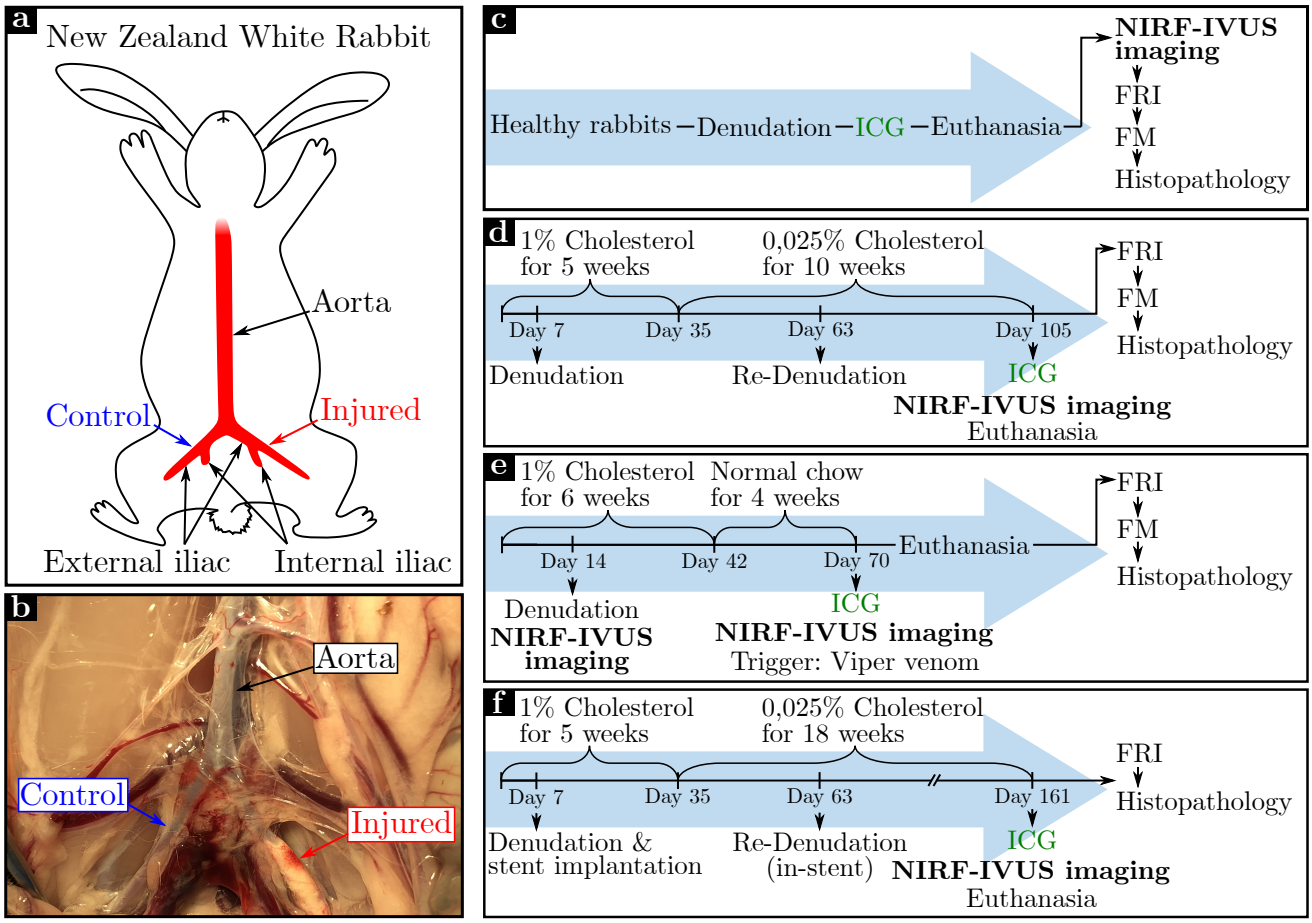

Figure 4.1: Overview of pre-clinical rabbit models of atherosclerosis. **a** - Illustrative description of relevant anatomy of the pre-clinical rabbit models; **b** - Picture of involved arteries of the pre-clinical rabbit models in situ; **c** - Description of the rabbit model of acute endothelial injury; **d** - Description of the rabbit model of chronic atherosclerosis; **e** - Description of the rabbit model of atherosclerosis and acute atherothrombosis; **f** - Description of the rabbit model of neoatherosclerosis; In all panels: FRI = Fluoresence Reflectance Imaging; FM = Fluroescence Microscopy.

1) **Acute endothelial injury:** This group aims to provide a simplified pilot model and improve the understanding of the location, distribution and accumulation of ICG in injured vs. non-injured arterial tissue in a healthy organism. For this purpose, one of the iliac arteries was injured via balloon denudation, ICG was administered at a dose of 5 mg/kg and the animal was euthanized 30 min post ICG injection (Fig. 4.1-c). As a next step, the aorta and iliac arteries were excised to perform ex vivo NIRF-IVUS imaging, and fluorescence reflectance imaging (FRI). Finally, the arteries were divided into segments, embedded in O.C.T compound (Tissue-Tek, Sakura Finetek, Staufen, Germany), snap frozen using dry ice and cut into 7-10 μm sections for fluorescence microscopy (FM) and corresponding histopathology for validation.

2) **Chronic atherosclerosis:** This model has the purpose to understand the precise location, distribution and accumulation of ICG in diseased vs. non-diseased arterial tissue in an atherosclerotic organism. Thus, it combines vascular injury to initiate the atherosclerosis with a high-cholesterol diet for several weeks (Fig. 4.1-d). Specifically, one of the iliac arteries was injured twice, at day 7 and 63, while a ratio of 1% and 0.025% cholesterol

was included in the diet for 5 and 10 weeks, respectively. On day 105, 1 mg/kg ICG was administered and in vivo NIRF-IVUS was performed around 30 min post ICG injection. Next, the animal was euthanized and arteries were excised to perform FRI and prepare the tissue for FM and histopathology as described above.

3) **Atherosclerosis and acute atherothrombosis:** Similar like the chronic atherosclerosis group, this model aims to provide insights into the pharmacological properties of ICG when interacting with diseased vs. non-diseased arterial tissue in an atherosclerotic organism. For this purpose, vascular injury was induced once at day 14 while feeding high-cholesterol diet (1%) for 6 and normal chow for 4 weeks (Fig. 4.1-e). In contrast to the standard chronic atherosclerosis group, this model also included additional in vivo NIRF-IVUS imaging at an early time point (Day 14) after the acute injury. The recorded NRIF signals can be then compared to signals detected during imaging at the end of the study timeline on day 70. Furthermore, this model involved systemic administration of Russell's Viper venom to trigger a thrombus reaction after in vivo NIRF-IVUS imaging is completed. The goal of this procedure is to investigate if NIRF-IVUS can detect ICG deposition in atherosclerotic tissue areas which are prone to thrombus formation. Similar like for the previous models, arteries are excised after euthanisia, imaged with FRI and the tissue is prepared for FM and histopathology.

4) **Neoatherosclerosis:** The previously presented study groups model native atherosclerosis and aim to investigate the feasibility of NIRF-IVUS to detect high-risk plaques. In contrast, the neoatherosclerotic group attempts to model in-stent restenosis which is a mechanism that often leads to clinical complications after initial PCI [91, 92]. Thus, the goal of this model is to investigate if NIRF-IVUS can detect increased ICG accumulation also in areas of neoatherosclerosis. For this purpose, vascular injury was induced and a stent was implanted in the same area on day 7 (Fig. 4.1-e). Balloon denudation was repeated in the stented region on day 63, while a high-cholesterol diet of 1% and 0.025% had been fed for 5 and 18 weeks, respectively. Finally, ICG at a dose of 1 mg/kg was administered on day 161, followed by in vivo NIRF-IVUS imaging around 50-60 min post ICG injection. The arteries were excised after euthanasia and imaged with FRI. FM was not possible in this case because stented tissue needs to be embedded in Methyl Methacrylate (MMA) to be cut with a laser microtome for preparation of histological slides.

The 3.2F prism catheter was used for all pre-clinical experiments and NIRF-IVUS imaging speed was set to 2 fps. PMT sensitivity was adjusted for the individual atherosclerotic model to adapt the dynamic range accordingly but was kept constant between NIRF imaging of injured and control arteries to ensure comparability. NIRF excitation power was limited to 14 mW (Measured as optical output at the catheter) to adhere to MPE limits. A guidewire was inserted into the sheath of the NIRF-IVUS catheter to be able to steer the catheter and advance it into the target region for recording imaging pullbacks of the vessel wall. The following sections present the results of exemplary experiments of the individual study groups.

4.2 Results of a Rabbit Model of Acute Endothelial Injury

Figure 4.2 presents the imaging results and histological validation of a rabbit model of acute endothelial injury. Initially, both iliac arteries were healthy as validated with baseline angiography (Fig. 4.2-a). Dilation of the lumen (Red arrows) can be observed as a consequence of the balloon denudation in the right iliac artery (RIA, Fig. 4.2-b). In contrast, regular blood flow was observed in the the left iliac artery (LIA) which served as a healthy control (Fig. 4.2-b). Ex vivo FRI and intravascular NIRF imaging detected increased fluorescence intensity in the injured artery compared to the control (Fig. 4.2-c). Note that FRI indicated slightly increased FRI signal also in the Aorta which is probably due to the catheterization process resulting in unintended vascular injury and corresponding ICG uptake. FM revealed mild ICG accumulation in the intimal layer of the injured vessel (Fig. 4.2-d), whereas no ICG signals were found in the tissue of the control artery (Fig. 4.2-e). Histological assessment of both arteries, injured and control, did now show any signs of lipid accumulation or inflammation as validated by Oil Red O (ORO) and H&E staining. This histological result was expected since this model does not consider development of atherosclerotic lesions over an extended time period. Tissue sections were also stained with CD31 which can be used to reveal the presence of endothelial cells. While, CD31 staining indicated overall functioning endothelium in the control artery (Fig. 4.2-e, blue box), the absence of brown staining signal (Fig. 4.2-d, red box) validated the presence of endothelial damage in the denudated artery. In conclusion, figure 4.2 indicates that NIRF-IVUS can identify acute lesions via ICG detection in a rabbit model of acute endothelial injury.

4.3 Results of a Rabbit Model of Chronic Atherosclerosis

Figure 4.3 presents the imaging results and histological validation of a rabbit model of chronic atherosclerosis. Baseline angiography on day 7, prior to denudation, showed both iliac arteries in a healthy condition (Fig. 4.3-a). In contrast, angiography on day 63, post re-denudation (Fig. 4.3-b), revealed compromised blood flow indicative for a stenotic segment (red arrows) in the injured LIA (red box) as opposed to regular blood flow in the RIA (blue box) serving as a control. In vivo NIRF imaging detected significantly increased ICG signal in the injured artery in comparison to the control (Fig. 4.3-c). Note that the rapid difference in fluorescence intensity which can be observed as a diagonal line in the NIRF map of the injured artery, can be attributed to signal attenuation by the guidewire. The detected contrast in ICG uptake between injured and healthy tissue was later confirmed by ex vivo FRI of the excised arteries. Furthermore, FM and histopathological assessment of the atherosclerotic vessel (Fig. 4.3-d) confirmed the devlopment of a distinct stenosis with ICG accumulation in areas of lipid-deposition (ORO, red droplets) and foam cell formation (Movat pentachrome (MP) and H&E) in the subendothelial tissue layer. As opposed to the injured artery, no ICG uptake and pathological characteristics were observed for the healthy control (Fig. 4.3-e). In summary, these results validate the successful induction and progression of an atherosclerotic lesion in the rabbit model. Moreover, they confirm the feasibility of detecting chronic atherosclerotic lesions in vivo by NIRF-IVUS imaging of local ICG deposition in areas of lipid accumulation and inflammatory activity.

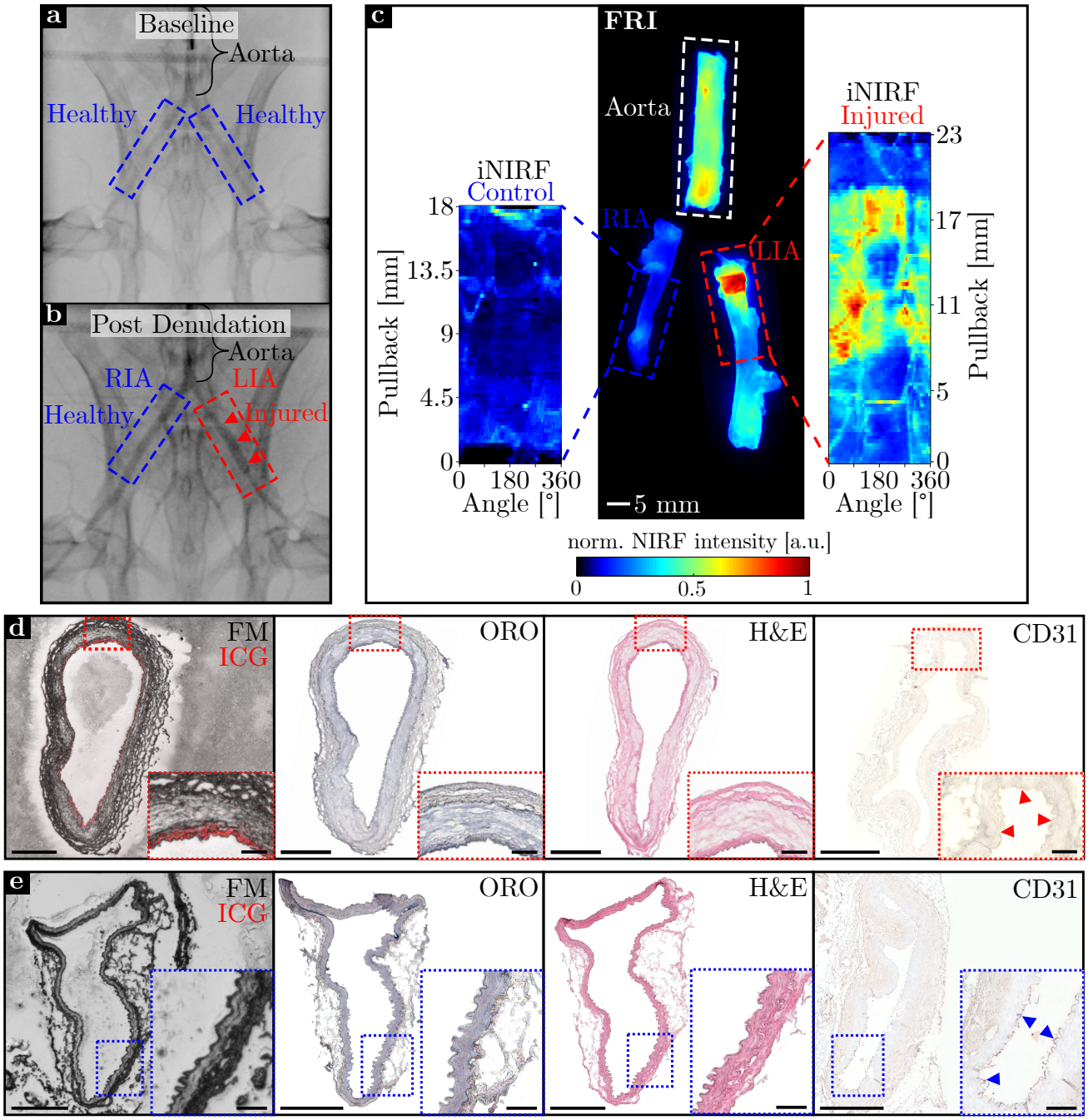

Figure 4.2: Imaging results and histological validation of a rabbit model of acute endothelial injury. **a** - Baseline angiography image reveals regular blood flow in both iliac arteries (Blue boxes); **b** - Post denudation angiography indicates regular blood flow in the RIA functioning as a control (Blue box) and a dilated lumen (Red arrows) in the denudated LIA (Red box); **c** - Ex vivo FRI and iNIRF imaging show increased ICG signal in the injured compared to to control artery; **d** - FM and histology staining of an exemplary tissue section of the injured iliac artery. FM showing ICG uptake in the intimal layer (Red box) in a tissue area with acute endothelial damage (CD31, red arrows) and without signs for lipid accumulation or inflammation (ORO, H&E, red boxes); **e** - FM and histology staining of an exemplary tissue section of the control iliac artery; FM confirming absence of ICG uptake (Blue box) in healthy tissue areas with functioning endothelium (CD31, blue box) and without signs for lipid accumulation or inflammation (ORO, H&E, blue boxes); Scale bars: 500μm and 100μm (zoom in); In all panels: RIA= Right iliac artery; LIA = Left iliac artery; FRI = Fluorescence reflectance imaging; iNIRF = Intravascular NIRF imaging; FM = Fluorescence microscopy; ORO = Oil Red O.

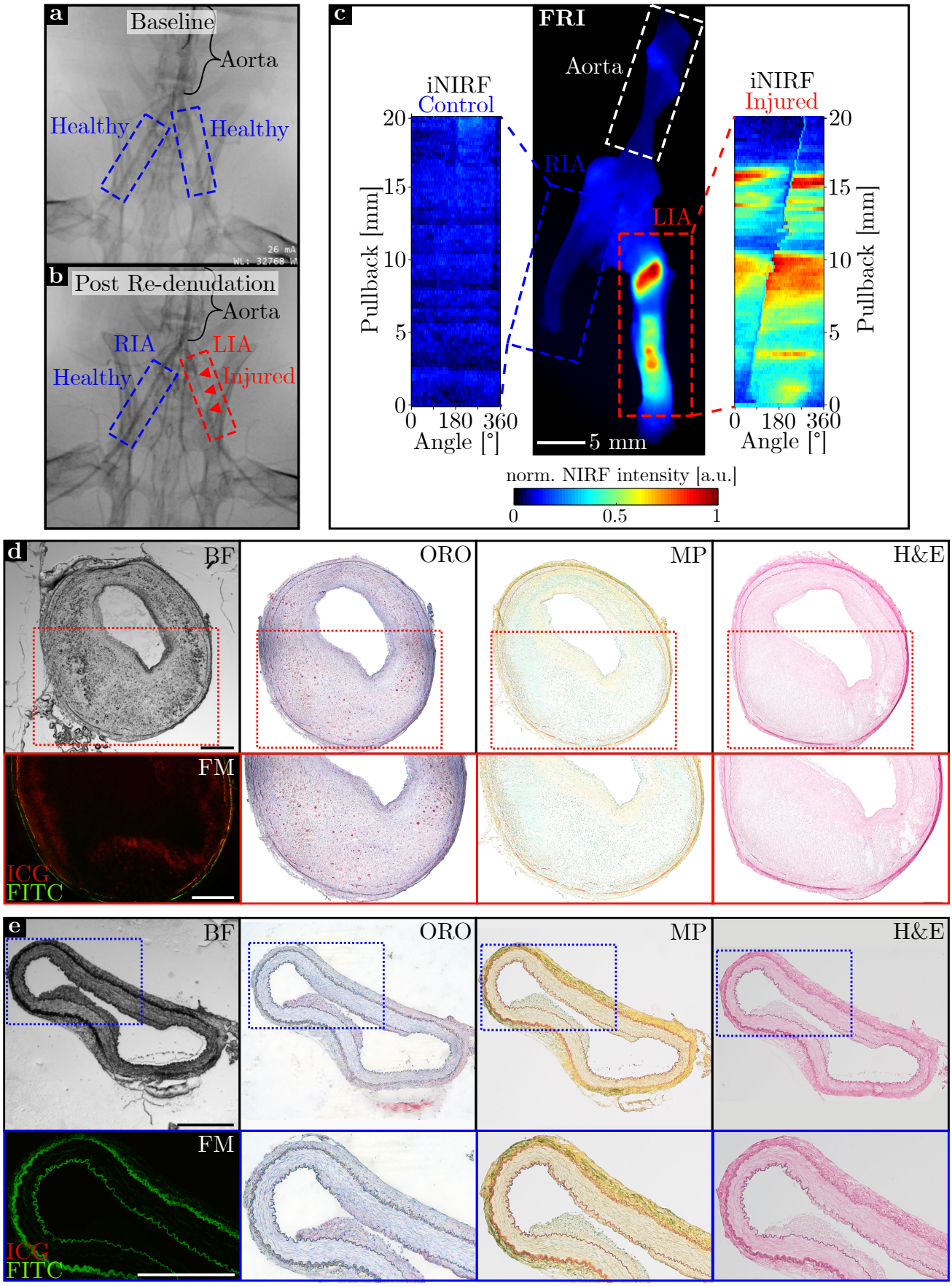
a
Baseline
Aorta
Healthy
Healthy
b
Post Re-denudation
Aorta
RIA
LIA
Healthy
Injured
c
FRI
Aorta
RIA
LIA
iNIRF
Control
iNIRF
Injured
Pullback [mm]
Angle [°]
5 mm
norm. NIRF intensity [a.u.]
d
BF
ORO
MP
H&E
FM
ICG
FITC
e
BF
ORO
MP
H&E
FM
ICG
FITC

Figure 4.3 ***(previous page)*****: Imaging results and histological validation of a rabbit model of chronic atherosclerosis. a** - Baseline angiography image reveals regular blood flow in both iliac arteries (Blue boxes); **b** - Post re-denudation angiography indicates regular blood flow in the RIA functioning as a control (Blue box) and a stenotic segment (Red arrows) in the denudated LIA (Red box); **c** - In vivo iNIRF imaging and ex vivo FRI detect increased ICG signal in the injured compared to to control artery; **d** - FM and histology staining of an exemplary tissue section of the injured iliac artery; FM detecting ICG accumulation (Red box) in the subendothelial tissue areas staining positive for lipid-deposition (ORO, red droplets, red box) and foam cell formation (Movat pentachrome (MP) and H&E, Red boxes); **e** - FM and histology staining of an exemplary tissue section of the control iliac artery; FM confirming the absence of ICG uptake (Blue box) in healthy tissue regions (ORO, MP, and H&E, blue boxes); All scale bars: 500 μm; In all panels: RIA = Right iliac artery; LIA = Left iliac artery; FRI = Fluorescence reflectance imaging; iNIRF = Intravascular NIRF imaging; BF = Bright-field Microscopy; FM = Fluorescence Microscopy; FITC = Fluorescein channel for autofluorescence; ORO = Oil Red O; MP = Movat Pentachrome.

4.4 Results of a Rabbit Model of Atherosclerosis and Acute Atherothrombosis

The rabbit model of atherosclerosis and acute atherothrombosis involves early in vivo imaging on day 14 after introduction of endothelial injury (Fig. 4.1-e).
Considering the preceding high-cholesterol diet, the rabbit can be regarded as hyperlipidemic on the day the acute vascular injury is induced. In comparison, the model of acute injury (Section 4.2) induces acute injury in healthy tissue. Figure 4.4 presents the imaging results of this hyperlipidemic rabbit after acute injury. As in previously presented animal experiments, baseline angiography prior to the balloon denudation showed both iliac arteries in normal condition (Fig. 4.4-a). A small vascular dilation was observed in angiography images after denudation in the LIA compared to the RIA which served as a healthy control (Fig. 4.4-b). In order to complete this preliminary imaging session, in vivo NIRF-IVUS imaging was performed which detected a modestly increased ICG signal in iNIRF pullback maps of the injured compared to the control artery (Fig. 4.4-c).

In vivo NIRF imaging of the same rabbit at day 70 confirmed previous findings of increased ICG signal detection in the injured vs. the control artery (Fig. 4.5-a). These findings were further validated with ex vivo macroscopic FRI of the excised arteries after the experiments (Fig. 4.5-a). In addition, the detected ICG signal was significantly increased when comparing iNIRF imaging results from day 70 (Fig. 4.5-a) to day 14 (Fig. 4.4-c). Figure 4.5-b displays angiography prior to administration of the thrombus trigger revealing compromised blood flow indicative for a stenotic segment (red arrows) in the injured LIA (red box) in contrast to regular blood flow in the healthy RIA (blue box). Trigger administration resulted in thrombus formation, which occluded both iliac arteries as visible in angiography (Fig. 4.5-c). FM of an exemplary tissue section sampled from the injured iliac artery revealed ICG accumulation in the media layer, within a sector between the 11 and 2 o'clock position (Fig. 4.5-d). Histological assessment showed lipid accumulation (ORO) within areas of intima and media thickening (MP). Furthermore, CD31 staining indicated a compromised endothelial layer (Red arrows) at the intima suggesting endoluminal diffusion of ICG into deeper artery layers. In contrast, FM

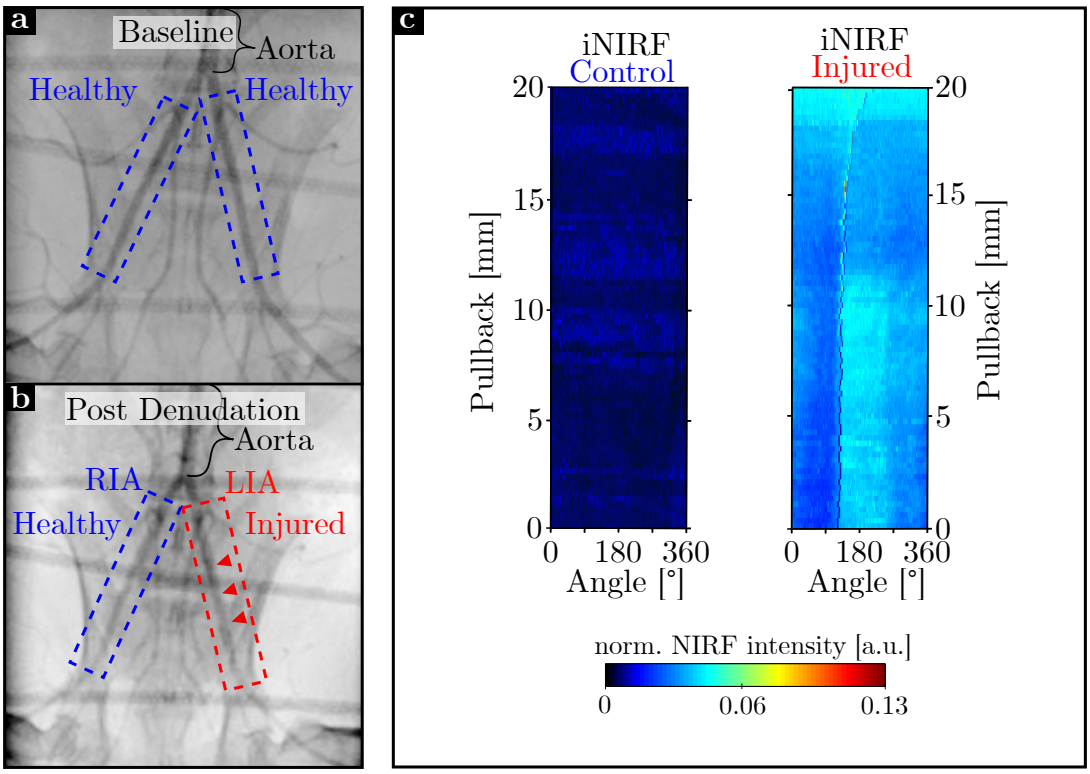

Figure 4.4: Imaging results of a hyperlipidemic rabbit after acute injury. **a** - Baseline angiography image reveals regular blood flow in both iliac arteries (Blue boxes); **b** - Post denudation angiography indicates regular blood flow in the RIA functioning as a control (Blue box) and a slightly dilated lumen (Red arrows) in the denudated LIA (Red box); **c** - In vivo iNIRF imaging shows slightly increased ICG signal in the injured compared to to control artery; In all panels: RIA = Right iliac artery; LIA = Left iliac artery; iNIRF = Intravascular NIRF imaging.

imaging of an exemplary tissue section sampled from the control iliac artery did not show any ICG accumulation as well as pathological tissue changes in the histological stainings (Fig. 4.5-e). Notably, this also applied to the CD31 staining which indicated an intact endothelial layer at the endoluminal border (Blue arrows).
Overall, these results further demonstrate that intravascular NIRF imaging can detect ICG in vivo which specifically correlated to areas of pathological changes in the atherosclerotic rabbit model. Additionally, higher ICG signals were detected in late-stage compared to early stage lesions which will be further discussed in section 4.6. In this imaging experiments no specific correlation between thrombus formation and ICG signal was detected since a thrombus was also found in the control artery with no significant ICG uptake.

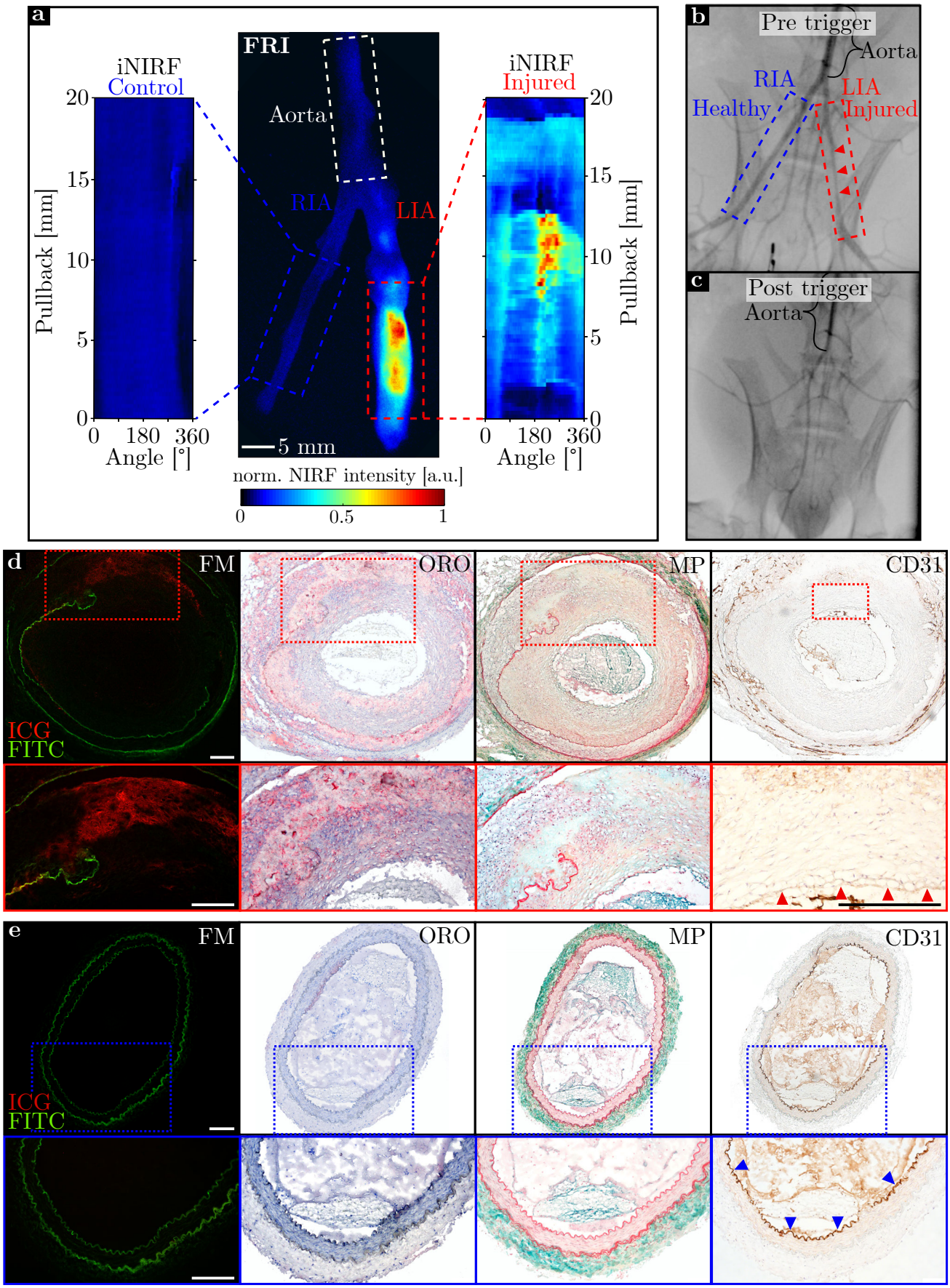
a
iNIRF
Control
FRI
Aorta
RIA
LIA
iNIRF
Injured
Pullback [mm]
Angle [°]
5 mm
norm. NIRF intensity [a.u.]
b
Pre trigger
Aorta
RIA
Healthy
LIA
Injured
c
Post trigger
Aorta
d
FM
ORO
MP
CD31
ICG
FITC
e
FM
ORO
MP
CD31
ICG
FITC

Figure 4.5 ***(previous page)*****: Imaging results and histological validation of a rabbit model of atherosclerosis and acute atherothrombosis.** **a** - Ex vivo FRI image and in vivo NIRF imaging of aorta and control and injured iliac arteries; **b** - Angiography image prior trigger administration; **c** - Angiography image post trigger administration; **d** - FM and histology staining of an exemplary tissue section of the injured iliac artery; FM revealed ICG accumulation in the media layer (Red box) which stained positive for lipid accumulation (ORO, red box) within areas of intima and media thickening (MP, red box) and endothelial damage (CD31, blue box); **e** - FM and histology staining of an exemplary tissue section of the control iliac artery; FM confirming the absence of ICG uptake (Blue box) in healthy tissue regions (ORO, MP, and CD31, blue boxes); All scale bars: 500 μm; In all panels: RIA = Right iliac artery; LIA = Left iliac artery; FRI = Fluorescence reflectance imaging; iNIRF = Intravascular NIRF imaging; FM = Fluorescence Microscopy; FITC = Fluorescein channel for autofluorescence; ORO = Oil Red O; MP = Movat Pentachrome.

4.5 Results of a Rabbit Model of Neoatherosclerosis

Figure 4.6 displays the imaging results and histological validation of a rabbit model of neoatherosclerosis. Baseline angiography on day 7 prior to denudation and stent implantation indicated regular blood flow in both iliac arteries (Fig. 4.6-a). Angiography recorded after stent implantation (Fig. 4.6-b) indicated increased lumen diameter in the stented segment (Red arrows) in the injured LIA (Red box) as opposed to regular blood flow in the RIA which served as a control for consecutive analysis (Blue box). Figure 4.6-c shows in vivo NIRF maps and ex vivo FRI imaging including en face views for improved visualization of ICG distribution inside the lumen. For this purpose, arteries were cut longitudinally and carefully folded open to expose the lumen for FRI imaging. In vivo NIRF imaging detected significantly increased ICG signal in the injured and stented artery in comparison to the control. Similar like in Fig. 4.3-c and 4.4-c, the rapid difference in fluorescence intensity which can be observed as a diagonal line in the NIRF map of the injured and stented artery, can be attributed to signal attenuation by the guidewire. Ex vivo FRI imaging confirmed the difference in ICG uptake between the the control and the injured/stented artery. Furthermore, the ICG distribution in the en face FRI image agreed well with the in vivo NIRF pullback map. Histological analysis confirmed the development of neoatherosclerosis in the injured/stented artery (Fig. 4.6-d). Specifically, intima thickening with foam cell formation overlaying the primary tissue layer including the stent struts (Red arrows) can be observed in MP and H&E staining. On the contrary, the control artery featured healthy tissue as validated by MP and H&E histological staining.

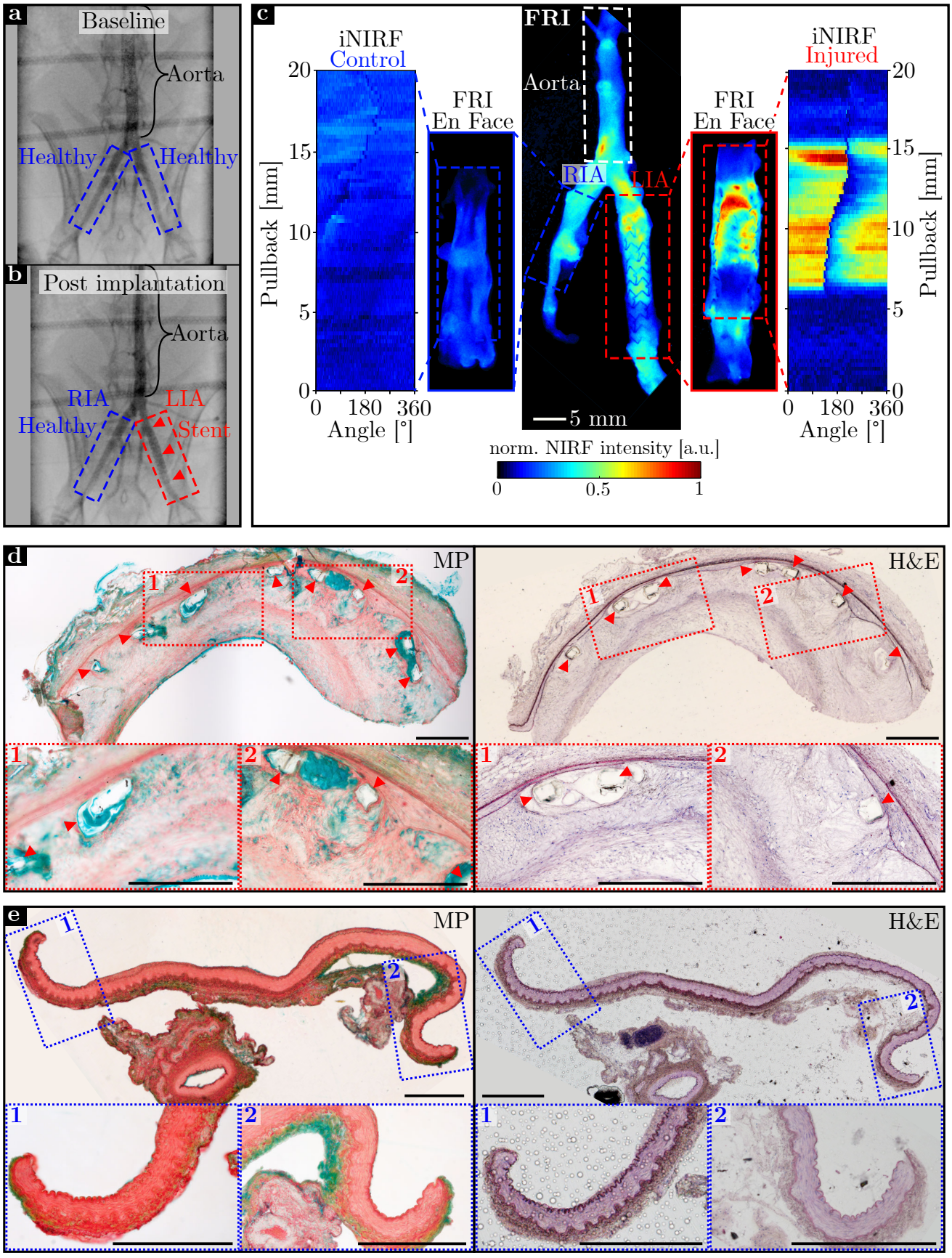
a
Baseline
Aorta
Healthy
Healthy
b
Post implantation
Aorta
RIA
LIA
Healthy
Stent
c
iNIRF
Control
FRI
En Face
FRI
Aorta
RIA
LIA
5 mm
FRI
En Face
iNIRF
Injured
Pullback [mm]
Angle [°]
norm. NIRF intensity [a.u.]
0
0.5
1
d
MP
H&E
e
MP
H&E

Figure 4.6 *(previous page)*: Imaging results and histological validation of a rabbit model of neoatherosclerosis. **a** - Baseline angiography image reveals regular blood flow in both iliac arteries (Blue boxes); **b** - Post stent implanation angiography indicates regular blod flow in the RIA functioning as a control (Blue box) and a dilated lumen (Red arrows) in the stented LIA (Red box); **c** - Ex vivo FRI (En face) and in vivo iNIRF imaging show increased ICG signal in the injured compared to to control artery; **d** - Histology staining of an exemplary tissue section of the injured and stented iliac artery confirms the presence of neoatherosclerosis in the form of intima thickening with foam cell formation overlaying the primary tissue layer including the stent struts (MP, H&E, red arrows); **e** - Histology staining of an exemplary tissue section of the control iliac artery indicates healthy tissue regoins (MP, H&E, blue arrows); Scale bars: 500μm; In all panels: RIA= Right iliac artery; LIA = Left iliac artery; FRI = Fluoresence reflectance imaging; iNIRF = Intravascular NIRF imaging; MP = Movat pentachrome.

4.6 Discussion and Conclusion

Table 4.1 summarizes the imaging experiments in the different pre-clinical rabbit models of atherosclerosis. So far, NIRF-IVUS imaging was performed in 2 animals with acute endothelial injury ex vivo and, in vivo, in 1 animal of the chronic atherosclerotic group, 6 animals out of the atherosclerotic and atherothrombotic group on day 14 and 70 and 4 animals out of the neoatherosclerotic group. To quantify the specificity of NIRF-IVUS detection of ICG in the different groups, the ratio between the average fluorescence intensity in the injured and control artery was calculated. A higher ICG signal was detected by NIRF imaging in the injured vs. the control artery in all groups. The highest specificity was found in the chronic atherosclerotic group for which NIRF imaging indicated a 3.9 times higher ICG uptake in the injured compared to the control artery.

Group	**Number of finished experiments**	**NIRF signal specificity (Injured vs. control)**
Acute	2 (Ex vivo)	3.3
Chronic atherosclerotic	1 (In vivo)	3.9
Atherosclerotic/ Atherothrombotic - Day14	6 (In vivo)	2
Atherosclerotic/ Atherothrombotic - Day70	6 (In vivo)	2.9
Neoatherosclerotic	4 (In vivo)	1.7

Table 4.1: Summary of finished pre-clinical imaging experiments.

Furthermore, ICG signal specificity increased in the atherosclerotic and atherothrombotic group from 2 to 2.9 between day 14 and 70. This finding indicates a higher ICG uptake in chronic lesions with increased vascular permeability when compared to tissue with acute vascular injuries which suggests that NIRF-IVUS is feasible to monitor atherosclerotic disease progression by detecting ICG accumulation in the tissue. The specificity in detecting acute injuries was higher in the acute group compared to atherosclerotic and atherothrombotic group (Day 14). However, a higher ICG concentration was administered in the acute group (5 mg/kg vs. 1 mg/kg body weight) and the arteries were imaged ex vivo during water perfusion. Both factors simplify ICG signal detection by NIRF-IVUS and, thus, could be the explanation for the difference in NIRF

signal specificity. It must be mentioned, that at this stage it is difficult to compare imaging results between the different groups because only a limited amount of experiments have been completed.

Besides the complications in regards to the animal models like unintended total occlusion of injured artery preventing NIRF-IVUS imaging on the final experiment day, challenges have been also identified for the imaging process during the presented experiments. For instance, during the course of 3 in vivo measurements , blood was sucked inside the catheter sheath through the hole used for saline flushing. This predominantly happened when perfusion pressure inside the sheath was smaller than intravascular blood pressure due to damages of the catheter sheath, e.g increased diameters in the sheath outlet. As a results, the blood inside the catheter sheath either attenuated NIRF signals significantly or increased NIRF noise levels due to remaining ICG in the blood. Thus, it is important to ensure the integrity of the catheter sheaths (Ideally using a new sheath for every in vivo imaging experiment) to maintain perfusion pressure inside the catheter sheath. Moreover, IVUS image quality should be further improved as already mentioned in section 3.8 which is specifically important for in vivo imaging due to weak US signals, artery motion, catheter bending and blood flow.

In conclusion, this pre-clinical imaging study provides strong evidence that intravascular NIRF-IVUS can identify atherosclerosis in vivo by detecting ICG accumulation in lesions of different atherosclerotic animal models. Furthermore, no complications were reported for a total number of 17 in vivo intravascular imaging sessions which indicates that the developed 3.2F NIRF-IVUS catheter is safe to use for intravascular imaging applications.

Chapter 5

Intravascular NIRF-IVUS Imaging of ICG-perfused Human Coronary Arteries Ex Vivo

5.1 Introduction

The potential of intravascular NIRF-IVUS/IVOCT for the detection of atherosclerosis has been investigated in various pre-clinical animal models in vivo as already presented in previous sections (1.5.4, 4). Although, artificially induced atherosclerosis in larger animals, like rabbits and swine, can model certain plaque characteristics like endothelial damage and lipid deposition, it fails to fully reflect the complexity and the interplay of different pathological mechanism found in human plaques [93]. Therefore, an imaging study was conducted previously to validate the detection of pathological markers in human tissue. In this pilot study, intravascular NIRF-OCT was used to investigate plaques excised from human carotid arteries [85]. For this purpose, five patients received ICG injection prior to carotid endarterectomy and plaques were imaged ex vivo after surgical removal. Intravascular NIRF-OCT imaging revealed ICG diffusion into plaques through areas of endothelial disruption (leakage) and ICG accumulation in the presence of macrophages, lipids and intraplaque haemorrhage.
Although this work provided valuable insights on ICG detection in human tissue by intravascular NIRF, a limitation of this study was that only highly advanced atherosclerotic tissue in the form of late-stage plaques excised from carotid arteries were investigated. Furthermore, the analysis was limited to a qualitative correlation between the presence of atheroma altered pathological markers and detected NIRF signals, thus, leaving the potential for a quantitative assessment unexplored.

Therefore, there is still a need for more thorough human tissue studies, notably in whole coronary arteries, which cannot be excised from living patients and where atherosclerosis and severe clinical events like MI represents the number one cause of death worldwide. Specifically, there is a current lack of evidence regarding the correlation between ICG, detected by intravascular NIRF(-IVUS), and pathological markers of atherosclerosis over a range of different disease stages, including healthy tissue or early lesions, to validate initial findings and test the limits of the method. Additionally, previous studies lack a correlation of ICG concentration accumulated in tissue with atherosclerotic characteristics in a quantitative manner. A quantitative assessment of atherosclerosis by intravascular NIRF-IVUS would further underline the value of this hybrid imaging modality for the investigation of CAD.

To address this need, 15 whole coronary artery segments, excised from human cadaver hearts, were perfused with ICG to image a range of atherosclerotic disease stages, and healthy artery tissue post-mortem. NIRF signals were correlated with pathological markers of atherosclerosis (endothelial damage, lipid accumulation, and inflammation), as validated by histological staining and FM. Moreover, the correlation between NIRF signals of ICG detected in coronary tissue and the abundance of inflammatory markers and overall pathological scoring of co-registered tissue sectors was quantified. While the post-mortem study does not recapitulate all in-vivo conditions, such as functional atheroma features and blood flow, it allowed for the first time to investigate the performance of intravascular NIRF imaging of ICG in human coronary arteries over a range of atherosclerotic disease stages, including healthy tissue and early-stage lesions, in a quantitative manner.

5.2 Experimental Methods

5.2.1 Tissue Preparation

Coronary arteries were excised from hearts of 11 donors (Table 5.1; Written informed consent was provided by family members of patients deceased at Deutsches Herzzentrum München and Klinikum Rechts der Isar as approved by the ethics committee of Technical University of Munich; Aktenzeichen 291/18 S) within 48 hours of death and flushed with cold PBS.

Number, n	**11**
Age in years, mean +/- SD	76.7 +/- 7.7
Sex	
male, n	5
female, n	6
Cause of death, n (%)	
Cardiovascular	3 (27)
STEMI	2 (18)
Heart failure	1 (9)
Non-cardiovascular	7 (63)
Pulmonary cause	4 (36)
Sepsis	2 (18)
Hemorrhage	1 (9)
Unknown	1 (9)
Medical history, n (%)	
Hypertension	6 (54)
Current or former smoker	2 (18)
Diabetes Mellitus	2 (18)
Prior MI	2 (18)
Prior CABG	1 (9)

Table 5.1: Clinical characteristics of coronary artery specimen donors; STEMI: ST-Elevation myocardial infarction; MI: Myocardial infarction; CABG: Coronary artery bypass graft.

Next, coronary artery segments were prepared for the experiments by trimming off excessive adjacent fat and ligating side branches to avoid i) unspecific ICG uptake on the outside of the

artery and ii) establish an adequate perfusion pressure to flush out air bubbles compromising IVUS image quality. Exclusion criterion for the imaging study was a high degree of luminal stenosis which would have prevented insertion of the imaging catheter without risking introduction of artificial tissue damage. The average length of the coronary artery segments was 33 mm (Range: 9-50 mm) after preparations were completed.

5.2.2 ICG Perfusion and Intravascular Imaging

Artery segments were mounted into a custom-made holder (Similar like in [79, 94]) and perfused with a peristaltic pump (Ecoline, ISMATEC, Cole-Parmer, Wertheim, Germany) for 5 min with 500 ml of ICG (VERDYE, Diagnostic Green, Aschheim-Dornach, Germany) which was dissolved in phosphate-buffered saline (PBS) to a final concentration of 20 μM (Fig. 5.1-a).

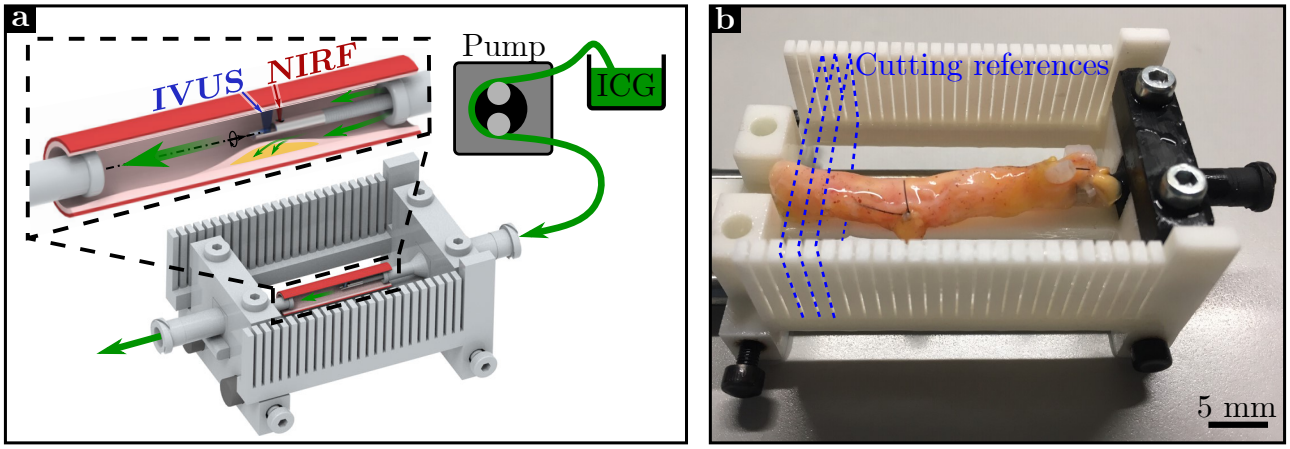

Figure 5.1: Coronary artery holder for ex vivo perfusion and intravascular imaging. **a** - Ex vivo ICG perfusion of human coronary arteries fixed in a holder prior to intravascular NIRF-IVUS imaging; **b** - Excised human coronary artery fixed in a 3D-printed holder for co-registration of imaging data and histology.

After ICG perfusion, coronary arteries were flushed with 500 ml of cold PBS for 5 min to wash out remaining ICG in the arterial lumen. Next, the holder with the arteries was mounted into a PBS bath and imaged with intravascular NIRF-IVUS while perfusing PBS through the arterial lumen to enable IVUS imaging. The coronary artery segments were imaged with the 3.7F prism catheter operating at a rotation speed of 142 rpm and a pullback speed of 0.5 mm/s to acquire helical scans of the intimal arterial wall. The pullback distance varied for the the different artery segments ranging between 10-50 mm (i.e. 40-200 cross-sectional NIRF-IVUS imaging frames per artery).

5.2.3 Fluorescence Microscopy and Histology

After NIRF-IVUS imaging was completed, artery segments were divided into two groups for further processing. The first sub-group (n=4) was processed for histology immediately by cutting the artery segments to 2 mm sub-segments with guidance provided by the cutting references which were implemented in the artery holder (Fig. 5.1-b). The sub-segments were embedded in O.C.T. compound (Tissue-Tek, Sakura Finetek, Staufen, Germany) and, finally, fresh-frozen with dry ice. Representative slides were cut with a cryotome at 10 μm thickness and a fluorescent microscope (BX41, Olympus, Tokio Japan; Camera: C11440-36U, Hamamatsu, Japan) was used to detect accumulated ICG (ICG channel, Excitation/Emission = 730/776

nm) and tissue autofluorescence (FITC channel, Excitation/Emission = 495/520 nm) which is attributed to endogenous fluorophores like elastin and collagen in the arterial tissue (See section 1.3.2.2). Finally, histological sections were stained with Movat Pentachrome (MP), CD68, alpha-smooth muscle actin (αSMA), CD31 and Oil Red O (ORO) for histological analysis (Overview of histological stainings provided in A.1). The second sub-group (n=11) was kept in the artery holder and fixed in paraformaldehyde solution 4% in PBS (sc-281692, Santa Cruz Biotechnology Inc., Dallas, Texas, USA) for 24-48 hours first. Arteries of the second sub-group were then imaged with a commercially available IVOCT system (Abbot, Dragonfly OPTIS, Plymouth, USA) to provide detailed imaging information of the artery lumen for supporting the co-registration of NIRF-IVUS imaging data with histology (See section 5.2.4). After IVOCT imaging was completed, artery segments were cut to 2 mm sub-segments, similar like the first group, and embedded in paraffin afterwards. Histological sections were cut with a microtome to a 10 μm thickness and were stained with H&E, MP, CD68 and αSMA for histological analysis (see table A.1).

5.2.4 Co-registration Between NIRF-IVUS Imaging Data and Histology

The analysis of this work required precise angular and axial co-registration between intravascular NIRF-IVUS data and histology. Thus, angular markers were installed which were visible in the imaging data and histology to enable angular co-registration. Specifically, the artery holder featured a structure creating a reference signal at the 180° position (Blue box) in all hybrid NIRF-IVUS frames (Fig. 5.2-a). Furthermore, additional IVOCT imaging pullbacks were acquired to provide detailed information about the coronary lumen to support co-registration with histology (Fig. 5.2-b) as mentioned in 5.2.3. Due to limited penetration depth of IVOCT, the angular maker of the artery holder was not visible in the IVOCT images. Thus, a coronary guidewire was inserted into the artery holder to create a reference signal at the 180° position (Blue box) at the end of the IVOCT imaging pullbacks. The pullback position provided information for the axial co-registration for both, NIRF-IVUS and IVOCT imaging data. After completion of intravascular imaging, arteries were marked at the 0°/360° position with tissue ink to provide an indicator for angular orientation (Fig. 5.2-c). Furthermore, cutting references were implemented into the holder (Fig. 5.1-b) to enable division of arteries into 2-3 mm sub-segments for axial co-registration as already mentioned in section 5.2.3. The combined information of axial and angular markers in both data sets, the imaging frames and histology sections, allowed to precisely co-register all data to each other.

5.2.5 NIRF-IVUS Post-processing and Imaging Analysis

NIRF intensities of all data-sets were normalized to each other to account for small differences in ICG concentration used for perfusing the arteries and potential changes in NIRF sensitivity of the system due to e.g. misalignments in the optical detection path or contamination of the NIRF sensor located in the catheter. Since data was collected over a time span of 12 months, this normalization ensured that data sets were comparable to each other. For this purpose, a sample of the ICG perfusate was filled into a glass-capillary prior to every artery scan and was imaged with the NIRF-IVUS system to record NIRF reference values. After the NIRF-IVUS image acquisition for all coronary arteries was completed, reference values were used to normalize the individual data sets to the peak value of averaged NIRF intensities recorded during all reference measurements.

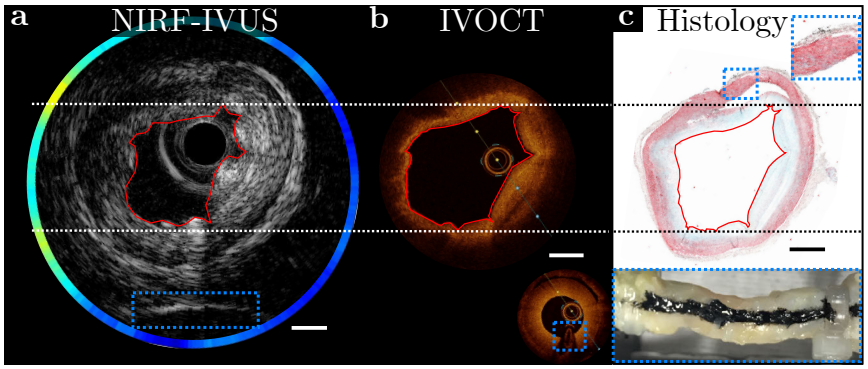

Figure 5.2: Angular co-registration between intravascular NIRF-IVUS imaging data and histology. **a** - Exemplary NIRF-IVUS frame of coronary tissue showcasing IVUS reference signal (Blue box) as an angular marker at the 180° location; **b** - Co-registered IVOCT frame of coronary tissue showcasing IVOCT reference signal of an inserted guidewire (Blue box) as an angular marker at the 180° location; **c** - Co-registered histology section stained with MP indicating tissue ink as an angular marker at the 0°/360° location (Blue boxes); In all panels: Lumen was outlined in red; NIRF: Near-infrared Fluorescence; IVUS: Intravascular ultrasound; IVOCT: Intravascular optical coherence tomography; MP: Movat pentachrome; Scale bars: 1 mm.

In addition to this normalization, intravascular NIRF data needs to be corrected for signal variation due to changes in distance between the sensor and the artery wall throughout the imaging pullback. This correction removes the influence of the distance on the detected NIRF signals and allows to transfer NIRF intensity to ICG concentration values. To address this need, a distance-dependent correction model was constructed which was based on phantom measurements of an ICG-Lipid-Agar patch. In contrast to NIRF measurements of ICG dissolved in a transparent solution like saline, NIRF measurements of ICG dissolved in lipid [95] allowed to resemble the diffusive optical properties expected in artery tissue [96, 97] and corresponding signal detection more closely. The patch was created as previously described in section 3.7.1. In short, 6 ml of 20% Intralipid (I141-100ML, Sigma-Aldrich) was heated to 90°C and 3% of Agar (A0950 Agar, Noble, United States Biological) was dissolved. The mixture was cooled down and 10 μL of ICG (5 mg/ml dissolved in DMSO) was added when the mixture reached around 40°C to create a final concentration of 10.7 μM. The liquid mixture was then poured between two microscope cover slips to solidify and create the final patch.
Next, the patch was placed in a tilted position into a 3D-printed phantom to record NIRF-IVUS measurements at variable distances (0-3.5 mm) between the patch and the sheath of the NIRF-IVUS catheter (Fig. 5.3-a). Fig. 5.3-b shows an exemplary NIRF map of the ICG-Lipid-Agar patch acquired during an imaging pullback and figure 5.3-c displays an exemplary IVUS frame of the patch in polar coordinates indicating the distance (d) between the catheter sheath and the surface of the patch. The measurements were repeated 4 times to average NIRF intensities (Highest 5 values averaged per frame) which were then plotted versus the distance from the sheath to the patch (Quantified by IVUS). This allowed to fit a two-term exponential function (Fig. 5.3-d) used as a distance-dependent correction function α(d), according to eq. 5.1:

$$\alpha(d) = 281.7 * e^{(-0.0027*d)} + 593.8 * e^{(-0.000355*d)}. \tag{5.1}$$

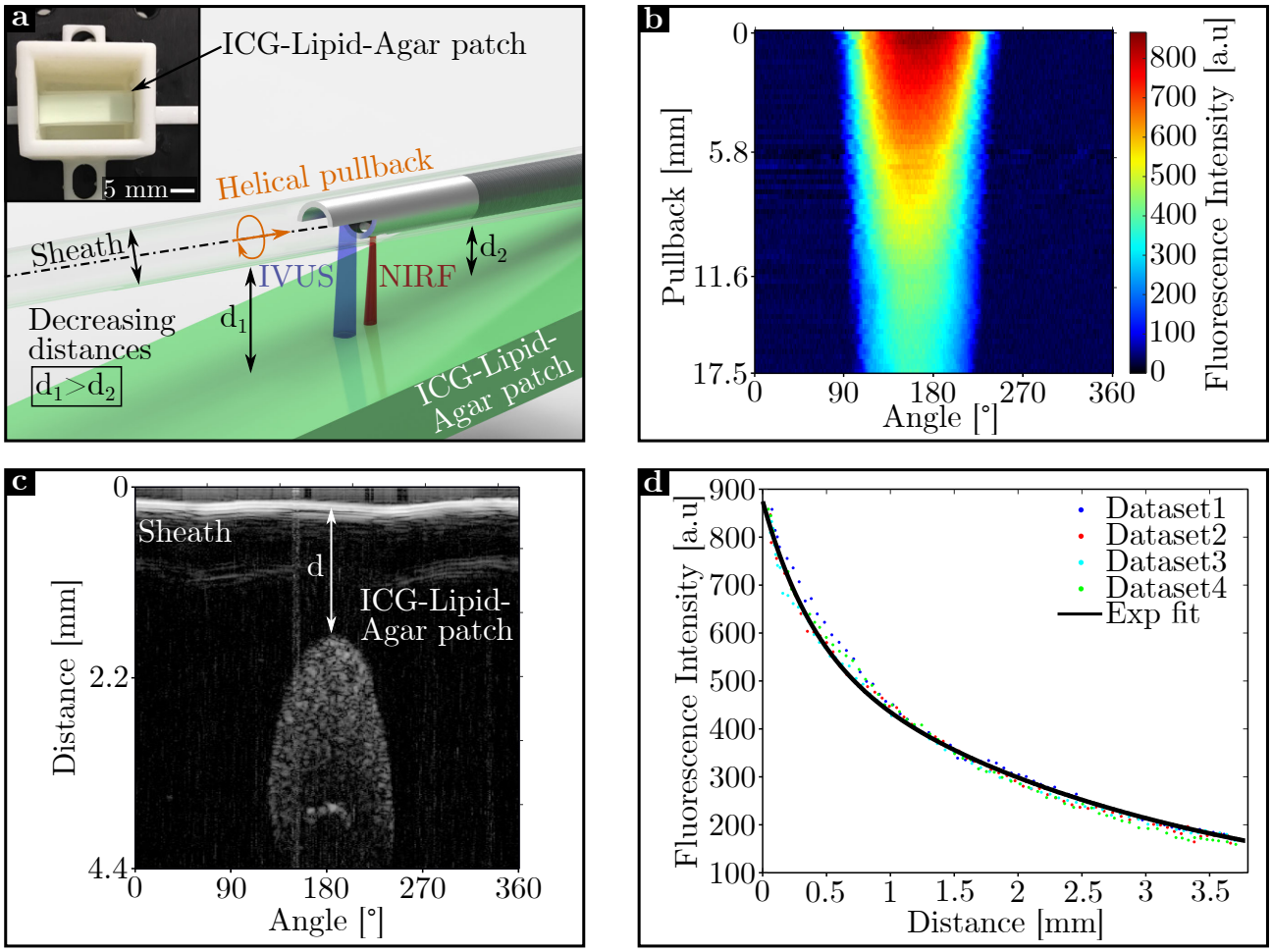

Figure 5.3: Development of a distance-dependent correction model for intravascular NIRF signals using an ICG-lipid-agar phantom. **a** - Picture and illustration of the NIRF-IVUS phantom measurements of an ICG-Lipid-Agar patch at variable distances to the imaging catheter; **b** - NIRF map of ICG-Lipid-Agar patch for an exemplary imaging pullback; **c** - Exemplary IVUS frame of the phantom measurements showing the catheter sheath and ICG-Lipid-Agar patch; **d** - Results of the phantom measurements showing recorded NIRF intensity of the ICG-Lipid-Agar patch at variable distances with corresponding exponential model fit; In all panels: NIRF: Near-infrared Fluorescence; IVUS: Intravascular ultrasound; ICG: Indocyanine green.

This function was then applied to correct NIRF signals, acquired from coronary artery tissue, for the distance between sheath and the coronary artery wall (Quantified by IVUS) according to (Eq. 5.2):

$$I_{Cor} = \frac{I_{Raw}}{\alpha(d)} \tag{5.2}$$

where I_{Cor} is the distance-corrected NIRF intensity and I_{Raw} is the uncorrected NIRF intensity acquired during NIRF-IVUS imaging pullbacks of the coronary arteries. Finally, I_{Cor} values were converted into ICG concentration by referring to the known ICG concentration of 10.7 μM in the Lipid-Agar patch and assuming a linear relationship between NIRF intensity and ICG concentration.

Furthermore, a processing scheme was developed for image analysis of the paraffin-embedded second sub-group of arteries to investigate the correlation of NIRF signals to signs of inflammation (See result section 5.3.3). For this purpose, image scans of co-registered histology sections stained for the presence of macrophages with CD68 were binarized using a pre-defined pixel-threshold range for the individual channels in the HSV colour space (H:0-1; S: 0.164-1; V:0-0.826). The threshold range was determined prior to the analysis on basis of exemplary histology sections marking CD68-positve pixels as 1 and all remaining as 0. This pixel threshold was kept constant for consecutive binarization of all CD68 stained histology sections included in the analysis. As a next step, binarized images were transformed from cartesian to polar coordinates to define a ROI measured as tissue depth of 500 μm from the artery lumen and divide NIRF and histology data in co-registered 30° sectors (S_1-S_{12}, n=792) for further analysis. Next, the density of CD68-positive pixels ((Number of pixels = 1)/(Number of pixels = 0)) was calculated in the ROI for each sector. Finally, Pearson correlation coefficient was calculated correlating density values to the average ICG concentration detected in the same sector by NIRF-IVUS.
Moreover, histology sections of arteries of both sub-groups were divided into 30° sectors and classified as either healthy, xanthoma, fibroatheroma, fibrous/fibrocalcific plaques and luminal calcification by a pathologist who was blinded to the NIRF-IVUS data. Finally, average ICG concentration detected by NIRF-IVUS per sector was correlated to corresponding pathological scoring and a two-sample t-test was used to investigate if the differences in average ICG concentrations between the different pathological classifications was significant.

5.3 Results

5.3.1 Intravascular NIRF-IVUS Imaging of Plaques and Healthy Tissue in Human Coronary Arteries

Figure 5.4 shows NIRF-IVUS imaging results of a RCA that was perfused with ICG in the designated artery holder (Fig. 5.1-b) prior to imaging. Figure 5.4-a displays a picture of the imaged segment of the RCA and the corresponding distance-corrected (See section 5.2.5) NIRF map indicating exemplary pullback locations which were co-registered with FM and histology (Fig. 5.4-b-d). A high ICG concentration (Red and orange box) was detected in a plaque with tissue regions staining positive for lipid accumulation (ORO - orange box), macrophage infiltration (CD68 - orange box) and endothelial dysfunction (CD31 – red box; red arrows indicating compromised endothelial layer) as shown in figure 5.4-b. ICG accumulation was confirmed in the intimal and deeper region of the plaque (Orange box) by FM. In contrast, low ICG concentration (Blue box) was detected in areas staining positive for functional endothelium (CD31-blue box; blue arrows indicating healthy endothelial layer). Similar correlations were observed in other plaques found at different locations within this RCA segment and also in additional arteries indicating detection of increased ICG concentration in superficial but also deeper plaque regions staining positive for lipid accumulation (ORO; Fig. 5.4-c-d, Fig. B.1-b-c, Fig. B.2-b-d), inflammatory activity (CD68; Fig. 5.4c-d, Fig. B.1-b-c, Fig. B.2-c-d) and endothelial dysfunction (CD31; Fig. B.2-b-c) as opposed to healthy tissue regions (Fig. B.1-d) with functional endothelium (Fig. B.2-b-c). The detection of low ICG uptake in healthy tissue areas by NIRF-IVUS was further confirmed when imaging a left internal mammary artery (LIMA) used as a coronary bypass in one of the patients and for which histological assessment did not show any pathological changes (Fig. B.3-b-e).

In this artery, increased ICG concentrations were only detected in tissue areas which showed signs of endothelial damage as indicated in co-registered (Metal clip, Green arrow) IVOCT (Red box, Fig. B.3-b).
NIRF-IVUS imaging also revealed increased ICG concentration accumulated in deeper plaque areas with presence of neovascularization (CD31 staining; Fig. B.1-b, Fig. B.2-c-d). In some cases, single neovessels could be co-registered with local ICG hotspots in FM (Indicated by *) suggesting vasa vasorum interna as a potential transport mechanism for ICG into deeper regions of coronary atheroma.

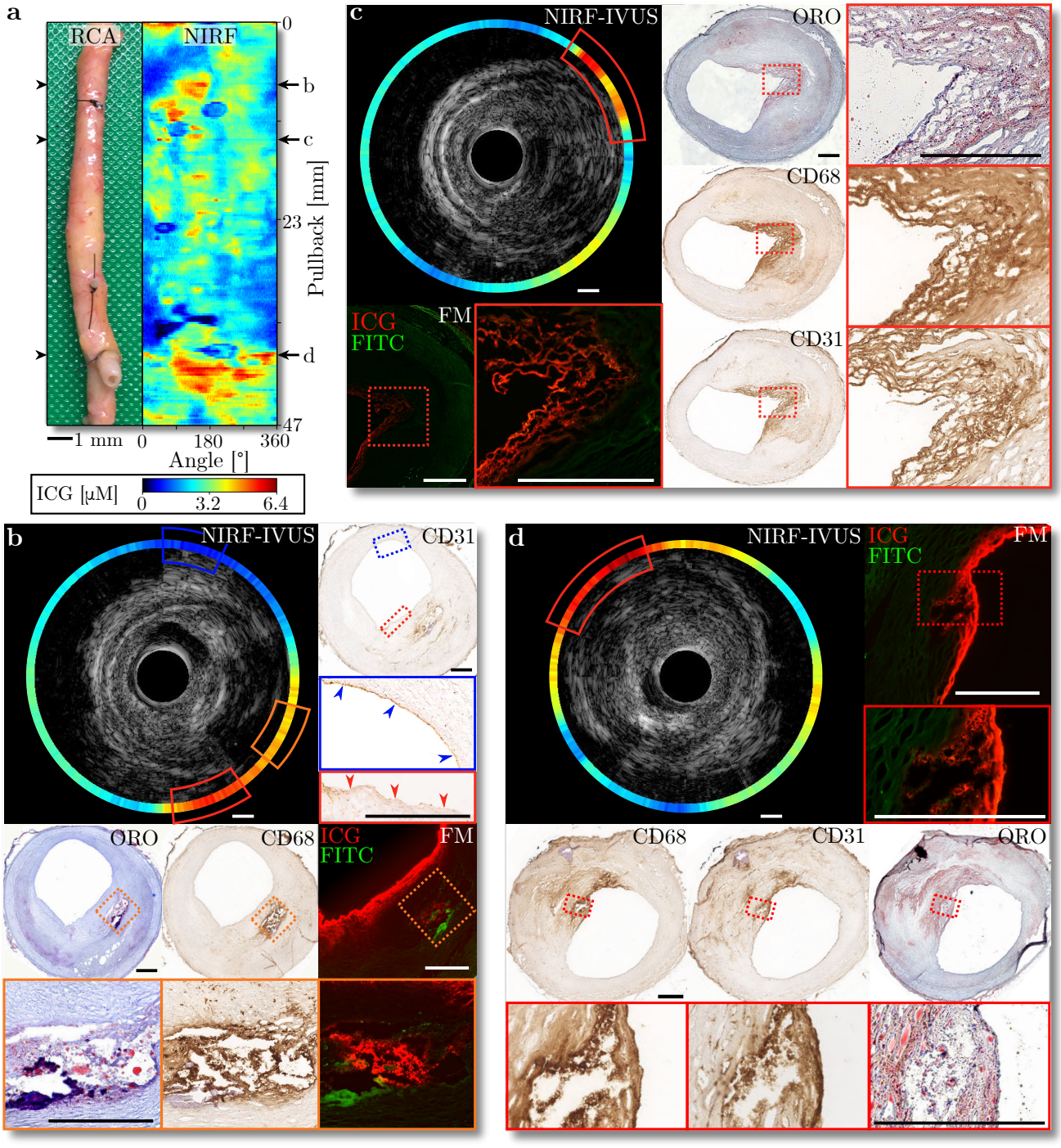

Figure 5.4 ***(previous page)*****: Intravascular NIRF-IVUS imaging of an ICG-perfused coronary artery showing high NIRF signals in plaque areas of lipid accumulations, macrophage infiltration and endothelial dysfunction.** **a** - Picture and corresponding NIRF map of an ICG-perfused Right Coronary Artery (RCA); **b** - High NIRF signal (Red and orange box) in regions staining positive for lipid accumulation (ORO- orange box), macrophage infiltration (CD68- orange box) and endothelial dysfunction (CD31 – red box; red arrows indicating compromised endothelial layer) and corresponding ICG detection in in FM. Low NIRF signal (blue box) in area staining positive for functional endothelium (CD31-blue box; blue arrows indicating healthy endothelial layer); **c** - High NIRF signal (red box) in a coronary plaque featuring a lipid-rich (ORO - red box) inflamed (CD68 – red box) surface area including neovascularization (CD31 – red box) and corresponding ICG detection in FM; **d** - High NIRF signal in a luminal area of a coronary plaque staining positive for lipid accumulation (ORO-red box) and macrophage infiltration (CD68 – red box) and corresponding ICG detection in FM. In all panels: NIRF: Near-infrared Fluorescence; IVUS: Intravascular Ultrasound; FM: Fluorescence Microscopy; ORO: Oil Red O; ICG: Indocyanine Green; FITC: Fluorescein channel for autofluorescence; Scale bars: 500 μm.

Finally, during NIRF-IVUS investigations of a stented LAD (Fig. B.4) increased ICG uptake was found in a plaque area located in an unstented region of the artery segment (Red box, Fig. B.4-b). In contrast, lower ICG concentrations were detected in stented artery segment with predominantly calcified and healthy tissue (Fig. B.4-c-e). Unfortunately, immunohistology staining was not possible for this stented artery due to the necessity of embedding the tissue in MMA for preparing tissue sections with a laser microtome. Therefore, a more detailed histological assessment was not possible for this specimen.

5.3.2 Intravascular NIRF-IVUS Imaging of Early Lesions in Human Coronary Arteries

Fig. 5.5 demonstrates NIRF-IVUS imaging of an ICG-perfused coronary artery with predominantly healthy tissue and early lesions. This artery segment was embedded in paraffin to cut co-registered (See section 5.2.4) sections for histological staining after intravascular measurements, to correlate NIRF signals to signs of initial stages of inflammation. Fig. 5.5-a displays a picture of a segment of a LCX and the corresponding distance-corrected (See section 5.2.5) NIRF map indicating exemplary pullback locations which were co-registered with histology (Fig. 5.5-b-e). A low ICG-concentration was detected in healthy tissue sections as validated by histological staining indicating normal arterial composition (MP) featuring smooth muscle cells (αSMA) without any signs for inflammation (CD68; Fig. 5.5-b-c, Fig. B.3). In contrast, Fig. 5.5-d-e demonstrates increased ICG concentration as detected with NIRF-IVUS (Red boxes) in early lesions featuring inflammation in the form of foam cell formation (MP, CD68) and an absence of smooth muscle cells (αSMA).

5.3.3 Correlation of Intravascular NIRF-IVUS Signals to the Severity of Tissue Inflammation

Motivated by these findings, we sought out to correlate the detected ICG concentration per tissue sectors with the severity of CD68 positive staining (Fig. 5.6) to explore the ability of NIRF-IVUS to quantify inflammatory progression in human atherosclerosis (see section 5.2.5).

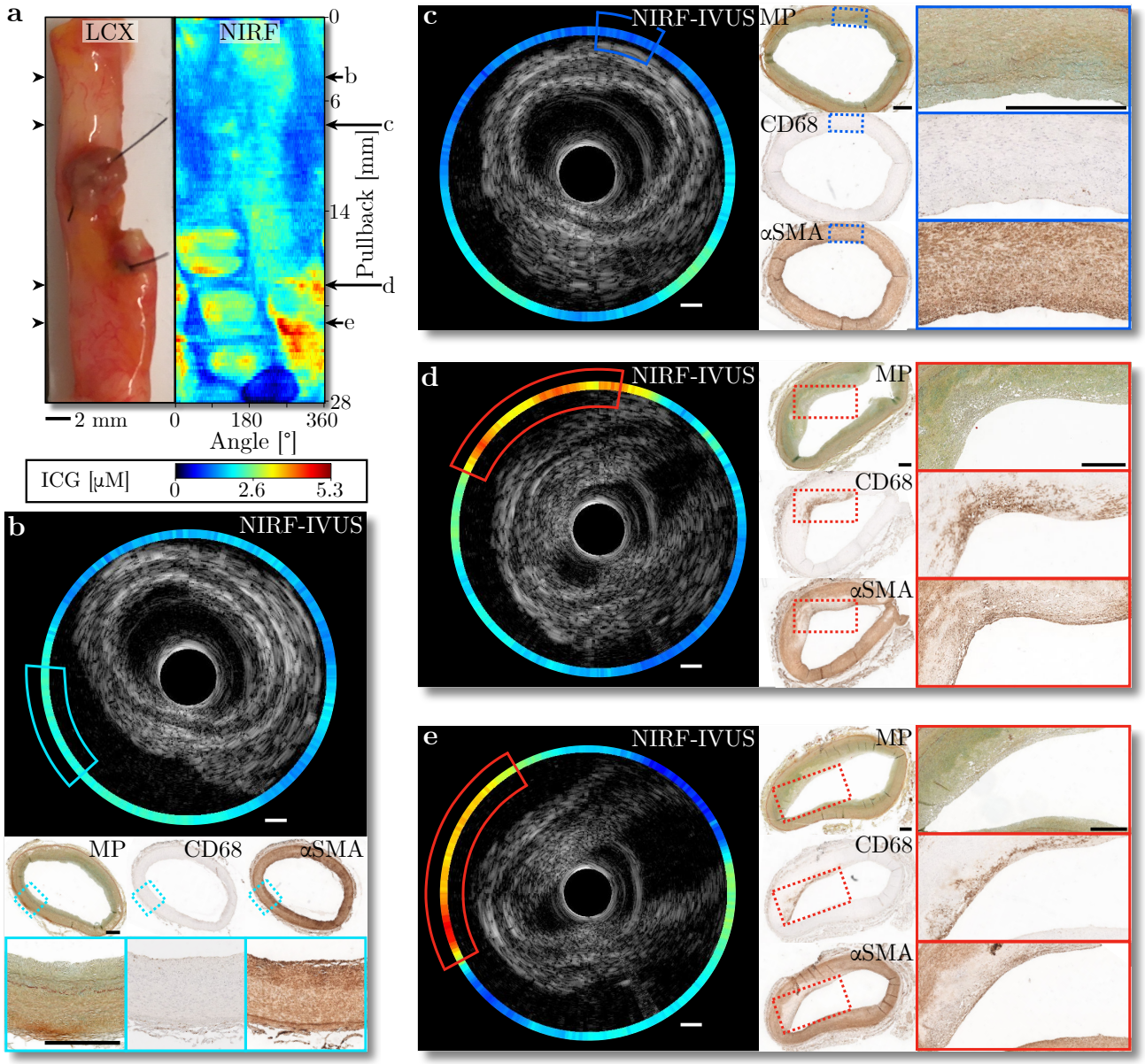

Figure 5.5: Intravascular NIRF-IVUS imaging of healthy tissue and early atherosclerotic lesions in a human coronary artery. a - Picture and corresponding NIRF map of an ICG-perfused Left Anterior Descending (LAD) artery; **b-c** - Low NIRF signal in healthy tissue regions as validated by MP, CD68 and αSMA staining; **d-e** - High NIRF signal in early lesions showing subendothelial macrophage infiltration (foam cell formation) as validated by MP, CD68 and αSMA staining. In all panels: NIRF: Near-infrared Fluorescence; IVUS: Intravascular Ultrasound; MP: Movat Pentachrome; αSMA: alpha-smooth muscle actin; ICG: Indocyanine Green. Scale bars: 500 μm.

Figure 5.6-a shows an exemplary NIRF-IVUS frame acquired during imaging of an artery segment of a LCX. Figure 5.6-b displays the original image of a histology section which was co-registered with the exemplary NIRF-IVUS imaging frame (shown in Fig. 5.6-a) and stained with CD68 highlighting the presence of macrophages (Brown signal). The segmented lumen is outlined in red, and the CD68-positive pixels are indicated as white pixels in the binarized histology image (Fig. 5.6-c).

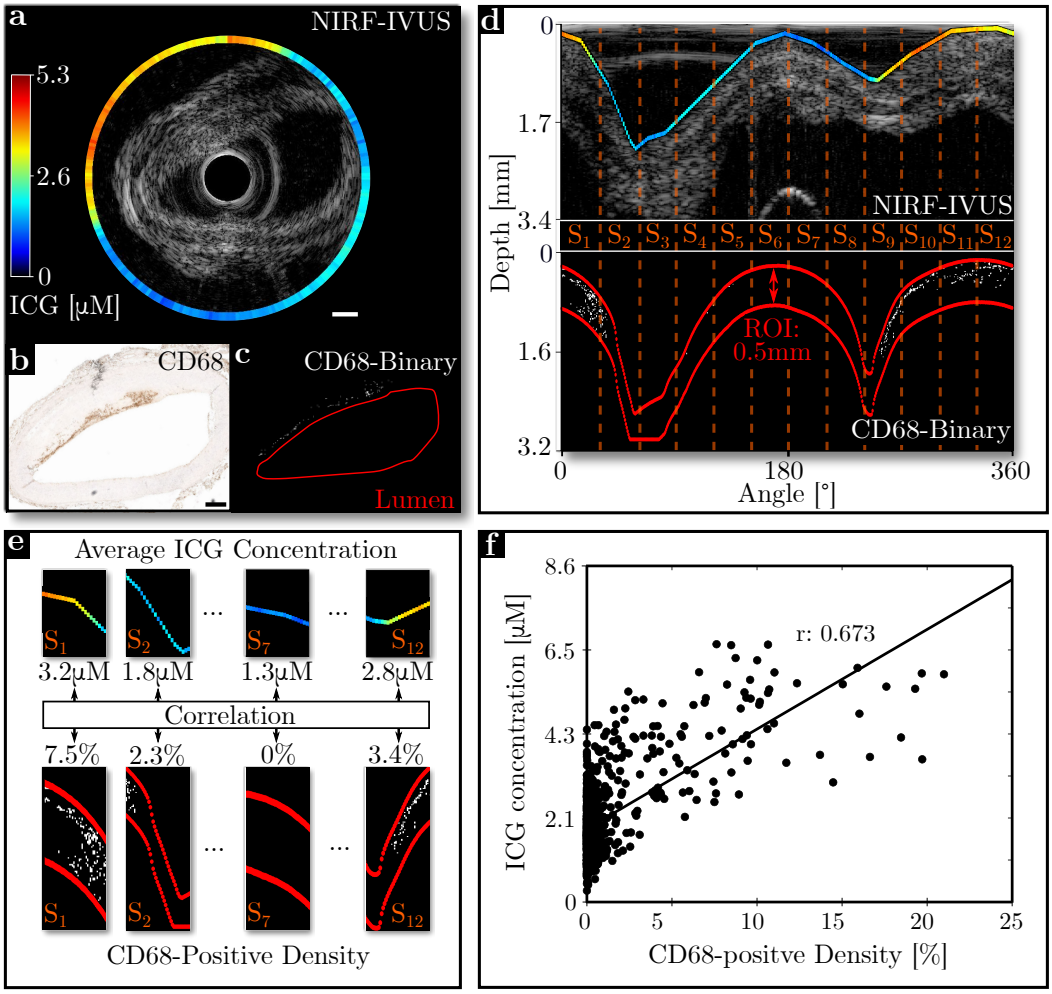

Figure 5.6: Correlation of quantified ICG concentration by NIRF-IVUS to corresponding density of CD68 positive staining indicative for macrophage burden in coronary lesions. **a** - Exemplary NIRF-IVUS frame of ICG-perfused coronary artery in cartesian coordinates; **b** - Matching histology section of CD68-staining in cartesian coordinates; **c** - Converted binary image of histology section showing white pixels as CD68 positive and black pixels as CD68 negative; **d** - Co-registration between NIRF data, projected on the corresponding IVUS image, and binary image of matching CD68 histology section in polar coordinates indicating the ROI defined as 0.5 mm tissue depth measured from the lumen; **e** - Correlation between average ICG concentration and density of CD68-positive binary signal in the ROI per 30° tissue sectors (S_1-S_{12}); **f** - Significant positive correlation between quantified ICG concentration and corresponding density of CD68 positive staining indicative for macrophage burden in coronary lesions; Pearson correlation coefficient, r, calculated with N=792 and $p<0.01$; Line of identity shown in black; In all panels: NIRF: Near-infrared Fluorescence; IVUS: Intravascular Ultrasound; ROI: Region of Interest; ICG: Indocyanine Green; Scale bars: 500 μm.

Transformation of the images from cartesian (shown in Fig. 5.6-a-c) to polar coordinates enabled to i) define a region of interest (ROI) measuring 0.5 mm in depth in the binarized image of the histology section, ii) divide the NIRF and histology data into co-registered 30° sectors (Fig. 5.6-d) and iii) calculate the density of CD68-positive pixels in the ROIs to correlate them to the average ICG concentration detected per sector (Fig. 5.6-e). We found a significant and strong positive correlation (r=0.673, $p \leq 0.01$) between detected ICG concentration and calculated

CD68-positive density for all sectors (n=792) defined in every coronary artery segment included in this analysis (Fig. 5.6-f).

5.3.4 Correlation of Intravascular NIRF-IVUS Signals to the Pathological Scoring of Coronary Artery Tissue

Finally, the detected ICG concentration was correlated to pathological scoring on basis of 30° sectors in histology sections for all coronary arteries imaged in this study (Fig. 5.7).
Exemplary NIRF-IVUS frames are shown together with co-registered histology sections which were stained with MP (Fig. 5.7-a-i). Sectors were identified as healthy (Fig. 5.7-a-b; Light blue box), Xanthoma (Fig. 5.7-c-d; Green box), Fibroatheroma (Fig. 5.7-e-f; Red box), Fibrous/Fibrocalcific plaques (Fig. 5.7g-h; Blue box) and as tissue regions with luminal calcification (Fig. 5.7-i-j; Dark blue box). The average ICG concentration detected was 1.8 µM in healthy sectors (n=486), 2.7 µM in sectors classified as Xanthoma (n=349), 3.2 µM in sectors classified as Fibroatheroma (n=210), 1.9 µM in sectors classified as Fibrous/Fibrocalcific plaques (n=23) and 1.7 µM in sectors classified as luminal calcification (n=19). We found significantly higher ICG concentration in sectors classified as fibroatheroma compared to healthy (°), Xanthoma (**), Fibrous/Fibrocalcific plaques (***) and luminal calcification (°°°). Furthermore, we found significantly smaller ICG concentration in sectors classified as healthy compared Xanthoma (*), in Fibrous/Fibrocalcific plaques compared to Xanthoma (°°) and in areas of luminal calcification compared to Xanthoma (•) (Fig. 5.7-k).

5.4 Discussion and Conclusion

This chapter presents an ex vivo NIRF-IVUS imaging study to i) investigate the correlation of ICG signals to pathological markers of atheroma, ii) demonstrate the potential of NIRF-IVUS for the detection of early lesions, and iii) quantify the dependency of detected ICG concentration to the severity of sub-endothelial inflammation and to the progression of atherosclerotic disease stage over the entire luminal circumference in whole human coronary segments.
The study allowed to confirm previously suggested correlations between detected ICG and pathological markers of atheroma like inflammation, lipid accumulations and signs of endothelial leakage and neovascularization in human coronary arteries for the first time. Furthermore, this study involved tissue which featured a variety of disease stages enabling a comparison of detected ICG concentrations in relation to atherosclerotic progression. A significantly increased ICG concentrations was found in tissue sectors classified as advanced stage, like fibroatheroma (Average ICG concentration = 3.2 µM), compared to early-stage Xanthoma (Average ICG concentration = 2.7 µM) and healthy tissue sectors (Average ICG concentration = 1.8 µM). The detection of healthy artery tissue with NIRF-IVUS was demonstrated specifically when imaging a LIMA bypass which is commonly known for its unique biological properties protecting it from atherosclerosis and, therefore making it a superior choice for coronary artery bypass grafting [98, 99]. The detected ICG concentration averaged over the entire pullback length (38 mm) of th bypass was 33% lower than concentrations found in tissue of other arteries classified as Xanthoma and 44% lower than in tissue classified as fibroatheroma. Additionally, the analysis of this study revealed lower ICG concentrations accumulated in fibrous/fibrocalcific plaques (1.9 µM) and calcified luminal regions (1.7 µM) which supports the hypothesis that macroscopic calcifications block or slow down ICG diffusion mechanisms.

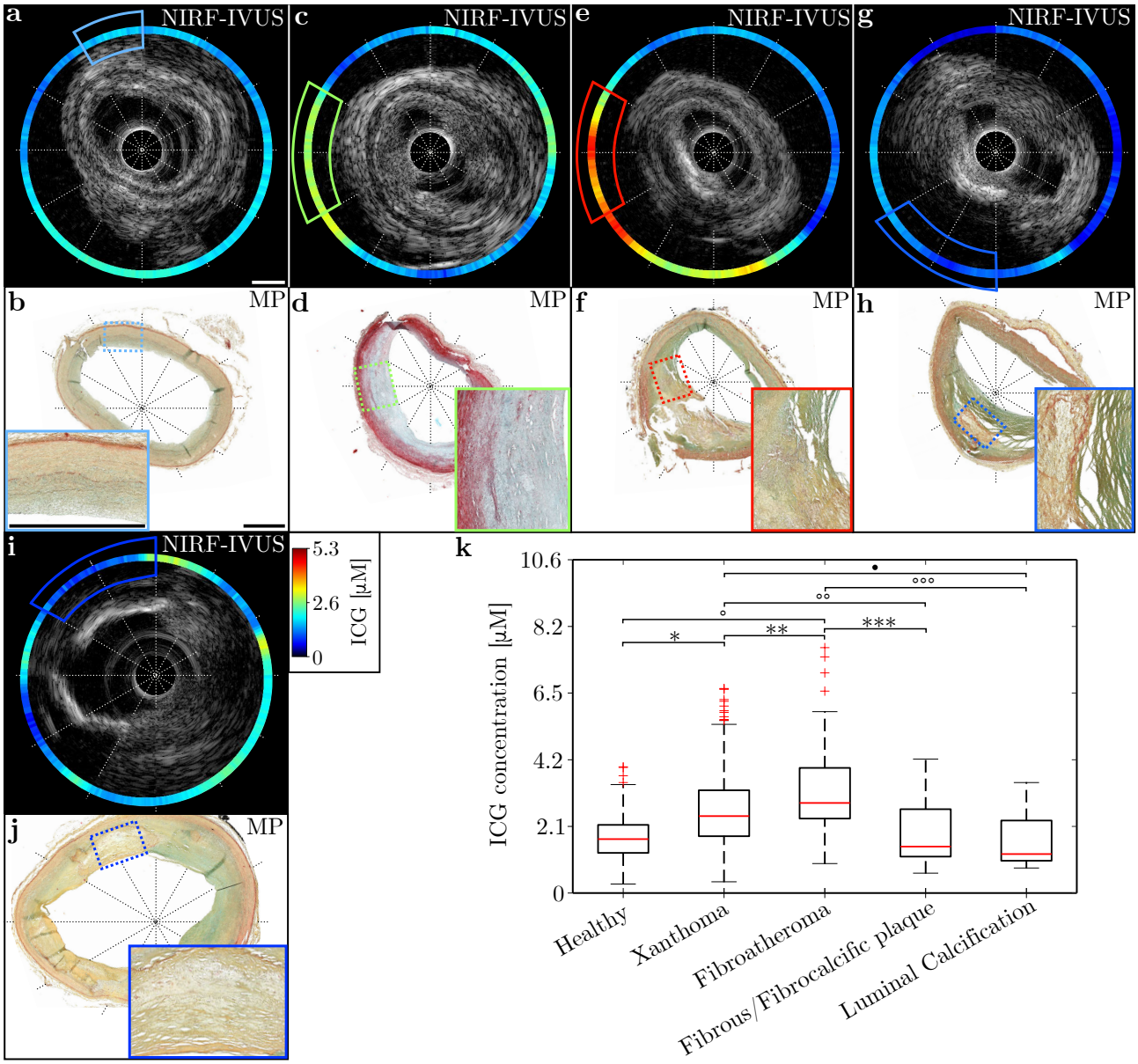

Figure 5.7: NIRF-IVUS quantification of ICG concentration correlates to pathological scoring of coronary tissue evaluated per 30° sections. Exemplary NIRF-IVUS frames with co-registered histological tissue sections stained with MP indicating 30° tissue segments classified as **a-b** - healthy, **c-d** - Xanthoma, **e-f** - Fibroatheroma, **g-h** - fibrous or fibrocalcific plaque, **i-j** - luminal calcification; **k** - Correlation between detected ICG concentration averaged per 30° sector and co-registered pathological classification of the tissue; For all significant differences $p < 0.01$ as calculated by two-sample t-test; Median indicated as red line; Outliers indicated as red crosses; In all panels: NIRF: Near-infrared Fluorescence; IVUS: Intravascular Ultrasound; MP: Movat Pentachrome; ICG: Indocyanine Green; Scale bars: 500 μm.

Overall, these findings demonstrate the potential of NIRF-IVUS to investigate human atherosclerosis with high specificity in combination with ICG suggesting increased NIRF signals in more advanced and potentially vulnerable plaques compared to healthy or fibrous/fibrocalcific plaques which are often regarded as more stable lesions [8, 13, 14]. This is further underlined by preliminary NIRF-IVUS imaging of a stented coronary artery which revealed contrast in ICG uptake between an exposed plaque without stent coverage and tissue regions stabilized by a stent.

Besides aiming for the detection of pathological markers correlated to plaque vulnerability, the identification of early atherosclerotic lesions could be an additional strategy to estimate disease progression and potentially avoid fatal events in the future. Although it is known that not every intracoronary lesion leads to a clinical event, estimation of overall inflammatory burden present in coronary tissue, including early-stage lesions, could help to evaluate the systemic atherosclerotic risk [100]. This study introduces the ability of NIRF-IVUS to provide the imaging contrast required to detect early-stage lesions featuring initial foam cell formation close (ROI: 500 µm measured from lumen) to the leaky endothelium. Estimation of inflammatory burden is further supported by a quantitative analysis which demonstrated that intravascular NIRF-IVUS can quantify ICG concentrations which strongly correlate (r: 0.67) to the severity of macrophage density. This correlation therefore suggests that the analysis of intravascular NIRF signals could be a promising tool for monitoring inflammatory progression in atherosclerosis of coronary arteries.

It must mentioned that this ex vivo imaging study fails to replicate all in vivo conditions like intravascular blood flow and a functional endothelial barrier. While the presence of intravasuclar blood flow attenuates NIRF signals and calls for sophisticated correction methods, the absence of an intact endothelial barrier could potentially be responsible for unspecific ICG uptake resulting in increased NIRF imaging background which was also occasionally observed in this study. However, excision of coronary arteries is not subject of any planned clinical procedure which hinders an ex vivo imaging study of whole coronary segments with prior in vivo ICG administration in contrast to a previous study focusing on excised plaques retrieved as the result of planned carotid endarterectomy [85]. It is also hypothesized that the robust NIRF contrast between diseased and healthy tissue found in this cadaver study could even further improve when investigating ICG uptake in functioning coronary arteries in vivo. In this study, an ICG-Lipid-Agar phantom was used to construct a distance-dependent correction model and to correlate NIRF intensities to ICG concentration. Adding lipid as a light scattering element allowed to simulate NIRF measurements of ICG accumulated in the artery wall and plaque tissue more closely than ICG measurements in a non-diffuse environment like saline or DMSO. This approach could be further refined in the future by characterizing and adapting the presented proof-of-concept phantom to match the optical properties expected in coronary plaque tissue more accurately.

Ultimately, the findings of this work must be evaluated during a large-scale in vivo human imaging study using a clinical dose of ICG to detect NIRF signals through intravascular blood flow and correlate them to suggested pathological markers.

Chapter 6

Correction of Intravascular NIRF signals for Attenuation by Blood

6.1 Introduction

Due to reduced light attenuation in the NIR spectral region (Fig. 1.23), NIRF agents can be excited and corresponding signals can be detected through blood as mentioned in section 1.5.4. This advantage can be capitalized when combining intravascular NIRF with IVUS which, in contrast to IVOCT, does not require flushing for blood clearing in the vessel to generate images. However, light attenuation is not constant during the operation of intravascular NIRF imaging through blood which results in corresponding NIRF signal variation. Intravascular NIRF imaging aims to quantify fluorophore concentration in the vascular wall to correlate it to pathological markers of atherosclerosis and potentially to disease progression (see section 5.3.3). Variable intravascular blood attenuation challenges these ambitions because it compromises the dependency between detected NIRF signals and fluorophore concentration in the tissue. Therefore, accurate fluorophore quantification requires a reliable correction method for light attenuation by intravascular blood flow.

In general, light attenuation during intravascular NIRF imaging is dependent on two independent parameters:

1) The distance between the NIRF detector and the vessel wall which contains the fluorophore.

2) The blood attenuation which is influenced by the optical properties of blood at the operating wavelength of NIRF.

In order to address this challenge, the general strategy aims to combine information about the sensor-wall distance and blood attenuation into a correction model to account for the influence of both parameters. However, an accurate correction method needs to take the dynamic nature of both parameters into account. This variability is explained in more detail below.
Due to the anatomy of coronary arteries with typical variations in lumen diameter, curvatures of the vessel outline and the vessel motion caused by the heart beat, the distance between the NIRF detector and vascular wall changes depending on the angular and axial location of the imaging catheter throughout helical pullback scans. Since NIRF is combined with IVUS in a hybrid imaging catheter, precise co-registration of the two modalities is possible as described throughout this thesis. Analysis of co-registered IVUS images enables accurate measurements of the distance between the NIRF detector and the vessel wall throughout the rotation of every imaging

frame as demonstrated in this work (see chapter 5) and previous publications [86,88–90,101,102].

The optical properties of blood are dependent on a variety of parameters which could potentially influence overall blood attenuation during intravascular NIRF measurements. Figure 6.1 provides an overview of these parameters including variations of hematocrit [102], fluctuations in blood flow [103,104] as a function of vessel type, intravascular location, and pathological state [105], osmolarity influencing the shape of erythrocytes [104] and hemoglobin oxygenation [106].

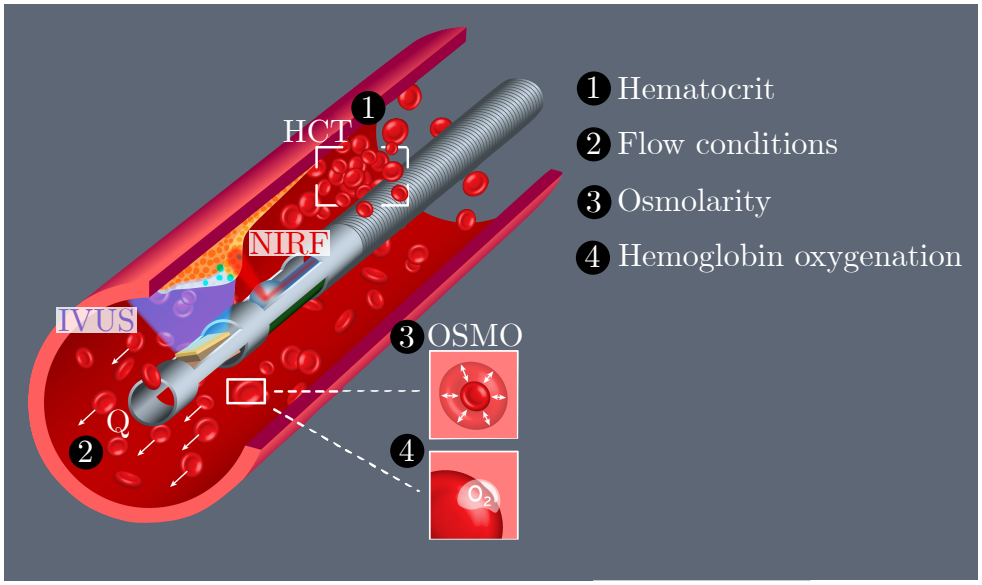

Figure 6.1: Parameters influencing intravascular blood attenuation.

Due to the presented dependencies, blood attenuation can be regarded as a variable process with spatiotemporal properties. When referring to the dependencies introduced in figure 6.1 potential changes can be expected between ex vivo and in vivo imaging conditions, between patients and even over the course of one single imaging pullback.

Previous works estimated blood attenuation by measuring fluorescent targets through blood in phantoms [86,90]. However, ex vivo blood phantom measurements poorly replicate physiological parameters that affect in vivo blood attenuation, while only producing average attenuation values that do not reflect dynamic conditions in vivo [89]. In order to overcome accuracy limitations due to differences in the physical characteristics of ex vivo and in vivo blood, blood attenuation has also been estimated in vivo in pre-clinical models by measuring fluorophores that were injected directly into the outer wall of an animal artery [89]. However, this method was designed for pre-clinical research and has no immediate potential for clinical translation because the direct injection of fluorophore into arterial tissue is not suitable for humans. Arterial fluorophore injection is also limited in pre-clinical studies because the NIRF measurements for estimating attenuation must be acquired in a separate calibration animal instead of the actual target animal, again yielding average attenuation values. Lastly, a method was proposed and tested on excised animal tissue to estimate attenuation factors using simultaneously acquired optoacoustic measurements of blood haematocrit from a hybrid NIRF-IVUS-optoacoustic imaging catheter [102]. However, haematocrit may not account for all parameters influencing blood attenuation in vivo and, most importantly, adding an additional imaging modality to a NIRF-IVUS catheter increases its complexity, which introduces further challenges to clinical

translation such as decreased sensitivity due to required time separation of signals and increased catheter cross-section required to accommodate larger optical fibres for combined NIRF and optoacoustic measurements.
Thus, current proposed methods for estimating NIRF signal attenuation by blood do not account for all parameters influencing blood attenuation in vivo and provide only average attenuation values which can introduce errors when employed in the correction model, or are unsuitable for clinical application.

6.2 A Fluorophore-coated Guidewire for Correcting Intravascular NIRF Signals for Attenuation due to Blood

Within the scope of this thesis, a new method was developed to address current challenges for correcting NIRF signals for blood attenuation accurately. This new method offers an adaptive correction scheme which is tailored not only to each patient but to each imaging frame collected during the intravascular iamging pullback. In particular, it is hypothesized that a NIRF reference signal could provide means for an accurate attenuation measurements when acquired during the intravascular imaging of the vessel wall. For this purpose, a fluorescent coating could be applied to the guidewire which is used to steer the NIRF-IVUS catheter. The underlying premise is that collection of attenuated NIRF signals from the fluorophore-coated guidewire can be employed to compute a factor describing blood attenuation for each frame location, thus taking into account local and general blood attenuation characteristics. It is then proposed to combine this position-(frame-)dependent blood attenuation with NIRF detector-to-vessel wall distance computed on basis of IVUS data to create an accurate correction scheme for intravascular NIRF imaging. The strategy was motivated by the recent development of biocompatible fluorescence coatings [107, 108] that could lead to a viable solution for the clinical application of such a correction scheme.

6.2.1 Methods

6.2.1.1 Data Acquisition and Guidewire Coating

All data of this chapter were acquired with a 3.2F ball lens catheter at 60 rpm rotation speeds and 0.25 mm/s pullback speeds. In order to create a reference for intravascular NIRF measurements,

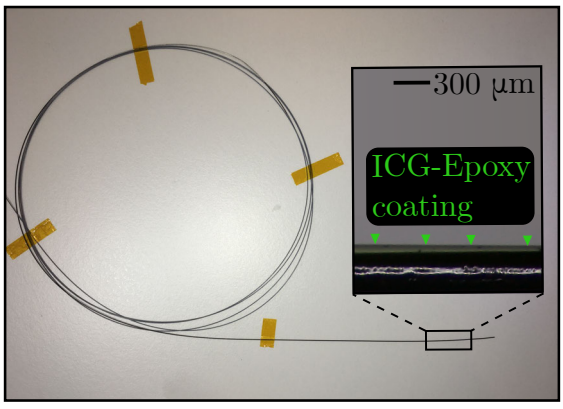

Figure 6.2: Fluorophore-coated guidewire.

a ICG-epoxy coating was applied to a standard clinical guidewire with a 0.35 mm diameter (PT^2 Moderate Support, Boston Scientific Corporation, Marlborough, MA, USA) as described in the following. A solution of ICG and standard epoxy resin was prepared by mixing both components at a ratio to create an ICG concentration of 50 µM. After approx. 5 min of curing the mixture developed a higher viscosity and was then filled into a glass capillary with two open ends. Next, the guidewire was slowly pulled through the capillary to deposit a thin (45 μm) and homogeneous layer of the ICG-epoxy mixture. Finally, the ICG-epoxy mixture on the guidewire was cured at room temperature for 1 hour to afford the fluorescent coating (Fig. 6.2).

6.2.1.2 Calibration Measurements

The correction method consists of a calibration step (Fig. 6.3-a), which is performed once for every guidewire prior to tissue measurements (Fig. 6.3-b). For this calibration step, the fluorophore-coated guidewire was measured through water in a phantom with varying distances (0.1 to 1 mm) between the guidewire and the catheter sheath wall to

i) calculate a correction factor for water (C_w, eq. 6.1) and

ii) construct a look-up-table containing NIRF signals for variable distances.

The water correction factor was used to account for NIRF signal loss between the NIRF sensor and the sheath wall (Fig. 6.3-c, eq. 6.2-6.3) and between the sheath wall and tissue to calculate ground truth values (Section 6.2.1.3, 6.2.1.4, eq. 6.6). The data from the look-up-table served as reference values to calculate a correction factor for blood attenuation (C_b, eq. 6.4). The calibration phantom can be described as a 3D printed reservoir which was 26x21x18 mm (LxWxH) in size and featured designated placeholders that allowed the guidewire to be angled relative to the imaging catheter to create varying distances between the guidewire and the catheter sheath wall (Fig. 6.3-a).

6.2.1.3 Ex Vivo Tissue Measurements

A fresh pig heart was collected from a butcher shop and a 40 mm segment of the right coronary artery with an inner diameter of approximately 2.8 mm was excised and positioned into a designated perfusion holder (Fig. 6.3-d). An aqueous solution of ICG (38 μM) was injected into the media layer of the artery to create a localized target fluorescence signal in the tissue. The fluorophore-coated guidewire (described in 6.2.1.1) was inserted into the vessel lumen first, followed by the imaging catheter. By inserting the guidewire into an opening at the distal end of the catheter sheath, the imaging catheter was guided to its starting position for imaging next to the guidewire, similar to the configuration in standard clinical interventions (see Fig. 6.3-b). Figure 6.3-d shows the ROI visualizing the location of fluorophore injection and the segment for final data analysis. Two NIRF-IVUS pullbacks of the artery were performed in a water bath while perfusing it once with water (as a control) and once with a solution of 75% blood diluted with an isotonic solution of aqueous 0.9% NaCl (Fig. C.1). Finally, the attenuated NIRF maps were corrected frame-by-frame by using the NIRF reference signals acquired from the guidewire as described in section 6.2.1.4.

In order to evaluate the quantification accuracy of the method, the quantified ICG concentrations obtained after correction of blood attenuation were compared to the ground truth values calculated from the control measurements through water (Section 6.2.1.2, eq. 6.6) for every data point in the NIRF map exceeding the background noise which was defined as values with SNR>2.

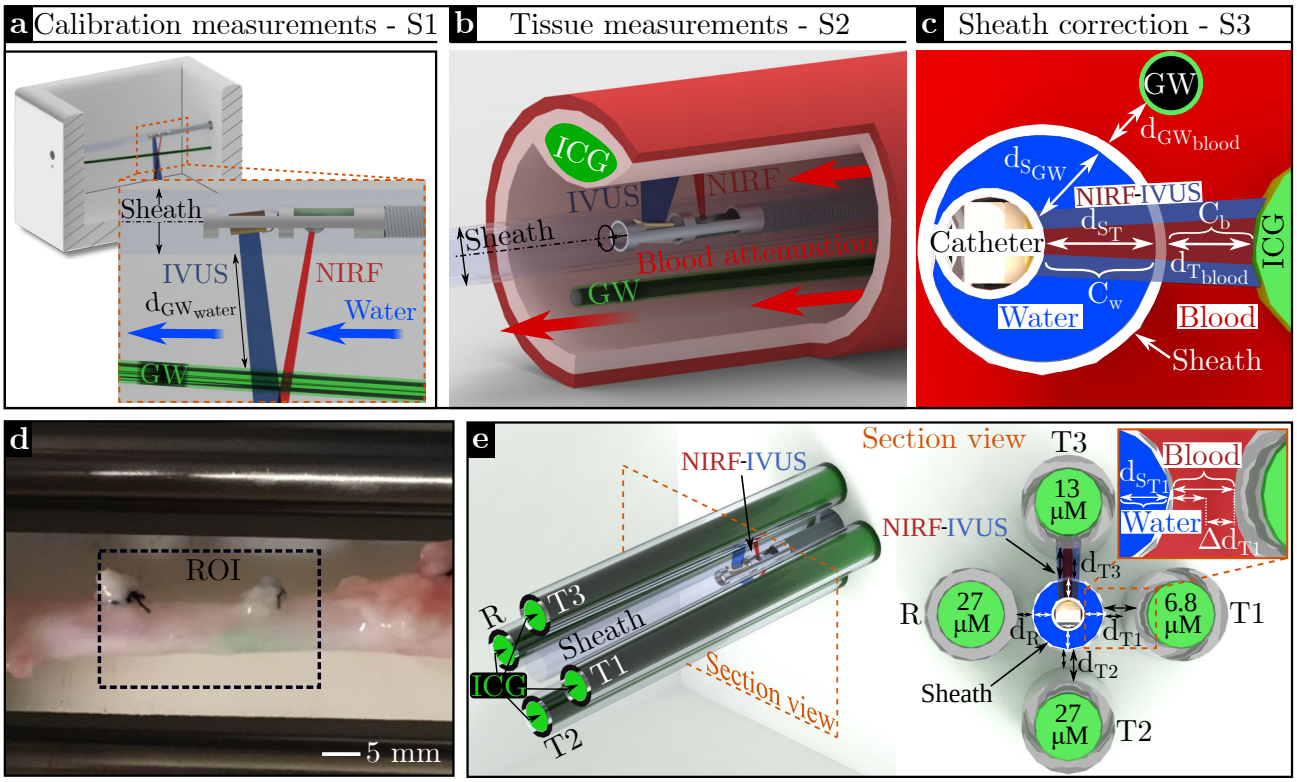

Figure 6.3: Fluorophore-coated guidewire - Methods. a - Schematic of the calibration phantom used to obtain NIRF-IVUS measurements of the fluorophore-coated guidewire at variable distances (sheath-guidewire distances, $d_{GW_{water}}$ in water) to provide a correction factor for NIRF signal loss in water (C_w, eq. 6.1) and construct a look-up-table containing NIRF reference signals; **b** - Schematic of an intravascular measurement of an ICG-injected artery perfused with blood, with the adjacent fluorophore-coated guidewire providing reference signals for the calculation of frame-by-frame correction factors for NIRF attenuation in blood (C_b, eq. 6.4). **c** - Cross-sectional schematic of an intravascular measurement showing the distances between the catheter and the sheath ($d_{S_{GW}}$ and d_{S_T}, used to correct for signal loss in water within the sheath see eq. 6.2-6.3), the sheath and the guidewire $d_{GW_{blood}}$ and the sheath and the tissue $d_{T_{blood}}$ containing ICG; **d** - Image of an ICG injected porcine coronary artery indicating region of interest (ROI) for imaging and correction analysis; **e** - Schematic of the capillary phantom. The phantom contains 3 different target capillaries (T1-3) and a reference (R) capillary that simulates the fluorophore-coated guidewire, each filled with solutions of ICG at different concentrations. The target capillaries are positioned at variable distances (d_{T1-3}) creating a range (Δd_{T1-3}) and the reference capillary at a fixed distance (d_R) from the catheter sheath. All capillaries are exposed to signal loss in water (C_w) inside the sheath ($d_{S_{T1-3}}$,d_{S_R}) and attenuation due to blood (C_b) outside the sheath; In all panels: NIRF: Near-infrared fluorescence; IVUS: Intravascular ultrasound; ICG: Indocyanine green; GW: guidewire; ROI: Region of interest.

6.2.1.4 Fluorescence Signal Correction

Before the individual steps of the correction methods are described in more detail, additional points must be clarified:

1. The fluorophore-coated guidewire was measured concurrently with the vessel wall to enable readouts that accurately depict the true distribution of ICG in the tissue. The necessity and general concept of using references to achieve standardization and more accurate

measurements in fluorescence imaging has been previously described [109].

2. The same fluorophore (ICG) was used to coat the guidewire and to create target signals via tissue injection which allowed to transfer corrected NIRF signals of the tissue from intensity to concentration values as described in S5.

3. Light attenuation by blood in intravascular fluorescence imaging was modelled as an exponential function of the distance between the outer wall of catheter sheath and the vessel wall or fluorophore-coated guidewire as previously demonstrated [86, 88–90, 102].

4. The NIRF signals of the guidewire were segmented from tissue signals using the co-registered IVUS data. This allows to distinguish NIRF signals of the guidewire from signal of the tissue even though intravascular NIRF signals only provide one dimensional information on location (Angle) and lack depth information.

Correction factors for blood attenuation were calculated for each frame (see details below) by comparing NIRF signals of the guidewire acquired during the tissue measurements through blood to the reference values obtained during the calibration measurements through water. Fluorophore concentrations in the tissue were calculated using these blood correction factors and the known distances between the catheter and the artery wall (manually delineated in co-registered IVUS frames). In all calculations, the NIRF signal loss in the water-filled gap between the NIRF sensor and the catheter sheath is accounted for. The steps of the correction method for a typical measurement are described in detail below (S1-S5):

S1) First, an imaging pullback is performed with the imaging catheter in a calibration phantom (Section 6.2.1.2) to obtain NIRF-IVUS measurements of the fluorophore-coated guidewire through water at variable distances (Fig. 6.3-a). For each frame acquired during the imaging pullback, the average intensity value for the guidewire was obtained from the NIRF modality ($I_{GW_{water}}$) and the distance between the guidewire and the sheath wall ($d_{GW_{water}}$) was calculated from the co-registered IVUS modality. Using the intensity and distance values obtained from an entire imaging pullback in the phantom, a correction factor for the signal loss during water measurements (C_w $[mm^{-1}]$) was extracted using an exponential fitting model (Eq. 6.1):

$$I_{GW_{water}} = I_{0_{GW_{water}}} * e^{-C_w * d_{GW_{water}}} \tag{6.1}$$

where $I_{GW_{water}}$ is the measured intensity of the guidewire in water and $I_{0_{GW_{water}}}$ is the incident intensity determined by the model fit.

S2) Next, the same catheter and guidewire from S1 are inserted into an ex vivo coronary artery and an imaging pullback during blood perfusion (Fig. 6.3-b, section 6.2.1.3) is performed. For each frame acquired during the imaging pullback, the average intensity value for the guidewire ($I_{GW_{blood}}$) and many intensity values for the ICG-injected tissue ($I_{GT_{water}}$) were obtained from the NIRF modality. Furthermore, the distances between the NIRF detector and the sheath wall at the angular locations of the guidewire ($d_{S_{GW}}$) and the tissue (d_{S_T}) through water and the distances between the sheath wall and the guidewire ($d_{GW_{blood}}$) and tissue ($d_{T_{blood}}$) through blood were calculated from the co-registered IVUS modality (Fig. 6.3-c).

S3) The propagation of NIRF signals through both blood ($d_{GW_{blood}}$ and $d_{T_{blood}}$) and water ($d_{S_{GW}}$) and d_{S_T}) was considered first, before the values obtained in S1 and S2 could be applied to correct the tissue signals ($I_{T_{blood}}$) for attenuation by blood. This two media-propagation trough

water and blood was accounted for by removing the water's contributions to the signals using C_w, as shown in eq. 6.2-6.3:

$$I_{T^*} = I_{T_{blood}} * e^{-C_w * d_{S_T}} \tag{6.2}$$

$$I_{GW^*} = I_{GW_{blood}} * e^{-C_w * d_{S_{GW}}} \tag{6.3}$$

where I_{T^*} and I_{GW^*} is the water-corrected NIRF intensity from the tissue and guidewire, respectively.

S4) Next, a correction factor for blood attenuation (C_b $[mm^{-1}]$) was calculated for each frame of the artery measurement using the water-corrected intensity of the guidewire (I_{GW^*}) and the intensity of the guidewire acquired in the calibration measurement ($I_{GW_{water}}$) at the same distance from the sheath ($d_{GW_{blood}}$= $d_{GW_{water}}$), while assuming equal incident intensities ($I_{0_{GW_{water}}}$= $I_{0_{GW_{blood}}}$); eq. 6.4).

$$C_b = \frac{log(\frac{I_{GW_{water}}}{I_{GW^*}})}{d_{GW_{water/blood}}} - C_w \tag{6.4}$$

S5) Finally, the water-corrected NIRF intensities from the tissue for each frame (I_{T^*}) were corrected for the signal attenuation from blood using the corresponding frame-specific correction factor for blood attenuation (C_b), as shown in eq. 6.5:

$$I_{T^{**}} = I_{T^*} * e^{C_b * d_{T_{blood}}} \tag{6.5}$$

where $I_{T^{**}}$ is the final blood-corrected NIRF intensity of the tissue and $d_{T_{blood}}$ is the distance between the sheath wall and the tissue containing the ICG. The NIRF intensities from the tissue acquired during the control measurements ($I_{T_{water}}$) were corrected for the signal loss during water measurements using the respective water correction factor (C_w) for that frame (eq. 6.6):

$$I_{GT} = I_{T_{water}} * e^{C_w * (d_{T_{water}} - d_{S_T})} \tag{6.6}$$

where I_{GT} is the ground truth NIRF intensity of the tissue and $d_{T_{water}}$ is the distance between the outer sheath wall and the tissue containing the ICG through water. The conversion of $I_{T^{**}}$ and I_{GT} to ICG concentrations was estimated by using I_{GW^*} as a reference and correlating it to the known ICG concentration in the guidewire coating.

6.2.1.5 Validation of the Method With a Capillary Phantom Experiment

Two phantoms were used to further validate the accuracy and robustness of fluorescence signal correction for variable imaging conditions using a guidewire-like reference signal: 1) a capillary-calibration (calibration measurements) and 2) a target phantom (Fig. 6.3-e). The capillary-calibration phantom replicated the calibration measurements in section 6.2.1.2 and contained only a single capillary filled with 27 µM ICG dissolved in DMSO, which was angled to create imaging distances ranging from 0.45 to 1.6 mm (similar like Fig. 6.3-a). The target phantom simulated NIRF signals at different concentrations and distances using three glass capillaries (25 µl per capillary), which were filled with 6.8 (T1), 13 (T3) and 27 (T2) µM ICG dissolved in DMSO and angled within the phantom to create variable distances (d_{T1-3}) between the wall of the catheter sheath and the targets, ranging from 0.55 to 1 mm (Fig. 6.3-e). A fourth capillary was filled with the same ICG concentration as in the capillary-calibration phantom (27 µM), fixed at 0.45 mm distance (dR), and was used to acquire a frame-by-frame reference (R)

signal. NIRF intensities in both the target and capillary-calibration phantoms were recorded via helical pullbacks similar to the tissue measurements. Recorded NIRF intensities were dependent on the distance between the sheath wall and the capillaries, as well as the distance between the sheath wall and the NIRF detector ($d_{S_{T1-3}}$ and d_{S_R}), see Fig. 6.3-e) as mentioned in section 6.2.1.4.
While the capillary-calibration phantom was imaged through water, the target phantom was imaged through water (as a control) and solutions of blood diluted to 75% and 50% with an isotonic solution of aqueous 0.9% NaCl. The data from the capillary-calibration measurement was fit with an exponential function to model NIRF signal loss during water measurements. Finally, the blood-attenuated intensity of the target capillaries within the target phantom was corrected by using the reference signal as described in section 6.2.1.4 and the agreement of the corrected intensities with the ground truth values calculated from the control measurements through water (similar like in section 6.2.1.4, eq. 6.6) was compared to estimate the correction accuracy. Furthermore, corrected NIRF intensities were correlated to ICG concentrations to estimate the accuracy of fluorophore quantification.

6.2.2 Results

6.2.2.1 Correcting Signal attenuation by Blood in Tissue Measurements Using a Fluorophore-coated Guidewire as a Reference

Figure 6.4 shows NIRF-IVUS measurements of a fluorophore-coated guidewire inside of an ICG-injected ex vivo pig coronary artery (see Methods section 6.2.1.3) that was perfused alternately with blood (Fig. C.1-a) and water (as a control), recorded to assess the feasibility of correcting NIRF signals for blood attenuation on a frame-by-frame basis using the guidewire signal as a reference. Figure 6.4-a displays acquired uncorrected NIRF maps of imaging pullbacks through water and 75%-Blood dilution. As expected, the recorded NIRF intensities were significantly lower in the presence of blood due to increased attenuation when compared to the measurements in water. Furthermore, the fluorescent signals from the guidewire showed variable intensities throughout the pullbacks due to changing distances from the sheath (Fig. C.1-b), as quantified by IVUS (Fig. C.1-c). The intensity distribution of the signal from the ICG in the tissue is affected by both post-injection fluorophore diffusion and variations in sheath-tissue distance. Figure 6.4-b shows the corresponding NIRF maps after correction of the intensities (see Methods section 6.2.1.4 and 6.3-a-c) to afford ICG concentrations throughout the pullback (see colorbar). Figure 6.4-c shows acquired uncorrected and corrected concentration profiles of the guidewire and the tissue from three exemplary frames (Fig. 6.4-a-b, F28, F33 and F40), to more closely evaluate quantification accuracy.
The quantified concentrations based on the corrected water measurements served as the ground truth (see Methods section 6.2.1.3-6.2.1.4, eq. 6.6). The estimated ICG concentrations in blood corresponded well to these ground truth measurements in water for both the signals from the guidewire and the tissue. After correction, the calculated ICG concentrations in the tissue measured through blood were 89% (Variance = 9.6%) accurate on average compared to the measurements through water which yielded an improvement of 2.2-fold compared to uncorrected measurements.

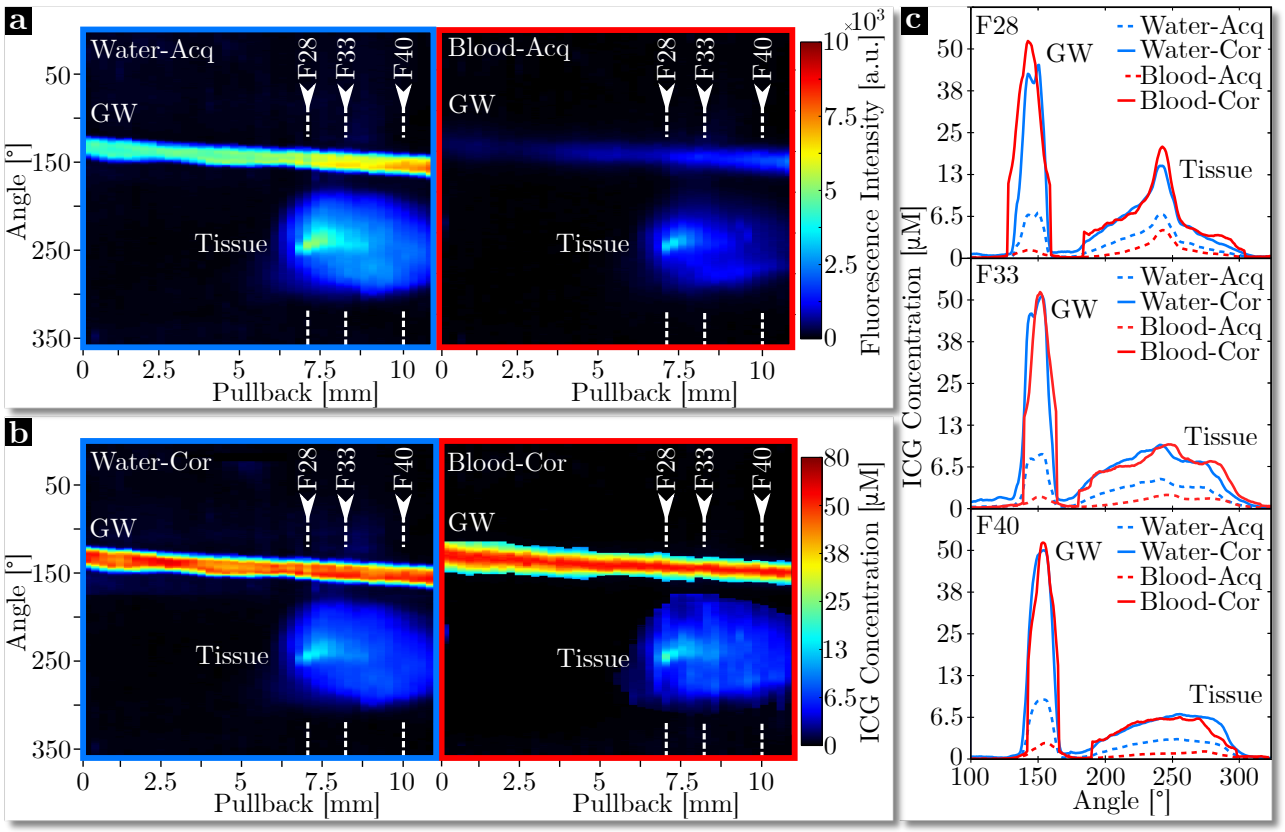

Figure 6.4: Validation of the correction method in an excised pig artery. a - Acquired uncorrected intravascular NIRF maps of an ICG injected porcine artery measured through water and a 75% blood solution, showing NIRF signals from both the guidewire (GW) and tissue; **b** - The same intravascular NIRF maps as in a- after correction showing quantified ICG concentrations; **c** - Selected frames showing uncorrected intensity values and corresponding corrected ICG concentrations for the GW and tissue signals through blood and water; In all panels: ICG: Indocyanine green; GW: Guidewire; Acq: Acquired; Cor: Corrected.

6.2.2.2 Evaluating Attenuation Correction Efficacy Versus Distance and Fluorophore Concentration in a Capillary phantom

Figure 6.5 depicts the results of the capillary phantom experiment, carried out to evaluate the efficacy of using a linear fluorescent reference (similar to a guidewire) to correct for signal attenuation by blood at different distances and ICG concentrations (see Methods section 6.2.1.5). A capillary-calibration phantom that contained only a single reference capillary at an angle afforded distance-controlled measurements for the estimation of correction factors for signal loss during water measurements (C_w, see Methods section 6.2.1.2). The target phantom contained four ICG-filled glass capillaries, three of which served as the fluorescent target signals while the fourth was used as the source of the reference signal (Fig. 6.3-e). The phantoms were filled sequentially with pure water and blood at two dilutions (50% and 75%) and imaged to simulate different degrees of light attenuation. Both phantoms were measured with a helical pullback scan using a 3.2F NIRF-IVUS catheter.

Pullback measurements of the capillary-calibration phantom afforded dozens of data points (Intensity values averaged per frame) at distances of 0.5 mm to 1.6 mm from the sheath wall. These data points were fit with an exponential function to retrieve a correction factor in water (Fig. C.2-a; R^2 for fit, 0.99). The fitted exponential functions indicate increasing attenuation

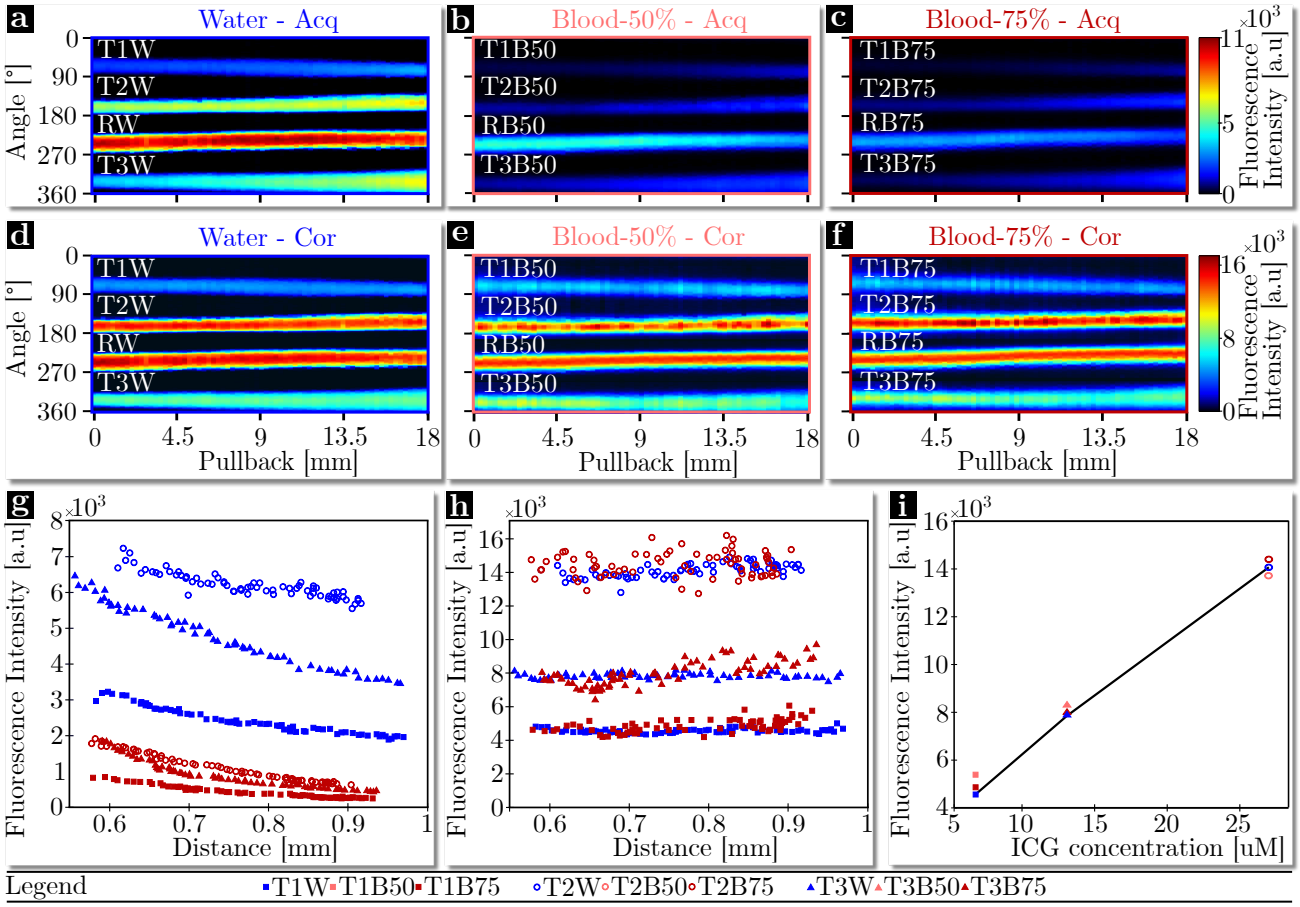

Figure 6.5: Validation of correction method in capillary phantoms: Acquired uncorrected NIRF maps of reference and target capillaries measured through **a** - water, **b** - 50% blood, and **c** - 75% blood; Corrected NIRF maps of reference and target capillaries measured through **d** - water, **e** - 50% blood, and **f** - 75% blood; **g** - Acquired uncorrected NIRF intensities from the target capillaries measured in the target phantom through water (T1-3W) and 75%-blood mixture (T1-3B75) plotted versus imaging distance between the sheath wall and capillary; **h** - Corrected NIRF intensities ($I_{T^{**}}$) from the target capillaries measured in the target phantom through water (T1-3W) and 75%-blood mixture (T1-3B75) plotted versus imaging distance between the sheath wall and capillary; **i** - Quantification of ICG concentration via corrected NIRF intensities ($I_{T^{**}}$, averaged per pullback) of the 3 different target capillaries measured through water, 50% blood, and 75% blood; Annotation key: Acq: Acquired; Cor: Corrected; T1-3W: Target capillaries 1-3 measured in water; T1-3B50: Target capillaries 1-3 measured in 50% blood mixture; T1-3B75: Target capillaries 1-3 measured in 75% blood mixture; RW: Reference capillary measured in water; RB50: Reference capillary measured in 50% blood mixture; RB75: Reference capillary measured in 75% blood mixture; ICG: Indocyanine green.

with increasing distance. The average correction factor for water measurements (C_w) was estimated to be 0.0009 mm^{-1}.

Figure 6.5-a-c displays acquired uncorrected NIRF maps of the reference capillary (R-) and all three target capillaries (T1-3-) acquired throughout the pullback of the target phantom when measured through water (RW, T1-3W), the 50% blood dilution (RB50, T1-3B50) and the 75% blood dilution (RB75, T1-3B75). As expected, fluorescence intensities decreased with increasing blood content and the concomitant increase in light attenuation.

Subsequently, averaged intensity values of the reference capillary (substituting for the guidewire)

recorded during target measurements at distances ranging between 0.43 to 0.53 mm in blood (RB50 and RB75, Fig. 6.5-b-c and Fig. C.2-b) were used to quantify C_b, (see Methods section 6.2.1.4). The average correction factors for the blood measurements were 0.0028 mm^{-1} and 0.0034 mm^{-1} for the 50%-Blood ($C_{b50\%}$) and 75%-Blood ($C_{b75\%}$) dilutions, respectively (Fig. C.2-c). These calculated values agree well (98% accuracy) with extracted correction factors ($C_{b50\%} = 0.0028\ mm^{-1}$; $C_{b75\%} = 0.0033\ mm^{-1}$) from a model fit ($R^2$ for fits, 0.99) applied to validation measurements of a capillary, containing the same ICG concentration as the reference, imaged in the capillary-calibration phantom at distances of 0.5 mm to 1.6 mm from the sheath wall through 50%-Blood and 75%-Blood dilutions (Fig. C.2-d). The variance of the calculated blood correction factors over all imaging frames in the target phantom was found to be 4.8% and 2.8% for calculated Cb50% and Cb75%, respectively.
Finally, we evaluated the correction accuracy of our method by applying the calculated blood correction factors ($C_{b50\%}$, and $C_{b75\%}$) to correct the NIRF signal intensities from the target capillaries, which were compared with the ground truth values measured in water. Figure 6.5-d-f display corrected NIRF maps of the reference capillary, and three target capillaries measured through water, 50%-blood, and 75%-blood. Because the target capillaries were angled within the phantom (see Methods section 6.2.1.5), their uncorrected NIRF intensities were acquired at distances ranging from 0.55 to 1 mm from the sheath wall to the capillary, resulting in average variances of 13% in water, 32% in 50%-blood, and 39% in 75%-blood. Furthermore, the acquired uncorrected NIRF intensities of target capillaries containing the same ICG concentration measured through 50%-blood (Fig. 6.5-b and Fig. C.2-e) and 75%-blood (Fig. 6.5-c,g) did not agree with measurements in water (Fig. 6.5-a,g and Fig. C.2-e) due to varying NIRF attenuation. In contrast, corrected NIRF intensities of all target capillaries through both 50%-blood (Fig. 6.5-e and Fig. C.2-f) and 75%-blood (Fig. 6.5-f,h) show good agreement with the corrected water measurements (Fig. 6.5-d,h and Fig. C.2-f) over all acquired frames and imaging distances. Additionally, we observed that the average variances of the corrected intensities over all imaging frames decreased by 10% for the water measurements, 23% for the 50%-blood measurements, and 31% for the 75%-blood measurements. Finally, Fig. 6.5-i compares quantified ICG concentrations converted from corrected NIRF intensities of the blood measurements of the 3 target capillaries with the ground truth, which shows that our method achieved an average accuracy of 91% (average variance = 4.3%) which is a 4.5-fold improvement over uncorrected measurements.

Furthermore, we sought to quantify the impact of correcting for sensor-to-sheath distance by calculating the difference in intensity-quantification accuracy if signal loss inside of the sheath is neglected. For this analysis we used the measurements through the 75% blood mixture. Due to natural bending of the probe, the distance between the sensor and the wall of the sheath varies at the angular locations of the different target capillaries ($d_{S_{T1-3}}$), as seen both in an exemplary IVUS frame (Fig. C.3-b) and quantified distances from an entire pullback (Fig. C.3-c). Figure C.3-d shows corrected NIRF intensities of the target capillaries measured through blood with and without additional correction for sensor-to-sheath distance. Sheath-corrected intensities agree better with the ground truth values than the uncorrected intensities. Figure C.3-e shows that accuracy in ICG quantification improved by 10% for T1, 5% for T3, and 19% for T2, which provides evidence that the additional sheath correction becomes more relevant with increasing sensor-to-sheath distances ($d_{S_{T3}} < d_{S_{T1}} < d_{S_{T2}}$), see Fig. C.3-c). Moreover, the variances of the blood-corrected intensities decreased or were unchanged when additional sheath-correction was applied (-2% for T1, 0% for T2 and -5% for T3).

6.3 Discussion

NIRF-IVUS imaging has the potential to improve assessment of coronary plaques by quantifying intravascular NIRF tracers located in the artery without the need for saline flushing, however this necessitates the accurate correction of blood attenuation for acquired NIRF signals. The work of this chapter demonstrated that a fluorophore-coated coronary guidewire could be employed as a NIRF reference to facilitate the accurate frame-by-frame correction of NIRF signals through blood during ex vivo intravascular measurements. The major advantage of this approach is that it can account for the spatiotemporal variations of intravascular blood attenuation by enabling the estimation frame-specific blood-attenuation correction factors, overcoming the limitations of previous methods that calculated average corrections factors [86, 87, 89, 90].

Results of this proof-of-concept study show it is feasible to calculate correction factors for different levels of blood attenuation from NIRF reference signals that are simultaneously acquired to tissue or phantom measurements. In an ex vivo porcine coronary artery perfused with 75% blood dilution, the method enabled the quantification of ICG within the arterial wall with an average accuracy of 89% compared to ground truth measurements in water. Consistent quantification accuracy was found throughout the pullback (Variance = 9.6%) for variable guidewire positions ranging from 0.5 to 0.85 mm (Fig. C.1-b) within an arterial lumen similar in size to human coronary arteries. Furthermore, phantom capillary experiments demonstrated that the method has the potential to achieve quantification accuracies as high as 91% with variances as low as 4.3% for a range of ICG concentrations (6.8, 13 and 27 µM) and for different attenuation conditions (50% and 75% blood dilutions). The higher and more consistent accuracy results from the capillary experiments compared to the tissue experiments (accuracy: 91% vs 89% and variance: 4.3% vs 9.6%) can be explained by higher variations in the corrected intensities of the guidewire compared to the reference capillary (7% vs 2.9%). Therefore, while the proof-of-concept guidewire afforded high quantification accuracy, the capillary experiments suggest that increasing the homogeneity and stability of the fluorescent coating could yield more accurate blood correction factors. Lastly, it was found that the accuracy of ICG quantification was independent of the distance from the catheter sheath to the fluorescent target, as shown for distances ranging from 0.09 to 0.4 mm in the tissue and 0.55 to 1 mm the capillary experiments. ICG concentrations as low as 3.7 µM were detected and quantified in the tissue (Fig. 6.4) and 13 µM in the capillary experiment (Fig. 6.5 and Fig. C.2) through blood at maximum distances of 0.4 and 1 mm, respectively.

A two-media model was used to account for NIRF signal loss in water inside of the catheter sheath and blood attenuation between the sheath and the ICG located in the tissue or capillary. An improvement in ICG quantification accuracy of up to 19% was found for experiments in a capillary phantom when this additional sheath-correction was applied. The overall impact of the sheath-correction depends on the sensor-sheath distance (d_S), as can be observed in the results for the phantom measurements (Fig. C.3-b-e). Because the location of the catheter within the sheath can vary during measurements, this additional correction could greatly improve fluorophore quantification in future intravascular NIRF imaging studies. Previous studies utilized the Twersky model for fluorescence signal correction, which is based on a 2-term exponential function [86, 89, 90, 102]. In this study, a simplified 1-term exponential correction model was employed which was validated for a range of blood attenuation levels by recording NIRF signals from a fluorophore-coated guidewire through different blood concentrations (Fig. C.4). This model, contrary to 2-term exponential models which introduce additional parameters, allows for a unique solution of our derived system of equations for the estimation of blood correction

factors at high post-processing speeds. The method of correcting intravascular NIRF signals is both simple and accurate and has several advantages that could pave the way for in vivo studies and eventual clinical translation. First, all NIRF measurements in this study were carried out using a NIRF-IVUS catheter with dimensions appropriate for human application (see section 6.2.1.1). Second, the method converts the coronary guidewire to an active component of intravascular NIRF-IVUS imaging, rather than a hindrance that blocks tissue signals and leaves a shadow in the data that impedes analysis. Third, high quantification accuracies were achieved using clinically approved ICG as a target fluorophore, despite ICG's low quantum yield (2.9%, [34]), in contrast to other studies which used higher quantum yield NIRF dyes like Alexa680 (36%), Alexa750 (12%) and DiR (25%) [86,89,90,102]. Nevertheless, our method is not inherently limited to the use of ICG, and alternative fluorophores could be employed and tested in the future. Furthermore, the principle of using a guidewire as a reference standard could be translated to other intravascular fluorescence imaging modalities like fluorescence lifetime imaging and near-infrared autofluorescence or alternative optical methods like near-infrared spectroscopy and photo/optoacoustic in combination with a suitable coating [51]. Even when blood is cleared from the vessel during intravascular measurements, an in vivo reference signal could improve standalone or hybrid imaging with IVUS or IVOCT by providing means for calibration, standardization, and quality control.

Some limitations remain to be addressed in future studies. The NIRF-IVUS measurements here were carried out at imaging speeds of 1 fps, which was sufficient for the proof-of-concept but would likely introduce motion artefacts in vivo. NIRF measurements were presented in blood dilutions of 50% and 75% (approx. 20% and 30% haematocrit) instead of whole blood to account for the greater attenuation of ex vivo compared to in vivo blood [89]. In addition, blood attenuation of NIRF signals in vivo might be more dynamic than the ex vivo perfusion used in this work. In vivo studies are needed to ascertain the magnitude of these effects including IVUS distance measurements under beating heart conditions with accuracy sufficient for the proposed correction method. The guidewire in this study was coated with ICG mixed with epoxy incresing its diamter by 25 % on average as a proof of concept. A biocompatible compatible fluorescent coating, such as the combination of cyanine dyes with a biocompatible polymer PMMA [108], must be evaluated to enable in vivo studies, while improving the coating mechanism by i) replacing the existing standard guidewire coating with a thinner fluorescent coating instead of overlaying it and ii) increasing the homogeneity of the coating, could reduce its footprint and yield higher quantification precision.Lastly, similar like in previous studies [81, 86, 88–90, 102], the method considers light attenuation only by intraluminal blood flow and not by plaque tissue. This additional attenuation of NIRF signals could be relevant when detecting fluorophores located in deeper tissue layers, however, previous studies have indicated that attenuation characteristics of plaque tissue is reduced compared to blood [110] and ICG predominantly accumulates in human plaque areas close to the vascular lumen [85]. Furthermore, there is currently no reliable technique that can quantify the distance between the vascular wall and the fluorescent source located in deeper vascular tissue layers using signals recorded with intravascular NIRF-IVUS/IVOCT.

In summary, a new method was developed that utilizes a fluorophore-coated guidewire as a reference to accurately estimate blood attenuation in the form of correction factors on a frame-by-frame basis during intravascular NIRF measurements. The method facilitates correction of NIRF signals and consequent ICG quantification with high accuracy while offering the potential for straight-forward integration into clinical procedures.

Chapter 7

Conclusion and Outlook

The aim of the work presented in this thesis was to provide next steps towards the clinical translation of the intravascular NIRF-IVUS imaging technology. This was achieved by 4 major contributions as illustrated in Fig. 7.1:

1) **Improvements of the NIRF-IVUS imaging system and catheter:** Two miniaturized imaging catheters (3.7F and 3.2F) with corresponding imaging systems were devloped (Chapter 2). Notably, the 3.2F system achieved the size requirements for intracoronary applications in humans. Both imaging systems were thoroughly characterized for intravascular imaging applications with bench top methods and phantom experiments (3). Moreover, the 3.2F system was further improved to enable high-speed imaging for the first time. This can be regarded as an essential achievement since imaging at high frame rates and pullback speeds is a fundamental prerequisite for the clinical translation of NIRF-IVUS imaging in the future.

2) **Pre-clinical in vivo imaging:** The 3.2F system was tested in various atherosclerotic rabbit models in vivo. It was demonstrated that the 3.2F NIRF-IVUS system can detect ICG uptake in atherosclerotic lesions with endothelial injury and foam cell formation in vivo. In addition, high contrast was observed for NIRF imaging of ICG accumulated in atherosclerotic lesions compared to healthy control arteries which is an important finding regarding the in vivo detection efficiency of NIRF-IVUS imaging in combination with ICG.

3) **Human cadaver study:** For the first time, NIRF-IVUS imaging was applied for investigating human coronary arteries which confirmed previously suggested correlations between detected ICG and pathological markers of atheroma like inflammation, lipid accumulations and signs of endothelial leakage and neovascularization. Furthermore, it was demonstrated that NIRF-IVUS could be applied to detect early lesions and quantify the severity of sub-endothelial inflammation and the progression of atherosclerotic disease states over the entire luminal circumference.

4) **Correction of NIRF signals for blood attenuation:** A new method was developed to correct NIRF signals for blood attenuation using a fluorophore-coated guidewire. This new method has the potential to enable more accurate signal correction and ICG quantification while providing a viable solution for clinical application.

These contributions further improved the technical specification of intravascular NIRF-IVUS and demonstrate that this hybrid imaging technology could be a valuable tool to support the assessment of CAD in the clinics. In order to complete the translation of NIRF-IVUS imaging into a clinical environment, future steps are required as outlined in the following (Fig. 7.1):

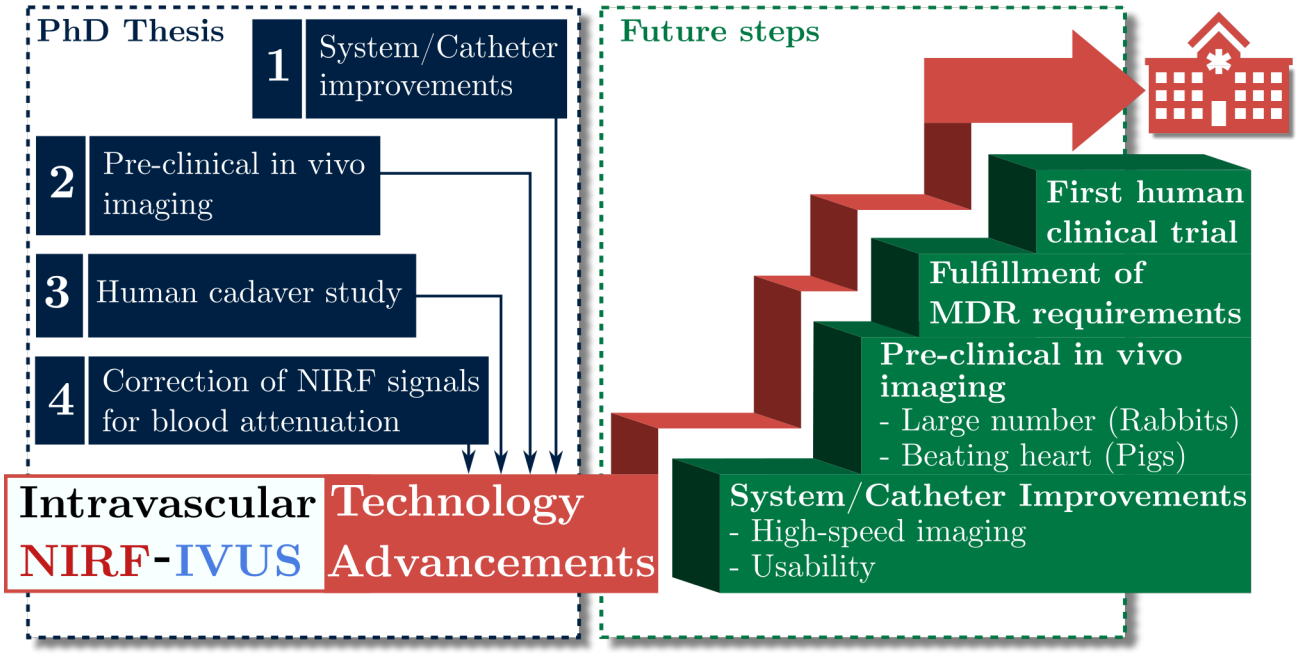

Figure 7.1: Clinical translation of intravascular NIRF-IVUS; MDR: Medical Device Regulations.

1) **Further system and catheter improvements:** Besides the technical improvements suggested in section 3.8, future efforts should target the system's capability for high-speed imaging. While substantial progress has been achieved within the frame of this thesis by enhancing the imaging speed by a factor of 4, additional improvements could further increase the speed (As a reference: Clinical IVUS systems usually operate at 1800 rpm, or 30 fps) and the system's stability during operation. This could be realized by implementing a double-layer torque coil into the catheter design which would improve the transmission of the rotational force from the pullback module to the sensor tip to reduce the catheter's vulnerability towards friction. This design feature has already proven to be successful in commercial high-speed IVOCT systems, especially in the case of catheter bending which is expected when inserting intravascular imaging catheters into coronary arteries in vivo. Moreover, a new rotational motor should be integrated which can provide the required torque to rotate the back-end system and catheter at speeds > 1200 rpm without compromising its accuracy. Finally, the interface between the imaging catheter and the back-end system could be re-designed to enable more coaxial catheter rotation inside the sheath which would further improve image quality.

While the usability of the current system was sufficient for the phantom and pre-clinical experiments described in this thesis, it should be enhanced for potential clinical application. For this purpose, the software could be targeted to improve the GUI and image display. Moreover, the pullback-module should be re-designed to make it more compact and modular which would allow to place it on the surgery table next to the patient as it is common practice for commercially available intravascular imaging systems. Additionally, the adapter for optical connection between catheter and the back-end system should be changed. While the current FC/APC adapter reduces back-reflections especially in low NA fibers (e.g 0.22 used in the catheters and systems presented in this thesis),

they require more time and care for connectorization. Switching to a different connector type, e.g a LC connector, will allow to exchange disposable imaging catheters more easily and faster in a pre-clinical and future clinical environment.

2) **Pre-clinical in vivo imaging:** In vivo imaging in atherosclerotic rabbit models should be continued to validate the findings presented in this thesis in a larger number of rabbits. This will enable a meaningful analysis in regards to how robust NIRF-IVUS imaging is for detection of atherosclerotic markers in vivo. As a next step, NIRF-IVUS imaging needs to be validated in a beating heart which resembles human conditions more closely than imaging experiments in illiac arteries of rabbits. For this purpose, an in vivo study should be designed to apply NIRF-IVUS imaging in pig coronary arteries. These experiments will be a realistic test for in vivo human applications since the anatomy of pig and human hearts are similar. In vivo imaging in pig coronary arteries will also enable a safety study according to good laboratory practices (GLP) to validate the risk-free application of NIRF-IVUS catheters. Major challenges for intravascular NIRF-IVUS imaging can be expected during these experiments. These can be summarized as i) a higher prevalence of catheter bending which will significantly enhance helical pullback friction, ii) tissue motion which could result in imaging artefacts and iii) a increased vessel lumen which will hold a larger blood volume between the catheter sheath and the vascular wall and, thus, will increase attenuation of NIRF signals compared to imaging in rabbits.

3) **First human clinical trail:** In order to apply for a clinical investigation of the NIRF-IVUS imaging technology in the form of a first-in-human trial, an investigator's brochure and a clinical investigation plan needs to be prepared. The brochure needs to provide information for identification and description of the NIRF-IVUS imaging catheter including instructions for use and maintenance. Furthermore, pre-clinical data needs to be summarized and aspects regarding the fulfillment of the safety requirements need to be addressed. This should include a report of the GLP safety study and a risk-benefit analysis. Ultimately, catheter production will need to be outsourced to a medical device manufacturer which can deliver NIRF-IVUS catheter that comply with the requirements for medical design and manufacture of of EU Medical Device Regulations, article 62 & Annex I, chapter II as well as respective ISO norms (14155 & 10993).

List of Figures

List of Tables

Bibliography

[1] https://www.who.int/news-room/fact-sheets/detail/cardiovascular-diseases-(cvds). Accessed: 2023-01-17.

[2] J. Stewart, G. Manmathan, and P. Wilkinson, "Primary prevention of cardiovascular disease: A review of contemporary guidance and literature," *JRSM Cardiovasc Dis*, vol. 6, p. 2048004016687211, 2017.

[3] M. J. Davies, N. Woolf, and W. B. Robertson, "Pathology of acute myocardial-infarction with particular reference to occlusive coronary thrombi," *British Heart Journal*, vol. 38, no. 7, pp. 659–664, 1976.

[4] E. G. Nabel, "A tale of coronary artery disease and myocardial infarction (vol 366, pg 54, 2012)," *New England Journal of Medicine*, vol. 366, no. 10, pp. 970–970, 2012.

[5] J. C. Brown, T. E. Gerhardt, and E. Kwon, *Risk Factors For Coronary Artery Disease*. 2022. Brown, Jonathan C. Gerhardt, Thomas E. Kwon, Edward Study Guide Book Chapter.

[6] K. Thayse, N. Kindt, S. Laurent, and S. Carlier, "Vcam-1 target in non-invasive imaging for the detection of atherosclerotic plaques," *Biology (Basel)*, vol. 9, no. 11, 2020.

[7] S. R. Botts, J. E. Fish, and K. L. Howe, "Dysfunctional vascular endothelium as a driver of atherosclerosis: Emerging insights into pathogenesis and treatment," *Front Pharmacol*, vol. 12, p. 787541, 2021.

[8] C. Stefanadis, C. K. Antoniou, D. Tsiachris, and P. Pietri, "Coronary atherosclerotic vulnerable plaque: Current perspectives," *Journal of the American Heart Association*, vol. 6, no. 3, 2017.

[9] P. A. Cahill and E. M. Redmond, "Vascular endothelium - gatekeeper of vessel health," *Atherosclerosis*, vol. 248, pp. 97–109, 2016.

[10] R. Ross, "The pathogenesis of atherosclerosis - a perspective for the 1990s," *Nature*, vol. 362, no. 6423, pp. 801–809, 1993.

[11] K. S. Cunningham and A. I. Gotlieb, "The role of shear stress in the pathogenesis of atherosclerosis (vol 85, pg 9, 2005)," *Laboratory Investigation*, vol. 85, no. 7, pp. 942–942, 2005.

[12] K. Skalen, M. Gustafsson, E. K. Rydberg, L. M. Hulten, O. Wiklund, T. L. Innerarity, and J. Boren, "Subendothelial retention of atherogenic lipoproteins in early atherosclerosis," *Nature*, vol. 417, no. 6890, pp. 750–754, 2002.

[13] X. Shi, J. Gao, Q. S. Lv, H. D. Cai, F. Wang, R. D. Ye, and X. F. Liu, "Calcification in atherosclerotic plaque vulnerability: Friend or foe?," *Frontiers in Physiology*, vol. 11, 2020.

[14] G. Pugliese, C. Iacobini, C. B. Fantauzzi, and S. Menini, "The dark and bright side of atherosclerotic calcification," *Atherosclerosis*, vol. 238, no. 2, pp. 220–230, 2015.

[15] K. Yahagi, F. D. Kolodgie, F. Otsuka, A. V. Finn, H. R. Davis, M. Joner, and R. Virmani, "Pathophysiology of native coronary, vein graft, and in-stent atherosclerosis," *Nat Rev Cardiol*, vol. 13, no. 2, pp. 79–98, 2016.

[16] R. Kramme, K. P. Hoffmann, and R. Pozos, *Handbook of Medical Technology*. Springer, 2011.

[17] D. Kane, W. Grassi, R. Sturrock, and P. V. Balint, "A brief history of musculoskeletal ultrasound: 'from bats and ships to babies and hips'," *Rheumatology (Oxford)*, vol. 43, no. 7, pp. 931–3, 2004.

[18] K. Dussik, "On the possibility of using ultrasound waves as adiagnostic aid," *Zeitschrift für Neurologie und Psychatrie*, 1942.

[19] T. L. Szabo and P. A. Lewin, "Piezoelectric materials for imaging," *Journal of Ultrasound in Medicine*, 2007.

[20] S. Bridal, J. Correas, and G. Berger, *Ultrasound Imaging*, book section 3, pp. 79–101. 2007.

[21] Q. Zhou, K. H. Lam, H. Zheng, W. Qiu, and K. K. Shung, "Piezoelectric single crystal ultrasonic transducers for biomedical applications," *Progress in Materials Science*, vol. 66, pp. 87–111, 2014.

[22] A. G. Webb, *Introduction to Biomedical Imaging*. John Wiley and Sons, 2003.

[23] W. Mcdicken and T. Anderson, *Basic physics of medical ultrasound*. 2011.

[24] A. Soubret and V. Ntziachristos, *Optical Imaging and Tomography*, book section 5, pp. 149–181. John Wiley and Sons, 2007.

[25] V. Ntziachristos, "Fluorescence molecular imaging," *Annu Rev Biomed Eng*, vol. 8, pp. 1–33, 2006.

[26] M. Monici, *Cell and tissue autofluorescence research and diagnostic applications*, pp. 227–256. Biotechnology Annual Review, 2005.

[27] A. N. Bashkatov, E. A. Genina, V. I. Kochubey, and V. V. Tuchin, "Optical properties of human skin, subcutaneous and mucous tissues in the wavelength range from 400 to 2000nm," *Journal of Physics D: Applied Physics*, vol. 38, no. 15, pp. 2543–2555, 2005.

[28] N. Bosschaart, G. J. Edelman, M. C. Aalders, T. G. van Leeuwen, and D. J. Faber, "A literature review and novel theoretical approach on the optical properties of whole blood," *Lasers Med Sci*, vol. 29, no. 2, pp. 453–79, 2014.

[29] F. Martelli, S. Del Bianco, A. Ismaelli, and G. Zaccanti, *Light Propagation Through Biological Tissue and Other Diffusive Media*. SPIE, 2010.

[30] V. Ntziachristos, C. Bremer, and R. Weissleder, "Fluorescence imaging with near-infrared light: new technological advances that enable in vivo molecular imaging," *Eur Radiol*, vol. 13, no. 1, pp. 195–208, 2003.

[31] J. T. Alander, I. Kaartinen, A. Laakso, T. Patila, T. Spillmann, V. V. Tuchin, M. Venermo, and P. Valisuo, "A review of indocyanine green fluorescent imaging in surgery," *Int J Biomed Imaging*, vol. 2012, p. 940585, 2012.

[32] M. V. Marshall, J. C. Rasmussen, I. C. Tan, M. B. Aldrich, K. E. Adams, X. Wang, C. E. Fife, E. A. Maus, L. A. Smith, and E. M. Sevick-Muraca, "Near-infrared fluorescence imaging in humans with indocyanine green: A review and update," *Open Surg Oncol J*, vol. 2, no. 2, pp. 12–25, 2010.

[33] S. Luo, E. Zhang, Y. Su, T. Cheng, and C. Shi, "A review of nir dyes in cancer targeting and imaging," *Biomaterials*, vol. 32, no. 29, pp. 7127–38, 2011.

[34] E. D. Cosco, I. Lim, and E. M. Sletten, "Photophysical properties of indocyanine green in the shortwave infrared region," *ChemPhotoChem*, vol. 5, no. 8, pp. 727–734, 2021.

[35] https://www.thermofisher.com/de/de/home/references/molecular-probes-the-handbook/tables/fluorescence-quantum-yields-and-lifetimes-for-alexa-fluor-dyes.html. Accessed: 2023-01-17.

[36] https://www.aatbio.com/resources/quantum-yield/cy7_cyanine_7. Accessed: 2023-01-17.

[37] S. Zhu, R. Tian, A. L. Antaris, X. Chen, and H. Dai, "Near-infrared-ii molecular dyes for cancer imaging and surgery," *Adv Mater*, vol. 31, no. 24, p. e1900321, 2019.

[38] P. D. Adamson and D. E. Newby, "Non-invasive imaging of the coronary arteries," *Eur Heart J*, vol. 40, no. 29, pp. 2444–2454, 2019.

[39] B. Brooks, "Intra-arterial injection of sodium iodid," *Journal of the American Medical Association*, 1924.

[40] E. Moniz, "The arterial encephalography its importance in the location of cerebral tumors," *Revue Neurologique*, vol. 48, pp. 72–89, 1927.

[41] P. Garrone, G. Biondi-Zoccai, I. Salvetti, N. Sina, I. Sheiban, P. R. Stella, and P. Agostoni, "Quantitative coronary angiography in the current era: principles and applications," *J Interv Cardiol*, vol. 22, no. 6, pp. 527–36, 2009.

[42] S. Napel, M. P. Marks, G. D. Rubin, M. D. Dake, C. H. McDonnell, S. M. Song, D. R. Enzmann, and J. Jeffrey, R. B., "Ct angiography with spiral ct and maximum intensity projection," *Radiology*, vol. 185, no. 2, pp. 607–10, 1992.

[43] S. Achenbach, "Computed tomography coronary angiography," *J Am Coll Cardiol*, vol. 48, no. 10, pp. 1919–28, 2006.

[44] C. Thomsen and J. Abdulla, "Characteristics of high-risk coronary plaques identified by computed tomographic angiography and associated prognosis: a systematic review and meta-analysis," *European Heart Journal-Cardiovascular Imaging*, vol. 17, no. 2, pp. 120–129, 2016.

[45] R. Hajhosseiny, A. Bustin, C. Munoz, I. Rashid, G. Cruz, W. J. Manning, C. Prieto, and R. M. Botnar, "Coronary magnetic resonance angiography: Technical innovations leading us to the promised land?," *JACC Cardiovasc Imaging*, vol. 13, no. 12, pp. 2653–2672, 2020.

[46] K. Hirai, T. Kido, T. Kido, R. Ogawa, Y. Tanabe, M. Nakamura, N. Kawaguchi, A. Kurata, K. Watanabe, O. Yamaguchi, M. Schmidt, C. Forman, and T. Mochizuki, "Feasibility of contrast-enhanced coronary artery magnetic resonance angiography using compressed sensing," *J Cardiovasc Magn Reson*, vol. 22, no. 1, p. 15, 2020.

[47] J. P. Finn, K. Nael, V. Deshpande, O. Ratib, and G. Laub, "Cardiac mr imaging: State of the technology," *Radiology*, vol. 241, no. 2, pp. 338–354, 2006.

[48] B. Tavitian, R. Trébossen, R. Pasqualini, and F. Dollé, *In Vivo Radiotracer Imaging - Textbook of in vivo Imaging in Vertebrates*, book section 4, pp. 103–147. Wiley and Sons, 2007.

[49] N. V. Joshi, A. T. Vesey, M. C. Williams, A. S. V. Shah, P. A. Calvert, F. H. M. Craighead, S. E. Yeoh, W. Wallace, D. Salter, A. M. Fletcher, E. J. R. van Beek, A. D. Flapan, N. G. Uren, M. W. H. Behan, N. L. M. Cruden, N. L. Mills, K. A. A. Fox, J. H. F. Rudd, M. R. Dweck, and D. E. Newby, "F-18-fluoride positron emission tomography for identification of ruptured and high-risk coronary atherosclerotic plaques: a prospective clinical trial," *Lancet*, vol. 383, no. 9918, pp. 705–713, 2014.

[50] G. S. Mintz and G. Guagliumi, "Intravascular imaging in coronary artery disease," *The Lancet*, vol. 390, no. 10096, pp. 793–809, 2017.

[51] G. van Soest, L. Marcu, B. E. Bouma, and E. Regar, "Intravascular imaging for characterization of coronary atherosclerosis," *Current Opinion in Biomedical Engineering*, vol. 3, pp. 1–12, 2017.

[52] J. Wild and J. Reid, "Examination by 15mc pulsed ultrasound," in *Ultrasound in Biology and Medicine: A Symposium*, p. 30, American Institute of Biological Sciences.

[53] N. Bom, C. T. Lancée, and F. C. Van Egmond, "An ultrasonic intracardiac scanner," *Ultrasonics*, vol. 10, no. 2, pp. 72–76, 1972.

[54] P. G. Yock, D. T. Linker, B. A. J. Angelsen, and Tech, "Two-dimensional intravascular ultrasound: Technical development and initial clinical experience," *Journal of the American Society of Echocardiography*, vol. 2, no. 4, pp. 296–304, 1989.

[55] D. Huang, E. A. Swanson, C. P. Lin, J. S. Schuman, W. G. Stinson, W. Chang, M. R. Hee, T. Flotte, K. Gregory, C. A. Puliafito, and J. G. Fujimoto, "Optical coherence tomography," *Science*, vol. 254, no. 5035, pp. 1178–1181, 1991.

[56] M. E. Brezinski, G. J. Tearney, B. E. Bouma, J. A. Izatt, M. R. Hee, E. A. Swanson, J. F. Southern, and J. G. Fujimoto, "Optical coherence tomography for optical biopsy - properties and demonstration of vascular pathology," *Circulation*, vol. 93, no. 6, pp. 1206–1213, 1996.

[57] T. Roleder, J. Jakala, G. L. Kaluza, L. Partyka, K. Proniewska, E. Pociask, W. Zasada, W. Wojakowski, Z. Gasior, and D. Dudek, "The basics of intravascular optical coherence tomography," *Postepy Kardiol Interwencyjnej*, vol. 11, no. 2, pp. 74–83, 2015.

[58] D. Ochijewicz, M. Tomaniak, L. Koltowski, A. Rdzanek, A. Pietrasik, and J. Kochman, "Intravascular imaging of coronary artery disease: recent progress and future directions," *J Cardiovasc Med (Hagerstown)*, vol. 18, no. 10, pp. 733–741, 2017.

[59] M. Ono, H. Kawashima, H. Hara, C. Gao, R. Wang, N. Kogame, K. Takahashi, P. Chichareon, R. Modolo, M. Tomaniak, J. J. Wykrzykowska, J. J. Piek, I. Mori, B. K. Courtney, W. Wijns, F. Sharif, C. Bourantas, Y. Onuma, and P. W. Serruys, "Advances in ivus/oct and future clinical perspective of novel hybrid catheter system in coronary imaging," *Front Cardiovasc Med*, vol. 7, p. 119, 2020.

[60] T. Ma, M. Yu, Z. Chen, C. Fei, K. Shung, and Q. Zhou, "Multi-frequency intravascular ultrasound (ivus) imaging," *IEEE Transactions on Ultrasonics, Ferroelectrics, and Frequency Control*, vol. 62, no. 1, pp. 97–107, 2015.

[61] Z. A. Ali, A. Maehara, P. Généreux, R. A. Shlofmitz, F. Fabbiocchi, T. M. Nazif, G. Guagliumi, P. M. Meraj, F. Alfonso, H. Samady, T. Akasaka, E. B. Carlson, M. A. Leesar, M. Matsumura, M. O. Ozan, G. S. Mintz, O. Ben-Yehuda, and G. W. Stone, "Optical coherence tomography compared with intravascular ultrasound and with angiography to guide coronary stent implantation (ilumien iii: Optimize pci): a randomised controlled trial," *The Lancet*, vol. 388, no. 10060, pp. 2618–2628, 2016.

[62] J. S. Jang, Y. J. Song, W. Kang, H. Y. Jin, J. S. Seo, T. H. Yang, D. K. Kim, K. I. Cho, B. H. Kim, Y. H. Park, H. G. Je, and D. S. Kim, "Intravascular ultrasound-guided implantation of drug-eluting stents to improve outcome: a meta-analysis," *JACC Cardiovasc Interv*, vol. 7, no. 3, pp. 233–43, 2014.

[63] S. J. Hong, B. K. Kim, D. H. Shin, C. M. Nam, J. S. Kim, Y. G. Ko, D. Choi, T. S. Kang, W. C. Kang, A. Y. Her, Y. H. Kim, S. H. Hur, B. K. Hong, H. Kwon, Y. Jang, M. K. Hong, and I.-X. Investigators, "Effect of intravascular ultrasound-guided vs angiography-guided everolimus-eluting stent implantation: The ivus-xpl randomized clinical trial," *JAMA*, vol. 314, no. 20, pp. 2155–63, 2015.

[64] N. Meneveau, G. Souteyrand, P. Motreff, C. Caussin, N. Amabile, P. Ohlmann, O. Morel, Y. Lefrancois, V. Descotes-Genon, J. Silvain, N. Braik, R. Chopard, M. Chatot, F. Ecarnot, H. Tauzin, E. Van Belle, L. Belle, and F. Schiele, "Optical coherence tomography to optimize results of percutaneous coronary intervention in patients with non-st-elevation acute coronary syndrome: Results of the multicenter, randomized doctors study (does optical coherence tomography optimize results of stenting)," *Circulation*, vol. 134, no. 13, pp. 906–17, 2016.

[65] M. Moore, T. Spencer, D. Salter, P. Kearney, T. Shaw, I. Starkey, P. Fitzgerald, R. Erbel, A. Lange, N. McDicken, G. Sutherland, and K. Fox, "Characterisation of coronary atherosclerotic morphology by spectral analysis of radiofrequency signal: in vitro intravascular ultrasound study with histological and radiological validation," *Heart*, vol. 79(5), 1998.

[66] A. Nair, B. D. Kuban, E. M. Tuzcu, P. Schoenhagen, S. E. Nissen, and D. G. Vince, "Coronary plaque classification with intravascular ultrasound radiofrequency data analysis," *Circulation*, vol. 106, no. 17, pp. 2200–6, 2002.

[67] G. W. Stone, A. Maehara, A. J. Lansky, B. De Bruyne, E. Cristea, G. S. Mintz, R. Mehran, J. McPherson, N. Farhat, S. P. Marso, H. Parise, B. Templin, R. White, Z. Zhang, and P. W. Serruys, "A prospective natural-history study of coronary atherosclerosis," *New England Journal of Medicine*, vol. 364, no. 3, pp. 226–235, 2011.

[68] S. E. Nissen, "Ivus virtual histology: Unvalidated gimmick or useful technique?," *J Am Coll Cardiol*, vol. 67, no. 15, pp. 1784–1785, 2016.

[69] H. Khraishah and F. A. Jaffer, "Intravascular molecular imaging: Near-infrared fluorescence as a new frontier," *Front Cardiovasc Med*, vol. 7, p. 587100, 2020.

[70] S. Waxman, F. Ishibashi, and J. D. Caplan, "Rationale and use of near-infrared spectroscopy for detection of lipid-rich and vulnerable plaques," *J Nucl Cardiol*, vol. 14, no. 5, pp. 719–28, 2007.

[71] S. Waxman, S. R. Dixon, P. L'Allier, J. W. Moses, J. L. Petersen, D. Cutlip, J. C. Tardif, R. W. Nesto, J. E. Muller, M. J. Hendricks, S. T. Sum, C. M. Gardner, J. A. Goldstein, G. W. Stone, and M. W. Krucoff, "In vivo validation of a catheter-based near-infrared spectroscopy system for detection of lipid core coronary plaques: initial results of the spectacl study," *JACC Cardiovasc Imaging*, vol. 2, no. 7, pp. 858–68, 2009.

[72] C. M. Gardner, H. Tan, E. L. Hull, J. B. Lisauskas, S. T. Sum, T. M. Meese, C. Jiang, S. P. Madden, J. D. Caplan, A. P. Burke, R. Virmani, J. Goldstein, and J. E. Muller, "Detection of lipid core coronary plaques in autopsy specimens with a novel catheter-based near-infrared spectroscopy system," *JACC Cardiovasc Imaging*, vol. 1, no. 5, pp. 638–48, 2008.

[73] A. S. Schuurman, M. Vroegindewey, I. Kardys, R. M. Oemrawsingh, J. M. Cheng, S. de Boer, H. M. Garcia-Garcia, R. J. van Geuns, E. S. Regar, J. Daemen, N. M. van Mieghem, P. W. Serruys, E. Boersma, and K. M. Akkerhuis, "Near-infrared spectroscopy-derived lipid core burden index predicts adverse cardiovascular outcome in patients with coronary artery disease during long-term follow-up," *Eur Heart J*, vol. 39, no. 4, pp. 295–302, 2018.

[74] M. Wu, G. Springeling, M. Lovrak, F. Mastik, S. Iskander-Rizk, T. Wang, H. M. van Beusekom, A. F. van der Steen, and G. Van Soest, "Real-time volumetric lipid imaging in vivo by intravascular photoacoustics at 20 frames per second," *Biomed Opt Express*, vol. 8, no. 2, pp. 943–953, 2017.

[75] Y. Cao, J. Hui, A. Kole, P. Wang, Q. Yu, W. Chen, M. Sturek, and J. X. Cheng, "High-sensitivity intravascular photoacoustic imaging of lipid-laden plaque with a collinear catheter design," *Sci Rep*, vol. 6, p. 25236, 2016.

[76] J. Hui, Y. Cao, Y. Zhang, A. Kole, P. Wang, G. Yu, G. Eakins, M. Sturek, W. Chen, and J. X. Cheng, "Real-time intravascular photoacoustic-ultrasound imaging of lipid-laden plaque in human coronary artery at 16 frames per second," *Sci Rep*, vol. 7, no. 1, p. 1417, 2017.

[77] H. Qin, Y. Zhao, J. Zhang, X. Pan, S. H. Yang, and D. Xing, "Inflammation-targeted gold nanorods for intravascular photoacoustic imaging detection of matrix metalloproteinase-2 (mmp2) in atherosclerotic plaques," *Nanomedicine-Nanotechnology Biology and Medicine*, vol. 12, no. 7, pp. 1765–1774, 2016.

[78] B. Wang, A. Karpiouk, D. Yeager, J. Amirian, S. Litovsky, R. Smalling, and S. Emelianov, "Intravascular photoacoustic imaging of lipid in atherosclerotic plaques in the presence of luminal blood," *Opt Lett*, vol. 37, no. 7, pp. 1244–6, 2012.

[79] J. Bec, D. Vela, J. E. Phipps, M. Agung, J. Unger, K. B. Margulies, J. A. Southard, L. M. Buja, and L. Marcu, "Label-free visualization and quantification of biochemical markers of atherosclerotic plaque progression using intravascular fluorescence lifetime," *JACC Cardiovasc Imaging*, vol. 14, no. 9, pp. 1832–1842, 2021.

[80] M. A. Calfon, A. Rosenthal, G. Mallas, A. Mauskapf, R. N. Nudelman, V. Ntziachristos, and F. A. Jaffer, "In vivo near infrared fluorescence (nirf) intravascular molecular imaging of inflammatory plaque, a multimodal approach to imaging of atherosclerosis," *J Vis Exp*, no. 54, 2011.

[81] F. A. Jaffer, M. A. Calfon, A. Rosenthal, G. Mallas, R. N. Razansky, A. Mauskapf, R. Weissleder, P. Libby, and V. Ntziachristos, "Two-dimensional intravascular near-infrared fluorescence molecular imaging of inflammation in atherosclerosis and stent-induced vascular injury," *J Am Coll Cardiol*, vol. 57, no. 25, pp. 2516–26, 2011.

[82] H. Yoo, J. W. Kim, M. Shishkov, E. Namati, T. Morse, R. Shubochkin, J. R. McCarthy, V. Ntziachristos, B. E. Bouma, F. A. Jaffer, and G. J. Tearney, "Intra-arterial catheter for simultaneous microstructural and molecular imaging in vivo," *Nat Med*, vol. 17, no. 12, pp. 1680–4, 2011.

[83] S. Lee, M. W. Lee, H. S. Cho, J. W. Song, H. S. Nam, D. J. Oh, K. Park, W. Y. Oh, H. Yoo, and J. W. Kim, "Fully integrated high-speed intravascular optical coherence tomography/near-infrared fluorescence structural/molecular imaging in vivo using a clinically available near-infrared fluorescence-emitting indocyanine green to detect inflamed lipid-rich atheromata in coronary-sized vessels," *Circ Cardiovasc Interv*, vol. 7, no. 4, pp. 560–9, 2014.

[84] S. Kim, M. W. Lee, T. S. Kim, J. W. Song, H. S. Nam, H. S. Cho, S. J. Jang, J. Ryu, D. J. Oh, D. G. Gweon, S. H. Park, K. Park, W. Y. Oh, H. Yoo, and J. W. Kim, "Intracoronary dual-modal optical coherence tomography-near-infrared fluorescence structural-molecular imaging with a clinical dose of indocyanine green for the assessment of high-risk plaques and stent-associated inflammation in a beating coronary artery," *Eur Heart J*, vol. 37, no. 37, pp. 2833–2844, 2016.

[85] J. W. Verjans, E. A. Osborn, G. J. Ughi, M. A. Calfon Press, E. Hamidi, A. P. Antoniadis, M. I. Papafaklis, M. F. Conrad, P. Libby, P. H. Stone, R. P. Cambria, G. J. Tearney, and F. A. Jaffer, "Targeted near-infrared fluorescence imaging of atherosclerosis: Clinical and intracoronary evaluation of indocyanine green," *JACC Cardiovasc Imaging*, vol. 9, no. 9, pp. 1087–1095, 2016.

[86] A. J. Dixon and J. A. Hossack, "Intravascular near-infrared fluorescencecatheter with ultrasound guidance andblood attenuation correction," *Journal of Biomedical Optics*, 2013.

[87] M. Abran, G. Cloutier, M. H. Cardinal, B. Chayer, J. C. Tardif, and F. Lesage, "Development of a photoacoustic, ultrasound and fluorescence imaging catheter for the study of atherosclerotic plaque," *IEEE Trans Biomed Circuits Syst*, vol. 8, no. 5, pp. 696–703, 2014.

[88] M. Abran, B. E. Stahli, N. Merlet, T. Mihalache-Avram, M. Mecteau, E. Rheaume, D. Busseuil, J. C. Tardif, and F. Lesage, "Validating a bimodal intravascular ultrasound (ivus) and near-infrared fluorescence (nirf) catheter for atherosclerotic plaque detection in rabbits," *Biomed Opt Express*, vol. 6, no. 10, pp. 3989–99, 2015.

[89] D. Bozhko, E. A. Osborn, A. Rosenthal, J. W. Verjans, T. Hara, S. Kellnberger, G. Wissmeyer, S. V. Ovsepian, J. R. McCarthy, A. Mauskapf, A. F. Stein, F. A. Jaffer, and V. Ntziachristos, "Quantitative intravascular biological fluorescence-ultrasound imaging of coronary and peripheral arteries in vivo," *Eur Heart J Cardiovasc Imaging*, vol. 18, no. 11, pp. 1253–1261, 2017.

[90] S. Kellnberger, G. Wissmeyer, M. Albaghdadi, Z. Piao, W. Li, A. Mauskapf, P. Rauschendorfer, G. J. Tearney, V. Ntziachristos, and F. A. Jaffer, "Intravascular molecular-structural imaging with a miniaturized integrated near-infrared fluorescence and ultrasound catheter," *J Biophotonics*, vol. 14, no. 10, p. e202100048, 2021.

[91] M. Joner, A. V. Finn, A. Farb, E. K. Mont, F. D. Kolodgie, E. Ladich, R. Kutys, K. Skorija, H. K. Gold, and R. Virmani, "Pathology of drug-eluting stents in humans: delayed healing and late thrombotic risk," *J Am Coll Cardiol*, vol. 48, no. 1, pp. 193–202, 2006.

[92] G. Nakazawa, F. Otsuka, M. Nakano, M. Vorpahl, S. K. Yazdani, E. Ladich, F. D. Kolodgie, A. V. Finn, and R. Virmani, "The pathology of neoatherosclerosis in human coronary implants bare-metal and drug-eluting stents," *J Am Coll Cardiol*, vol. 57, no. 11, pp. 1314–22, 2011.

[93] B. E. Veseli, P. Perrotta, G. R. A. De Meyer, L. Roth, C. Van der Donckt, W. Martinet, and G. R. Y. De Meyer, "Animal models of atherosclerosis," *European Journal of Pharmacology*, vol. 816, pp. 3–13, 2017.

[94] H. Fatakdawala, D. Gorpas, J. W. Bishop, J. Bec, D. L. Ma, J. A. Southard, K. B. Margulies, and L. Marcu, "Fluorescence lifetime imaging combined with conventional intravascular ultrasound for enhanced assessment of atherosclerotic plaques: an ex vivo study in human coronary arteries," *Journal of Cardiovascular Translational Research*, vol. 8, no. 4, pp. 253–263, 2015.

[95] B. Aernouts, R. Van Beers, R. Watte, J. Lammertyn, and W. Saeys, "Dependent scattering in intralipid (r) phantoms in the 600-1850 nm range," *Optics Express*, vol. 22, no. 5, pp. 6086–6098, 2014.

[96] W. F. Cheong, S. A. Prahl, and A. J. Welch, "A review of the optical-properties of biological tissues," *Ieee Journal of Quantum Electronics*, vol. 26, no. 12, pp. 2166–2185, 1990.

[97] M. Keijzer, R. R. Richardskortum, S. L. Jacques, and M. S. Feld, "Fluorescence spectroscopy of turbid media - autofluorescence of the human aorta," *Applied Optics*, vol. 28, no. 20, pp. 4286–4292, 1989.

[98] S. Kraler, P. Libby, P. C. Evans, A. Akhmedov, M. O. Schmiady, M. Reinehr, G. G. Camici, and T. F. Luscher, "Resilience of the internal mammary artery to atherogenesis: Shifting from risk to resistance to address unmet needs," *Arterioscler Thromb Vasc Biol*, vol. 41, no. 8, pp. 2237–2251, 2021.

[99] F. Otsuka, K. Yahagi, K. Sakakura, and R. Virmani, "Why is the mammary artery so special and what protects it from atherosclerosis?," *Ann Cardiothorac Surg*, vol. 2, no. 4, pp. 519–26, 2013.

[100] M. J. Bom, D. J. van der Heijden, E. Kedhi, J. van der Heyden, M. Meuwissen, P. Knaapen, S. A. J. Timmer, and N. van Royen, "Early detection and treatment of the vulnerable coronary plaque: Can we prevent acute coronary syndromes?," *Circ Cardiovasc Imaging*, vol. 10, no. 5, 2017.

[101] G. Mallas, D. H. Brooks, A. Rosenthal, R. N. Nudelman, A. Mauskapf, F. A. Jaffer, and V. Ntziachristos, "Improving quantification of intravascular fluorescence imaging using structural information," *Phys Med Biol*, vol. 57, no. 20, pp. 6395–406, 2012.

[102] D. Bozhko, A. Karlas, D. Gorpas, and V. Ntziachristos, "Optoacoustic sensing of hematocrit to improve the accuracy of hybrid fluorescence-ultrasound intravascular imaging," *J Biophotonics*, vol. 11, no. 10, p. e201700255, 2018.

[103] M. Friebel, J. Helfmann, G. Muller, and M. Meinke, "Influence of shear rate on the optical properties of human blood in the spectral range 250 to 1100 nm," *Journal of Biomedical Optics*, vol. 12, no. 5, 2007.

[104] A. Roggan, M. Friebel, K. Dorschel, A. Hahn, and G. Muller, "Optical properties of circulating human blood in the wavelength range 400-2500 nm," *Journal of Biomedical Optics*, vol. 4, no. 1, pp. 36–46, 1999.

[105] K. S. Sakariassen, L. Orning, and V. T. Turitto, "The impact of blood shear rate on arterial thrombus formation," *Future Science Oa*, vol. 1, no. 4, 2015.

[106] M. Friebel, J. Helfmann, U. Netz, and M. Meinke, "Influence of oxygen saturation on the optical scattering properties of human red blood cells in the spectral range 250 to 2000 nm," *Journal of Biomedical Optics*, vol. 14, no. 3, 2009.

[107] Y. Yong, M. Y. Qiao, A. Chiu, S. Fuchs, Q. S. Liu, Y. Pardo, R. Worobo, Z. Liu, and M. L. Ma, "Conformal hydrogel coatings on catheters to reduce biofouling," *Langmuir*, vol. 35, no. 5, pp. 1927–1934, 2019.

[108] A. H. Ashoka, S. H. Kong, B. Seeliger, B. Andreiuk, R. V. Soares, M. Barberio, M. Diana, and A. S. Klymchenko, "Near-infrared fluorescent coatings of medical devices for image-guided surgery," *Biomaterials*, vol. 261, 2020.

[109] M. Koch, P. Symvoulidis, and V. Ntziachristos, "Tackling standardization in fluorescence molecular imaging," *Nature Photonics*, vol. 12, no. 9, pp. 505–515, 2018.

[110] F. A. Jaffer, C. Vinegoni, M. C. John, E. Aikawa, H. K. Gold, A. V. Finn, V. Ntziachristos, P. Libby, and R. Weissleder, "Real-time catheter molecular sensing of inflammation in proteolytically active atherosclerosis," *Circulation*, vol. 118, no. 18, pp. 1802–9, 2008.

List of Publications

First author Publications

1. **Philipp Rauschendorfer**, Georg Wissmeyer, Farouc Jaffer, Dimitris Gorpas, Vasilis Ntziachristos, *Accounting for blood attenuation in intravascular near-infrared fluorescence-ultrasound imaging using a fluorophore-coated guidewire*, under revision with Journal of Biomedical Optics (14.12.22).

2. **Philipp Rauschendorfer***, Tobias Lenz*, Farouc Jaffer, Dimitris Gorpas, Michael Joner & Vasilis Ntziachristos, *Intravascular NIRF-IVUS imaging of cardiovascular disease risk factors in human coronary arteries*, under preparation.

3. **Philipp Rauschendorfer***, Claudia Hofmann*, Dimitris Gorpas, Vasilis Ntziachristos, *Intravascular NIRF-IVUS imaging for clinical use*, under preparation.

Other Publications

1. Stephan Kellnberger*, Georg Wissmeyer*, Mazen Albaghdadi, Zhonglie Piao, Wenzhu Li, Adam Mauskapf, **Philipp Rauschendorfer**, Guillermo J. Tearney, Vasilis Ntziachristos, Farouc A. Jaffer, *Intravascular molecular-structural imaging with a miniaturized integrated near-infrared fluorescence and ultrasound catheter* Journal of Biophotonics, 2021 Jun 23, Volume14, Issue10.

2. Masaru Seguchi, Alp Aytekin, Tobias Lenz, Philipp Nicol, Grace R Klosterman, Alicia Beele, Emina Sabic, Léa Utsch, Aseel Alyaqoob, Dimitris Gorpas, Vasilis Ntziachristos, Farouc A Jaffer, **Philipp Rauschendorfer**, Michael Joner, *Intravascular molecular imaging: translating pathophysiology of atherosclerosis into human disease conditions*, European Heart Journal - Cardiovascular Imaging, 25.08.2022, jeac163.

(* These authors contributed equally)

Appendix A

Histological staining of artery tissue

Staining type	Staining target	Visual appearance
Hematoxylin and Eosin (H&E)	Artery structure	Nuclei: Blue, dark purple Cytoplasm and ECM: Shades of pink
Movat Pentachrome (MP)	Artery structure	Elastic Fibers: Black to Blue/Black; Nuclei: Blue/Black; Collagen: Yellow; Reticular Fibers: Yellow; Mucin: Bright Blue; Fibrin: Bright Red; Muscle: Red
Oil Red O (ORO)	Lipids	Red
CD31	Endothelial cells	Brown
CD68	Macrophages	Brown
alpha-smooth Muscle Actin (αSMA)	Smooth muscle cells	Brown

Table A.1: Overview of histopahtologial stainings used in the framework of this thesis; ECM: Extracellular Matrix.

Appendix B

Intravascular NIRF-IVUS Imaging of ICG-perfused Human Coronary Arteries Ex Vivo

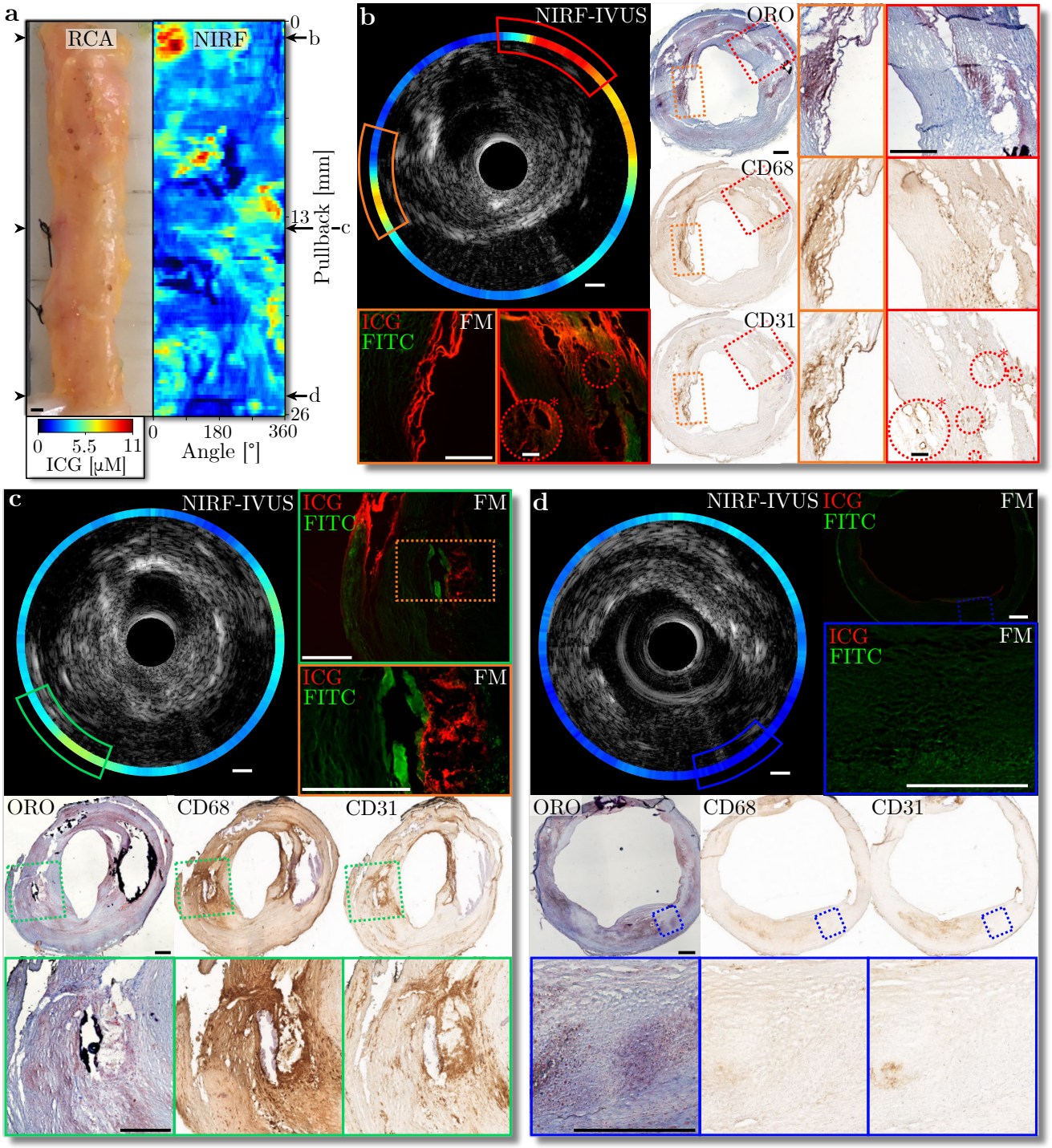
a
RCA
NIRF
0
b
13
c
26
d
Pullback [mm]
0 5.5 11
ICG [μM]
0 180 360
Angle [°]
b
NIRF-IVUS
ICG
FITC
FM
ORO
CD68
CD31
c
NIRF-IVUS
ICG
FITC
FM
ORO
CD68
CD31
d
NIRF-IVUS
ICG
FITC
FM
ORO
CD68
CD31

Figure B.1 ***(previous page)*****: Intravascular NIRF-IVUS imaging of an ICG-perfused coronary artery showing high NIRF signals in plaque areas of lipid accumulations, macrophage infiltration and neovascularization.** **a** - Picture and corresponding NIRF map of an ICG-perfused Right Coronary Artery (RCA); **b** - High NIRF signal (Red and orange box) in fibroatheroma staining positive for lipid accumulation (ORO- red and orange box), macrophage infiltration (CD68- red and orange box) and neovascularization (CD31 – circles in red box; Scale bar zoom in*: 100 μm) and corresponding ICG detection in in FM (Orange and red box; Co-registered areas of neovascularization shown as circles in red box, scale bar zoom in*: 100 μm); **c** - Increased NIRF signal (green box) in a coronary plaque region identified as fibroatheroma featuring a lipid-rich (ORO - green box) necrotic core with macrophage infiltration (CD68 – green box) and corresponding ICG detection in in FM (Green and orange box); **d** - Low NIRF signal (Blue box) in healthy tissue region without significant lipid accumulation (ORO - blue box), macrophage infiltration (CD68 – blue box) and neovascularization (CD31 – blue box) and absence of ICG detected in FM (Blue box). In all panels: NIRF: Near-infrared Fluorescence; IVUS: Intravascular Ultrasound; FM: Fluorescence Microscopy; ORO: Oil Red O; ICG: Indocyanine Green; FITC: Fluorescein channel for autofluorescence; Scale bars: 500 μm.

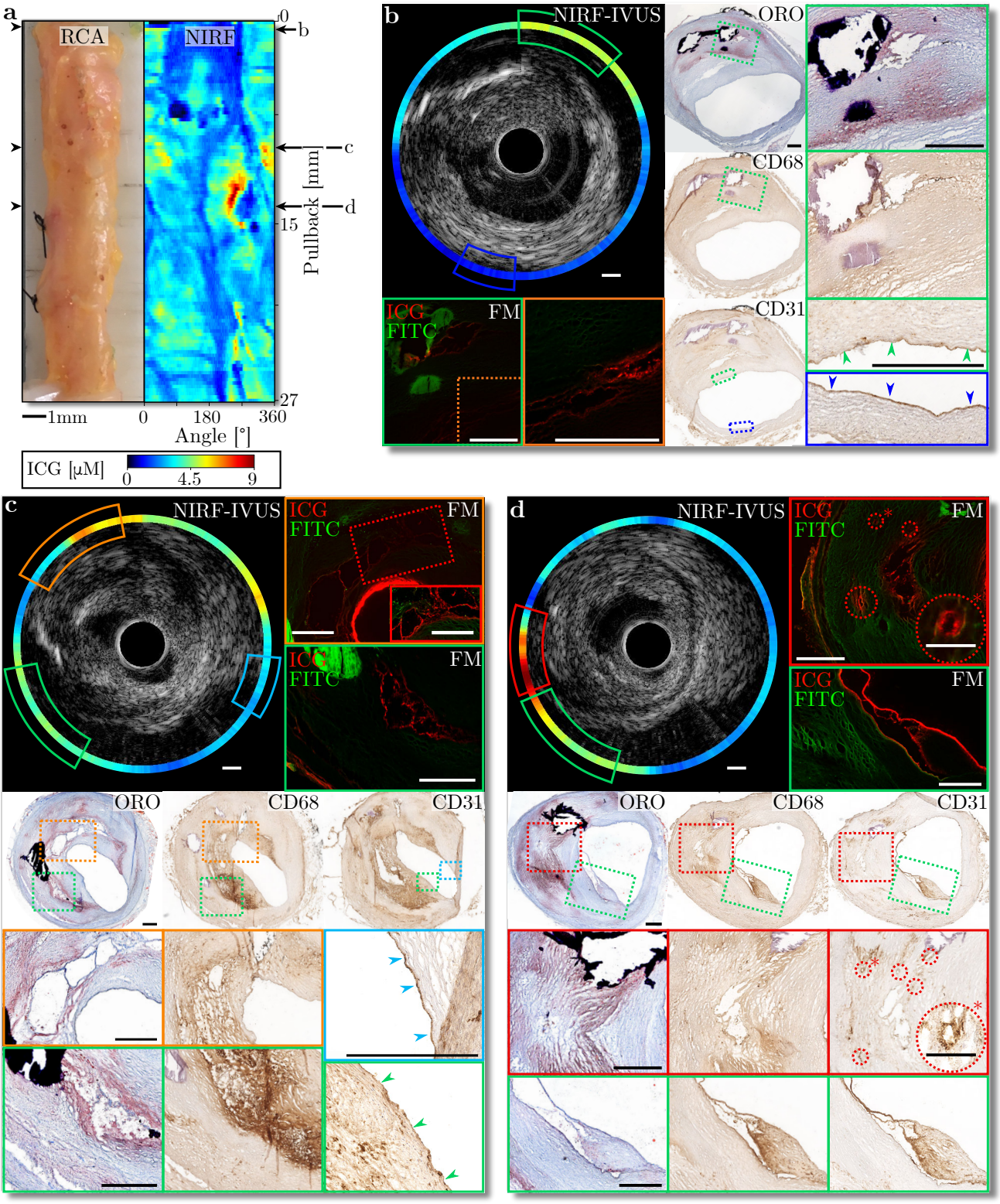
a
RCA
NIRF
0
b
c
d
15
27
Pullback [mm]
1mm
0
180
360
Angle [°]
ICG [µM]
0
4.5
9
b
NIRF-IVUS
ICG
FITC
FM
ORO
CD68
CD31
c
NIRF-IVUS
ICG
FITC
FM
ORO
CD68
CD31
d
NIRF-IVUS
ICG
FITC
FM
ORO
CD68
CD31

Figure B.2 ***(previous page)*****: Intravascular NIRF-IVUS imaging of an ICG-perfused coronary artery detects high ICG concentrations in plaque areas of lipid accumulations, macrophage infiltration, endothelial dysfunction, and neovascularization.** **a** - Picture and corresponding NIRF map of an ICG-perfused Right Coronary Artery (RCA); **b** - Increased ICG concentration detected with NIRF-IVUS (Green box) in fibroatheroma featuring areas staining positive for lipid accumulation (ORO - green box), no significant macrophage infiltration (CD 68 - blue box) and endothelial disruption (CD31 – green box) with corresponding ICG detection in FM (Green and orange box) in contrast to small ICG concentration (Blue box) found in healthy tissue region with intact endothelium (CD31 – blue box); **c** - Increased ICG concentration detected with NIRF-IVUS (Orange and green box) in fibroatheroma featuring lipid accumulation (ORO - green box), macrophage infiltration (CD68 – orange and green box) and endothelial dysfunction with corresponding ICG detection in FM (orange and red box) in contrast to small ICG concentration (Blue box) found in healthy tissue region with intact endothelium (CD31 – blue box); **d** - High ICG concentration detected with NIRF-IVUS (Red and green box) in fibroatheroma featuring lipid accumulation (ORO - red box), macrophage infiltration (CD68 – green box) and neovascularization (CD31 – circles in red box; Scale bar zoom in*: 100 μm) with corresponding ICG detection in FM (red and green box; Co-registered areas of neovascularization shown as circles in red box, scale bar zoom in*: 100 μm). In all panels: NIRF: Near-infrared Fluorescence; IVUS: Intravascular Ultrasound; FM: Fluorescence Microscopy; ORO: Oil Red O; ICG: Indocyanine Green; FITC: Fluorescein channel for autofluorescence; Scale bars: 500 μm.

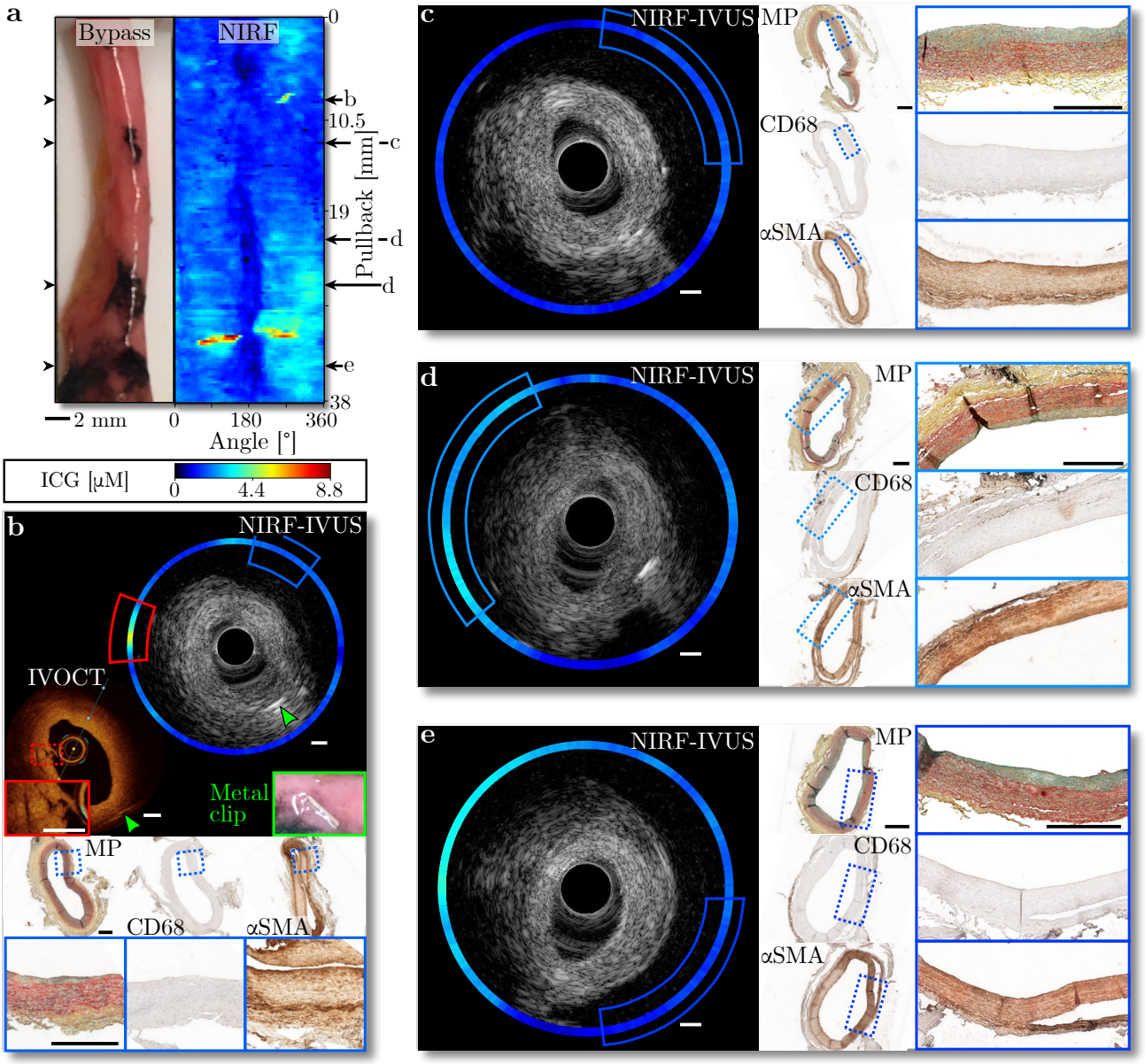

Figure B.3: Intravascular NIRF-IVUS imaging of an ICG-perfused coronary bypass detects low ICG concentrations in healthy tissue regions. a - Picture and corresponding NIRF map of an ICG-perfused bypass; **b** - Low ICG concentration detected with NIRF-IVUS (Blue box) in healthy tissue regions (MP – Blue box) without the presence of macrophages (CD68, αSMA – Blue box). Increased ICG concentration (Red box) detected with NIRF-IVUS (Red box) in a tissue area showing signs of endothelial damage visible in co-registered (Metal clip as additional angular marker – Green arrow) IVOCT (Red box); **c-e** - Low ICG concentration detected with NIRF-IVUS (Blue box) in healthy tissue regions (MP – Blue box) without the presence of macrophages (CD68, αSMA – Blue box). In all panels: NIRF: Near-infrared Fluorescence; IVUS: Intravascular Ultrasound; IVOCT: Intravascular OCT; MP: Movat Pentachrome; αSMA: alpha-smooth muscle actin; ICG: Indocyanine Green; Scale bars: 500 μm.

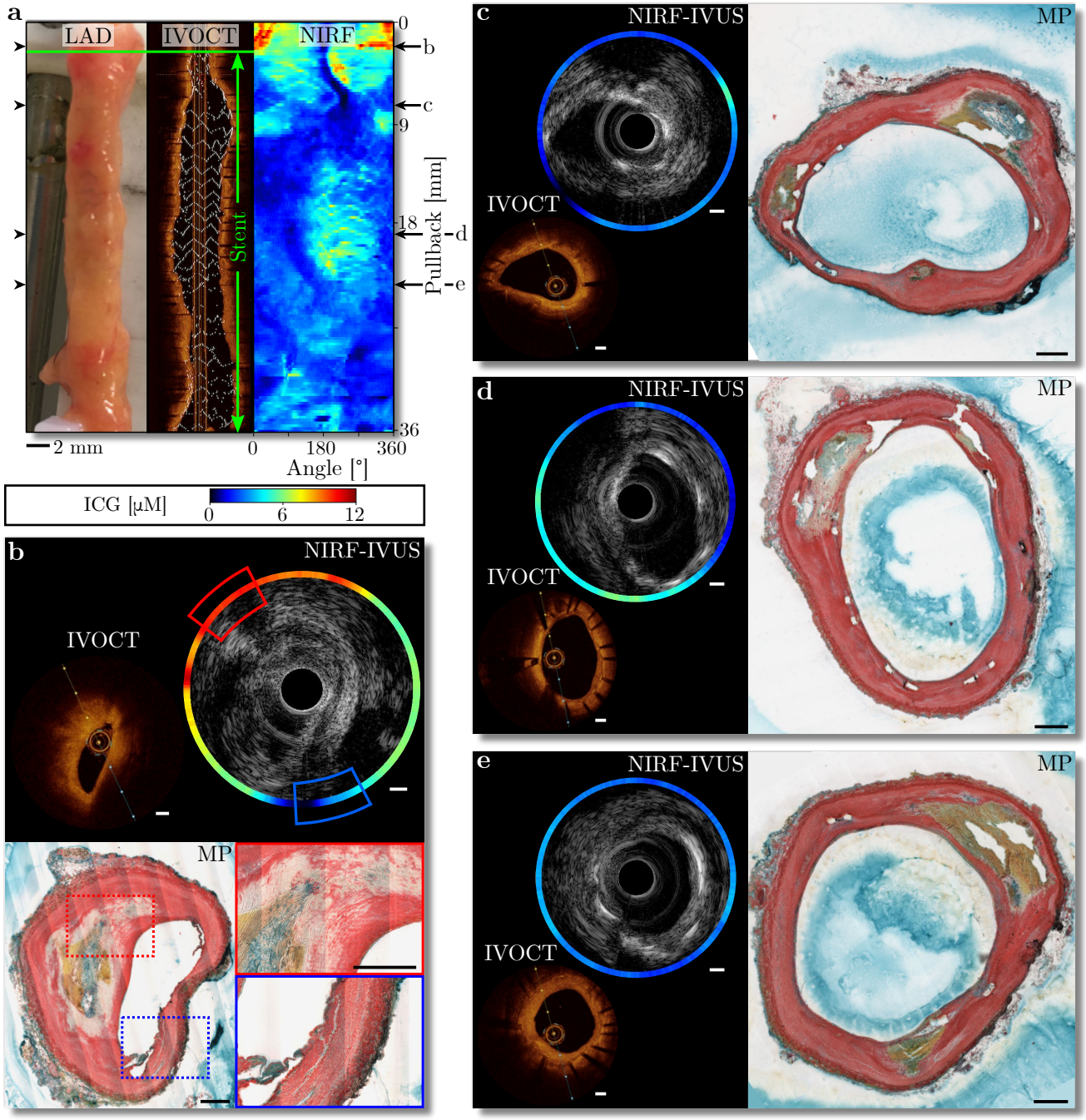

Figure B.4: Intravascular NIRF-IVUS imaging of an ICG-perfused coronary artery detects high ICG concentration in plaque area and low ICG concentrations in stented tissue regions. **a** - Picture and corresponding IVOCT and NIRF map of an ICG-perfused LAD indicating stented tissue region between the pullback positions 3mm and 36mm; **b** - High ICG concentration detected with NIRF-IVUS (Red box) in plaque area (MP – Red box) in contrast to low ICG concentration (Blue box) detected in healthy tissue region (MP – Blue box); **c-e** - Low ICG concentration detected with NIRF-IVUS in stented tissue regions; In all panels: NIRF: Near-infrared Fluorescence; IVUS: Intravascular Ultrasound; IVOCT: Intravascular OCT; MP: Movat Pentachrome; ICG: Indocyanine Green; Scale bars: 500 μm.

Appendix C

Correction of Intravascular NIRF signals for Attenuation by Blood

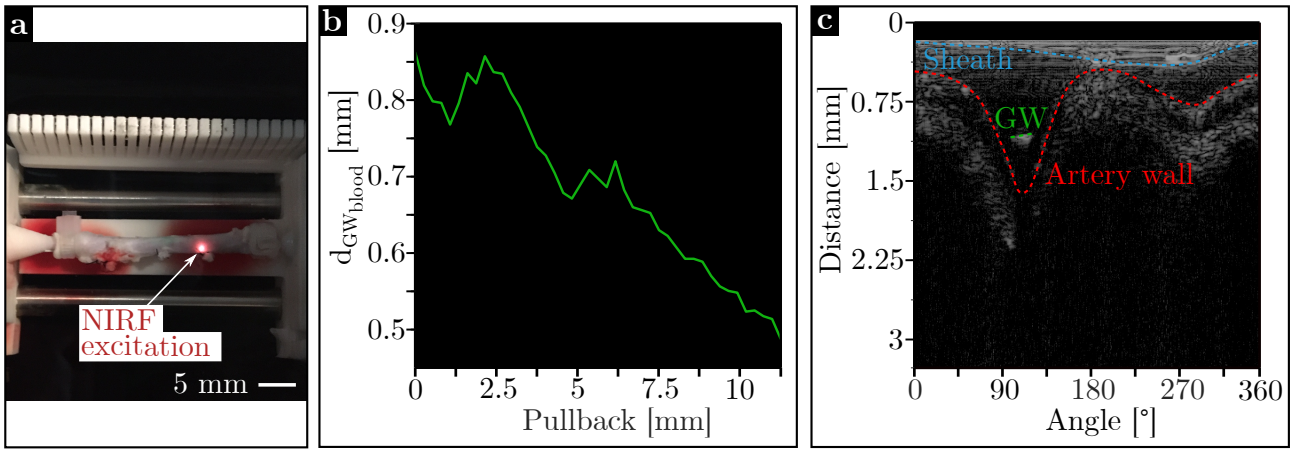

Figure C.1: Validation of the correction method in an excised pig artery - Supplementary. **a** - NIRF-IVUS measurements of a porcine coronary artery placed in a water bath and perfused with blood; **b** - Distance between the fluorophore-coated guidewire and the catheter sheath measured during blood perfused tissue measurements ($d_{GW_{blood}}$) per pullback position (frame); **c** - Exemplary IVUS imaging frame in polar coordinates showing distances from the sensor to the catheter sheath, the fluorophore-coated guidewire (GW), and the artery wall tissue.

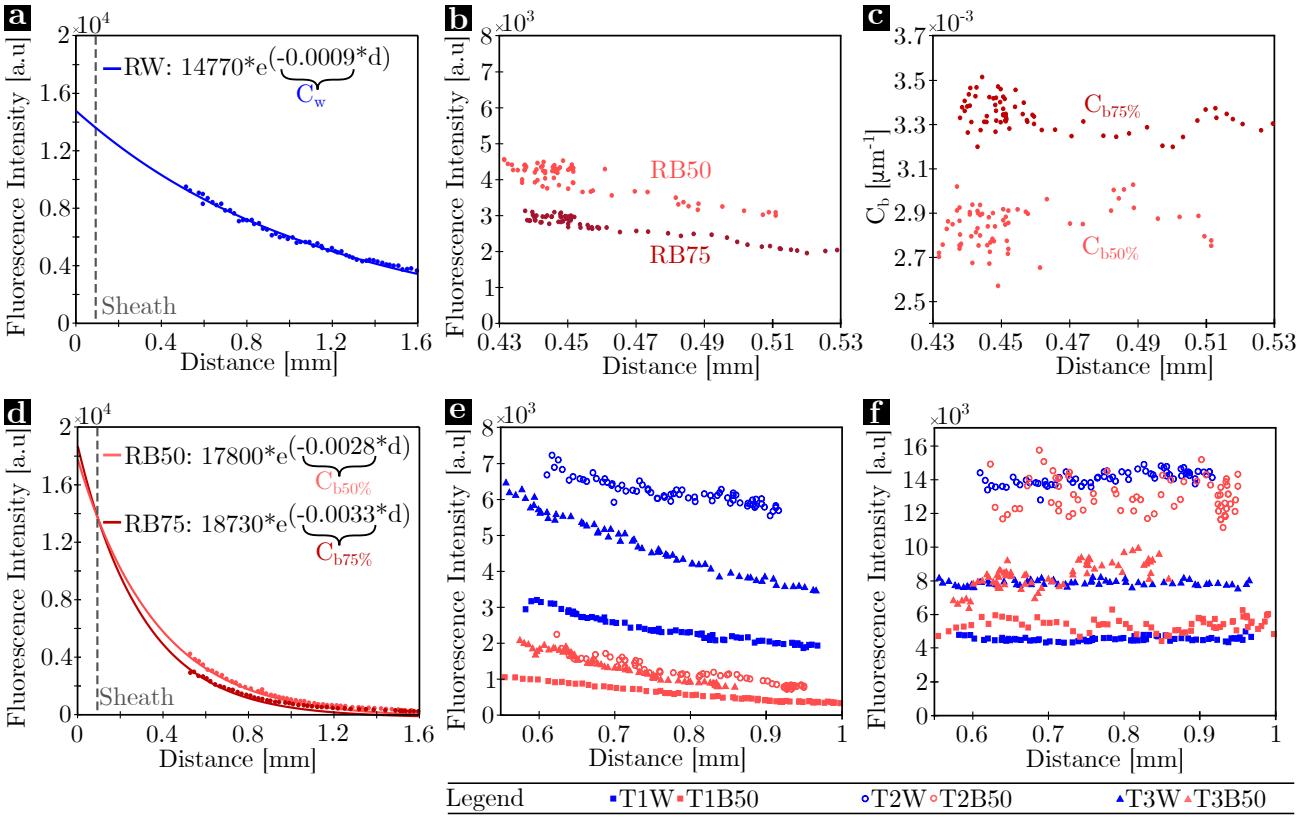

Figure C.2: Validation of correction method for intravascular NIRF with capillary phantoms - Supplementary. **a** - Measurements of the capillary-calibration phantom in water showing NIRF intensities (Averaged per frame) versus distance from the NIRF sensor to the reference capillary, with corresponding model fits (Data points shown as dots and fits as solid lines); **b** - NIRF intensity values (Averaged per frame) of the reference capillary recorded during target measurements in 50% blood (RB50) and 75% blood (RB75) at distances from the sheath wall to the reference capillary ranging between 0.43 to 0.53 mm; **c** - Calculated correction factor (C_b) for the 50% and 75% blood mixtures versus distance from the sheath wall to the reference capillary for each frame; **d** - Validation measurements for calculated values of C_b showing NIRF intensities (Averaged per frame) of the reference capillary in both blood dilutions versus distance from the NIRF sensor to the reference capillary, with corresponding model fits and values for C_b (Data points shown as dots and fits as solid lines); **e** - Acquired uncorrected NIRF intensities (Averaged per frame) from the target capillaries measured in the target phantom through water (T1-3W) and 50%-blood mixture (T1-3B50) plotted versus imaging distance between the sheath wall and capillary; **f** - Corrected NIRF intensities (IT**, averaged per frame) from the target capillaries measured in the target phantom through water (T1-3W) and 50%-blood mixture (T1-3B50) plotted versus imaging distance between the sheath wall and capillary; Annotation key: T1-3W: Target capillaries 1-3 measured in water; T1-3B50: Target capillaries 1-3 measured in 50% blood mixture; RW: Reference capillary measured in water; RB50: Reference capillary measured in 50% blood mixture; RB75: Reference capillary measured in 75% blood mixture; $C_{b50\%}$: Calculated correction factor for the 50% blood mixture; $C_{b75\%}$: Calculated correction factor for the 75% blood mixture.

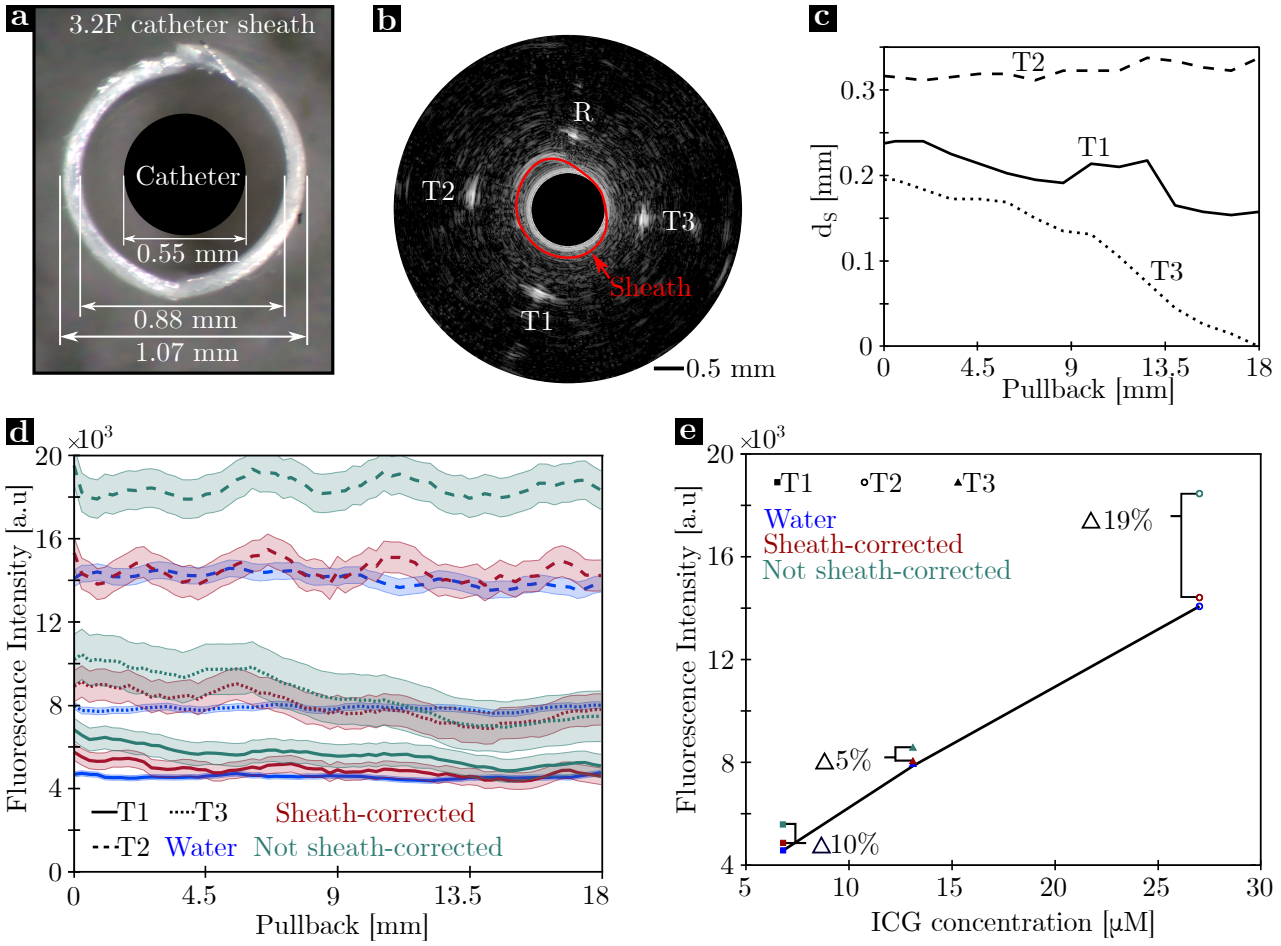

Figure C.3: Considering catheter location inside of the sheath improves overall accuracy in attenuation correction as demonstrated with measurements through 75% blood mixture in capillary phantom. **a** - Cross-sectional image visualizing the dimensions of the NIRF-IVUS catheter inserted into a size 3.2F sheath; **b** - Exemplary IVUS imaging frame showing the three target capillaries, the reference capillary and the sheath; **c** - Sensor-sheath distance (d_S) recorded by IVUS at the angular location of the three target capillaries over pullback distance; **d** - Corrected intensities of the blood measurements with and without additional sheath correction and corrected intensities measured through water as the ground truth; Averaged (n=5 Samples) intensities are shown as lines and standard deviation is shown as shaded areas; **e** - Accuracy increase of ICG quantification of target capillaries facilitated by additional sheath correction. Annotation key: T1-3: Target capillaries 1-3; R: Reference capillary.

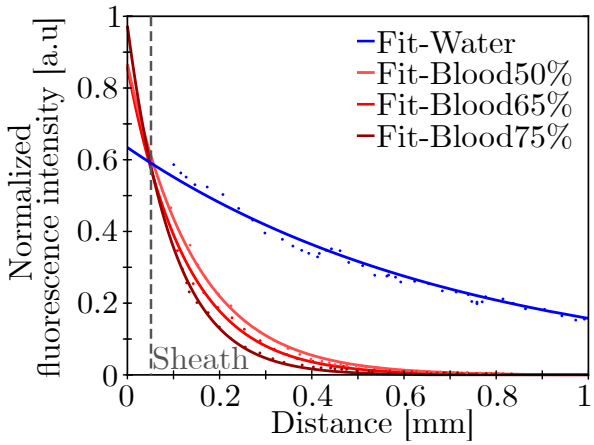

Figure C.4: NIRF measurements of the fluorophore-coated guidewire imaged through water and blood mixtures of 50, 65 and 75% with corresponding 1-term exponential model (Averaged NIRF intensities shown as points and fits as solid lines; R^2 for all fits = 0.99).